Modeling and Control of a Stewart Platform Mounted on a Moving Body

（移動体上に設置されたスチュワートプラットフォームのモデル化と制御）

防衛大学校理工学研究科後期課程

装備・基盤工学系専攻　装備システム工学教育研究分野

大野　建幸

令和３年３月

TABLE OF CONTENTS

TABLE OF CONTENTS i
LIST OF FIGURES iv
LIST OF TABLES vii
ABSTRACT OF THE DISSERTATION viii
CHAPTER 1: INTRODUCTION 10
1.1 Background 10
1.2 Previous Study for a Base-Fixed Stewart Platform 11
1.3 Previous Study for a Base-Moving Stewart Platform 11
1.4 Objectives 12
1.5 Outline of the Dissertation 12
CHAPTER 2: KINEMATICS OF A BASE-MOVING STEWART PLATFORM 14
2.1 Introduction 14
2.2 Description of a Stewart Platform 15
2.3 Configuration Space Defined by Coordinate Frames 17
2.3.1 Coordinate Frames Along Path (i) 17
2.3.2 Moving Coordinate Frames Along Path (ii) 23
2.3.3 Loop Closure Constraints 30
2.4 Velocities of the Coordinate Frames 31
2.4.1 Velocities of the Coordinate Frames along Path(i) 31
2.4.2 Velocities of the Coordinate Frames along Path(ii) 35
2.4.3 Loop Closure Constraints on Velocities 38
2.4.4 Equations for Inverse Instantaneous Kinematics 39
2.5 Implementation of Inverse Kinematics Control 40
2.6 Concluding Remarks 41

2.7 Appendix 42
2.7.1 Appendix 2.A: Kinematics for Design and Workspace Analyses 42
2.7.2 Appendix 2.B: Proof of Eq. (2.26b) 48
CHAPTER 3: KINETICS OF A BASE-MOVING STEWART PLATFORM 50
3.1 Introduction 50
3.2 The Principle of Virtual Work for Multi-Body Systems 50
3.2.1 Kinematics Using Moving Coordinate Frames 51
3.2.2 Hamilton's Principle 53
3.2.3 The Principle of Virtual Work for Multi-Body Systems 58
3.3 Equations of Motion for a Stewart Platform 60
3.3.1 Terms Associated with Variation of Kinetic Energy 61
3.3.2 Generalized Velocities and Virtual Displacements 63
3.3.3 Virtual Work of Gravitational Potential Energy 65
3.3.4 Virtual Work by Linear Actuator Forces and Damping Couples 66
3.3.5 Loop Closure Constraints on Velocities and Virtual Displacements 66
3.3.6 [B^*]-Expressions Using Essential Velocities and Displacements 68
3.3.7 Virtual Work $\delta W(t)$ and Effective Force ($F^*(t)$) 68
3.3.8 Compact Equations of Motion 70
3.3.9 Static Equilibrium Equations 71
3.4 Inverse Dynamics Control 72
3.4.1 Control Objective 72
3.4.2 Implementation of Inverse Dynamics Control 73
3.5 Experimental Results 76
3.5.1 Experimental Setup 76
3.5.2 Results and Discussion 78
3.6 Control Simulations 81
3.6.1 Nonlinear Robust Controller Design 81

3.6.2 Simulation Results and Discussion 86
3.7 Concluding Remarks 89
3.8 Appendix 90
3.8.1 Appendix 3.A: Equation of Motion for $\phi_3^{(2k/2k-1)}(t)$ 90
3.8.2 Appendix 3.B: Time Derivatives of $[B^*]$-Submatrices 90
CHAPTER 4: FORECASTING OF FUTURE BASE MOTION AND MODEL PREDICTIVE CONTROL 93
4.1 Introduction 93
4.2 Time Series Forecasting of Future Base Motion 93
4.2.1 Long Short Term Memory 94
4.2.2 LSTM Training 97
4.2.3 Real-Time Forecast 100
4.3 Model Predictive Controller Design 105
4.4 Control Simulation and Experiment Using MPC with LSTM 110
4.4.1 Settings for Control Simulation and Experiment 110
4.4.2 Simulation Results 111
4.4.3 Experimental Results 114
4.5 Concluding Remarks 117
CHAPTER 5: CONCLUSION 118
APPENDIX: PLANAR THREE DEGREES-OF-FREEDOM MANIPULATOR 119
A.1 Description of a Planar Three Degrees-Of-Freedom Manipulator 119
A.2 Kinematics of a 3-Dof Planar Platform 121
A.3 Kinetics of a 3-Dof Planar Platform 129
ACKNOWLEDGEMENTS 134
REFERENCES 135
PUBLICATIONS 140

LIST OF FIGURES

Figure 2.1: A Stewart platform 15

Figure 2.2: (a) A modified directed graph and (b) representative closed loop 16

Figure 2.3: A relative representation of the top-plate frame from the base-plate frame 17

Figure 2.4: (a) A plane view of the top plate, body-(13) and (b) an elevation for the socket of a spherical joint at T_k 21

Figure 2.5: (a) A plane view of the base plate and (b) the elevation of center of UJ cross-links, B_k, k=1,…,6 24

Figure 2.6: The rotations of UJ cross and the lower leg body-(2k-1) at B_k: 26

Figure 2.7: Coordinate frames on the k^{th} leg 27

Figure 2.8: Flowchart of inverse kinematics control of a base-moving Stewart platform 40

Figure 2.9: The workspace $s_c^{(13/0)}$ for (a) $\psi_1^{TB}(t) = \psi_2^{TB}(t) = \psi_3^{TB}(t) = 0°$, (b) $\psi_1^{TB}(t) = 10°$, $\psi_2^{TB}(t) = \psi_3^{TB}(t) = 0°$, and (c) $\psi_1^{TB}(t) = 20°$, $\psi_2^{TB}(t) = \psi_3^{TB}(t) = 0°$ 47

Figure 3.1: Subsystem velocities and virtual displacements 62

Figure 3.2: Velocities and virtual displacements of TB-subsystem and leg-(k) 64

Figure 3.3: A control flowchart of the Stewart platform compensator 74

Figure 3.4: A scale model of a Stewart platform installed on a motion generator 76

Figure 3.5: Plots of the input base-plate configuration and the controlled top-plate configuration: (a) displacement in the x_1-direction, (b) displacement in the x_2-direction, (c) displacement in the x_3-direction, (d) Tait-Bryan angle $\psi_1^{TB}(t)$, (e) Tait-Bryan angle $\psi_2^{TB}(t)$, and (f) Tait-Bryan angle $\psi_3^{TB}(t)$ 79

Figure 3.5: Block diagram of the IDC with $H\infty$ controller 81

Figure 3.6: $H\infty$ control configuration 83

Figure 3.7: Simulation results of the input base-plate configuration and the controlled top-plate configuration: (a) displacement in the x_3-direction, (b) Tait-Bryan angle $\psi_1^{TB}(t)$, (c) Tait-Bryan angle $\psi_2^{TB}(t)$ 87

Figure 3.8: RMS errors of (a) displacement in the x_3-direction, (b) Tait-Bryan angle $\psi_1^{TB}(t)$, (c) Tait-Bryan angle $\psi_2^{TB}(t)$ versus frequency change (0.1-8 Hz) 88

Figure 4.1: (a) RNN structure and (b) representation of RNN for a hidden unit over time 95

Figure 4.2: LSTM Block 96

Figure 4.3: Forecasting of the *i*th-step ahead using LSTM 97

Figure 4.4: Training and validation data 98

Figure 4.5: Comparison of training loss for different learning rates 99

Figure 4.6: Training loss and validation loss 99

Figure 4.7: (a) RMSE and (b) fitting rate for different combinations of hidden layers, units, and epochs 101

Figure 4.8: RMSE and fitting rate for different forecasting horizons 101

Figure 4.9: Real-time forecasted accelerations in (a) the longitudinal direction and (b) the lateral direction 103

Figure 4.10: Comparison of 5 steps (0.2 s) ahead forecasted longitudinal response (sudden stop) by LSTM trained with (a) data 1 and (b) data 2, and (c) ARIMA model 104

Figure 4.11: Comparison of 5 steps (0.2 s) ahead forecasted lateral response (rapid lane change) by LSTM trained with (a) data 3 and (b) data 4, and (c) ARIMA model 104

Figure 4.12: Prediction with modified constraint 109

Figure 4.13: Framework of the Stewart platform compensator with LSTM forecasting 111

Figure 4.14: Extension of the actuator 1 when applying (a) IDC and (b) MPC with LSTM forecasting 112

Figure 4.15: Input actuation force of the actuator 1 for when applying MPC with LSTM forecasting 112

Figure 4.16: Comparison of simulation results by IDC and MPC with LSTM forecasting: (a) displacement in the x_3-direction, (b) Tait-Bryan angle $\psi_1{}^{TB}(t)$, (c) Tait-Bryan angle $\psi_2{}^{TB}(t)$ 113

Figure 4.17: Real-time forecasted response of 5 steps (0.2 s) ahead Tait-Bryan angle $\psi_1{}^{TB}(t)$ by LSTM 115

Figure 4.18: Experimental results of extension of the actuator 1 when applying (a) IDC and (b) MPC with LSTM forecasting, and (c) actuation force of the actuator 1 for each control method 116

Figure 4.19: Results of Tait-Bryan angle $\psi_1{}^{TB}(t)$ of controlled top plate against the motion of the base plate for MPC with LSTM forecasting and IDC 116

Figure A.1: A planar three degrees-of-freedom manipulator 120

Figure A.2: (a) A modified directed graph and (b) representative closed loop 120

Figure A.3: Configuration of a 3-dof planar platform 121

Figure A.4: (a) A relative representation of the manipulator frame from the top-plate frame and (b) a relative representation of the T_k-frame from the top-plate frame.....123

Figure A.5: Frame connections along path(ii) 124

Figure A.6: (a) Relative representations of the B_k-frame of body-(0) from the base-plate frame, and the B_k-frame of body-(2k-1) from the B_k-frame of body-(0), and (b) Relative representations of the T_k-frame of body-(2k) from the (2k)-frame, and T_k-frame of body-(7) from the T_k-frame of body-(2k).....124

LIST OF TABLES

Table 2.1: Geometrical properties of a scale model Stewart platform.....47

Table 3.1: Dynamic properties of a scale model Stewart platform.....76

Table 3.2: Comparison of errors and compensation rates between IDC and IKC.....80

Table 3.2: RMS errors.....88

Table 4.1: MPC parameters 111

Table 4.2: Comparison of errors and compensation rates between MPC with LSTM and IDC.....116

ABSTRACT OF THE DISSERTATION

The dissertation presents modeling and control of a six degrees-of-freedom Stewart platform mounted on a moving vehicle or a ship. A Stewart platform consists of two parallel plates, referred to as top and base plates, which are connected by six actuated legs.

For safe transportation of a patient or sensitive equipment, a compensation mechanism is required to stabilize the motion induced by a vehicle or ship. In a medical room of a hospital ship, the rotation and vertical translation of the floor must be properly isolated from the wave-induced motion of the ship. On a moving vehicle, when a patient is transported by ambulance in an emergency, a patient receives accelerations in longitudinal and lateral directions. The accelerations can be reduced by actively controlling the angles of a bed. Then it becomes essential to design an active compensation system for a surgery table or bed installed on the top plate of a Stewart platform in a vehicle and ship. The contents of the dissertation are summarized as follows.

Firstly, Chapter 1 describes the background, motivation, and objective of this dissertation.

In Chapter 2, the moving frame method is employed to describe the kinematics of the three-dimensional multibody system. A brief introduction to the moving frame method is also presented. For the manipulator system comprised of jointed bodies, a graph tree is utilized, which visually illustrates how the constituent bodies are connected to each other. At the end of the chapter, the workspace analysis is performed considering kinematic and joint constraints, and the boundary of the workspace is searched numerically.

In Chapter 3, analytical equations of motion are developed for a Stewart platform whose motion of the base plate is moved and prescribed. In the kinetic analysis, the principle of virtual work is employed, in which system virtual displacements are expressed through B-matrix by essential virtual displacements, reflecting the connection of the rigid body system. The resulting equations of motion are used to experimentally assess the performance of a model-based controller to stabilize the top plate from the motion of the base plate. To compare the control performance of inverse dynamics control which utilize the equations of motion with that of inverse kinematics

control, scale model experiments are presented, showing better tracking performance of the inverse dynamics control.

In Chapter 4, to compensate a time-delay due to measurement, computation and tracking time, Long Short Term Memory (LSTM), a deep learning method for time series forecasting, is applied to forecast future motion caused by a ship or a moving vehicle. Then scale model experiments are performed employing model predictive control. Combining with the LSTM forecasting of future base motion, the tracking performance and compensation rate are improved compared with simple inverse dynamics control without forecasting.

Finally, this dissertation is concluded in Chapter 5, including the summary of each chapter.

CHAPTER 1: INTRODUCTION

1.1 Background

An emergency ambulance service is important to quickly transport patients as providing immediate life-saving care. The injured or sick patients during emergency transportation receive accelerations in longitudinal and lateral directions as the vehicle travels. It has been pointed out that this change in acceleration affects the hemodynamics of the patients and causes blood pressure fluctuations, which may worsen the condition of patients with heart disease and brain disease [1]. Therefore, compensation systems have been proposed to reduce the accelerations acting on patients by actively tilting a bed in an ambulance according to the accelerations acting on the vehicle [2-5].

In addition, a medical ship performs an increasingly crucial role as a floating hospital which provides primary care to injured and ill persons in disaster relief and to those who have not been able to receive medical treatment in isolated islands. However, due to the rolling, pitching, and heaving motions of ships induced by ocean waves, medical operations become challenging tasks. Especially, to perform teleoperated surgery, the surgery table and the base of robot arms must be stabilized for accurate surgical operations.

Furthermore, when manipulators, which require precise positioning, operate in moving vehicles or ships, the control tasks become overwhelming due to undesirable large rigid-body rotation and translation of the tool mount. For safe transportation of sensitive equipment using a vehicle, the transmission of undesirable rotation and translation induced by the moving vehicle should be mitigated.

To remedy these situations, it becomes beneficial to develop a Stewart platform to compensate undesirable translation, rotation, and acceleration of a vehicle and ship by stabilizing the orientation and crude position of its platform or top table, onto which various precision tools or bed are attached. A Stewart platform consists of two parallel plates, referred to as top and base plates, which are connected by six linear actuators [6]. By attaching the equipment or the manipulator to the top plate of the Stewart platform and optimally actuating the six legs, the top plate's position and orientation are maintained in desirable configuration even if the base plate moves due to the motion of the ship or the vehicle.

1.2 Previous Study for a Base-Fixed Stewart Platform

Base-fixed Stewart platforms have been popularly utilized in flight simulators, vehicle driving simulators, and immersed virtual-reality theaters in amusement parks. Kinematics and dynamics of fixed-base Stewart platforms have been investigated by many researchers to control the platforms to enable those applications, for example [7-11]. For design and control of the platforms, equations of motion must be derived.

To derive equations of motion for multi-body systems, there are three methods available: (i) the Newton-Euler method, (ii) Lagrange's method, and (iii) the variational methods. For real-time control of a Stewart platform whose base plate is fixed, equations of motion were derived by previous researchers [9,10,12] using the Newton-Euler method which results in Newton-Euler type equations with reaction forces and couples. By eliminating those reactions, compact equations of motion were obtained in vector form involving vector cross products. Other researchers [8,13,14] employed Lagrange's method to derive compact equations of motion directly without involving reaction forces and couples. In addition, the variational methods were also employed to derive the equations of motion [15] including Kane's method [16]. Notably, for general multi-body systems, Wittenburg [17] presented a versatile method for systematically deriving equations of motion utilizing the *principle of virtual power*. This is a *weighted-residual equation* incorporating Newton's and Euler's equations for constituent bodies and has not been derived variationally from a physical principle

Control applications to the base-fixed Stewart platforms have been studied from simple PID control to linear and nonlinear control scheme such as inverse dynamic control [11], robust control using H_∞ control [11,18], sliding mode control [19-23], and model predictive control [24, 25].

1.3 Previous Study for a Base-Moving Stewart Platform

In contrast, for base-moving Stewart platforms, only a couple of applications have been reported. Previous researchers employed proportional-derivative (PD) controllers using *inverse kinematics* derived from geometrical relations [26, 27]. Due to the complexity of the problem, velocity computations and derivation of equations of motion for a base-moving Stewart platform has not been reported. For effective and fast position control of the top plate of a base-moving Stewart platform it is desirable to derive equations of motion to explore nonlinear control schemes.

When implementing active control with actuators, there exists a time delay from the time when the mount motion is measured until the states of the bed reach their target states. This delay causes tracking error for the system. Then, to actively compensate ship motion incorporating the time delays in real-time measurements, computation, and tracking, autoregressive (AR) model was used to estimate the system states [28]. AR model can be used to forecast steady time series data but is not applicable to unsteady motion such as a sudden large wave and vehicle acceleration.

1.4 Objectives

In response to the need described above, the objectives of this study are:

1. To present kinematics, including velocity computations of a Stewart platform whose base plate translates and rotates.
2. To develop the equations of motion for a nonlinear system of base-moving Stewart platform.
3. To forecast the future motion of moving objects to compensate time delay and enhance the tracking accuracy.
4. To apply a nonlinear control scheme while accounting for constraints, inertia, nonlinearity, and forecasting.

1.5 Outline of the Dissertation

This dissertation consists of five major chapters. The present chapter, Chapter 1, introduce the background, previous studies, and objectives.

Chapter 2 presents kinematic computations of a Stewart platform under prescribed mount motion where a moving frame method is employed to facilitate accurate description of the kinematics [29, 30]. In the moving frame method, vector bases of body-attached coordinate frames are explicitly shown to express vectors and rotation matrices. Writing the vector bases with Frankel's compact notation [31], the difficulty and ambiguity of the vector method to express the velocity and acceleration vectors of a moving point relative to a moving body are resolved. In addition, a graph representation is employed to describe joint connections of the platform to identify closed loops [17]. Finally, the workspace analysis is performed for design.

Chapter 3 describes the development of the equations of motion for a translating and rotating Stewart platform utilizing the principle of virtual work. The analytical

equations of motion are presented in matrix form for dynamic analyses of the platform. It is expected that the resulting equations will be critical for the design and control of a base-moving Stewart platform. At the end of the chapter, experimental results utilizing a scale model are presented to compare the control performance of an inverse dynamics controller to that of an inverse kinematics controller.

Chapter 4 presents the time series forecasting of future mount motion and adaptation of model predictive control (MPC). To forecast future motion acting on a vehicle or floor of a ship, *Long Short Term Memory* (LSTM) [32], one of the deep learning methods which has a *Recurrent Neural Network* (RNN) structure, is used as a time series forecasting method for predicting future data using past data. Then MPC is designed for the base-moving Stewart platform in which the optimization problem for the nonlinear system must be solved numerically. To this end, a continuation and generalized minimum residual method (C/GMRES) is adopted to realize fast computation within a sampling time [33]. Through the use of LSTM and MPC, scale model experiments are carried out to evaluate the effectiveness.

Finally, Chapter 5 concludes the dissertation by denoting the unique contribution of this study.

CHAPTER 2: KINEMATICS OF A BASE-MOVING STEWART PLATFORM

2.1 Introduction

Regarding the representation of configuration spaces of multi-body systems, Joseph-Louis Lagrange (1736-1813) defined configuration spaces using vectors consisting of generalized coordinates or displacements. Fortunately, in the early 20th century, due to the advent of matrix Lie groups pioneered by Sophus Lie (1842-1899), in addition to vectors in $\mathbb{R}^n$, the set of differentiable rotation matrices: the *special orthogonal group SO*(3) has been utilized to define the configuration space of multi-body systems [34]. Specifically, in the configuration space of a multi-body system, each rigid body is mathematically expressed by the position vector of the origin of a body-attached coordinate system in $\mathbb{R}^3$, expressed with respect to an inertial coordinate system, and the rotation matrix in *SO*(3) of the body-attached coordinate axes from the inertial coordinate axes [29,30,35].

In this chapter, first, the multi-body connection of a base-moving Stewart platform is expressed by using a directed graph to reveal closed loops [17]. Second, by attaching principal coordinate systems to constituent bodies at their centers of mass, moving coordinate frames are defined. Coordinate frames are also attached to joints. Third, to define the configuration space of the Stewart platform, the connections of body- and joint-attached coordinate frames are expressed mathematically employing the *special Euclidian group*, *SE*(3), which combines both *SO*(3) and $\mathbb{R}^3$. Fourth, loop closure constraints are obtained along a representative closed loop in the configuration space (as well as in velocities). They are solved analytically for inverse kinematics. Fifth, velocities of moving frames are computed incorporating the Lie algebra: *so*(3) of *SO*(3). The advantage of expressing the frame connections by using *SE*(3)-matrices is that *the readers can compute frame velocities unambiguously since the coordinate vector bases are explicitly shown*. Finally, in the Appendix 2.A, workspace analysis is performed for the preliminary design of a Stewart platform. The velocities of body-attached coordinate frames computed here are utilized to derive analytical equations of motion for inverse dynamics control in Chapter 3.

2.2 Description of a Stewart Platform

Figure 2.1 illustrates a Stewart platform in its reference configuration. To identify bodies of the multi-rigid body system, body numbers are assigned to constituent bodies and shown in a pair of parentheses. *Body-(0)*: base plate is attached to the floor of a moving ship or a vehicle. As a result, the base plate translates and rotates due to the motion of the vehicle. *Body-(13)* represents a top plate or platform on which some sensitive equipment or a manipulator is mounted. Body-(0) and body-(13) are connected by six identical legs, referred to as *leg-(k)*, k=1,⋯,6. Leg-(*k*) consists of lower leg, *body-(2k-1)*, and upper leg, *body-(2k)*, jointed by an actuated translational joint, ATJ-(*k*), between them. The objective of a controller is to maintain a desired attitude of the top plate to mitigate the motion of the base plate by changing their ATJ lengths at each time.

In leg-(*k*) shown in Fig. 2.1, the lower leg, body-(2*k*-1), is jointed to body-(0) by a universal joint (UJ), named UJ-(*k*), whereas the upper leg, body-(2*k*), is jointed to body-(13) by a spherical joint (SJ), called SJ-(*k*). The base yoke of UJ-(*k*) is fixed to body-(0), which journals one axis of the UJ cross. The cross of UJ-(*k*) is referred to as UJ-(*k*) *cross*. Its center is located at a point B_k. The attachment of the lower leg, body-(2*k*-1), to the other axis of UJ-(*k*) cross is facilitated by the yoke hub at the lower end of body-(2*k*-1) to pivot freely around this axis. The upper end of the upper leg, body-(2*k*), has a spherical ball, referred to as SJ-(*k*) *ball*, with its center at point T_k. The spherical ball fits into the SJ-(*k*) *socket* fixed to body-(13).

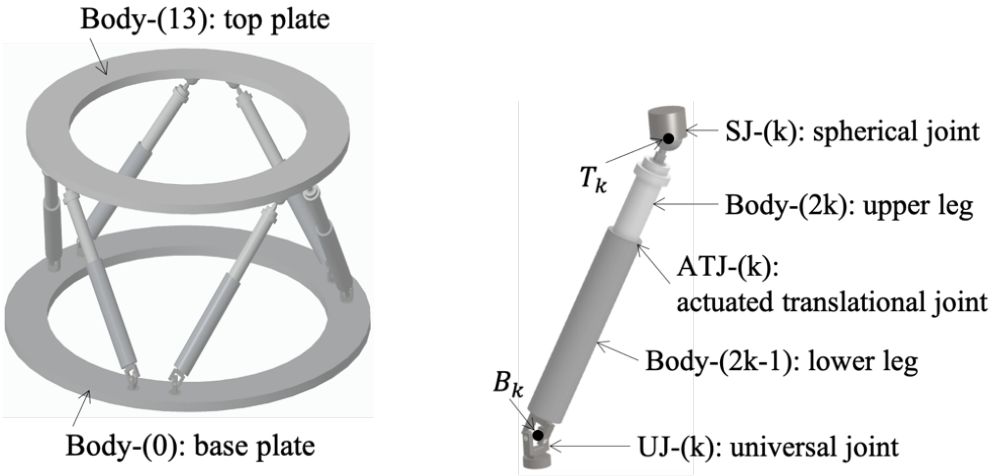

(a) (b)

Figure 2.1: A Stewart platform

A directed graph of the Stewart platform is presented in Fig. 2.2(a). In the graph vertices represent rigid bodies, and lines show joint connections. The graph is "modified" by enlarging the vertices for the base plate, body-(0), and the top plate, body-(13), to show the leg attachment points B_k for universal joints, UJ-(k), and T_k for spherical joints, SJ-(k), for leg-(k), $k = 1, \cdots, 6$. In the graph body-(14), not shown in Fig. 2.1, represents a manipulator, which is rigidly attached to the top plate.

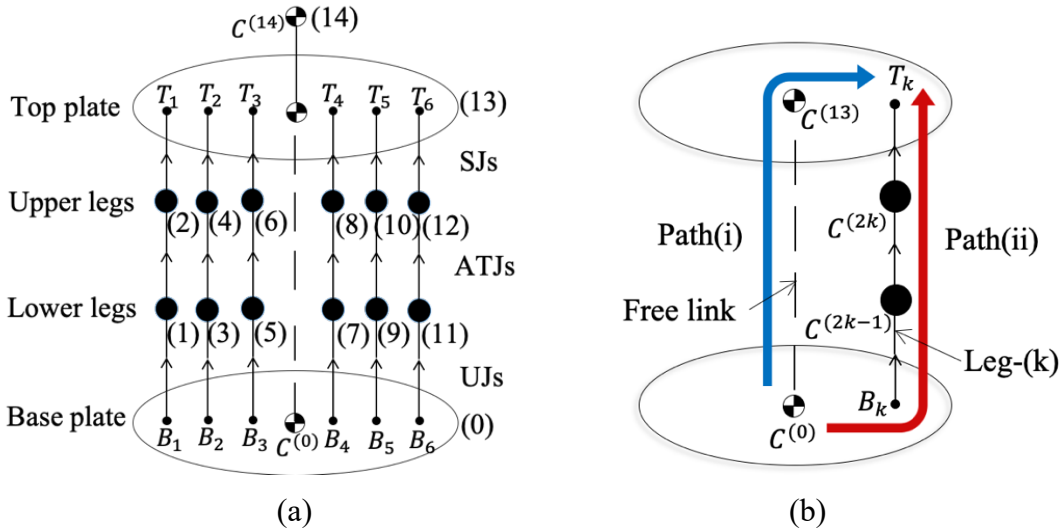

Figure 2.2: (a) A modified directed graph and (b) representative closed loop

The graph in Fig. 2.2(a) reveals that there are closed loops formed by 15 pairs of different legs. Instead of dealing with individual pairs, the loop closure constraints can be treated efficiently by considering a generic closed loop shown in Fig. 2.2(b). The loop is formed by a *free link* between body-(0) and body-(13), shown by a broken line, and leg-(k). In the figure, $C^{(\alpha)}$ represent the center of mass of body-(α). Along path (i) one starts from the center of mass of body-(0), $C^{(0)}$, moves along the free link to that of body-(13), $C^{(13)}$, and heads toward the center T_k of the semi-spherical cavity of SJ-(k) socket, which is rigidly attached to body-(13). Along path (ii) one starts from $C^{(0)}$ to the center B_k of UJ-(k) cross, moves along the axis of leg-(k) passing the centers of mass of body-(2k-1), $C^{(2k\text{-}1)}$, and body-(2k), $C^{(2k)}$, and reaches the center T_k of SJ-(k) ball. Finally, one fits SJ-(k) ball of the upper leg into SJ-(k) socket on body-(13). This fitting of SJ-(k) ball into SJ-(k) socket is mathematically described by *loop closure constraints*.

To commence kinematics the *configuration space* is defined along the generic closed loop in Fig. 2.2(b) by attaching orthonormal coordinate systems at the centers of mass of constituent bodies as well as at the joints. The completion of both paths yields *configurational loop closure constraints* at SJ-(k). Then velocities of the attached coordinate frames will be computed to obtain: (i) the *loop-closure constrains on velocities* and (ii) the translational and angular velocities of each body at its center of mass, which will be utilized in chapter 3 to compute the equations of motion for the Stewart platform.

2.3 Configuration Space Defined by Coordinate Frames

The configuration space is defined along each path of the generic closed loop in Fig. 2.2(b) by attaching moving coordinate frames at joints and the centers of mass of rigid bodies and expressing their interconnections.

2.3.1 Coordinate Frames Along Path (i)

Figure 2.3 depicts the free link between body-(0) and body-(13), shown in Fig. 2.2(b). To begin, an *inertial coordinate frame* is defined to express position vectors of the origins of moving coordinate frames.

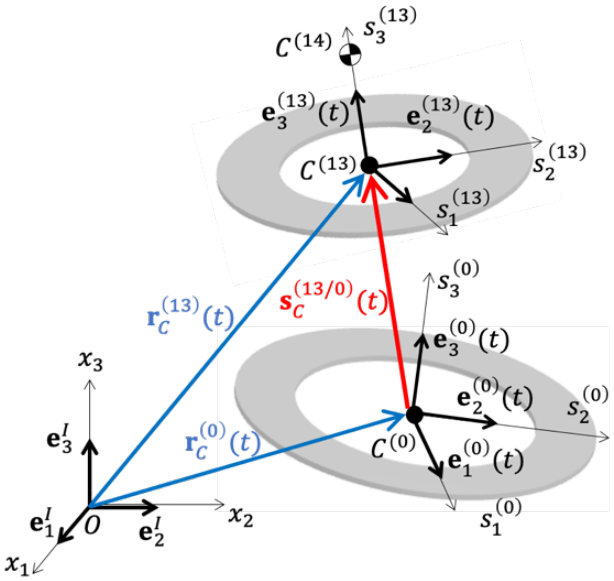

Figure 2.3: A relative representation of the top-plate frame from the base-plate frame

2.3.1.1 Inertial Frame

A fixed cartesian coordinate system $\{x_1 \;\; x_2 \;\; x_3\}$ is defined with its origin, expressed by zero vector $\mathbf{0}$. The unit vectors of the coordinate axes define a vector basis $(\mathbf{e}_1^I \;\; \mathbf{e}_2^I \;\; \mathbf{e}_3^I)$, which is compactly written as $\mathbf{e}^I$ utilizing Frankel's notation [31]. The vector basis $\mathbf{e}^I$ and its origin $\mathbf{0}$ define the *inertial coordinate frame* written as: $(\mathbf{e}^I, \mathbf{0})$, [29, 30]

Using the inertial vector basis $\mathbf{e}^I$, the position vector of the center of mass, for example, $C^{(0)}$ of body-(0) is expressed as:

$$\mathbf{r}_C^{(0)}(t) = \mathbf{e}^I x_C^{(0)}(t), \tag{2.1a}$$

where

$$\mathbf{e}^I \equiv (\mathbf{e}_1^I \;\; \mathbf{e}_2^I \;\; \mathbf{e}_3^I), \tag{2.1b}$$

$$x_C^{(0)}(t) \equiv \begin{pmatrix} x_{1C}^{(0)}(t) \\ x_{2C}^{(0)}(t) \\ x_{3C}^{(0)}(t) \end{pmatrix}. \tag{2.1c}$$

In Frankel's notation, all vector bases are stored in 1 × 3 row matrices and components in 3 × 1 column matrices. In this dissertation, $\{x_1 \;\; x_2 \;\; x_3\}$ is exclusively used for the inertial coordinate system, while $\{s_1 \;\; s_2 \;\; s_3\}$ is used for body-attached, orthonormal coordinate systems. Furthermore, only right-handed coordinate systems are considered.

2.3.1.2 Body-(0) Frame: $\left(\mathbf{e}^{(0)}(t) \;\; \mathbf{r}_C^{(0)}(t)\right)$

To define the body-(0) coordinate frame a principal coordinate system $\{s_1^{(0)} \; s_2^{(0)} \; s_3^{(0)}\}$ is attached to body-(0) at its center of mass, $C^{(0)}$, with the $s_3^{(0)}$-axis normal to the plane of the base plate, spanned by the $s_1^{(0)}$, $s_2^{(0)}$-axes. The coordinate unit vectors define the vector basis $\mathbf{e}^{(0)}(t) \equiv (\mathbf{e}_1^{(0)}(t) \;\; \mathbf{e}_2^{(0)}(t) \;\; \mathbf{e}_3^{(0)}(t))$. Using the vector basis $\mathbf{e}^{(0)}(t)$ and the position vector of its origin $\mathbf{r}_C^{(0)}(t)$, the *body-(0) frame* is defined as $\left(\mathbf{e}^{(0)}(t) \;\; \mathbf{r}_C^{(0)}(t)\right)$. The configuration of body-(0) is defined by expressing its frame connection to $(\mathbf{e}^I \;\; \mathbf{0})$. To this end, the attitude of $\mathbf{e}^{(0)}(t)$ relative to $\mathbf{e}^I$ is expressed using a 3 × 3 rotation matrix $R^{(0)}(t)$ with determinant one:

$$\mathbf{e}^{(0)}(t) = \mathbf{e}^I R^{(0)}(t), \tag{2.2a}$$

where

$$\mathbf{e}^{(0)}(t) \equiv \left(\mathbf{e}_1^{(0)}(t) \quad \mathbf{e}_2^{(0)}(t) \quad \mathbf{e}_3^{(0)}(t)\right). \tag{2.2b}$$

In the expanded form, the rotation matrix is written as:

$$R^{(0)}(t) \equiv \begin{bmatrix} R_{11}^{(0)}(t) & R_{12}^{(0)}(t) & R_{13}^{(0)}(t) \\ R_{21}^{(0)}(t) & R_{22}^{(0)}(t) & R_{23}^{(0)}(t) \\ R_{31}^{(0)}(t) & R_{32}^{(0)}(t) & R_{33}^{(0)}(t) \end{bmatrix} \tag{2.2c}$$

Equation (2.2a) is read as "$\mathbf{e}^{(0)}(t)$ is obtained by applying the rotation $R^{(0)}(t)$ to $\mathbf{e}^I$". The inverse relation of Eq. (2.2a) is

$$\mathbf{e}^I = \mathbf{e}^{(0)}(t)\left(R^{(0)}(t)\right)^T \tag{2.2d}$$

where a superposed 'T' attached to a matrix symbol implies the transposition of the matrix.

Using Eq. (2.2a) and the components $x_C^{(0)}(t)$ of $\mathbf{r}_C^{(0)}(t)$ in Eq. (2.1c), the connection of $\left(\mathbf{e}^{(0)}(t) \quad \mathbf{r}_C^{(0)}(t)\right)$ to $(\mathbf{e}^I \quad \mathbf{0})$ is defined by using a 4 × 4 *frame-connection matrix* $E^{(0)}(t)$ as:

$$\left(\mathbf{e}^{(0)}(t) \quad \mathbf{r}_C^{(0)}(t)\right) = (\mathbf{e}^I \quad \mathbf{0})\, E^{(0)}(t), \tag{2.3a}$$

where

$$E^{(0)}(t) = \begin{bmatrix} R^{(0)}(t) & x_C^{(0)}(t) \\ 0_{1\times 3} & 1 \end{bmatrix}, \tag{2.3b}$$

and $0_{1\times 3} \equiv (0 \quad 0 \quad 0)$.

Equation (2.3a) shows that $\left(\mathbf{e}^{(0)}(t) \quad \mathbf{r}_C^{(0)}(t)\right)$ is obtained by applying the rotation $R^{(0)}(t)$ and the parallel translation $x_C^{(0)}(t)$ to $(\mathbf{e}^I \quad \mathbf{0})$.

In this chapter, an inertial coordinate frame is selected to be the body-(0) frame at $t = 0$, *i.e.*, $(\mathbf{e}^I \quad \mathbf{0}) = \left(\mathbf{e}^{(0)}(0) \quad \mathbf{r}_C^{(0)}(0)\right)$, with initial values $x_C^{(0)}(0) = 0$ and $R^{(0)}(0) = I_3$: the 3 × 3 identity matrix in Eq. (2.3b).

The set of differentiable rotation matrices forms the *special orthogonal group*: *SO*(3) [31, 34], and that of differentiable frame connection matrices forms the *special Euclidean group* [29, 30, 35]. (Here, the adjective "special" means that all member matrices have a determinant one.) Both *SO*(3) and *SE*(3) are matrix Lie groups with the *basic group properties*, expressed for *SE*(3): (i) their products belong to *SE*(3), (ii) their inverse matrices belong to *SE*(3), and (iii) associativity holds in matrix multiplications,

for example [31, 34]. The members of *SO*(3) also satisfy the same group properties. As Lie matrix groups, *SO*(3) and *SE*(3) come with their Lie algebras: *so*(3) and *se*(3), respectively, which describe the flow of matrix members with time near their identity matrix. In dynamics, the Lie algebras express angular velocities and translational velocities of each body [29, 30].

In robotics, frame connection matrices of *SE*(3) are called *homogeneous transformations*, see for example [35], where the time rate of transformations, comparable to the Lie algebra, are not mentioned. Also, in robotics using the *screw theory* [36] and the *product of exponentials formula* [37], homogeneous coordinates of *SE*(3) were utilized to derive equations of motion by Murray *et al*. [38].

Returning to path (i) in Fig. 2.2 (b) and Fig. 2.3 along with the free link, the frame is defined for the top plate, body-(13).

2.3.1.3 Body-(13) Frame: $\left(\mathbf{e}^{(13)}(t) \quad \mathbf{r}_C^{(13)}(t)\right)$

A principal coordinate system $\{s_1^{(13)}\ s_2^{(13)}\ s_3^{(13)}\}$ is attached to body-(13) at its center of mass, $C^{(13)}$, with the $s_3^{(13)}$-axis normal to the plane of the plate. The coordinate vector basis $\mathbf{e}^{(13)}(t)$ is defined by the unit coordinate vectors as: $\mathbf{e}^{(13)}(t) \equiv \left(\mathbf{e}_1^{(13)}(t) \quad \mathbf{e}_2^{(13)}(t) \quad \mathbf{e}_3^{(13)}(t)\right)$. The position vector of $C^{(13)}$ is expressed by $\mathbf{r}_C^{(13)}(t)$. Now, *body-(13) frame* is defined as: $\left(\mathbf{e}^{(13)}(t) \quad \mathbf{r}_C^{(13)}(t)\right)$. As illustrated in Fig. 2.3, $\mathbf{r}_C^{(13)}(t)$ is expressed by adding the relative position vector of $C^{(13)}$ measured from $C^{(0)}$, written as $\mathbf{s}_C^{(13/0)}(t) = \mathbf{e}^{(0)}(t)s_C^{(13/0)}(t)$ to $\mathbf{r}_C^{(0)}(t)$. The rotation of $\mathbf{e}^{(13)}(t)$ relative to $\mathbf{e}^{(0)}(t)$ is expressed by $R^{(13/0)}(t)$. As a result, the connection of $\left(\mathbf{e}^{(13)}(t) \quad \mathbf{r}_C^{(13)}(t)\right)$ to $\left(\mathbf{e}^{(0)}(t) \quad \mathbf{r}_C^{(0)}(t)\right)$ is expressed by the frame connection matrix $E^{(13/0)}(t)$ as:

$$\left(\mathbf{e}^{(13)}(t) \quad \mathbf{r}_C^{(13)}(t)\right) = \left(\mathbf{e}^{(0)}(t) \quad \mathbf{r}_C^{(0)}(t)\right)E^{(13/0)}(t), \tag{2.4a}$$

where

$$E^{(13/0)}(t) \equiv \begin{bmatrix} R^{(13/0)}(t) & s_C^{(13/0)}(t) \\ 0_{1\times 3} & 1 \end{bmatrix}. \tag{2.4b}$$

In this dissertation, the matrices or vectors with a superscript "(j/i)" imply those of frame-(j) relative to frame-(i). Therefore, for example, in Eq. (2.4a), $E^{(13/0)}(t)$ expressed the frame connection of body-(13) frame relative to body-(0) frame.

In the reference configuration at $t = 0$, shown in Fig. 2.1, $\left(\mathbf{e}^{(13)}(0) \quad \mathbf{r}_C^{(13)}(0)\right)$ is obtained by parallel translating body-(0) frame $\left(\mathbf{e}^{(0)}(0) \quad \mathbf{r}_C^{(0)}(0)\right)$ vertically from $C^{(0)}$

to $C^{(13)}$ by distance $\hat{h}^{(0)}$ without any rotation. Therefore, the initial values of the elements of $E^{(13/0)}(0)$ are: $R^{(13/0)}(0) = I_3$ and $s_C^{(13/0)}(0) = \hat{h}^{(0)} e_3$, where e_3 represents a 3 × 1 unit column matrix: $e_3 \equiv (0 \quad 0 \quad 1)^T$.

Next along path (i) from $C^{(13)}$ one advances to SJ-(k) socket with its center at T_k.

2.3.1.4 SJ-(k) Socket Frame at T_k on Body-(13): $\left(\mathbf{e}_{T_k}^{(\mathbf{SJ\ 13})}(t) \quad \mathbf{r}_{T_k}(t)\right)$

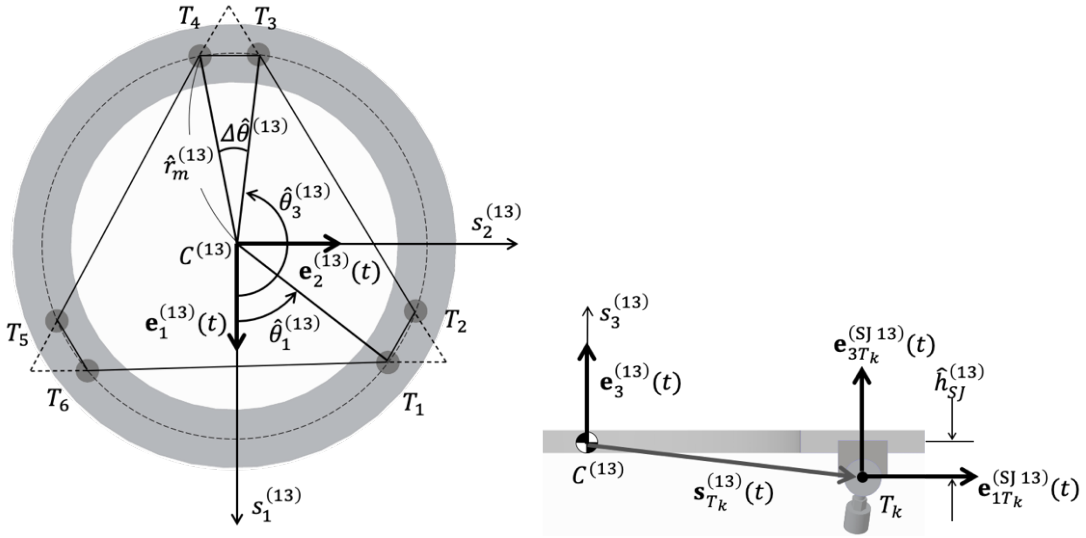

(a) (b)

Figure 2.4: (a) A plane view of the top plate, body-(13) and (b) an elevation for the socket of a spherical joint at T_k

In Fig. 2.4 (a) T_1, T_2, …, T_6 on the circle of radius $\hat{r}_m^{(13)}$ express the centers of the semi-spherical cavity of sockets of six spherical joints (SJs). They form a hexagon, obtained by truncating an equilateral triangle by the radius $\hat{r}_m^{(13)}$, which is slightly smaller than the radius of the circumscribing circle of the triangle. The relative coordinates $\hat{s}_{T_k}^{(13)}$ of point T_k with respect to $\mathbf{e}^{(13)}(t)$ remain constant:

$$\mathbf{s}_{T_k}^{(13)}(t) = \mathbf{e}^{(13)}(t)\hat{s}_{T_k}^{(13)}, \quad k = 1, 2, \dots, 6, \tag{2.5a}$$

where $\hat{s}_{3\,T_k}^{(13)} = -\hat{h}_{SJ}^{(13)}$ as shown in Fig. 2.4 (b):

$$\hat{s}_{T_k}^{(13)} = \begin{pmatrix} \hat{r}_m^{(13)} \cos\hat{\theta}_k^{(13)} \\ \hat{r}_m^{(13)} \sin\hat{\theta}_k^{(13)} \\ -\hat{h}_{SJ}^{(13)} \end{pmatrix} \tag{2.5b}$$

and denoting the truncation angle by $\Delta\hat{\theta}^{(13)}$, which is less than $\pi/3$, $\hat{\theta}_k^{(13)}$ in Fig. 2.4 (a) is expressed as:

$$\hat{\theta}_1^{(13)} = \frac{\pi}{3} - \frac{1}{2}\Delta\hat{\theta}^{(13)} \quad , \hat{\theta}_2^{(13)} = \frac{\pi}{3} + \frac{1}{2}\Delta\hat{\theta}^{(13)},$$
$$\hat{\theta}_3^{(13)} = \pi - \frac{1}{2}\Delta\hat{\theta}^{(13)} \, , \; \hat{\theta}_4^{(13)} = \pi + \frac{1}{2}\Delta\hat{\theta}^{(13)}, \tag{2.5c}$$
$$\hat{\theta}_5^{(13)} = \frac{5\pi}{3} - \frac{1}{2}\Delta\hat{\theta}^{(13)}, \quad \hat{\theta}_6^{(13)} = \frac{5\pi}{3} + \frac{1}{2}\Delta\hat{\theta}^{(13)}.$$

In this dissertation, time independent quantities are shown with superposed hat: "^".

Along path (i) SJ-*(k) socket frame at T_k on body-(13)*: $\left(\mathbf{e}_{T_k}^{(\mathrm{SJ}\,13)}(t) \quad \mathbf{r}_{T_k}(t)\right)$ is defined by parallel translating $\mathbf{e}^{(13)}(t)$ to T_k by $\hat{s}_{T_k}^{(13)}$and rotating the translated vector basis until $\mathbf{e}_{1\,T_k}^{(\mathrm{SJ}\,13)}$ points in the radial direction. Thus, the frame connection of $\left(\mathbf{e}_{T_k}^{(\mathrm{SJ}\,13)}(t) \quad \mathbf{r}_{T_k}(t)\right)$ to body-(13) frame is written as:

$$\left(\mathbf{e}_{T_k}^{(\mathrm{SJ}\,13)}(t) \quad \mathbf{r}_{T_k}(t)\right) = \left(\mathbf{e}^{(13)}(t) \quad \mathbf{r}_C^{(13)}(t)\right) \hat{E}_{T_k}^{(\mathrm{SJ}\,13/13)}, \tag{2.6a}$$

where

$$\hat{E}_{T_k}^{(\mathrm{SJ}\,13/13)} = \begin{bmatrix} R_{3\,T_k}(\hat{\theta}_k^{(13)}) & \hat{s}_{T_k}^{(13)} \\ 0_{1\times 3} & 1 \end{bmatrix}, \tag{2.6b}$$

and $R_{3\,T_k}(\hat{\theta}_k^{(13)})$ represents the elementary rotation about $\mathbf{e}_3^{(13)}(t)$ by $\hat{\theta}_k^{(13)}$ to point $\mathbf{e}_{1\,T_k}^{(\mathrm{SJ}\,13)}$ in the radial direction:

$$R_{3\,T_k}(\hat{\theta}_k^{(13)}) \equiv \begin{bmatrix} \cos\hat{\theta}_k^{(13)} & -\sin\hat{\theta}_k^{(13)} & 0 \\ \sin\hat{\theta}_k^{(13)} & \cos\hat{\theta}_k^{(13)} & 0 \\ 0 & 0 & 1 \end{bmatrix}. \tag{2.6c}$$

2.3.1.5 Summary of Path (i) Frame Connection

Along path (i) SJ-(k) socket frame at T_k on body-(13) is also expressed with respect to body-(0) frame by combining Eqs. (2.6a) and (2.4a):

$$\left(\mathbf{e}_{T_k}^{(\mathrm{SJ}\,13)}(t) \quad \mathbf{r}_{T_k}(t)\right)_{path\ (i)} = \left(\mathbf{e}^{(0)}(t) \quad \mathbf{r}_C^{(0)}(t)\right)\left(E_{T_k}^{(\mathrm{SJ}\,13/0)}(t)\right)_{path\ (i)}, \tag{2.7a}$$

where the components of the frame connection matrix are defined as:

$$\left(E_{T_k}^{(\mathrm{SJ}\,13/0)}(t)\right)_{path\ (i)} \equiv \begin{bmatrix} R_{T_k}^{(\mathrm{SJ}\,13/0)}(t) & s_{T_k}^{(\mathrm{SJ}\,13/0))}(t) \\ 0_{1\times 3} & 1 \end{bmatrix}_{path\ (i)}, \tag{2.7b}$$

and from Eqs. (2.6a) and (2.4a):

$$\left(E_{T_k}^{(\mathrm{SJ}\,13/0)}(t)\right)_{path\ (i)} = E^{(13/0)}(t)\,\hat{E}_{T_k}^{(\mathrm{SJ}\,13/13)}. \tag{2.7c}$$

The computation of their components yields

$$\left(R_{T_k}^{(\mathrm{SJ}\,13/0)}(t)\right)_{path\ (i)} = R^{(13/0)}(t)\,R_{3\,T_k}(\hat{\theta}_k^{(13)}), \tag{2.7d}$$

$$\left(s_{T_k}^{(\mathrm{SJ}\,13/0))}(t)\right)_{path\ (i)} = R^{(13/0)}(t)\hat{s}_{T_k}^{(13)} + s_C^{(13/0)}(t). \tag{2.7e}$$

This completes the definition of frame connections along path (i). However, at this point, for the computation of kinetic energy in chapter 3, the configuration of a manipulator mounted on the top plate, is defined.

2.3.1.6 Body-(14) Frame: $\left(\mathbf{e}^{(14)}(t) \quad \mathbf{r}_C^{(14)}(t)\right)$

As shown in Fig. 2.2 (a) and Fig. 2.3, a manipulator, body-(14), is mounted on the top plate. In this paper, the manipulator is approximated as a rigid body with its center of mass located on the $s_3^{(13)}$-axis at the elevation $\hat{h}^{(14/13)}$. Body-(14) frame $\left(\mathbf{e}^{(14)}(t) \quad \mathbf{r}_C^{(14)}(t)\right)$ is therefore established by parallel translating $\left(\mathbf{e}^{(13)}(t) \quad \mathbf{r}_C^{(13)}(t)\right)$ along the $s_3^{(13)}$-axis by $\hat{h}^{(14/13)}$ without any rotation:

$$\left(\mathbf{e}^{(14)}(t) \quad \mathbf{r}_C^{(14)}(t)\right) = \left(\mathbf{e}^{(13)}(t) \quad \mathbf{r}_C^{(13)}(t)\right)\hat{E}^{(14/13)}, \tag{2.8a}$$

where using $e_3 \equiv (\,0 \;\; 0 \;\; 1\,)^T$,

$$\hat{E}^{(14/13)} = \begin{bmatrix} I_3 & \hat{h}^{(14/13)} e_3 \\ 0_{1\times 3} & 1 \end{bmatrix}. \tag{2.8b}$$

2.3.2 Moving Coordinate Frames Along Path (ii)

Moving coordinate frames necessary to define the frame connections of path (ii) are briefly discussed. On leg-(k), first, two frames are employed at the center B_k of UJ-(k) cross: UJ-(k) *cross frame* and UJ-(k) *leg frame* to describe the rotation of the lower leg, body-(2k-1). One axis of the cross is journaled by the base yoke fixed to body-(0) and the other axis is journaled by the yoke of body-(2k-1). Second, to describe the length change induced by the actuated translational joint, ATJ-(k), principal coordinate systems are attached to both body-(2k-1) and the upper leg, body-(2k), at their centers of mass of *body-(2k-1) frame* and *body-(2k) frame*. Third, advancing along the axis of the upper leg to the center T_k of the spherical ball, SJ-(k) *ball frame at T_k on body-(2k)* is defined. Finally, SJ-(k) ball frame at T_k on body-(2k) is connected to *SJ-(k) socket frame at T_k on body-(13)* to mathematically fit the spherical ball into the SJ socket on body-(13). This summarizes the frames to be defined along path (ii).

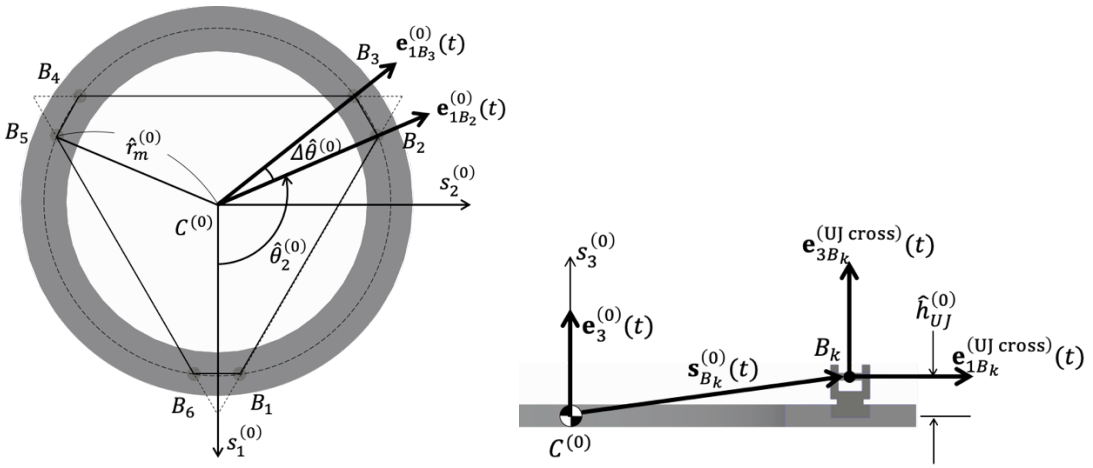

(a) (b)

Figure 2.5: (a) A plane view of the base plate and (b) the elevation of center of UJ cross-links, B_k, k=1,…,6

2.3.2.1 UJ-(k) Cross Frame at B_k on Body-(0): $\left(\mathbf{e}_{B_k}^{(\text{UJ cross})}(t) \quad \mathbf{r}_{B_k}(t)\right)$

Figure 2.5(a) illustrates a plan view of the base plate, body-(0). In the figure, the centers of cross of universal joints (UJs) are shown by points B_1, B_2, …, B_6 on the circle of radius $\hat{r}_m^{(0)}$, which are numbered in the counterclockwise direction. They form a hexagon, obtained by truncating an equilateral triangle by the radius $\hat{r}_m^{(0)}$ which is slightly smaller than the circumscribing circle of the triangle. Figure 5(b) shows for leg-(k) an elevation of the base yoke of UJ-(k) with the center of cross at B_k. The base yoke on body-(0) journals one axis of the cross pointing in the *radial direction*. (The other axis of the cross is journaled by the yoke of the lower leg: body-(2k-1).)

The relative position vector $\mathbf{s}_{B_k}^{(0)}(t)$ of point B_k is expressed with respect to $\mathbf{e}^{(0)}(t)$:

$$\mathbf{s}_{B_k}^{(0)}(t) = \mathbf{e}^{(0)}(t)\hat{s}_{B_k}^{(0)}, \quad k = 1, 2, \dots, 6, \tag{2.9a}$$

where the coordinates $\hat{s}_{B_k}^{(0)}$ are obtained from Figs. 2.5(a) and 2.5(b) with the elevation $\hat{h}_{UJ}^{(0)}$ as:

$$\hat{s}_{B_k}^{(0)} = \begin{pmatrix} \hat{r}_m^{(0)}\cos\hat{\theta}_k^{(0)} \\ \hat{r}_m^{(0)}\sin\hat{\theta}_k^{(0)} \\ \hat{h}_{UJ}^{(0)} \end{pmatrix}, \tag{2.9b}$$

and denoting the truncated angle by $\Delta\hat{\theta}^{(0)}$, which is less than $\pi/3$, $\hat{\theta}_k^{(0)}$'s are defined as:

$$\hat{\theta}_1^{(0)} = \frac{1}{2}\Delta\hat{\theta}^{(0)}, \quad \hat{\theta}_2^{(0)} = \frac{2\pi}{3} - \frac{1}{2}\Delta\hat{\theta}^{(0)},$$

$$\hat{\theta}_3^{(0)} = \frac{2\pi}{3} + \frac{1}{2}\Delta\hat{\theta}^{(0)}, \hat{\theta}_4^{(0)} = \frac{4\pi}{3} - \frac{1}{2}\Delta\hat{\theta}^{(0)}, \tag{2.9c}$$

$$\hat{\theta}_5^{(0)} = \frac{4\pi}{3} + \frac{1}{2}\Delta\hat{\theta}^{(0)}, \hat{\theta}_6^{(0)} = 2\pi - \frac{1}{2}\Delta\hat{\theta}^{(0)}.$$

UJ-(k) cross rotates freely around the cross axis pivoted by the base yoke. To describe the rotation of the cross, UJ-(k) *cross frame at B_k on body-(0)*: $\left(\mathbf{e}_{B_k}^{(\mathrm{UJ\ cross})}(t) \quad \mathbf{r}_{B_k}(t)\right)$ is defined. The unit coordinate vector $\mathbf{e}_{1\,B_k}^{(\mathrm{UJ\ cross})}$ represents the axis of rotation of the cross, $\mathbf{e}_{2\,B_k}^{(\mathrm{UJ\ cross})}$ is the other axis of cross journaled by the yoke of the lower leg, body (2k-1), and $\mathbf{e}_{3\,B_k}^{(\mathrm{UJ\ cross})}$ shows the axis of the leg. As a result, the plane of the cross is spanned by $\mathbf{e}_{1\,B_k}^{(\mathrm{UJ\ cross})}$ and $\mathbf{e}_{2\,B_k}^{(\mathrm{UJ\ cross})}$. The cross frame is obtained by parallel translating $\mathbf{e}^{(0)}(t)$ to B_k by $\hat{s}_{B_k}^{(0)}$ and orienting the translated $\mathbf{e}_1^{(0)}(t) = \mathbf{e}_{1\,B_k}^{(\mathrm{UJ\ cross})}$ in the radial direction. Subsequently, the cross rotates about $\mathbf{e}_{1\,B_k}^{(\mathrm{UJ\ cross})}$ by angle $\phi_1^{(k)}(t)$. Therefore, the connection of UJ-(k) cross frame at B_k on body-(0) to body-(0) frame is expressed as:

$$\left(\mathbf{e}_{B_k}^{(\mathrm{UJ\ cross})}(t) \quad \mathbf{r}_{B_k}(t)\right) = \left(\mathbf{e}^{(0)}(t) \quad \mathbf{r}_C^{(0)}(t)\right)\begin{bmatrix} R_{3\,B_k}\left(\hat{\theta}_k^{(0)}\right) R_{1\,B_kUJ}(\phi_1^{(k)}(t)) & \hat{s}_{B_k}^{(0)} \\ 0_{1\times 3} & 1 \end{bmatrix}, \tag{2.10a}$$

where $R_{3\,B_k}(\hat{\theta}_k^{(0)})$ expresses the elementary rotation about $\mathbf{e}_3^{(0)}(t)$ by the angle $\hat{\theta}_k^{(0)}$ to orient $\mathbf{e}_{1\,B_k}^{(\mathrm{UJ\ cross})}$ in the radial direction:

$$R_{3\,B_k}(\hat{\theta}_k^{(0)}) \equiv \begin{bmatrix} \cos\hat{\theta}_k^{(0)} & -\sin\hat{\theta}_k^{(0)} & 0 \\ \sin\hat{\theta}_k^{(0)} & \cos\hat{\theta}_k^{(0)} & 0 \\ 0 & 0 & 1 \end{bmatrix}, \tag{2.10b}$$

and R_{1B_kUJ} represents the subsequent elementary rotation about $\mathbf{e}_{1\,B_k}^{(\mathrm{UJ\ cross})}$ by $\phi_1^{(k)}(t)$:

$$R_{1B_kUJ}\left(\phi_1^{(k)}(t)\right) \equiv \begin{bmatrix} 1 & 0 & 0 \\ 0 & \cos\phi_1^{(k)}(t) & -\sin\phi_1^{(k)}(t) \\ 0 & \sin\phi_1^{(k)}(t) & \cos\phi_1^{(k)}(t) \end{bmatrix}. \tag{2.10c}$$

The first column of Eq. (2.10a): $\mathbf{e}_{B_k}^{(\mathrm{UJ\ cross})}(t) = \mathbf{e}^{(0)}(t)\, R_{3\,B_k}(\hat{\theta}_k^{(0)}) R_{1\,B_kUJ}(\phi_1^{(k)}(t))$ compactly expresses two sequence of rotations applied to the translated $\mathbf{e}^{(0)}(t)$ to B_k: the first rotation $R_{3\,B_k}(\hat{\theta}_k^{(0)})$ to orient $\mathbf{e}_{1\,B_k}^{(\mathrm{UJ\ cross})}$ in the radial direction and the second rotation $R_{1\,B_kUJ}(\phi_1^{(k)}(t))$ about $\mathbf{e}_{1\,B_k}^{(\mathrm{UJ\ cross})}$ by angle $\phi_1^{(k)}(t)$ to describe the cross rotation.

Next, to describe the rotation of the lower leg, body-(2k-1), at B_k the second frame is defined.

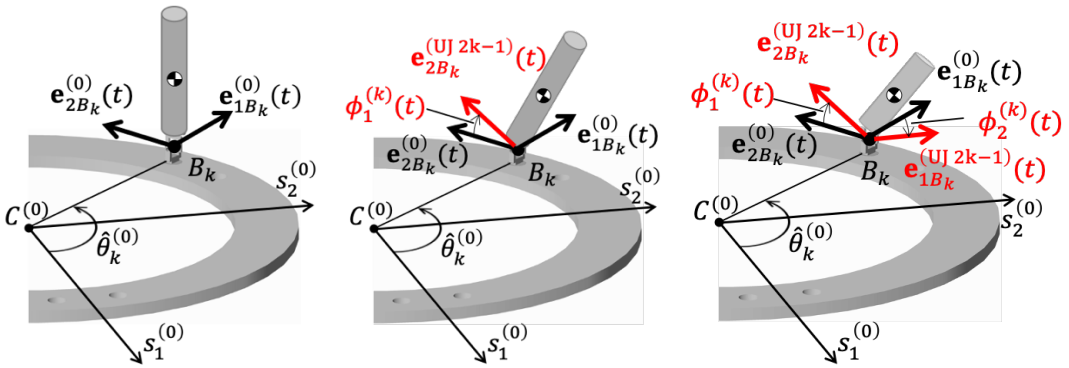

(a) (b) (c)

Figure 2.6: The rotations of UJ cross and the lower leg body-(2k-1) at B_k:
(a) $\phi_1^{(k)} = \phi_2^{(k)} = 0$; (b) $\phi_1^{(k)} \neq 0$, $\phi_2^{(k)} = 0$; (c) $\phi_1^{(k)} \neq 0$, $\phi_2^{(k)} \neq 0$.

2.3.2.2 UJ-(k) Leg Frame at B_k on Body-(2k-1): $\left(\mathbf{e}_{B_k}^{(\mathrm{UJ}\ 2k-1)}(t) \quad \mathbf{r}_{B_k}(t)\right)$

To describe the rotation of the lower leg at B_k, UJ-(k) *leg frame at B_k on body-(2k-1)*: $\left(\mathbf{e}_{B_k}^{(\mathrm{UJ}\ 2k-1)}(t) \quad \mathbf{r}_{B_k}(t)\right)$ is defined. The coordinate vector basis $\mathbf{e}_{B_k}^{(\mathrm{UJ}\ 2k-1)}(t)$ is defined so that $\mathbf{e}_{2\,B_k}^{(\mathrm{UJ}\ 2k-1)}(t) = \mathbf{e}_{2\,B_k}^{(\mathrm{UJ\ cross})}(t)$ express the cross axis journaled by the yoke of body-(2k-1) and $\mathbf{e}_{3\,B_k}^{(\mathrm{UJ}\ 2k-1)}(t)$ shows the leg axis. The associated coordinate system with the origin at B_k is defined as $\left\{s_{1B_k}^{(\mathrm{UJ}\ 2k-1)} \quad s_{2B_k}^{(\mathrm{UJ}\ 2k-1)} \quad s_{3\,B_k}^{(\mathrm{UJ}\ 2k-1)}\right\}$. UJ-($k$) leg frame on body-(2k-1) occupies the same origin $\mathbf{r}_{B_k}(t)$ as that of UJ-(k) cross frame. However, $\mathbf{e}_{B_k}^{(\mathrm{UJ}\ 2k-1)}(t)$ is relatively rotated by angle $\phi_2^{(k)}(t)$ with respect to $\mathbf{e}_{2B_k}^{(\mathrm{UJ}\ 2k-1)}(t)$, which shows the axis of the cross-link journaled by the yoke of body-(2k-1).

The lower leg, body-(2k-1), takes a vertical position where the cross plane remains parallel to the plane of the base plate, *i.e.*, no rotation about $\mathbf{e}_{1\,B_k}^{(\mathrm{UJ\ cross})}$, $\phi_1^{(k)} = 0$, and no rotation about $\mathbf{e}_{2B_k}^{(\mathrm{UJ}\ 2k-1)}(t)$, $\phi_2^{(k)} = 0$. The posture of the leg becomes that shown in Fig. 2.6 (b) when only the cross rotates about $\mathbf{e}_{1\,B_k}^{(\mathrm{UJ\ cross})}$ by $\phi_1^{(k)} \neq 0$ without any rotation about $\mathbf{e}_{2B_k}^{(\mathrm{UJ}\ 2k-1)}(t)$, $\phi_2^{(k)} = 0$. When both rotations take place about $\mathbf{e}_{1\,B_k}^{(\mathrm{UJ\ cross})}$ by $\phi_1^{(k)} \neq 0$ and about $\mathbf{e}_{2B_k}^{(\mathrm{UJ}\ 2k-1)}(t)$ by $\phi_2^{(k)} \neq 0$, the posture of the lower leg becomes that shown in Fig. 2.6(c). Observing that in the reference configuration, shown

in Fig. 2.1, the legs are not vertical to the plane of the base plate, both $\phi_1^{(k)}(0)$ and $\phi_2^{(k)}(0)$ take nonzero initial values (which are computed in the Appendix 2.A).

The connection of UJ-(k) leg frame at B_k on body-(2k-1) to UJ-(k) cross frame on body-(0) is expressed as:

$$\left(\mathbf{e}_{B_k}^{(\mathrm{UJ}\ 2k-1)}(t) \quad \mathbf{r}_{B_k}(t)\right) = \left(\mathbf{e}_{B_k}^{(\mathrm{UJ\ Cross})}(t) \quad \mathbf{r}_{B_k}(t)\right)\begin{bmatrix} R_{2B_k\mathrm{UJ}}(\phi_2^{(k)}(t)) & 0_{3\times1} \\ 0_{1\times3} & 1 \end{bmatrix}, \quad (2.11a)$$

where $R_{2B_kUJ}(\phi_2^{(k)}(t))$ represents the elementary rotation about $\mathbf{e}_{2B_k}^{(\mathrm{UJ}\ 2k-1)}(t)$ by $\phi_2^{(k)}(t)$:

$$R_{2B_k\mathrm{UJ}}\left(\phi_2^{(k)}(t)\right) \equiv \begin{bmatrix} \cos\phi_2^{(k)}(t) & 0 & \sin\phi_2^{(k)}(t) \\ 0 & 1 & 0 \\ -\sin\phi_2^{(k)}(t) & 0 & \cos\phi_2^{(k)}(t) \end{bmatrix}. \quad (2.11b)$$

To advance further along leg-(k) of path (ii), Fig. 2.7 illustrates the coordinate frames at joints and centers of mass which must be defined.

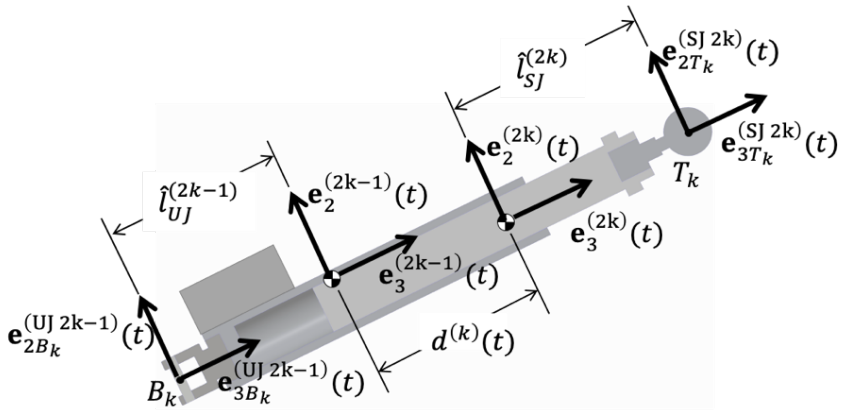

Figure 2.7: Coordinate frames on the k^{th} leg

2.3.2.3 Body-(2k-1) Frame: $\left(\mathbf{e}^{(2k-1)}(t) \quad \mathbf{r}_C^{(2k-1)}(t)\right)$

For the lower-leg, *body*-(2k-1) *frame* is defined at $C^{(2k\text{-}1)}$ by parallel translating the $\left\{s_{1B_k}^{(\mathrm{UJ}\ 2k-1)} \quad s_{2B_k}^{(\mathrm{UJ}\ 2k-1)} \quad s_{3\,B_k}^{(\mathrm{UJ}\ 2k-1)}\right\}$ coordinate system of UJ-(k) leg frame at B_k on body-(2k-1) to $C^{(2k\text{-}1)}$. Since body-(2k-1) holds a motor for actuating the translational joint, the center of mass $C^{(2k\text{-}1)}$ may slightly deviate from the axis of leg-(k). Including this deviation, the relative position vector of $C^{(2k\text{-}1)}$, $\mathbf{s}_{C/B_k}^{(2k-1)}(t)$, measured by UJ-($k$) leg frame at B_k is expressed as:

$$\mathbf{s}_{C/B_k}^{(2k-1)}(t) = \mathbf{e}_{B_k}^{(\mathrm{UJ}\ 2k-1)}(t)\hat{s}_{C/B_k}^{(2k-1)}, \quad (2.12a)$$

$$\hat{s}_{C/B_k}^{(2k-1)} = \begin{pmatrix} \Delta\hat{s}_{1C/B_k}^{(2k-1)} \\ \Delta\hat{s}_{2C/B_k}^{(2k-1)} \\ \hat{l}_{\mathrm{UJ}}^{(2k-1)} \end{pmatrix}, \tag{2.12b}$$

where $\Delta\hat{s}_{1C/B_k}^{(2k-1)}$ and $\Delta\hat{s}_{2C/B_k}^{(2k-1)}$ express the deviation of $C^{(2k\text{-}1)}$ from the axis of leg-(k), and $\hat{l}_{\mathrm{UJ}}^{(2k-1)}$denotes the $s_{3B_k}^{(\mathrm{UJ}\ 2k-1)}$-coordinate of $C^{(2k\text{-}1)}$ measured from B_k, as illustrated in Fig. 2.7.

The connection of body-(2k-1) frame at $C^{(2k\text{-}1)}$ to the UJ-(k) leg frame at B_k on body-(2k-1) is expressed by the frame connection matrix $E^{(2k-1/\mathrm{UJ}\ 2k-1)}(t)$:

$$\left(\mathbf{e}^{(2k-1)}(t) \quad \mathbf{r}_C^{(2k-1)}(t)\right) = \left(\mathbf{e}_{B_k}^{(\mathrm{UJ}\ 2k-1)}(t) \quad \mathbf{r}_{B_k}(t)\right)\begin{bmatrix} I_3 & \hat{s}_{C/B_k}^{(2k-1)} \\ 0_{1\times 3} & 1 \end{bmatrix}, \tag{2.13}$$

To prepare for the computation of kinetic energy, body-(2k-1) frame is expressed with respect to body-(0) frame by substituting Eqs. (2.10a) and (2.11a) into Eq. (2.13):

$$\left(\mathbf{e}^{(2k-1)}(t) \quad \mathbf{r}_C^{(2k-1)}(t)\right) = \left(\mathbf{e}^{(0)}(t) \quad \mathbf{r}_C^{(0)}(t)\right) E^{(2k-1/0)}(t), \tag{2.14a}$$

where

$$E^{(2k-1/0)}(t) \equiv \begin{bmatrix} R^{(2k-1/0)}(t) & s_C^{(2k-1/0)}(t) \\ 0_{1\times 3} & 1 \end{bmatrix}, \tag{2.14b}$$

and performing the multiplications using Eqs. (2.10b) and (2.11b), one finds

$$R^{(2k-1/0)}(t) = R_{3\,B_k}(\hat{\theta}_k^{(0)}) R_{1\,B_k UJ}(\phi_1^{(k)}(t)) R_{2B_k UJ}\left(\phi_2^{(k)}(t)\right), \tag{2.14c}$$

$$s_C^{(2k-1/0)}(t) = R^{(2k-1/0)}(t)\,\hat{s}_{C/B_k}^{(2k-1)} + \hat{s}_{B_k}^{(0)}, \tag{2.14d}$$

and where $\hat{s}_{B_k}^{(0)}$ was defined in Eq. (2.9b).

2.3.2.4 Body-(2k) Frame: $\left(\mathbf{e}^{(2k)}(t) \quad \mathbf{r}_C^{(2k)}(t)\right)$

The top end of the lower leg, body-(2k-1), has a mechanism to actively slide and passively rotate the cylindrical upper leg, body-(2k), to facilitate a translational joint. The $s_3^{(2k-1)}$-distance between the center of mass of body-(2k-1), $C^{(2k\text{-}1)}$, and that of body-(2k), $C^{(2k)}$, is expressed by $d^{(k)}(t)$, as illustrated in Fig. 2.7. The passive rotation with $\mathbf{e}_3^{(2k-1)}(t)$ by the angle $\phi_3^{(2k/2k-1)}(t)$ is expressed by the elementary rotation matrix: $R_{3\,\mathrm{ATJ}}\left(\phi_3^{(2k/2k-1)}(t)\right)$. *Body-(2k) frame* is now defined with respect to body-(2k-1) frame as:

$$\left(\mathbf{e}^{(2k)}(t) \quad \mathbf{r}_C^{(2k)}(t)\right) = \left(\mathbf{e}^{(2k-1)}(t) \quad \mathbf{r}_C^{(2k-1)}(t)\right) E^{(2k/2k-1)}(t), \tag{2.15a}$$

where

$$E^{(2k/2k-1)}(t) = \begin{bmatrix} R_{3\,\mathrm{TJ}}(\phi_3^{(2k/2k-1)}(t)) & s_C^{(2k/2k-1)}(t) \\ 0_{1\times 3} & 1 \end{bmatrix}, \tag{2.15b}$$

and their component matrices defined as:

$$R_{3\,\mathrm{TJ}}\left(\phi_3^{(2k/2k-1)}(t)\right) \equiv \begin{bmatrix} \cos\phi_3^{(2k/2k-1)}(t) & -\sin\phi_3^{(2k/2k-1)}(t) & 0 \\ \sin\phi_3^{(2k/2k-1)}(t) & \cos\phi_3^{(2k/2k-1)}(t) & 0 \\ 0 & 0 & 1 \end{bmatrix}, \tag{2.15c}$$

$$s_C^{(2k/2k-1))}(t) = \begin{pmatrix} -\Delta\hat{s}_{1C/B_k}^{(2k-1)} \\ -\Delta\hat{s}_{2C/B\,k}^{(2k-1)} \\ d^{(k)}(t) \end{pmatrix}. \tag{2.15d}$$

In Eq. (2.15d), the terms: $-\Delta\hat{s}_{1C/B_k}^{(2k-1)}$and $-\Delta\hat{s}_{2C/B_k}^{(2k-1)}$ place $C^{(2k)}$ back on the axis of leg-(k).

2.3.2.5 SJ-(k) Ball Frame at T_k on Body-(2k): $\left(\mathbf{e}_{T_k}^{(\mathrm{SJ}\,2k)}(t) \quad \mathbf{r}_{T_k}(t)\right)$

The top end of body-(2k) is the spherical ball of SJ-(k). The center of the ball is located at T_k, whose axial distance from $C^{(2k)}$ is $\hat{l}_{T_k}^{(2k)}$, as shown in Fig. 2.7. Therefore, SJ-(k) *ball fame at T_k on body*-(2k) is obtained by parallel translating body-(2k) frame to T_k by $e_3\hat{l}_{\mathrm{SJ}}^{(2k)}$ without any rotation:

$$\left(\mathbf{e}_{T_k}^{(\mathrm{SJ}\,2k)}(t) \quad \mathbf{r}_{T_k}(t)\right) = \left(\mathbf{e}^{(2k)}(t) \quad \mathbf{r}_C^{(2k)}(t)\right)\begin{bmatrix} I_3 & e_3\hat{l}_{\mathrm{SJ}}^{(2k)} \\ 0_{1\times 3} & 1 \end{bmatrix}. \tag{2.16}$$

2.3.2.6 SJ-(k) Socket Frame at T_k on Body-(13) Along Path (ii)

To conclude path (ii) the spherical ball must be fit into SJ-(k) socket at T_k on body-(13). This fitting is accomplished at T_k by rotating SJ-(k) ball frame to SJ-(k) socket frame at T_k on body-(13). The rotation is expressed by $R_{T_k\mathrm{SJ}}^{(\mathrm{SJ}\,13/2k)}(t)$

$$\left(\mathbf{e}_{T_k}^{(\mathrm{SJ}\,13)}(t) \quad \mathbf{r}_{T_k}(t)\right)_{path(ii)} = \left(\mathbf{e}_{T_k}^{(\mathrm{SJ}\,2k)}(t) \quad \mathbf{r}_{T_k}(t)\right)\begin{bmatrix} R_{T_k\mathrm{SJ}}^{(\mathrm{SJ}\,13/\mathrm{SJ}\,2k)}(t) & 0_{3\times 1} \\ 0_{1\times 3} & 1 \end{bmatrix}. \tag{2.17}$$

Combining Eqs. (2.16) and (2.17), SJ-(k) socket frame at T_k on body-(13) is expressed relatively with respect to body-(2k) frame as:

$$\left(\mathbf{e}_{T_k}^{(\mathrm{SJ}\,13)}(t) \quad \mathbf{r}_{T_k}(t)\right)_{path(ii)} = \left(\mathbf{e}^{(2k)}(t) \quad \mathbf{r}_C^{(2k)}(t)\right)E_{T_k}^{(\mathrm{SJ}\,13/2k)}(t), \tag{2.18a}$$

where the frame connection matrix $E_{T_k}^{(\mathrm{SJ}\,13/2k)}(t)$ is computed as:

$$E_{T_k}^{(\mathrm{SJ}\,13/2k)}(t) = \begin{bmatrix} R_{T_k\mathrm{SJ}}^{(\mathrm{SJ}\,13/\mathrm{SJ}\,2k)}(t) & e_3\hat{l}_{\mathrm{SJ}}^{(2k)} \\ 0_{1\times 3} & 1 \end{bmatrix}. \tag{2.18b}$$

Finally, SJ-(k) socket frame is expressed with respect to body-(0) frame using the frame connection matrix $\left(E_{T_k}^{(SJ\ 13/0)}(t)\right)_{path\ (ii)}$ as:

$$\left(\mathbf{e}_{T_k}^{(\mathrm{SJ}\ 13)}(t) \quad \mathbf{r}_{T_k}(t)\right)_{path\ (ii)} = \left(\mathbf{e}^{(0)}(t) \quad \mathbf{r}_C^{(0)}(t)\right)\left(E_{T_k}^{(\mathrm{SJ}\ 13/0)}(t)\right)_{path\ (ii)}, \quad (2.19a)$$

where the components of the frame connection matrix are defined as Eq. (2.7b) for path (i):

$$\left(E_{T_k}^{(\mathrm{SJ}\ 13/0)}(t)\right)_{path\ (ii)} \equiv \begin{bmatrix} R_{T_k}^{(\mathrm{SJ}\ 13/0)}(t) & s_{T_k}^{(\mathrm{SJ}\ 13/0)}(t) \\ 0_{1\times 3} & 1 \end{bmatrix}_{path\ (ii)}, \quad (2.19b)$$

and the components are obtained from Eqs. (2.14a), (2.15a) and (2.18a) as:

$$\left(E_{T_k}^{(\mathrm{SJ}\ 13/0)}(t)\right)_{path\ (ii)} = E^{(2k-1/0)}(t)E^{(2k/2k-1)}(t)E_{T_k}^{(\mathrm{SJ}\ 13/2k)}(t). \quad (2.19c)$$

The above multiplications with Eqs. (2.14c, d) yield:

$$\left(R_{T_k}^{(\mathrm{SJ}\ 13/0)}(t)\right)_{path\ (ii)} = R_{3\ B_k}(\hat{\theta}_k^{(0)})R_{1\ B_kUJ}(\phi_1^{(k)}(t))R_{2B_kUJ}\left(\phi_2^{(k)}(t)\right) \times R_{3\mathrm{TJ}}\left(\phi_3^{(2k/2k-1)}(t)\right)R_{T_k\mathrm{SJ}}^{(\mathrm{SJ}\ 13/\mathrm{SJ}\ 2k)}(t), \quad (2.19d)$$

$$\left(s_{T_k}^{(\mathrm{SJ}\ 13/0)}(t)\right)_{path\ (ii)} = R_{3\ B_k}(\hat{\theta}_k^{(0)})R_{1\ B_kUJ}(\phi_1^{(k)}(t))R_{2B_kUJ}\left(\phi_2^{(k)}(t)\right)e_3 l^{(k)}(t) + \hat{s}_{B_k}^{(0)}, \quad (2.19e)$$

where $l^{(k)}(t)$ denotes the total length of leg-(k):

$$l^{(k)}(t) \equiv \hat{l}_{\mathrm{UJ}}^{(\mathrm{UJ}\ 2k-1)} + d^{(k)}(t) + \hat{l}_{\mathrm{SJ}}^{(2k)}. \quad (2.19f)$$

This completes the computation frame connections along path (ii).

2.3.3 Loop Closure Constraints

The loop closure constraints are now expressed *with respect to the body-(0) frame* by equating Eqs. (2.7a, b) to Eqs. (2.19a, b):

$$\begin{bmatrix} R_{T_k}^{(\mathrm{SJ}\ 13/0)}(t) & s_{T_k}^{(\mathrm{SJ}\ 13/0)}(t) \\ 0_{1\times 3} & 1 \end{bmatrix}_{path\ (i)} = \begin{bmatrix} R_{T_k}^{(\mathrm{SJ}\ 13/0)}(t) & s_{T_k}^{(\mathrm{SJ}\ 13/0)}(t) \\ 0_{1\times 3} & 1 \end{bmatrix}_{path\ (ii)}, \quad (2.20a)$$

in components

$$\left(R_{T_k}^{(\mathrm{SJ}\ 13/0)}(t)\right)_{path\ (i)} = \left(R_{T_k}^{(\mathrm{SJ}\ 13/0)}(t)\right)_{path\ (ii)}, \quad (2.20b)$$

$$\left(s_{T_k}^{(\mathrm{SJ}\ 13/0)}(t)\right)_{path\ (i)} = \left(s_{T_k}^{(\mathrm{SJ}\ 13/0)}(t)\right)_{path\ (ii)}. \quad (2.20c)$$

Their components are expressed using Eqs. (2.7d, e) and (2.19d, e) as:

$$R^{(13/0)}(t)\ R_{3\ T_k}\left(\hat{\theta}_k^{(13)}\right) = R_{3\ B_k}(\hat{\theta}_k^{(0)})R_{1\ B_kUJ}(\phi_1^{(k)}(t))R_{2B_kUJ}\left(\phi_2^{(k)}(t)\right) \times R_{3\mathrm{TJ}}\left(\phi_3^{(2k/2k-1)}(t)\right)R_{T_k\mathrm{SJ}}^{(\mathrm{SJ}\ 13/\mathrm{SJ}\ 2k)}(t), \quad (2.20d)$$

$$R^{(13/0)}(t)\hat{s}_{T_k}^{(13)} + s_C^{(13/0)}(t) = R_{3\,B_k}(\hat{\theta}_k^{(0)})R_{1\,B_kUJ}(\phi_1^{(k)}(t))R_{2B_kUJ}\left(\phi_2^{(k)}(t)\right)e_3 l^{(k)}(t) + \hat{s}_{B_k}^{(0)}. \tag{2.20e}$$

The above constraints, expressed in configuration space, are classified as *holonomic constraints* [31]. As a result, the configuration is updated at each time by integrating the constraints on velocities starting from an initial configuration. The corresponding constraints on velocities will be computed in the next section.

In Appendix A, to facilitate design tools for determining dimensions of the platform *both inverse and forward kinematics problems are solved analytically* utilizing the loop closure equations. In the inverse kinematics problem, for a specified top-plate configuration: $R^{(13/0)}$ and $s_C^{(13/0)}$ one finds each leg configuration, $\phi_1^{(k)}$, $\phi_2^{(k)}$, $l^{(k)}$ and $R_{T_k\mathrm{SJ}}^{(\mathrm{SJ}\ 13/\mathrm{SJ}\ 2k)}$. The analytical equations for the inverse kinematics problem are utilized to find: (i) necessary *stroke* of the actuated translational joints (ATJs) and (ii) *workspace*, which shows the accessible top-plate configuration relative to the base plate.

2.4 Velocities of the Coordinate Frames

In this section velocities of the moving coordinate frames are computed. The input velocities of the base plate of the platform are measured at each time. Therefore, it is useful to express the loop closure constraints in velocities. In addition, for the computation of kinetic energy in chapter 3, translational and angular velocities will be computed at each center of mass of constituent bodies. The kinematically admissible velocities are used to update the configuration at each time by integration since the loop closure constraints are holonomic as shown in Eqs. (2.20b, c).

2.4.1 Velocities of the Coordinate Frames along Path(i)

2.4.1.1 Body-(0) Frame Velocity: $\left(\dot{\mathbf{e}}^{(0)}(t) \quad \dot{\mathbf{r}}_C^{(0)}(t)\right)$

The velocity of the origin of body-(0) frame, $\mathbf{r}_C^{(0)}(t)$, is obtained by taking the time derivative of Eq. (2.1a) expressing *time differentiation* with *superposed dots*:

$$\dot{\mathbf{r}}_C^{(0)}(t) = \mathbf{e}^I \dot{x}_C^{(0)}(t), \tag{2.21}$$

in which $\mathbf{e}^I$ is independent of time.

The attitude of body-(0) frame changes with time. Its velocity is obtained by taking the time derivative of Eq. (2.2a) and expressing the result by its own basis, $\mathbf{e}^{(0)}(t)$, using Eq. (2.2d):

$$\dot{\mathbf{e}}^{(0)}(t) = \mathbf{e}^I \dot{R}^{(0)}(t) = \mathbf{e}^{(0)}(t)\overleftrightarrow{\omega^{(0)}(t)}, \tag{2.22a}$$

where $\overleftrightarrow{\omega^{(0)}(t)}$ is referred to as the *skew symmetric angular velocity matrix* [28, 29]:

$$\overleftrightarrow{\omega^{(0)}(t)} \equiv \left(R^{(0)}(t)\right)^T \dot{R}^{(0)}(t) = \begin{bmatrix} 0 & -\omega_3^{(0)}(t) & \omega_2^{(0)}(t) \\ \omega_3^{(0)}(t) & 0 & -\omega_1^{(0)}(t) \\ -\omega_2^{(0)}(t) & \omega_1^{(0)}(t) & 0 \end{bmatrix}, \quad (2.22b)$$

which is a member the Lie algebra *so*(3) of *SO*(3).

The skew-symmetry of $\overleftrightarrow{\omega^{(0)}(t)}$ is easily proven by taking the time derivative of $\left(R^{(0)}(t)\right)^T R^{(0)}(t) = I_3$. In Eq. (2.22a), expressing $\dot{\mathbf{e}}^{(0)}(t)$ with respect to its own basis, $\mathbf{e}^{(0)}(t)$, is consistent with the definition of Lie algebra *so*(3): the velocity $\dot{R}^{(0)}(t)$ at $R^{(0)}(t)$ is left translated by $\left(R^{(0)}(t)\right)^{-1} = \left(R^{(0)}(t)\right)^T$ to the identity I_3 where the Lie algebra is defined, see for example [31].

From the elements of $\overleftrightarrow{\omega^{(0)}(t)}$ the *angular velocity vector* $\boldsymbol{\omega}^{(0)}(t)$ is defined as:

$$\boldsymbol{\omega}^{(0)}(t) = \mathbf{e}^{(0)}(t)\omega^{(0)}(t) = \begin{pmatrix} \mathbf{e}_1^{(0)}(t) & \mathbf{e}_2^{(0)}(t) & \mathbf{e}_3^{(0)}(t) \end{pmatrix} \begin{pmatrix} \omega_1^{(0)}(t) \\ \omega_2^{(0)}(t) \\ \omega_3^{(0)}(t) \end{pmatrix}. \quad (2.23)$$

For the computation of kinetic energy in chapter 3, it is convenient to express the velocity of the body-(0) frame as:

$$\begin{pmatrix} \dot{\mathbf{e}}^{(0)}(t) & \dot{\mathbf{r}}_C^{(0)}(t) \end{pmatrix} = \begin{pmatrix} \mathbf{e}^{(0)}(t)\overleftrightarrow{\omega^{(0)}(t)} & \mathbf{e}^I \dot{x}_C^{(0)}(t) \end{pmatrix} \quad (2.24)$$

since the rotational kinetic energy is expressed by $\omega^{(0)}(t)$ and mass moment of inertia with respect to $\mathbf{e}^{(0)}(t)$, while the translational kinetic energy is expressed by $\dot{x}_C^{(0)}(t)$ with $\mathbf{e}^I$, [29, 30].

The translational velocity $\dot{x}_C^{(0)}(t)$ is used to update $x_C^{(0)}(t)$ using available integration schemes for vectors. However, the updating of the rotation matrix $R^{(0)}(t)$, using given $\overleftrightarrow{\omega^{(0)}(t)}$ in Eq. (2.22b) at each time increment, requires an appropriate integration algorithm, such as *Rodrigues' rotation formula* [17], which assures that the updated rotation matrix remains in *SO*(3) [29, 39].

2.4.1.2 Body-(13) Frame Velocity: $\begin{pmatrix} \dot{\mathbf{e}}^{(13)}(t) & \dot{\mathbf{r}}_C^{(13)}(t) \end{pmatrix}$

The time derivative of Eq. (2.4a) expanded using Eq. (2.4b) yields the skew-symmetric angular-velocity matrix and the translational velocity at the center of mass of body-(13):

$$\begin{pmatrix} \dot{\mathbf{e}}^{(13)}(t) & \dot{\mathbf{r}}_C^{(13)}(t) \end{pmatrix} = \begin{pmatrix} \mathbf{e}^{(13)}(t)\overleftrightarrow{\omega^{(13)}(t)} & \mathbf{e}^I \dot{x}_C^{(13)}(t) \end{pmatrix} \quad (2.25)$$

To familiarize readers with the computations, the steps for taking the time derivative of the first column of Eq. (2.7a): $\mathbf{e}^{(13)}(t) = \mathbf{e}^{(0)}(t)R^{(13/0)}(t)$ are shown:

$$\begin{aligned}\dot{\mathbf{e}}^{(13)}(t) &= \dot{\mathbf{e}}^{(0)}(t)R^{(13/0)}(t) + \mathbf{e}^{(0)}(t)\,\dot{R}^{(13/0)}(t)\\ &= \boldsymbol{e}^{(0)}(t)\left(\overleftrightarrow{\omega^{(0)}(t)}R^{(13/0)(t)} + \dot{R}^{(13/0)(t)}(t)\right)\\ &= \boldsymbol{e}^{(13)}(t)\left(R^{(13/0)}(t)\right)^{T}\left(\overleftrightarrow{\omega^{(0)}(t)}R^{(13/0)(t)} + \dot{R}^{(13/0)(t)}(t)\right)\\ &= \boldsymbol{e}^{(13)}(t)\left\{\overleftrightarrow{\left(R^{(13/0)}(t)\right)^{T}\omega^{(0)}(t)} + \overleftrightarrow{\omega^{(13/0)}(t)}\right\}. \qquad (2.26a)\end{aligned}$$

In the last right-hand side of Eq. (2.26a) in a pair of braces, the following formula is used to obtain the first term:

$$\left(R(t)\right)^{T}\overleftrightarrow{\omega(t)}R(t) = \overleftrightarrow{\left(R(t)\right)^{T}\omega(t)}, \qquad (2.26b)$$

for $R(t) = R^{(13/0)}(t)$ and $\omega(t) = \omega^{(0)}(t)$, whose proof, presented in [29], is reproduced in the Appendix 2.B.

In the pair of braces, the second term defines the *relative skew-symmetric angular-velocity matrix*:

$$\overleftrightarrow{\omega^{(13/0)}(t)} = \left(R^{(13/0)}(t)\right)^{T}\dot{R}^{(13/0)}(t). \qquad (2.26c)$$

In vector form the first column of Eq. (2.25a) and Eq. (2.26a) are written as:

$$\omega^{(13)}(t) = \left(R^{(13/0)}(t)\right)^{T}\omega^{(0)}(t) + \omega^{(13/0)}(t). \qquad (2.27)$$

The time derivative of the second column of Eq. (2.4a): $\mathbf{r}_C^{(13)}(t) = \mathbf{r}_C^{(0)}(t) + \mathbf{e}^{(0)}(t)R^{(13/0)}(t)$ is computed as:

$$\begin{aligned}\dot{\mathbf{r}}_C^{(13)}(t) &= \dot{\mathbf{r}}_C^{(0)}(t) + \dot{\mathbf{e}}^{(0)}(t)s_C^{(13/0)}(t) + \mathbf{e}^{(0)}(t)\dot{s}_C^{(13/0)}(t)\\ &= \mathbf{e}^{I}\left\{\dot{x}_C^{(0)}(t) + R^{(0)}(t)\left(\overleftrightarrow{\omega^{(0)}(t)}\,s_C^{(13/0)}(t) + \dot{s}_C^{(13/0)}(t)\right)\right\}\\ &= \mathbf{e}^{I}\left\{\dot{x}_C^{(0)}(t) + R^{(0)}(t)\left(-\overleftrightarrow{s_C^{(13/0)}(t)}\omega^{(0)}(t) + \dot{s}_C^{(13/0)}(t)\right)\right\}, \qquad (2.28a)\end{aligned}$$

where on the right-hand side in a pair of braces, the first term is obtained by using the formula:

$$\overleftrightarrow{\omega^{(0)}(t)}\,s_C^{(13/0)}(t) = -\overleftrightarrow{s_C^{(13/0)}(t)}\omega^{(0)}(t), \qquad (2.28b)$$

which corresponds to the vector cross product: $\boldsymbol{\omega}^{(0)}(t) \times \mathbf{s}_C^{(13/0)}(t) = -\mathbf{s}_C^{(13/0)}(t) \times \boldsymbol{\omega}^{(0)}(t)$ (observing that both vectors are defined with respect to the body-(0) vector basis, $\mathbf{e}^{(0)}(t)$).

Equation (2.28a) yields the translational velocity of $C^{(13)}$ with respect to $\mathbf{e}^I$:

$$\dot{x}_C^{(13)}(t) = \dot{x}_C^{(0)}(t) + R^{(0)}(t)\left(-\overleftrightarrow{s_C^{(13/0)}(t)}\omega^{(0)}(t) + \dot{s}_C^{(13/0)}(t)\right). \tag{2.29}$$

In Eqs. (2.27) and (2.29), the velocities of the top-plate frame are expressed in terms of the excitation velocities, $\omega^{(0)}(t)$ and $\dot{x}_C^{(0)}(t)$, of the base plate and the relative velocities, $\omega^{(13/0)}(t)$ and $\dot{s}_C^{(13/0)}(t)$ of the top plate. Next SJ-(k) socket frame is the terminal frame of path (i).

2.4.1.3 SJ-(k) Socket Frame Velocities at T_k on Body-(13): $\left(\dot{\mathbf{e}}_{T_k}^{(\mathrm{SJ}\,13)}(t) \quad \dot{\mathbf{r}}_{T_k}(t)\right)_{path(i)}$

To compute the velocity of SJ-(k) socket frame at T_k on body-(13):

$$\left(\dot{\mathbf{e}}_{T_k}^{(\mathrm{SJ}\,13)}(t) \quad \dot{\mathbf{r}}_{T_k}(t)\right)_{path(i)} = \left(\mathbf{e}_{T_k}^{(\mathrm{SJ}\,13)}(t)\,\overleftrightarrow{\omega_{T_k}^{(\mathrm{SJ}\,13)}(t)} \quad \mathbf{e}^I\dot{x}_{T_k}(t)\right)_{path(i)}, \tag{2.30}$$

the time derivative of Eq. (2.6a) is computed to utilize the body-(13) frame velocities just computed in Eq. (2.27) and (2.29). The time derivative of the first column of Eq. (2.6a) is:

$$\begin{aligned}\dot{\mathbf{e}}_{T_k}^{(\mathrm{SJ}\,13)}(t) &= \mathbf{e}_{T_k}^{(\mathrm{SJ}\,13)}(t)\left(R_{3\,T_k}(\hat{\theta}_k^{(13)})\right)^T \overleftrightarrow{\omega^{(13)}(t)}\, R_{3\,T_k}(\hat{\theta}_k^{(13)}) \\ &= \mathbf{e}_{T_k}^{(\mathrm{SJ}\,13)}(t)\overleftrightarrow{\left(R_{3\,T_k}(\hat{\theta}_k^{(13)})\right)^T \omega^{(13)}(t)}\,,\end{aligned} \tag{2.31a}$$

using the formula in Eq. (2.26b).

In vector form, the first column of Eq. (2.30) and Eq. (2.31a) give

$$\omega_{T_k}^{(\mathrm{SJ}\,13)}(t) = \left(R_{3\,T_k}(\hat{\theta}_k^{(13)})\right)^T \omega^{(13)}(t). \tag{2.31b}$$

Substituting Eq. (2.27) into Eq. (2.31b), one obtains

$$\left(\omega_{T_k}^{(\mathrm{SJ}\,13)}(t)\right)_{path(i)} = \left(R_{3\,T_k}(\hat{\theta}_k^{(13)})\right)^T \left\{\left(R^{(13/0)}(t)\right)^T \omega^{(0)}(t) + \omega^{(13/0)}(t)\right\}. \tag{2.32}$$

The time derivative of the second column of Eq. (2.6a) is computed as:

$$\begin{aligned}\dot{\mathbf{r}}_{T_k}(t) = \mathbf{e}^I\dot{x}_{T_k}(t) &= \mathbf{e}^{(13)}(t)\overleftrightarrow{\omega^{(13)}(t)}\,\hat{s}_{T_k}^{(13)} + \mathbf{e}^I\dot{x}_C^{(13)}(t) \\ &= -\mathbf{e}^{(13)}(t)\overleftrightarrow{\hat{s}_{T_k}^{(13)}}\,\omega^{(13)}(t) + \boldsymbol{e}^I\dot{x}_C^{(13)}(t) \\ &= \mathbf{e}^I\left(-R^{(13)}(t)\overleftrightarrow{\hat{s}_{T_k}^{(13)}}\,\omega^{(13)}(t) + \dot{x}_C^{(13)}(t)\right).\end{aligned} \tag{2.33a}$$

Using $R^{(13)}(t) = R^{(0)}(t)R^{(13/0)}$, Eq. (2.33a) yields in components:

$$\dot{x}_{T_k}(t) = \dot{x}_C^{(13)}(t) - R^{(0)}(t)R^{(13/0)}(t)\overleftrightarrow{\hat{s}_{T_k}^{(13)}}\,\omega^{(13)}(t). \tag{2.33b}$$

The substitution of Eqs. (2.27) and (2.29) into Eq. (2.33b) gives the velocity at T_k of SJ-(k) along path (i)

$$\left(\dot{x}_{T_k}(t)\right)_{path(i)} = \dot{x}_C^{(0)}(t) - R^{(0)}(t)\overleftarrow{\left(s_C^{(13/0)}(t) + R^{(13/0)}(t)\hat{s}_{T_k}^{(13)}\right)}\omega^{(0)}(t)$$

$$+R^{(0)}(t)\left(-R^{(13/0)}(t)\overleftarrow{\hat{s}_{T_k}^{(13)}}\omega^{(13/0)}(t) + \dot{s}_C^{(13/0)}(t)\right). \quad (2.34)$$

The velocity of SJ-(k) socket frame at T_k on body-(13) is now expressed by Eqs. (2.30), (2.32) and (2.34).

2.4.1.4 Body-(14) Frame Velocity: $\left(\dot{\mathbf{e}}^{(14)}(t) \quad \dot{\mathbf{r}}_C^{(14)}(t)\right)$

The velocities of the body-(14) frame is computed by taking the time derivative of Eq. (2.8a):

$$\left(\dot{\mathbf{e}}^{(14)}(t) \quad \dot{\mathbf{r}}_C^{(14)}(t)\right) = \left(\mathbf{e}^{(14)}(t)\overleftarrow{\omega^{(14)}(t)} \quad \mathbf{e}^I\dot{x}_C^{(14)}(t)\right) \quad (2.35a)$$

The angular velocities and the translational velocities are easily obtained as:

$$\omega^{(14)}(t) = \omega^{(13)}(t), \quad (2.35b)$$

$$\dot{x}_C^{(14)}(t) = \dot{x}_C^{(13)}(t) - R^{(13)}(t)\overleftarrow{e_3\hat{h}^{(14/13)}}\omega^{(13)}(t). \quad (2.35c)$$

Equations (2.35b) and (2.35c) are typical recursive equations along the graph tree and further expressed using Eqs. (2.27) and (2.29) as:

$$\omega^{(14)}(t) = \left(R^{(13/0)}(t)\right)^T\omega^{(0)}(t) + \omega^{(13/0)}(t), \quad (2.36a)$$

$$\dot{x}_C^{(14)}(t) = \dot{x}_C^{(0)}(t) - R^{(0)}(t)\overleftarrow{\left(s_C^{(13/0)}(t) + R^{(13/0)}(t)e_3\hat{h}^{(14/13)}\right)}\omega^{(0)}(t)$$

$$+R^{(0)}(t)\left(-R^{(13/0)}(t)\overleftarrow{e_3\hat{h}^{(14/13)}}\omega^{(13/0)}(t) + \dot{s}_C^{(13/0)}(t)\right). \quad (2.36b)$$

2.4.2 Velocities of the Coordinate Frames along Path(ii)

Along path (ii) shown in Fig. 2.2(b) the velocities of body-(2k-1) frame of the lower leg and body-(2k) frame of the upper leg at their origins as well as those of SJ-(k) socket frame at T_k on body-(13) are computed.

2.4.2.1 Body-(2k-1) Frame Velocity: $\left(\dot{\mathbf{e}}^{(2k-1)}(t) \quad \dot{\mathbf{r}}_C^{(2k-1)}(t)\right)$

The frame velocities of the lower leg, body-(2k-1):

$$\left(\dot{\mathbf{e}}^{(2k-1)}(t) \quad \dot{\mathbf{r}}_C^{(2k-1)}(t)\right) = \left(\mathbf{e}^{(2k-1)}(t)\overleftarrow{\omega^{(2k-1)}(t)} \quad \mathbf{e}^I\dot{x}_C^{(2k-1)}(t)\right), \quad (2.37)$$

are computed by taking the time derivatives of each column of Eq. (2.14a) using Eqs. (2.14b, c). The first column of Eq. (2.14a) is

$$\mathbf{e}^{(2k-1)}(t) = \mathbf{e}^{(0)}(t)R^{(2k-1/0)}(t), \quad (2.38a)$$

and the second column:

$$\mathbf{r}_C^{(2k-1)}(t) = \mathbf{r}_C^{(0)}(t) + \mathbf{e}^{(0)}(t)\left(R^{(2k-1/0)}(t)\hat{s}_{C/B_k}^{(2k-1)} + \hat{s}_{B_k}^{(0)}\right). \quad (2.38b)$$

where $R^{(2k-1/0)}(t)$ was defined in Eq. (2.14c).

The time derivative of Eq. (2.38a) yields using Eq. (2.22a) and the formula in Eq (2.26b):

$$\overleftrightarrow{\omega^{(2k-1)}(t)} = \overleftrightarrow{\left(R^{(2k-1/0)}(t)\right)^T \omega^{(0)}(t)} + \overleftrightarrow{\omega^{(2k-1/0)}(t)}, \tag{2.39a}$$

where the relative skew-symmetric angular velocity matrix is defined as:

$$\overleftrightarrow{\omega^{(2k-1/0)}(t)} = \left(R^{(2k-1/0)}(t)\right)^T \dot{R}^{(2k-1/0)}(t), \tag{2.39b}$$

and its actual computation using Eq. (2.14c) gives

$$\overleftrightarrow{\omega^{(2k-1/0)}(t)} = \overleftrightarrow{\left(R_{2\,B_k\,UJ}(\phi_2^{(k)}(t)\right)^T e_1\dot{\phi}_1^{(k)}(t)} + \overleftrightarrow{e_2\dot{\phi}_2^{(k)}(t)}, \tag{2.39c}$$

incorporating

$$\left(R_{1\,B_kUJ}(\dot{\phi}_1^{(k)}(t)\right)^T \dot{R}_{1\,B_kUJ}(\dot{\phi}_1^{(k)}(t)) = \overleftrightarrow{e_1\dot{\phi}_1^{(k)}(t)}, \tag{2.39d}$$

$$\left(R_{2\,B_kUJ}(\dot{\phi}_2^{(k)}(t)\right)^T \dot{R}_{2\,B_kUJ}\left(\dot{\phi}_2^{(k)}(t)\right) = \overleftrightarrow{e_2\dot{\phi}_2^{(k)}(t)}, \tag{2.39e}$$

in which $e_1 \equiv (1 \quad 0 \quad 0)^T$ and $e_2 \equiv (0 \quad 1 \quad 0)^T$.

In vector form, Eqs. (2.39a) and (2.39c) become, respectively,

$$\omega^{(2k-1)}(t) = \left(R^{(2k-1/0)}(t)\right)^T \omega^{(0)}(t) + \omega^{(2k-1/0)}(t), \tag{2.40a}$$

$$\omega^{(2k-1/0)}(t) = \left(R_{2\,B_kUJ}\left(\phi_2^{(k)}(t)\right)\right)^T e_1\dot{\phi}_1^{(k)}(t) + e_2\dot{\phi}_2^{(k)}(t). \tag{2.40b}$$

The substitution of Eq. (2.40b) into Eq. (2.40a) gives in vector form:

$$\omega^{(2k-1)}(t) = \left(R^{(2k-1/0)}(t)\right)^T \omega^{(0)}(t) + \left(R_{2\,B_kUJ}\left(\phi_2^{(k)}(t)\right)\right)^T e_1\dot{\phi}_1^{(k)}(t) + e_2\dot{\phi}_2^{(k)}(t). \tag{2.40c}$$

Using Eq. (2.39b), the time derivative of Eq. (2.38b) yields

$$\dot{\mathbf{r}}_C^{(2k-1)}(t) = \dot{\mathbf{r}}_C^{(0)}(t) + \mathbf{e}^{(0)}(t)\overleftrightarrow{\omega^{(0)}(t)}\left(R^{(2k-1/0)}(t)\hat{s}_{C/B_k}^{(2k-1)} + \hat{s}_{B_k}^{(0)}\right) + \mathbf{e}^{(0)}(t)R^{(2k-1/0)}(t)\overleftrightarrow{\omega^{(2k-1/0)}(t)}\hat{s}_{C/B_k}^{(\mathrm{UJ}\ 2k-1)}. \tag{2.41a}$$

The velocity of $C^{(2k\text{-}1)}$ with $\mathbf{e}^I$ is obtained using Eqs. (2.2a), (2.22a) and (2.28b) as:

$$\dot{x}_C^{(2k-1)}(t) = \dot{x}_C^{(0)}(t) - R^{(0)}(t)\overleftrightarrow{R^{(2k-1/0)}(t)\hat{s}_{C/B_k}^{(2k-1)} + \hat{s}_{B_k}^{(0)}}\,\omega^{(0)}(t) - R^{(0)}(t)R^{(2k-1/0)}(t)\overleftrightarrow{\hat{s}_{C/B_k}^{(2k-1)}}\omega^{(2k-1/0)}(t) \tag{2.41b}$$

where

$$R^{(2k-1)}(t) = R^{(0)}(t)R^{(2k-1/0)}(t). \tag{2.41c}$$

Equations (2.40c) and (2.41b) with Eq. (2.40b) express the velocity components of body-(2k-1) frame in Eq. (2.37).

2.4.2.2 Body-(2k) Frame Velocity: $\left(\dot{\mathbf{e}}^{(2k)}(t) \quad \dot{\mathbf{r}}_C^{(2k)}(t)\right)$

The velocities of the body-(2k) frame at $C^{(2k)}$ are computed from Eq. (2.15a) as:

$$\left(\dot{\mathbf{e}}^{(2k)}(t) \quad \dot{\mathbf{r}}_C^{(2k)}(t)\right) = \left(\mathbf{e}^{(2k)}(t)\overleftrightarrow{\omega^{(2k)}(t)} \quad \mathbf{e}^I \dot{x}_C^{(2k)}(t)\right). \tag{2.42a}$$

The time derivative of the first column of Eq. (2.15a) gives in vector form:

$$\omega^{(2k)}(t) = \left(R_{3\text{TJ}}\left(\phi_3^{(2k/2k-1)}(t)\right)\right)^T \omega^{(2k-1)}(t) + e_3\dot{\phi}_3^{(2k/2k-1)}(t), \tag{2.42b}$$

while that of the second column yields, observing that in Eq. (2.15d) only $d^{(k)}(t)$ is time dependent:

$$\dot{x}_C^{(2k)}(t) = \dot{x}_C^{(2k-1)}(t) + R^{(2k-1)}(t)\left(-\overleftrightarrow{s_C^{(2k/2k-1)}(t)}\omega^{(2k-1)}(t) + e_3\dot{d}^{(k)}(t)\right), \tag{2.42c}$$

2.4.2.3 SJ-(k) Socket Frame Velocities at T_k on Body-(13): $\left(\dot{\mathbf{e}}_{T_k}^{(\text{SJ }13)}(t) \quad \dot{\mathbf{r}}_{T_k}(t)\right)_{path(ii)}$

To compute the velocity of SJ-(k) socket frame at T_k on body-(13):

$$\left(\dot{\mathbf{e}}_{T_k}^{(\text{SJ }13)}(t) \quad \dot{\mathbf{r}}_{T_k}(t)\right)_{path(ii)} = \left(\mathbf{e}_{T_k}^{(\text{SJ }13)}(t)\overleftrightarrow{\omega_{T_k}^{(\text{SJ }13)}(t)} \quad \mathbf{e}^I \dot{x}_{T_k}^{(\text{SJ }13)}(t)\right)_{path(ii)}, \tag{2.43a}$$

the time derivatives of the columns of Eq. (2.18a) are computed.

The time derivative of the first column gives in vector form:

$$\left(\omega_{T_k}^{(\text{SJ }13)}(t)\right)_{path(ii)} = \left(R_{T_k\text{SJ}}^{(\text{SJ }13/\text{SJ }2k)}(t)\right)^T \omega^{(2k)}(t) + \omega_{T_k\text{SJ}}^{(\text{SJ }13/\text{SJ }2k)}(t), \tag{2.43b}$$

where

$$\omega_{T_k\text{SJ}}^{(\text{SJ }13/\text{SJ }2k)}(t) = \left(R_{T_k\text{SJ}}^{(\text{SJ }13/\text{SJ }2k)}(t)\right)^T \dot{R}_{T_k\text{SJ}}^{(\text{SJ }13/\text{SJ }2k)}(t). \tag{2.43c}$$

The time derivative of the second column gives

$$\left(\dot{x}_{T_k}(t)\right)_{path\ (ii)} = \dot{x}_C^{(2k)}(t) - R^{(2k-1)}(t)R_{3\text{ TJ}}\left(\phi_3^{(2k/2k-1)}(t)\right)\overleftrightarrow{e_3\hat{l}_{\text{SJ}}^{(2k)}}\,\omega^{(2k)}(t). \tag{2.43d}$$

To write closure equations it is necessary to express the velocities of path (ii) in terms of $\omega^{(0)}(t)$, $\dot{\phi}_1^{(k)}(t)$, $\dot{\phi}_2^{(k)}(t)$, and $\omega_{T_k\text{SJ}}^{(\text{SJ }13/\text{SJ }2k)}(t)$. Thus Eq. (2.43b) is rewritten using Eqs. (2.42b) and (2.40c) as:

$$\begin{aligned}\left(\omega_{T_k}^{(\text{SJ }13)}(t)\right)_{path(ii)} &= \left(R_{T_k\text{SJ}}^{(\text{SJ }13/\text{SJ }2k)}(t)\right)^T \left(R_{3\text{ TJ}}(\phi_3^{(2k/2k-1)}(t))\right)^T \\ &\times\left\{\left(R^{(2k-1/0)}(t)\right)^T \omega^{(0)}(t) + \left(R_{2\,B_k\text{UJ}}\left(\phi_2^{(k)}(t)\right)\right)^T e_1\dot{\phi}_1^{(k)}(t) + e_2\dot{\phi}_2^{(k)}(t)\right\} \\ &+\left(R_{T_k\text{SJ}}^{(\text{SJ }13/\text{SJ }2k)}(t)\right)^T e_3\dot{\phi}_3^{(2k/2k-1)}(t) + \omega_{T_k\text{SJ}}^{(\text{SJ }13/\text{SJ }2k)}(t).\end{aligned} \tag{2.44a}$$

Similarly, Eq. (2.43d) is rewritten using Eqs. (2.42b, c), (2.41c), and (2.40c) as:

$$\left(\dot{x}_{T_k}(t)\right)_{path\ (ii)} = \dot{x}_C^{(0)}(t) - R^{(0)}(t)\overleftrightarrow{R^{(2k-1/0)}(t)e_3 l^{(k)}(t) + \hat{s}_{B_k}^{(0)}}\,\omega^{(0)}(t)$$
$$-R^{(2k-1)}(t)\overleftrightarrow{e_3 l^{(k)}(t)}\left\{\left(R_{2\,B_k\mathrm{UJ}}\left(\phi_2^{(k)}(t)\right)\right)^T e_1\dot{\phi}_1^{(k)}(t) + e_2\dot{\phi}_2^{(k)}(t)\right\}$$
$$+R^{(2k-1)}(t)e_3\dot{d}^{(k)}(t). \tag{2.44b}$$

2.4.3 Loop Closure Constraints on Velocities

The loop closure constraints on velocities in Fig. 2.2(b) are:

$$\left(\omega_{T_k}^{(\mathrm{SJ}\ 13)}(t)\right)_{path(i)} = \left(\omega_{T_k}^{(\mathrm{SJ}\ 13)}(t)\right)_{path(ii)}, \tag{2.45a}$$

$$\left(\dot{x}_{T_k}(t)\right)_{path(i)} = \left(\dot{x}_{T_k}(t)\right)_{path(ii)}. \tag{2.45b}$$

Equation (2.45a) is explicitly written using Eqs. (2.32) and (2.43b) as:

$$\left(R_{3\,T_k}(\hat{\theta}_k^{(13)})\right)^T\left\{\left(R^{(13/0)}(t)\right)^T\omega^{(0)}(t) + \omega^{(13/0)}(t)\right\}$$
$$= \left(R_{T_k\mathrm{SJ}}^{(\mathrm{SJ}\ 13/\mathrm{SJ}\ 2k)}(t)\right)^T\left(R_{3\,\mathrm{TJ}}(\phi_3^{(2k/2k-1)}(t))\right)^T$$
$$\times\left\{\left(R^{(2k-1/0)}(t)\right)^T\omega^{(0)}(t) + \left(R_{2\,B_k\mathrm{UJ}}\left(\phi_2^{(k)}(t)\right)\right)^T e_1\dot{\phi}_1^{(k)}(t) + e_2\dot{\phi}_2^{(k)}(t)\right\}$$
$$+\left(R_{T_k\mathrm{SJ}}^{(\mathrm{SJ}\ 13/\mathrm{SJ}\ 2k)}(t)\right)^T e_3\dot{\phi}_3^{(2k/2k-1)}(t) + \omega_{T_k\mathrm{SJ}}^{(\mathrm{SJ}\ 13/\mathrm{SJ}\ 2k)}(t). \tag{2.46a}$$

Similarly, Eq. (2.45b) is written explicitly using Eqs. (2.34) and (2.43d). After a slight simplification, it becomes

$$-\overleftrightarrow{\Delta s_{CL}^{(k)}(t)}\,\omega^{(0)}(t) - R^{(13/0)}(t)\overleftrightarrow{\hat{s}_{T_k}^{(13)}}\omega^{(13/0)}(t) + \dot{s}_C^{(13/0)}(t)$$
$$= R^{(2k-1/0)}(t)\left[-\overleftrightarrow{e_3 l^{(k)}(t)}\left\{\left(R_{2\,B_k\mathrm{UJ}}\left(\phi_2^{(k)}(t)\right)\right)^T e_1\dot{\phi}_1^{(k)}(t) + e_2\dot{\phi}_2^{(k)}(t)\right\} + e_3\dot{d}^{(k)}(t)\right]. \tag{2.46b}$$

where

$$\Delta s_{CL}^{(k)}(t) \equiv \left(s_C^{(13/0)}(t) + R^{(13/0)}(t)\hat{s}_{T_k}^{(13)}\right) - \left(\hat{s}_{B_k}^{(0)} + R^{(2k-1/0)}(t)e_3 l^{(k)}(t)\right). \tag{2.46c}$$

To simplify the subsequent presentation, the approximation $\phi_3^{(2k/2k-1)}(0) = 0$ is incorporated. $\phi_3^{(2k/2k-1)}(t)$, defined in Eqs. (2.15b, c), expresses the axial rotation of the upper leg, body-($2k$), relative to the lower leg, body-($2k$-1) with the initial value of: $\phi_3^{(2k/2k-1)}(t) = 0$. In the next chapter, it will be shown that $\phi_3^{(2k/2k-1)}(t)$ remains zero since its axial moment of inertia is negligible, and there is no external torque but some viscous damping. With this hindsight $\dot{\phi}_3^{(2k/2k-1)}(t)$ is neglected in Eq. (2.46a). The resulting equation gives the angular velocity at the spherical joint, SJ-(k), as:

$$\omega_{T_k\mathrm{SJ}}^{(2k/2k-1)}(t) = \left\{\left(R^{(13/0)}(t)\, R_{3\,T_k}(\hat{\theta}_k^{(13)})\right)^T - \left(R^{(2k-1/0)}(t)\, R_{T_k\mathrm{SJ}}^{(\mathrm{SJ}\,13/\mathrm{SJ}\,2k)}(t)\right)^T\right\}\omega^{(0)}(t) +$$

$$\left(R_{3\,T_k}(\hat{\theta}_k^{(13)})\right)^T \omega^{(13/0)}(t) - \left(R_{T_k\mathrm{SJ}}^{(\mathrm{SJ}\,13/\mathrm{SJ}\,2k)}(t)\right)^T \left\{\left(R_{2\,B_k\mathrm{UJ}}\left(\phi_2^{(k)}(t)\right)\right)^T e_1\dot{\phi}_1^{(k)}(t) + e_2\dot{\phi}_2^{(k)}(t)\right\}. \tag{2.47}$$

2.4.4 Equations for Inverse Instantaneous Kinematics

For kinematics-based control, Eq. (2.46a) deserves careful interpretations. At each time step for measured input disturbance: $\omega^{(0)}(t)$ and $\dot{x}^{(0)}(t)$ of the base plate, to counter-measure the motion of the base plate, the desired values of the top-plate velocities: $\omega^{(13/0)}(t)$ and $\dot{s}_C^{(13/0)}(t)$ are computed. This task is accomplished by controlling the actuated translational joint velocities: $\dot{d}^{(k)}(t)$ for inverse kinematics control (IKC) for $k = 1, 2, \cdots, 6$. The actuation of the leg also induces the universal joint motion: $\dot{\phi}_1^{(k)}(t)$, and $\dot{\phi}_2^{(k)}(t)$.

For the *inverse instantaneous kinematics* problem [40], Eq. (2.46b) is solved analytically for those velocities, stored in a 3 × 1 column matrix, $\dot{q}_L^{(k)}(t)$:

$$\dot{q}_L^{(k)}(t) \equiv \begin{pmatrix} \dot{\phi}_1^{(k)}(t) \\ \dot{\phi}_2^{(k)}(t) \\ \dot{d}^{(k)}(t) \end{pmatrix} = \begin{pmatrix} -w_2^{vel}(t)/(l^{(k)}(t)\cos\phi_2^{(k)}(t)) \\ w_1^{vel}(t)/l^{(k)}(t) \\ w_3^{vel}(t) \end{pmatrix}, \tag{2.48a}$$

where the left-hand side of Eq. (2.46b) is expressed by $w^{vel}(t)$ as:

$$w^{vel}(t) \equiv \left(R^{(2k-1/0)}(t)\right)^T \left(-R^{(13/0)}(t)\overleftrightarrow{\hat{s}_{T_k}^{(13)}}\omega^{(13/0)}(t) + \dot{s}_C^{(13/0)}(t) - \overleftrightarrow{\Delta s_{CL}^{(k)}(t)}\,\omega^{(0)}(t)\right), \tag{2.48b}$$

and

$$w^{vel}(t) \equiv \begin{pmatrix} w_1^{vel}(t) \\ w_2^{vel}(t) \\ w_3^{vel}(t) \end{pmatrix}. \tag{2.48c}$$

In Eq. (2.48a), one notes that $l^{(k)}(t) \neq 0$ and $\phi_2^{(k)}(t) \neq \pm\pi/2$ due to the leg constraints, discussed in the Appendix 2.A.

2.5 Implementation of Inverse Kinematics Control

Figure 2.8 illustrates a flowchart of IKC utilizing the inverse kinematics to feedforward the desired actuator displacements and PID for feedback control.

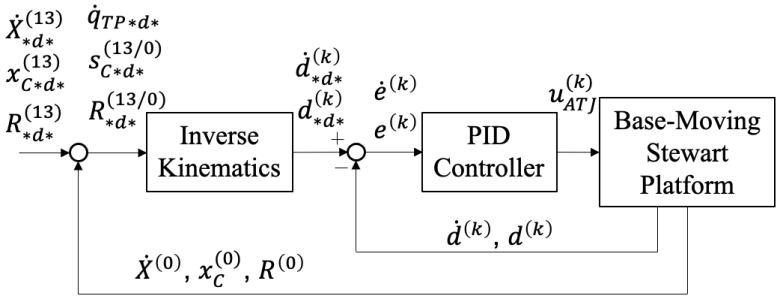

Figure 2.8: Flowchart of inverse kinematics control of a base-moving Stewart platform with PID feedback

In Fig. 2.8, the *desired relative top-plate* translational vector $s_{C*d*}^{(13/0)}(t)$ and the rotation matrix $R_{*d*}^{(13/0)}(t)$, and the corresponding velocities $(\dot{q}_{TP*d*}(t)) \equiv \left(\dot{s}_{C*d*}^{(13/0)}(t) \quad \omega_{*d*}^{(13/0)}(t)\right)^T$ with respect to the base-plate frame are computed from the *desired top-plate* translational vector $x_{C*d*}^{(13)}(t)$ and the rotation matrix $R_{*d*}^{(13)}(t)$, and the corresponding velocities $(\dot{X}_{*d*}^{(13)}(t)) \equiv \left(\dot{x}_{C*d*}^{(13)}(t) \quad \omega_{*d*}^{(13)}(t)\right)^T$ for *measured input base-plate* velocities $(\dot{X}^{(0)}(t)) \equiv \left(\dot{x}_C^{(0)}(t) \quad \omega^{(0)}(t)\right)^T$ and the corresponding translational vector $x_C^{(0)}(t)$ and the rotation matrix $R^{(0)}(t)$. From the inverse kinematics computation, desired velocities $\dot{d}_{*d*}^{(k)}(t)$ and displacements $d_{*d*}^{(k)}(t)$ of the actuated translational joints are derived. Then, by employing a PID controller for each actuator, a control input: $u_{ATJ}^{(k)}(t)$ is obtained from the errors, defined as the difference between the measured and the desired linear actuator velocities and extensions as:

$$u_{ATJ}^{(k)}(t) = K_p^{(k)} e^{(k)}(t) + K_i^{(k)} \int e^{(k)}(t)dt + K_d^{(k)} \dot{e}^{(k)}(t), \tag{2.49a}$$

where

$$e^{(k)}(t) \equiv d^{(k)}(t) - d_{*d*}^{(k)}(t), \;\; \dot{e}^{(k)}(t) \equiv \dot{d}^{(k)}(t) - \dot{d}_{*d*}^{(k)}(t) \tag{2.49b,c}$$

and where $K_p^{(k)}$, $K_i^{(k)}$, and $K_d^{(k)}$ are proportional, integral, and derivative gains.

2.6 Concluding Remarks

In this chapter for a base-moving Stewart platform, utilizing body- and joint-attached, orthonormal coordinate frames, the configuration space is mathematically defined employing 4 × 4 *frame connection matrices* of the *special Euclidian group*, *SE*(3), which combines both *SO*(3) and $\mathbb{R}^3$. Configurational loop closure constraints are presented for a representative closed loop and solved analytically for both inverse and forward kinematics (see Appendix 2.A). Next, the velocities of each moving coordinate frames are computed. In the computations, to be consistent with the Lie algebra *so*(3) of *SO*(3), skew-symmetric angular velocity matrices are defined first from the flow of rotation matrices with time, from which angular velocity vectors in $\mathbb{R}^3$ are defined. Using body-attached moving frames whose connections are rigorously expressed by frame connection matrices, readers can systematically and unambiguously compute frame velocities (since vector bases of moving frames are explicitly shown).

Finally, in the Appendix 2.A, workspace analysis is presented for the preliminary design of a Stewart platform. In the next chapter, utilizing the velocities of body-attached coordinate frames, analytical equations of motion are derived, and their control applications are presented.

2.7 Appendix

2.7.1 Appendix 2.A: Kinematics for Design and Workspace Analyses

A base-moving Stewart platform installed on a floor in a moving ship or vehicle is designed to maintain the desired position and attitude even if the base plate translates and rotates due to the motion of a moving vehicle. Therefore, the specification of the platform is described by its range of the relative position, $s_C^{(13/0)}(t) \in \mathbb{R}^3$ (=three-dimensional vector space), and the relative rotation, $R^{(13/0)}(t) \in SO(3)$, with respect to the base plate. They are components of the relative frame connection matrix $E^{(13/0)}(t)$ in Eqs. (2.4a, b). The workspace of the platform is defined by the reachable ranges of $s_C^{(13/0)}(t)$ and $R^{(13/0)}(t)$.

2.7.1.1 Inverse Kinematics for Leg Design

The preliminary design begins with choosing the dimensions of the base plate and the top plate. For the base plate in Fig. 2.5, the radius of the mid-circle, $\hat{r}_m^{(0)}$, the truncation angle, $\Delta\hat{\theta}^{(0)}$, and for the top plate in Fig. 2.4, $\hat{r}_m^{(13)}$ and $\Delta\hat{\theta}^{(13)}$ must be determined. Here, the truncation angles are assumed to be equal: $\Delta\hat{\theta} = \Delta\hat{\theta}^{(0)} = \Delta\hat{\theta}^{(13)}$, where $\Delta\hat{\theta} < \pi/3$. In addition, in the reference configuration shown in Fig. 2.1, the initial elevation $\hat{h}^{(0)}$ of the top plate from the base must be selected. From those values, the initial configuration of the platform, including the leg lengths, are computed utilizing the loop closure constraints in Eqs. (2.20d, e).

The next design step is, for a specified service environment, to select a set of *essential positions and attitudes* of the top plate relative to the base plate under service environments, which are crucial for the top plate to maintain the desired configuration to mitigate the motion of the base plate. Each of the *essential relative frame-connection matrices* between body-(13) frame and body-(0) frame is identified by "*" as:

$$E^{*(13/0)} = \begin{bmatrix} R^{*(13/0)} & s_C^{*(13/0)} \\ 0_{1\times 3} & 1 \end{bmatrix}. \tag{2.A1}$$

For a specified $E^{*(13/0)}$, finding the corresponding leg length, $l^{(k)}$, and the UJ rotation angles, $\phi_1^{(k)}$ and $\phi_2^{(k)}$ as well as the rotation at the SJ, $R_{T_kSJ}^{(SJ13/2k)}$ for leg-(k), $k = 1,\ 2, \cdots, 6$, define a problem of *inverse kinematics*. This can be analytically solved using the loop closure constraints, Eqs. (2.20d, e).

First, to determine $l^{(k)}$, and $\phi_1^{(k)}$ and $\phi_2^{(k)}$, Eq. (2.20e) is expressed with the unknowns on the left-hand side and the known matrices on the right as:

$$R_{1\,B_kUJ}\left(\phi_1^{(k)}\right)R_{2\,B_kUJ}\left(\phi_2^{(k)}\right)e_3 l^{(k)} = \left(R_{3\,B_k}(\hat{\theta}_k^{(0)})\right)^T\left(R^{*(13/0)}\hat{s}_{T_k}^{(13)} + s_C^{*(13/0)} - \hat{s}_{B_k}^{(0)}\right). \tag{2.A2}$$

After expanding the left-hand side using Eqs. (2.10c) and (2.11b), Eq. (2.A2) for leg-(k) becomes

$$\begin{pmatrix} l^{(k)}\sin\phi_2^{(k)} \\ -l^{(k)}\sin\phi_1^{(k)}\cos\phi_2^{(k)} \\ l^{(k)}\cos\phi_1^{(k)}\cos\phi_2^{(k)} \end{pmatrix} = \begin{pmatrix} w_1^{*(k)} \\ w_2^{*(k)} \\ w_3^{*(k)} \end{pmatrix}, \tag{2.A3a}$$

where the 3×1 column matrix $w^{*(k)}$ represents the known right-hand side of Eq. (2.A2):

$$\begin{pmatrix} w_1^{*(k)} \\ w_2^{*(k)} \\ w_3^{*(k)} \end{pmatrix} \equiv \left(R_{3\,B_k}(\hat{\theta}_k^{(0)})\right)^T\left(R^{*(13/0)}\hat{s}_{T_k}^{(13)} + s_C^{*(13/0)} - \hat{s}_{B_k}^{(0)}\right). \tag{2.A3b}$$

Equation (2.A3a) is solved analytically to give the *inverse kinematics equations* as:

$$\begin{pmatrix} l^{(k)} \\ \phi_1^{(k)} \\ \phi_2^{(k)} \end{pmatrix} = \begin{pmatrix} \sqrt{\left(w_1^{*(k)}\right)^2 + \left(w_2^{*(k)}\right)^2 + \left(w_3^{*(k)}\right)^2} \\ -\tan^{-1}\left(w_2^{*(k)}/w_3^{*(k)}\right) \\ \sin^{-1}\left(w_1^{*(k)}/\sqrt{\left(w_1^{*(k)}\right)^2 + \left(w_2^{*(k)}\right)^2 + \left(w_3^{*(k)}\right)^2}\right) \end{pmatrix}. \tag{2.A4}$$

For each essential relative frame-connection matrix, $E^{*(13/0)}$, of the top plate, for leg-(k), $k = 1, 2, \cdots, 6$, one finds the maximum leg length l_{max}, the minimum length l_{min} and maximum absolute values of $\phi_1^{(k)}$ and $\phi_2^{(k)}$, written as $|\phi_1|_{max}$ and $|\phi_2|_{max}$, respectively. From those values computed for selected, essential frame connection-matrices, one finds the *design values*: l_{max}^*, l_{min}^*, $|\phi_1^*|_{max}$ and $|\phi_2^*|_{max}$. The necessary *stroke* of the actuated translational joint (ATJ) is defined as $l_{max}^* - l_{min}^*$.

Second, the relative rotation at each spherical joint is computed from Eq. (2.20d) incorporating $\phi_3^{(2k/2k-1)} = 0$ as:

$$R_{T_kSJ}^{(SJ13/2k)} = \left(R_{3\,B_k}\left(\hat{\theta}_k^{(0)}\right)R_{1\,B_kUJ}\left(\phi_1^{(k)}\right)R_{2\,b_kUJ}\left(\phi_2^{(k)}\right)\right)^T R^{*(13/0)}R_{3\,T_k}(\hat{\theta}_k^{(13)}). \tag{2.A5}$$

Equations (2.A4) and (2.A5) with Eq. (2.A3b) are the analytical equations for *inverse kinematics*.

2.7.1.2 Initial Leg Configurations

The initial values of $l^{(k)}(0), \phi_1^{(k)}(0)$, $\phi_2^{(k)}(0)$ and $R_{T_k\mathrm{SJ}}^{(SJ13/2k)}(0)$ are required for all legs to define the initial configuration of the platform with an initial relative

elevation, $\hat{h}^{(0)}$, between the top and the base plates. Equations (2.A3) and (2.A4) are written for t=0 using $R^{(13/0)}(0) = I_3$ and $s_C^{(13/0)}(0) = e_3\hat{h}^{(0)}$. The resulting initial values are

$$\begin{pmatrix} l^{(k)}(0) \\ \phi_1^{(k)}(0) \\ \phi_2^{(k)}(0) \end{pmatrix} = \begin{pmatrix} \sqrt{\left(w_1^{(k)}(0)\right)^2 + \left(w_2^{(k)}(0)\right)^2 + \left(w_3^{(k)}(0)\right)^2} \\ -\tan^{-1}\left(w_2^{(k)}(0)/w_3^{(k)}(0)\right) \\ \sin^{-1}\left(w_1^{(k)}(0)/\sqrt{\left(w_1^{(k)}(0)\right)^2 + \left(w_2^{(k)}(0)\right)^2 + \left(w_3^{(k)}(0)\right)^2}\right) \end{pmatrix}, \quad (2.A6a)$$

where

$$\begin{pmatrix} w_1^{(k)}(0) \\ w_2^{(k)}(0) \\ w_3^{(k)}(0) \end{pmatrix} \equiv \left(R_{3\,B_k}(\hat{\theta}_k^{(0)})\right)^T \left(\hat{s}_{T_k}^{(13)} + e_3\hat{h}^{(0)} - \hat{s}_{B_k}^{(0)}\right), \quad (2.A6b)$$

whose components are computed explicitly using Eqs. (2.5b), (2.9b) and (2.10b) as:

$$\begin{pmatrix} w_1^{(k)}(0) \\ w_2^{(k)}(0) \\ w_3^{(k)}(0) \end{pmatrix} = \begin{pmatrix} \hat{r}_m^{(13)}\cos\left(\frac{\pi}{3} - \Delta\theta\right) - \hat{r}_m^{(0)} \\ (-1)^{k+1}\hat{r}_m^{(13)}\sin\left(\frac{\pi}{3} - \Delta\theta\right) \\ \hat{h}^{(0)} - \hat{h}_{SJ}^{(13)} - \hat{h}_{UJ}^{(0)} \end{pmatrix}. \quad (2.A6c)$$

The substitution of Eq. (2.A6c) into Eq. (2.A6a) yields the following initial values:

$$l(0) \equiv l^{(1)}(0) = l^{(2)}(0) = \cdots = l^{(6)}(0)$$

$$= \left\{\left(\hat{r}_m^{(13)}\right)^2 + \left(\hat{r}_m^{(0)}\right)^2 - 2\hat{r}_m^{(13)}\hat{r}_m^{(0)}\cos\left(\frac{\pi}{3} - \Delta\theta\right) + \left(\hat{h}^{(0)} - \hat{h}_{SJ}^{(13)} - \hat{h}_{UJ}^{(0)}\right)^2\right\}^{1/2}, \quad (2.A7a)$$

$$\phi_1^{(1)}(0) = \phi_1^{(3)}(0) = \phi_1^{(5)}(0) = -\phi_1^{(2)}(0) = -\phi_1^{(4)}(0) = -\phi_1^{(6)}(0)$$

$$= -\tan^{-1}\left\{\hat{r}_m^{(13)}\sin\left(\frac{\pi}{3} - \Delta\theta\right)/\left(\hat{h}^{(0)} - \hat{h}_{SJ}^{(13)} - \hat{h}_{UJ}^{(0)}\right)\right\}, \quad (2.A7b)$$

$$\phi_2^{(1)}(0) = \phi_2^{(2)}(0) = \phi_2^{(3)}(0) = \phi_2^{(4)}(0) = \phi_2^{(5)}(0) = \phi_2^{(6)}(0)$$

$$= -\sin^{-1}\left\{\left(\hat{r}_m^{(0)} - \hat{r}_m^{(13)}\cos\left(\frac{\pi}{3} - \Delta\theta\right)\right)/l(0)\right\}. \quad (2.A7c)$$

Equations (2.A7a-c) indicate that initial leg lengths, $l^{(k)}(0)$, and the leg rotation angles of the cross axis pivoted by the leg yokes, $\phi_2^{(k)}(0)$, are the same for all legs, while the rotation angles of the cross axis journaled to the base yoke, $\phi_1^{(k)}(0)$, are alternating. These initial values are consistent with the reference configuration, shown in Fig. 2.1.

The initial relative rotation at each spherical joint is obtained from Eq. (2.A5) as:

$$R_{T_kSJ}^{(SJ13/2k)}(0) = \left(R_{3\,B_k}\left(\hat{\theta}_k^{(0)}\right)R_{1\,B_kUJ}\left(\phi_1^{(k)}(0)\right)R_{2\,b_kUJ}\left(\phi_2^{(k)}(0)\right)\right)^T R_{3\,T_k}(\hat{\theta}_k^{(13)}). \quad (2.A8)$$

Next, the equations for forward kinematics are presented.

2.7.1.3 Forward Kinematics

In the forward kinematics, for a given "compatible set" of six leg configurations, one finds a top-plate configuration relative to a base-plate configuration, *i.e.*, $R^{(13/0)}$ and $s_C^{(13/0)}$. A compatible set of leg configurations indicates that they are consistent with the loop closure constraints. As a result, only leg-(1) configuration suffices to determine the top plate configuration. Let $l^{(1)}, \phi_1^{(1)}$, $\phi_2^{(1)}$ and $R_{T_1\mathrm{SJ}}^{(SJ13/2)}$ be prescribed. Then Equations (2.20d, e) for k=1, with the approximation of $\phi_3^{(2k/2k-1)} = 0$, can be used to find $R^{(13/0)}$ and $s_C^{(13/0)}$ as:

$$R^{(13/0)} = R_{3\,B_1}(\hat{\theta}_1^{(0)}) R_{1\,B_1\mathrm{UJ}}(\phi_1^{(1)}) R_{2B_1\mathrm{UJ}}\left(\phi_2^{(1)}\right) R_{T_1\mathrm{SJ}}^{(\mathrm{SJ13/SJ2})}\left(R_{3\,T_1}\left(\hat{\theta}_1^{(13)}\right)\right)^T, \quad \text{(2.A9a)}$$

$$s_C^{(13/0)} = R_{3\,B_1}\left(\hat{\theta}_1^{(0)}\right) R_{1\,B_1\mathrm{UJ}}\left(\phi_1^{(1)}\right) R_{2B_1\mathrm{UJ}}\left(\phi_2^{(1)}\right) e_3 l^{(1)} + \hat{s}_{B_1}^{(0)} - R^{(13/0)} \hat{s}_{T_1}^{(13)}. \quad \text{(2.A9b)}$$

The remaining task is to determine the compatible configurations for leg-(2), ⋯, leg-(6). Equation (2.20e) with Eq. (2.A9b) gives

$$R_{1\,B_k\mathrm{UJ}}\left(\phi_1^{(k)}\right) R_{2B_k\mathrm{UJ}}\left(\phi_2^{(k)}\right) e_3 l^{(k)} = \left(R_{3\,B_k}(\hat{\theta}_k^{(0)})\right)^T \left\{\hat{s}_{B_1}^{(0)} - \hat{s}_{B_k}^{(0)} + R^{(13/0)}\left(\hat{s}_{T_k}^{(13)} - \hat{s}_{T_1}^{(13)}\right)\right\}$$
$$+ R_3\left(\hat{\theta}_1^{(0)} - \hat{\theta}_k^{(0)}\right) R_{1\,B_1\mathrm{UJ}}\left(\phi_1^{(1)}\right) R_{2B_1\mathrm{UJ}}\left(\phi_2^{(1)}\right) e_3 l^{(1)}. \quad \text{(2.A10)}$$

Equation (2.A10) takes the same form as Eq. (2.A3a) by expressing the known right-hand side of Eq. (2.A10) as w^*. Then $l^{(k)}, \phi_1^{(k)}$ and $\phi_2^{(k)}$ are obtained as shown in Eq. (2.A4). The remaining $R_{T_1\mathrm{SJ}}^{(SJ13/2k)}$ can be easily computed from Eq. (2.20d).

2.7.1.4 Workspace of the Stewart Platform

The workspace of the platform is a set of accessible configurations of the top plate relative to that of the base plate, which are expressed by the accessible flame-connection matrices, $E^{(13/0)} \in SE(3)$ in Eqs. (2.4a, b). *$E^{(13/0)}$ may be interpreted as follows: $R^{(13/0)} \in SO(3)$ is attached to each accessible $s_C^{(13/0)} \in \mathbb{R}^3$ to show its accessible rotation.* Therefore, the workspace W^* is expressed by the frame connection matrix $E^{(13/0)}$ whose components satisfy Eq. (2.20e) as well as the leg constraints:

$$W^* = \left\{ E^{(13/0)} = \begin{bmatrix} R^{(13/0)} & s_C^{(13/0)} \\ 0_{1\times 3} & 1 \end{bmatrix} \text{ with } s_C^{(13/0)} \in \mathbb{R}^3 \text{ and } R^{(13/0)} \in SO(3) \middle| \right.$$
$$\left. \text{Eq. (20e)}, l_{min}^* \le l^{(k)} \le l_{max}^*, \left|\phi_1^{(k)}\right| \le |\phi_1^*|_{max}, \left|\phi_2^{(k)}\right| \le |\phi_2^*|_{max} \text{ for } k = 1,2,\cdots,6 \right\}. \quad \text{(2.A11)}$$

Although $R^{(13/0)}$ has nine components, the columns express the components of three orthonormal coordinate vectors, as Eq. (2.4a) shows. This orthonormality of the

columns yields six constraints. As a result, $R^{(13/0)}$ *is expressed "locally" by three angular coordinates*, such as *Euler angles* and *Tait-Bryan angles*, see for example [30]. Euler angles represent the rotation as a sequence of elementary rotations with the body-attached s_3-axis by θ^E, the s_1-axis by ϕ^E, and the s_3-axis by ψ^E as:

$$R^{(13/0)} = R_3(\theta^E)R_1(\phi^E)R_3(\psi^E). \tag{2.A12}$$

Euler angles fail to represent the rotation matrix at its critical point: $\sin\phi^E = 0$, *i.e.*, $\phi^E = 0$, where the inverse of Eq. (A12) does not exist, *i.e.*, *homeomorphism* is lost. Since the critical point of Euler angles corresponds to the reference configuration where the top plate and the base plate are parallel to each other, Euler angels are not qualified to express $R^{(13/0)}$. (It is noted here that the critical attitude is changed by adopting a different cyclic order of the Euler angle representation, such as the rotations about the axes 2-3-2 and 1-2-1.)

Tait-Bryan angles $(\psi_1^{TB} \quad \psi_2^{TB} \quad \psi_3^{TB})^T$ express each rotation as a sequence of elementary rotations:

$$R^{(13/0)} = R_1(\psi_1^{TB})R_2(\psi_2^{TB})R_3(\psi_3^{TB}), \tag{2.A13}$$

which has critical points at $\cos\psi_2^{TB} = 0$, *i.e.*, $\psi_2^{TB} = \pm\pi/2$. This critical point represents the configuration where the top plate becomes vertical to the base plate, which does not happen due the constraints on leg length in Eqs. (2.A4) and (2.A11). Therefore, Tait-Bryan angles are adopted to represents $R^{(13/0)}$ for the platform.

The inverse relation to Eq. (2.A13) away from the critical points is

$$\sin\psi_2^{TB} = R_{13}^{(13/0)}, \quad \cos\psi_2^{TB} = \sqrt{1-\left(R_{13}^{(13/0)}\right)^2} \text{ or } -\sqrt{1-\left(R_{13}^{(13/0)}\right)^2}$$

$$\sin\psi_1^{TB} = -R_{23}^{(13/0)}/\cos\psi_2^{TB}, \quad \cos\psi_1^{TB} = R_{33}^{(13/0)}/\cos\psi_2^{TB}$$

$$\sin\psi_3^{TB} = -R_{12}^{(13/0)}/\cos\psi_2^{TB}, \quad \cos\psi_3^{TB} = R_{11}^{(13/0)}/\cos\psi_2^{TB}. \tag{2.A14}$$

Using Tait-Bryan angles for the coordinates of $R^{(13/0)}$ and $\left(s_{1C}^{(13/0)} \quad s_{2C}^{(13/0)} \quad s_{3C}^{(13/0)}\right)^T$ for the coordinates of $s_C^{(13/0)}$, the workspace W^* of the platform is expressed by the *six coordinates*:

$$\left(\psi_1^{TB} \quad \psi_2^{TB} \quad \psi_3^{TB} \quad s_{1C}^{(13/0)} \quad s_{2C}^{(13/0)} \quad s_{3C}^{(13/0)}\right)^T \in \mathbb{R}^6$$

with the constraints in Eq. (2.A11). (Although Tait-Bryan angles $(\psi_1^{TB} \quad \psi_2^{TB} \quad \psi_3^{TB})^T$ are expressed in a column matrix, it is important to observe that they are not a vector.)

Recognizing the limitations of using three-dimensional plots to express the six-dimensional workspace, plots are only created *for limited rotations with* $\boldsymbol{e}_1^{(0)}$*, i.e.,*

$\psi_2^{TB} = \psi_3^{TB} = 0$ for the Stewart platform whose design values are listed in Table 2.1. The initial leg configurations are defined as follows: $\phi_1^{(1)}(0) = \phi_1^{(3)}(0) = \phi_1^{(5)}(0) = -13.1°$, $\phi_1^{(2)}(0) = \phi_1^{(4)}(0) = \phi_1^{(6)}(0) = 13.1°$, $\phi_2^{(k)}(0) = 14.1°$ and $d^{(k)}(0) = 0.05\text{m}$ for $k = 1, 2, \cdots, 6$.

Table 2.1: Geometrical properties of a scale model Stewart platform

$\hat{r}_m^{(0)}$	$\hat{r}_m^{(13)}$	$\Delta\hat{\theta}$	$\hat{h}^{(0)}$	$\hat{l}_{\text{UJ}}^{(2k-1)}$	$\hat{l}_{\text{SJ}}^{(2k)}$
0.1425m	0.1m	13°	0.34m	0.0925m	0.0675m
d_{min}	d_{max}	l_{min}	l_{max}	$\|\phi_1\|_{max}$	$\|\phi_2\|_{max}$
0m	0.1m	0.22m	0.32m	40°	40°

Figures 2.9 illustrate the plots of accessible $s_C^{(13/0)}$ for $\psi_1^{TB} = 0°$, $\psi_1^{TB} = 10°$, and $\psi_1^{TB} = 20°$, respectively, for $\psi_2^{TB} = \psi_3^{TB} = 0°$. These figures help users confirm that the selected essential configurations of the top table, adopted for the initial design, are indeed accessible.

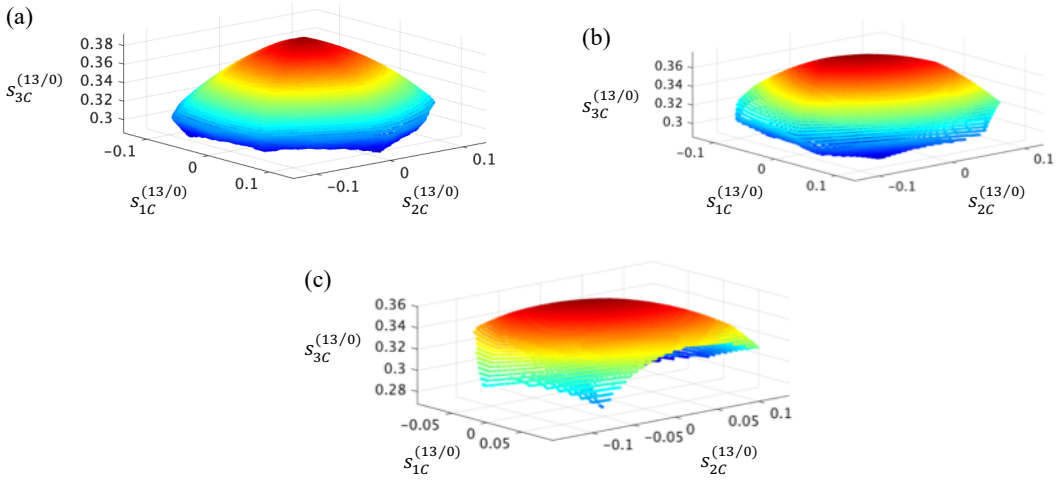

Figure 2.9: The workspace $s_c^{(13/0)}$ for (a) $\psi_1{}^{TB}(t) = \psi_2{}^{TB}(t) = \psi_3{}^{TB}(t) = 0°$, (b) $\psi_1{}^{TB}(t) = 10°$, $\psi_2{}^{TB}(t) = \psi_3{}^{TB}(t) = 0°$, and (c) $\psi_1{}^{TB}(t) = 20°$, $\psi_2{}^{TB}(t) = \psi_3{}^{TB}(t) = 0°$

In computations, it is necessary to keep a desired top-plate configuration within the workspace. It is observed and analytically confirmed that the boundary of workspace has cusps where a different actuator begins to be actuated. To keep the top-plate configuration within the workspace, two computational methods are available: (i) radial return and (ii) normal return. In this paper, the radial return method is adopted

since the normal return method experiences difficulties in computing normal directions near the cusps on the boundary. In the radial method, if a trial desired top-plate configuration goes outside the workspace, the corrected compromised state is proportionally pulled back to the origin to return to the inside of the workspace while staying as close as possible near the boundary.

2.7.2 Appendix 2.B: Proof of Eq. (2.26b)

Equation (2.26b) in three dimensions is derived by utilizing the following three equations, which are expressed by adopting the summation convention for repeated indices from 1 to 3.

The first equation is the definition of the skew-symmetric angular velocity matrix:

$$(\overleftrightarrow{\omega})_{m\,n} = -\epsilon_{m\,n\,k}\,\omega_k, \tag{2.B1}$$

where $\epsilon_{m\,n\,k}$ denotes the permutation symbol. Its value is one if the sequence (m, n, k) is an even permutation of (1, 2, 3), such as (2, 3, 1), (3, 1, 2); the value is -1 if the sequence is an odd permutation of (1, 2, 3), such as (2, 1, 3), (1, 3, 2), (3, 2, 1); and the value is zero for other cases, such as (1, 2, 2), (2, 3, 2), (1, 1, 1).

The second equation is the definition of rotation matrices, $R\,R^T = I_3$, written in the indicial form as:

$$R_{kq}R_{pq} = \delta_{kp}, \tag{2.B2}$$

where the Kronecker delta: $\delta_{kp} = 1$ if $k = p$ and $\delta_{kp} = 0$ if $k \neq p$.

The third equation is the definition of matrix determinant for a right-handed rotation matrix, whose determinant is one: $\det R = 1$:

$$\epsilon_{mnq}R_{mi}R_{nj}R_{qk} = \epsilon_{ijk}\det R = \epsilon_{ijk}. \tag{2.B3}$$

The (i, j) -element of the left-hand side of Eq. (2.26b) becomes, using Eqs. (2.B1-2.B3) in this order:

$$\begin{aligned}(R^T\overleftrightarrow{\omega}\,R)_{ij} = R_{mi}(\overleftrightarrow{\omega})_{mn}R_{nj} &= -R_{mi}\epsilon_{mnk}\omega_k R_{nj}\\ &= -\epsilon_{mnk}R_{mi}R_{nj}\omega_k = -\epsilon_{mnk}R_{mi}R_{nj}\delta_{kp}\omega_p\\ &= -\left(\epsilon_{mnk}R_{mi}R_{nj}R_{kq}\right)R_{pq}\omega_p = -\epsilon_{ijq}R_{pq}\omega_p\\ &= -\epsilon_{ijq}(R^T\omega)_q = \left(\overleftrightarrow{R^T\omega}\right)_{ij}.\end{aligned} \tag{2.B4}$$

As a result, Eq. (2.26b) is proven for element (i, j):

$$(R^T\overleftrightarrow{\omega}\,R)_{ij} = \left(\overleftrightarrow{R^T\omega}\right)_{ij}. \tag{2.B5}$$

For the readers who are familiar with the Lie group theory, the left-hand side of Eq. (2.26b) define the *adjoint representation* of $R^T \in SO(3)$, written as $Ad(R^T)$, which linearly transforms $\overleftrightarrow{\omega} \in so(3)$ into another skew symmetric matrix in $so(3)$ [31]. Identifying the components of skew symmetric matrices as vector components in $\mathbb{R}^3$ as shown in Eqs. (2.22b) and (2.23), Eq. (2.B5) states that for $\omega \in \mathbb{R}^3$, $Ad(R^T)$ becomes R^T in $\mathbb{R}^3$:

$$\begin{aligned} Ad(R^T): \quad \overleftrightarrow{\omega} &\longrightarrow R^T \overleftrightarrow{\omega}\, R \qquad \text{in } so(3), \\ \omega &\longrightarrow R^T \omega \qquad \text{in } \mathbb{R}^3. \end{aligned}$$

Readers are encouraged to learn a neat derivation of Eq. (2.26b) by Holm [35], where his $\widehat{(\,)}$-operation is our $\overleftrightarrow{(\,)}$-operation.

CHAPTER 3: KINETICS OF A BASE-MOVING STEWART PLATFORM

3.1 Introduction

In this chapter, the *principle of virtual work* is variationally derived from *Hamilton's principle* [29, 30] to facilitate a hybrid method bridging the gap between Lagrange's method and the Newton-Euler method. The resulting principle yields the same weighted-residual form as the principle of virtual power, employed by Wittenburg [17]. Utilizing the principle of virtual work, analytical equations of motion are derived for real-time control including actuator joint forces for *inverse dynamic control* as well as dynamic system simulations. Finally, experimental results utilizing a scale model are presented to compare the performance of an inverse dynamics controller (IDC) to that of an inverse kinematics controller (IKC). The comparison demonstrates that the performance of IDC utilizing the equations of motion of the platform system is superior to that of IKC.

3.2 The Principle of Virtual Work for Multi-Body Systems

To obtain equations of motion for a Stewart platform, the *principle of virtual work* is variationally derived from *Hamilton's principle*. In the past, the principle was postulated as a *weighted residual equation* incorporating Newton-Euler equations and referred to as the principle of virtual power [31]. In the variational derivation, the *constrained variation of virtual angular velocity* plays a key role.

The principle of virtual work bridges the gap between the Newton-Euler method [9,10,12] and Lagrange's method (if configuration space is defined by displacements without rotation matrices) [8,13,14]. If joint constraints are fully incorporated in the principle as essential generalized velocities (which will be defined in Eq. (3.4c)), the principle yields Lagrange's equations of motion, while if some constraints are not incorporated in the essential velocities, but are appended to the principle using Lagrange multipliers, it gives the Newton and Euler-type equations including reaction forces and couples associated with the unsatisfied velocity constraints in the essential velocities

In this section, after reviewing Frankel's compact notation for the kinematics of moving frames [31], the variations in vector space $\mathbb{R}^3$ and the *special orthogonal group* $SO(3)$ are examined for Hamilton's principle. While deriving the principle of virtual

work, an efficient way is discussed of incorporating kinematic constraints for joints and loop-closures into the essential velocities thereby into the equations of motion.

3.2.1 Kinematics Using Moving Coordinate Frames

In the previous chapter, kinematics for a multi-body system with *n* bodies was presented. It began by introducing an *inertial coordinate frame* $(\mathbf{e}^I \quad \mathbf{0})$, defined by a cartesian coordinate system $\{x_1 \quad x_2 \quad x_3\}$ with its origin at $\mathbf{0}$ and its coordinate vector basis $\mathbf{e}^I \equiv (\mathbf{e}_1^I \quad \mathbf{e}_2^I \quad \mathbf{e}_3^I)$. For each constituent body, body-(α), $\alpha = 1, 2, \cdots, n$, a *moving frame* $\left(\mathbf{e}^{(\alpha)}(t) \quad \mathbf{r}_C^{(\alpha)}(t)\right)$ was defined by attaching an orthonormal coordinate system $\{s_1^{(\alpha)} \quad s_2^{(\alpha)} \quad s_3^{(\alpha)}\}$ with an origin at its center of mass, $C^{(\alpha)}$, and defining the coordinate vector basis $\mathbf{e}^{(\alpha)}(t) \equiv \left(\mathbf{e}_1^{(\alpha)}(t) \quad \mathbf{e}_2^{(\alpha)}(t) \quad \mathbf{e}_3^{(\alpha)}(t)\right)$. The *configuration of body-(α)* is defined by the *frame connection matrix* $E^{(\alpha)}(t)$ with respect to the inertial frame, as shown in Eq. (2.3a):

$$\left(\mathbf{e}^{(\alpha)}(t) \quad \mathbf{r}_C^{(\alpha)}\right) = (\mathbf{e}^I \quad \mathbf{0})E^{(\alpha)}(t). \tag{3.1a}$$

In expanded form Eq. (3.1a) gives

$$\left(\mathbf{e}^{(\alpha)}(t) \quad \mathbf{r}_C^{(\alpha)}(t)\right) = \left(\mathbf{e}^I R^{(\alpha)}(t) \quad \mathbf{e}^I x_C^{(\alpha)}(t)\right). \tag{3.1b}$$

Equation (3.1b) states that the configuration of body-(α) is defined by: (i) the attitude of the body-attached vector basis $\mathbf{e}^{(\alpha)}(t)$ expressed by a rotation matrix: $R^{(\alpha)}(t) \in SO(3)$ from the inertial vector basis $\mathbf{e}^I$, and (ii) the origin of its center of mass, $x_C^{(\alpha)}(t) \in \mathbb{R}^3$.

The *velocity of body-(α) frame* is expressed as Eq. (2.24):

$$\left(\dot{\mathbf{e}}^{(\alpha)}(t) \quad \dot{\mathbf{r}}_C^{(\alpha)}(t)\right) = \left(\mathbf{e}^{(\alpha)}(t)\overleftrightarrow{\omega^{(\alpha)}(t)} \quad \mathbf{e}^I \dot{x}_C^{(\alpha)}(t)\right), \tag{3.2a}$$

where $\overleftrightarrow{\omega^{(\alpha)}(t)} \in so(3)$ is a *skew-symmetric angular velocity matrix*, which defines the *angular velocity vector* $\omega^{(\alpha)}(t) \in \mathbb{R}^3$, expressed with respect to $\mathbf{e}^{(\alpha)}(t)$, and $\dot{x}_C^{(\alpha)}(t) \in \mathbb{R}^3$ is the *velocity of the center of mass,* $C^{(\alpha)}$ with respect to $\mathbf{e}^I$.

From Eq. (3.2a) the *generalized velocities of body-*(α) are stored in a 6×1 matrix:

$$\left(\dot{X}^{(\alpha)}(t)\right) \equiv \begin{pmatrix} \dot{x}_C^{(\alpha)}(t) \\ \omega^{(\alpha)}(t) \end{pmatrix}. \tag{3.2b}$$

System generalized velocities for an *n*-body system are stored in a $6n \times 1$ column matrix, $\left(\dot{X}(t)\right)$, which assembles the generalized velocities of constituent bodies:

$$\left(\dot{X}(t)\right) \equiv \begin{pmatrix} \dot{X}^{(1)}(t) \\ \vdots \\ \dot{X}^{(n)}(t) \end{pmatrix} = \begin{pmatrix} \dot{x}_C^{(1)}(t) \\ \omega^{(1)}(t) \\ \vdots \\ \dot{x}_C^{(n)}(t) \\ \omega^{(n)}(t) \end{pmatrix}, \tag{3.3}$$

If constituent bodies are jointed, the system generalized velocities $\left(\dot{X}(t)\right)$ are expressed by *generalized velocities of joint displacements*. Let the column matrix of generalized velocities be expressed by a column matrix $(\dot{q}(t))$ with $\tilde{n}$ components. Then, $\left(\dot{X}(t)\right)$ is linearly expressed by $(\dot{q}(t))$ using a $6n \times \tilde{n}$ coefficient matrix $[B(t)]$ as:

$$\left(\dot{X}(t)\right) = [B(t)](\dot{q}(t)). \tag{3.4a}$$

In robotics $[B(t)]$-matrices are referred to as Jacobian matrices [38, 40]

In addition, there are n_C holonomic or non-holonomic constraints among the components of $(\dot{q}(t))$, such as the loop closure constraints, Eq. (I-46b). The degrees-of-freedom of $(\dot{q}(t))$ reduces from $\tilde{n}$ to $n^* = \tilde{n} - n_C$. A set of linearly independent n^* components of $(\dot{q}(t))$ defines *essential generalized velocity* $(\dot{q}^*(t))$, stored in an $n^* \times 1$ column matrix. Thus $(\dot{q}(t))$ is linearly expressed by $(\dot{q}^*(t))$ using an $\tilde{n} \times n^*$ matrix $[T(t)]$ as:

$$(\dot{q}(t)) = [T(t)](\dot{q}^*(t)). \tag{3.4b}$$

The system generalized velocity $\left(\dot{X}(t)\right)$ is now expressed linearly by the essential velocity $(\dot{q}^*(t))$, expressed by a $6n \times n^*$ matrix $[B^*(t)]$ as:

$$\left(\dot{X}(t)\right) = [B^*(t)](\dot{q}^*(t)), \tag{3.4c}$$

where $[B^*(t)]$ is obtained by substituting Eq. (3.4b) into Eq. (3.4a):

$$[B^*(t)] \equiv [B(t)][T(t)]. \tag{3.4d}$$

The velocity computations performed in Chapter 2 will be utilized to define Eqs. (3.4a) and (3.4b) explicitly for a Stewart platform.

Equations (3.4a-d) play a critical role for the subsequent derivation of equations of motion from the principle of virtual work. In this section, for simplicity, systems excited only by external forces are considered first since the systems excited by both external forces and prescribed excitation velocities are more complicated. (In the next section, for a Stewart platform under prescribed mount motion, it will be shown that Eqs. (3.4a) and (3.4b) include additional terms due to the prescribed velocities.)

3.2.2 Hamilton's Principle

Hamilton's principles are expressed by using either (i) configurational coordinates and their velocities (in the *tangent bundle*) or (ii) coordinates and associated momenta in the *phase space* (or cotangent bundle), see Frankel [31]. In this paper, the former Hamilton's principle using coordinates and velocities is employed, in which *Lagrangian* $L(t)$ is defined as the difference between *system kinetic energy* $K(t)$ and *system potential energy* $U(t)$:

$$L(t) \equiv K(t) - U(t). \tag{3.5}$$

Hamilton's principle is written for a time duration $t_0 \le t \le t_1$ as:

$$\delta \int_{t_0}^{t_1} L(t)dt + \int_{t_0}^{t_1} \delta W_{nc}(t)dt = 0, \tag{3.6a}$$

where δ-*operator denotes the variation* and δW_{nc} expresses the *virtual work done by non-conservative forces*. The substitution of Eq. (3.5) into Eq. (3.6a) yields

$$\int_{t_0}^{t_1} (\delta K(t) - \delta U(t) + \delta W_{nc}(t))dt = 0. \tag{3.6b}$$

3.2.2.1 Kinetic Energy $K(t)$ and Potential Energy $U(t)$

The system kinetic energy is expressed as the sum of the kinetic energies of n constituent bodies:

$$K(t) = \sum_{\alpha=1}^{n} K^{(\alpha)}(t). \tag{3.7a}$$

The kinetic energy of body-(α), $K^{(\alpha)}(t)$, is expressed by the generalized velocity of body-(α), $\left(\dot{X}^{(\alpha)}(t)\right)$ in Eq. (2b), and its mass matrix $\left[\widehat{M}^{(\alpha)}\right]$ as:

$$K^{(\alpha)}(t) = \frac{1}{2}\left(\dot{X}^{(\alpha)}(t)\right)^T \left[\widehat{M}^{(\alpha)}\right]\left(\dot{X}^{(\alpha)}(t)\right), \tag{3.7b}$$

where the body-(α) *mass matrix* is a constant, 6×6 symmetric positive-definite matrix, whose components are defined by the *mass* $\hat{m}^{(\alpha)}$ of body-(α) and its *mass-moment of inertia* with respect to the body-attached $s_i^{(\alpha)}$-coordinate system, $\hat{J}_C^{(\alpha)}$, which is a symmetric positive-definite 3×3 matrix:

$$\left[\widehat{M}^{(\alpha)}\right]_{6\times 6} \equiv \begin{bmatrix} \hat{m}^{(\alpha)} I_3 & 0_{3\times 3} \\ 0_{3\times 3} & \hat{J}_C^{(\alpha)} \end{bmatrix}, \tag{3.7c}$$

in which I_3 and $0_{3\times 3}$, respectively, denote the 3×3 identity matrix and the 3×3 zero matrix.

Let the *linear momentum vector* and the *angular momentum vector* of body-(α) be expressed as $\boldsymbol{L}_C^{(\alpha)}(t) = \mathbf{e}^I L_C^{(\alpha)}(t)$ and $\boldsymbol{H}_C^{(\alpha)}(t) = \mathbf{e}^{(\alpha)}(t) H_C^{(\alpha)}(t)$. Their components are written using Eqs. (3.7c) and (3.2b) as:

$$\begin{pmatrix} L_C^{(\alpha)}(t) \\ H_C^{(\alpha)}(t) \end{pmatrix} = \left[\widehat{M}^{(\alpha)}\right]\left(\dot{X}^{(\alpha)}(t)\right) = \begin{bmatrix} \hat{m}^{(\alpha)} I_3 & 0_{3\times3} \\ 0_{3\times3} & \hat{J}_C^{(\alpha)} \end{bmatrix} \begin{pmatrix} \dot{x}_C^{(\alpha)}(t) \\ \omega^{(\alpha)}(t) \end{pmatrix}. \tag{3.7d}$$

Equation (3.7a) is expressed compactly using the system generalized velocities in Eq. (3) as:

$$K(t) = \frac{1}{2}\left(\dot{X}(t)\right)^T \left[\widehat{M}\right]\left(\dot{X}(t)\right), \tag{3.8a}$$

where $\left[\widehat{M}\right]$ is the *system mass matrix* having the constituent mass matrices, $\left[\widehat{M}^{(\alpha)}\right]$, $\alpha = 1, \cdots, n$, on the diagonal:

$$\left[\widehat{M}\right]_{6n\times6n} \equiv \begin{bmatrix} \widehat{M}^{(1)} & 0_{3\times3} & 0_{3\times3} & \cdots & 0_{3\times3} & 0_{3\times3} \\ 0_{3\times3} & \widehat{M}^{(2)} & 0_{3\times3} & \cdots & 0_{3\times3} & 0_{3\times3} \\ 0_{3\times3} & 0_{3\times3} & \widehat{M}^{(3)} & \vdots & \vdots & \vdots \\ \vdots & \vdots & \vdots & \ddots & 0_{3\times3} & 0_{3\times3} \\ 0_{3\times3} & 0_{3\times3} & 0_{3\times3} & 0_{3\times3} & \widehat{M}^{(n-1)} & 0_{3\times3} \\ 0_{3\times3} & 0_{3\times3} & 0_{3\times3} & 0_{3\times3} & 0_{3\times3} & \widehat{M}^{(n)} \end{bmatrix}. \tag{3.8b}$$

The variation of the kinetic energy, $\delta K(t)$, is from Eq. (3.7a) written as:

$$\delta K(t) = \sum_{\alpha=1}^{n} \delta K^{(\alpha)}(t), \tag{3.9a}$$

where $\delta K^{(\alpha)}(t)$ is expressed from Eqs. (3.7b, d) introducing the *virtual generalized velocity* $\left(\delta\dot{X}^{(\alpha)}(t)\right)$ as:

$$\delta K^{(\alpha)}(t) = \left(\delta\dot{X}^{(\alpha)}(t)\right)^T \left[\widehat{M}^{(\alpha)}\right]\left(\dot{X}^{(\alpha)}(t)\right) = \left(\delta\dot{X}^{(\alpha)}(t)\right)^T \begin{pmatrix} L_C^{(\alpha)}(t) \\ H_C^{(\alpha)}(t) \end{pmatrix}, \tag{3.9b}$$

where the *virtual generalized velocity of body-(α)* is from Eq. (3.2b):

$$\left(\delta\dot{X}^{(\alpha)}(t)\right) \equiv \begin{pmatrix} \delta\dot{x}_C^{(\alpha)}(t) \\ \delta\omega^{(\alpha)}(t) \end{pmatrix}. \tag{3.9c}$$

Equation (3.9a) for the system can be written compactly using Eq. (3.8a) as:

$$\delta K(t) = \frac{1}{2}\left(\delta\dot{X}(t)\right)^T \left[\widehat{M}\right]\left(\dot{X}(t)\right), \tag{3.10a}$$

where the *virtual system generalized-velocity* is

$$\left(\delta\dot{X}(t)\right) \equiv \begin{pmatrix} \delta\dot{X}^{(1)}(t) \\ \vdots \\ \delta\dot{X}^{(n)}(t) \end{pmatrix} = \begin{pmatrix} \delta\dot{x}_C^{(1)}(t) \\ \delta\omega^{(1)}(t) \\ \vdots \\ \delta\dot{x}_C^{(n)}(t) \\ \delta\omega^{(n)}(t) \end{pmatrix}. \tag{3.10b}$$

To use Eq. (3.10a) in Hamilton's principle, Eq. (3.6b), $\delta\dot{x}_C^{(\alpha)}(t)$ and $\delta\omega^{(\alpha)}(t)$ in Eq. (3.10b) require close examinations of the *calculus of variations in both a vector space and SO(3)*, see Holm [35] and [29, 30]

3.2.2.2 Variations of $x_C^{(\alpha)}(t) \in \mathbb{R}^3$ and $R^{(\alpha)}(t) \in SO(3)$

To define the variation of the position vector $\mathbf{r}_C^{(\alpha)}(t) = \mathbf{e}^I x_C^{(\alpha)}(t)$ of the center of mass, $C^{(\alpha)}$, of body-(α), the inertial coordinates $x_C^{(\alpha)}(t)$ *is generalized in the three dimensional vector space* $\mathbb{R}^3$ *as the function of* t *and* ε: $x_C^{(\alpha)}(t;\, \varepsilon)$ with $x_C^{(\alpha)}(t;0) = x_C^{(\alpha)}(t)$, see Frankel [31]. The ε-derivative of $\mathbf{e}^I x_C^{(\alpha)}(t;\, \varepsilon)$ at $\varepsilon = 0$ defines the variation of $\mathbf{e}^I x_C^{(\alpha)}(t)$ as:

$$\delta \mathbf{r}_C^{(\alpha)}(t) = \mathbf{e}^I \delta x_C^{(\alpha)}(t) \equiv \mathbf{e}^I \frac{\partial}{\partial \varepsilon} x_C^{(\alpha)}(t;\, \varepsilon)\Big|_{\varepsilon=0}. \tag{3.11a}$$

Observing that mixed derivatives with t and ε commute for the integrability:

$$\mathbf{e}^I \frac{\partial^2 x_C^{(\alpha)}}{\partial \varepsilon\, \partial t} = \mathbf{e}^I \frac{\partial^2 x_C^{(\alpha)}}{\partial t\, \partial \varepsilon}, \tag{3.11b}$$

one finds that the t- and δ- operators acting on $x_C^{(\alpha)}$ commute, which is written in components:

$$\delta \dot{x}_C^{(\alpha)}(t) \equiv \delta\left(\frac{dx_C^{(\alpha)}(t)}{dt}\right) = \frac{d}{dt}\left(\delta x_C^{(\alpha)}(t)\right), \tag{3.12a}$$

and observing that $\delta \mathbf{e}^I = \mathbf{0}$, in vector form:

$$\delta \dot{\mathbf{r}}_C^{(\alpha)}(t) \equiv \delta\left(\frac{d\mathbf{r}_C^{(\alpha)}(t)}{dt}\right) = \frac{d}{dt}\left(\delta \mathbf{r}_C^{(\alpha)}(t)\right). \tag{3.12b}$$

The variations in vector space are often expressed as $x_C^{(\alpha)}(t;\, \varepsilon) = x_C^{(\alpha)}(t) + \varepsilon \eta^{(\alpha)}(t)$ utilizing an infinitely differentiable C^∞-function $\eta^{(\alpha)}(t)$ as its variation $\delta x_C^{(\alpha)}(t)$ since the addition of vectors gives another vector, see for example [41, 42]. However, in *SO*(3) *the addition of rotation matrices does not give a rotation matrix* since *SO(3) is not a vector space but a group*, *where the product of rotation matrices gives another rotation matrix*. Therefore, the variations of rotation matrices have to be defined carefully within *SO*(3).

Next, after defining the variation of $R^{(\alpha)}(t) \in SO(3)$, the variation of angular velocity $\delta\omega^{(\alpha)}(t)$ is examined to find that $\delta\omega^{(\alpha)}(t)$ *is not arbitrary but constrained* [29, 30, 35].

3.2.2.3 Constrained Variation of Virtual Angular Velocity: $\delta\boldsymbol{\omega}^{(\alpha)}(t)$

The variation of the moving vector basis $\mathbf{e}^{(\alpha)}(t) = \mathbf{e}^I R^{(\alpha)}(t)$ with $R^{(\alpha)}(t) \in SO(3)$ is defined by generalizing it as the function of t and ε: $\mathbf{e}^{(\alpha)}(t;\, \varepsilon) = \mathbf{e}^I R^{(\alpha)}(t;\, \varepsilon)$ with the condition: $R^{(\alpha)}(t;0) = R^{(\alpha)}(t)$. (A specific example of $R^{(\alpha)}(t;\, \varepsilon)$ is to "locally"

express $R^{(\alpha)}(t)$ as shown in Eq. (2.A9) using Euler angles $(\theta^E(t) \quad \phi^E(t) \quad \psi^E(t))^T$. Then one varies the Euler angles with ε as $(\theta^E(t;\,\varepsilon) \quad \phi^E(t;\,\varepsilon) \quad \psi^E(t;\,\varepsilon))^T$.)

The ε-derivative at $\varepsilon = 0$ yields $\delta\mathbf{e}^{(\alpha)}(t) = \mathbf{e}^I \delta R^{(\alpha)}(t)$ observing that $\delta\mathbf{e}^I = \mathbf{0}$:

$$\delta\mathbf{e}^{(\alpha)}(t) = \mathbf{e}^I \delta R^{(\alpha)}(t) \equiv \mathbf{e}^I \frac{\partial}{\partial\varepsilon} R^{(\alpha)}(t;\,\varepsilon)\Big|_{\varepsilon=0}. \tag{3.13a}$$

Equation (3.13a) expressed by its own basis using $\mathbf{e}^I = \mathbf{e}^{(\alpha)}(t)\big(R^{(\alpha)}(t)\big)^T$, defines the *skew-symmetric virtual angular-displacement matrix* $\overleftrightarrow{\delta\pi^{(\alpha)}(t)} \in so(3)$ as:

$$\delta\mathbf{e}^{(\alpha)}(t) = \mathbf{e}^{(\alpha)}(t)\overleftrightarrow{\delta\pi^{(\alpha)}(t)}, \tag{3.13b}$$

where

$$\overleftrightarrow{\delta\pi^{(\alpha)}(t)} \equiv \Big(R^{(\alpha)}(t)\Big)^T \delta R^{(\alpha)}(t). \tag{3.13c}$$

The mixed partial derivatives with t and ε commute for the integrability of $R^{(\alpha)}(t;\,\varepsilon)$ in the neighborhood of $\varepsilon = 0$ in the variational t, ε -plane [30]:

$$\mathbf{e}^I \left.\frac{\partial}{\partial\varepsilon}\frac{\partial R^{(\alpha)}}{\partial t}\right|_{\varepsilon=0} = \mathbf{e}^I \left.\frac{\partial}{\partial t}\frac{\partial R^{(\alpha)}}{\partial\varepsilon}\right|_{\varepsilon=0}, \tag{3.14a}$$

which gives in components:

$$\delta\dot{R}^{(\alpha)}(t) \equiv \delta\left(\frac{dR^{(\alpha)}(t)}{dt}\right) = \frac{d}{dt}\big(\delta R^{(\alpha)}(t)\big), \tag{3.14b}$$

and in vector form,

$$\delta\dot{\mathbf{e}}^{(\alpha)}(t) \equiv \delta\left(\frac{d\mathbf{e}^{(\alpha)}(t)}{dt}\right) = \frac{d}{dt}\big(\delta\mathbf{e}^{(\alpha)}(t)\big). \tag{3.14c}$$

The integrability condition Eq. (3.14c) of $\mathbf{e}^{(\alpha)}(t;\,\varepsilon) = \mathbf{e}^I R^{(\alpha)}(t;\,\varepsilon)$ reveals that *even though the virtual angular displacement $\delta\pi^{(\alpha)}$ is arbitrary, the virtual angular velocity $\delta\omega^{(\alpha)}(t)$ is not arbitrary, but is subjected to the following constraint*, written in vector form:

$$\delta\omega^{(\alpha)}(t) = \frac{d}{dt}\big(\delta\pi^{(\alpha)}(t)\big) + \overleftrightarrow{\omega^{(\alpha)}(t)}\delta\pi^{(\alpha)}(t). \tag{3.15}$$

Proof: Equation (3.15) is derived from Eq. (3.14c) using Eq. (3.13b) and Eq. (2.22a), written for body-(α):

$$\dot{\mathbf{e}}^{(\alpha)}(t) = \mathbf{e}^{(\alpha)}(t)\overleftrightarrow{\omega^{(\alpha)}(t)}. \tag{3.16}$$

To compute the left-hand side of Eq. (3.14c), the variation of Eq. (3.16) is computed:

$$\begin{aligned}\delta\left(\dot{\mathbf{e}}^{(\alpha)}(t)\right) &= \delta\left(\mathbf{e}^{(\alpha)}(t)\overleftrightarrow{\omega^{(\alpha)}(t)}\right) = \delta\mathbf{e}^{(\alpha)}(t)\overleftrightarrow{\omega^{(\alpha)}(t)} + \mathbf{e}^{(\alpha)}(t)\overleftrightarrow{\delta\omega^{(\alpha)}(t)} \\ &= \mathbf{e}^{(\alpha)}(t)\left(\overleftrightarrow{\delta\pi^{(\alpha)}(t)}\,\overleftrightarrow{\omega^{(\alpha)}(t)} + \overleftrightarrow{\delta\omega^{(\alpha)}(t)}\right).\end{aligned} \tag{3.17a}$$

To compute the right-hand side of Eq. (3.14c), the time derivative of Eq. (3.13b) is computed:

$$\frac{d}{dt}\left(\mathbf{e}^{(\alpha)}(t)\overleftrightarrow{\delta\pi^{(\alpha)}(t)}\right) = \dot{\mathbf{e}}^{(\alpha)}(t)\overleftrightarrow{\delta\pi^{(\alpha)}(t)} + \mathbf{e}^{(\alpha)}(t)\frac{d}{dt}\overleftrightarrow{\delta\pi^{(\alpha)}(t)}$$
$$= \mathbf{e}^{(\alpha)}(t)\left(\overleftrightarrow{\omega^{(\alpha)}(t)}\,\overleftrightarrow{\delta\pi^{(\alpha)}(t)} + \frac{d}{dt}\overleftrightarrow{\delta\pi^{(\alpha)}(t)}\right). \tag{3.17b}$$

Equating Eqs. (3.17a, b) and using the Lie bracket [29-31], one finds in $so(3)$:

$$\overleftrightarrow{\delta\omega^{(\alpha)}(t)} = \frac{d}{dt}\overleftrightarrow{\delta\pi^{(\alpha)}(t)} + \left[\overleftrightarrow{\omega^{(\alpha)}(t)},\ \overleftrightarrow{\delta\pi^{(\alpha)}(t)}\right] \tag{3.18a}$$

where

$$\left[\overleftrightarrow{\omega^{(\alpha)}(t)},\ \overleftrightarrow{\delta\pi^{(\alpha)}(t)}\right] \equiv \overleftrightarrow{\omega^{(\alpha)}(t)}\,\overleftrightarrow{\delta\pi^{(\alpha)}(t)} - \overleftrightarrow{\delta\pi^{(\alpha)}(t)}\,\overleftrightarrow{\omega^{(\alpha)}(t)}. \tag{3.18b}$$

Next, one observes that the *Lie bracket term shows the skew-symmetric form of the cross product between the two column vectors*: $\delta\omega^{(\alpha)} \times \delta\pi^{(\alpha)} = \overleftrightarrow{\delta\omega^{(\alpha)}}\delta\pi^{(\alpha)}$:

$$\left[\overleftrightarrow{\omega^{(\alpha)}(t)},\ \overleftrightarrow{\delta\pi^{(\alpha)}(t)}\right] = \overleftrightarrow{\overleftrightarrow{\omega^{(\alpha)}(t)}\delta\pi^{(\alpha)}(t)}. \tag{3.18c}$$

Combining Eqs. (3.18a) and (3.18c) and transforming the skew-symmetric equation to the equation in vector form, Eq. (3.15) is obtained from Eq. (3.14c).

Incorporating Eq. (3.15) into *virtual generalized velocity* of body-(α), Eq. (3.9c) is expressed, by introducing arbitrary *virtual generalized displacement* of body-(α), $\left(\delta\tilde{X}^{(\alpha)}(t)\right)$, as:

$$\left(\delta\dot{X}^{(\alpha)}(t)\right) = \frac{d}{dt}\left(\delta\tilde{X}^{(\alpha)}(t)\right) + \left[D^{(\alpha)}(t)\right]\left(\delta\tilde{X}^{(\alpha)}(t)\right), \tag{3.19a}$$

where $\left(\delta\tilde{X}^{(\alpha)}(t)\right)$ is

$$\left(\delta\tilde{X}^{(\alpha)}(t)\right) \equiv \begin{pmatrix}\delta x_C^{(\alpha)}(t)\\ \delta\pi^{(\alpha)}(t)\end{pmatrix}, \tag{3.19b}$$

and

$$\left[D^{(\alpha)}(t)\right] \equiv \begin{bmatrix}0_{3\times3} & 0_{3\times3}\\ 0_{3\times3} & \overleftrightarrow{\omega^{(\alpha)}(t)}\end{bmatrix}. \tag{3.19c}$$

Equation (3.19a) expresses in matrix form both integrability conditions: Eq. (3.12a) and Eq. (3.15).

Equation (3.19a) is also expressed for the *virtual system generalized-velocity* $\left(\delta\tilde{X}(t)\right)$ as:

$$\left(\delta\dot{X}(t)\right) = \frac{d}{dt}\left(\delta\tilde{X}(t)\right) + [D(t)]\left(\delta\tilde{X}(t)\right), \tag{3.20a}$$

where $\left(\delta\tilde{X}(t)\right)$ assembles $\left(\delta\tilde{X}^{(\alpha)}(t)\right)$, $\alpha = 1, \cdots, n$ as:

$$\left(\delta\tilde{X}(t)\right) \equiv \begin{pmatrix} \delta\tilde{X}^{(1)}(t) \\ \vdots \\ \delta\tilde{X}^{(n)}(t) \end{pmatrix} = \begin{pmatrix} \delta x_C^{(1)}(t) \\ \delta\pi^{(1)}(t) \\ \vdots \\ \delta x_C^{(n)}(t) \\ \delta\pi^{(n)}(t) \end{pmatrix}, \tag{3.20b}$$

and

$$[D(t)] \equiv \begin{bmatrix} 0_{3\times3} & 0_{3\times3} & 0_{3\times3} & 0_{3\times3} & \cdots & 0_{3\times3} & 0_{3\times3} \\ 0_{3\times3} & \overleftrightarrow{\omega^{(1)}} & 0_{3\times3} & 0_{3\times3} & \cdots & 0_{3\times3} & 0_{3\times3} \\ 0_{3\times3} & 0_{3\times3} & 0_{3\times3} & 0_{3\times3} & \cdots & 0_{3\times3} & 0_{3\times3} \\ 0_{3\times3} & 0_{3\times3} & 0_{3\times3} & \overleftrightarrow{\omega^{(2)}} & \cdots & 0_{3\times3} & 0_{3\times3} \\ \vdots & \vdots & \vdots & \vdots & \ddots & \vdots & \vdots \\ 0_{3\times3} & 0_{3\times3} & 0_{3\times3} & 0_{3\times3} & \cdots & 0_{3\times3} & 0_{3\times3} \\ 0_{3\times3} & 0_{3\times3} & 0_{3\times3} & 0_{3\times3} & \cdots & 0_{3\times3} & \overleftrightarrow{\omega^{(n)}} \end{bmatrix}. \tag{3.20c}$$

Replacing the time derivative in Eq. (3.4a) by ε-derivative, $\left(\delta\tilde{X}(t)\right)$ is also expressed linearly by *virtual generalized displacement* $(\delta\tilde{q}(t))$ using the same $[B(t)]$-matrix as:

$$\left(\delta\tilde{X}(t)\right) = [B(t)](\delta\tilde{q}(t)). \tag{3.21a}$$

If there are additional constraints among the components of $(\dot{q}(t))$ as shown by Eq. (3.4b), $(\delta\tilde{q}(t))$ is linearly expressed by *virtual essential generalize- displacement* $(\delta\tilde{q}^*(t))$ using the same $[T(t)]$-matrix as Eq. (3.4c)

$$(\delta\tilde{q}(t)) = [T(t)](\delta\tilde{q}^*(t)). \tag{3.21b}$$

The substitution of Eq. (3.21b) into Eq. (3.21a) yields the similar equation to Eq. (3.4c) using the same $[B^*(t)]$-matrix defined in Eq. (3.4d):

$$\left(\delta\tilde{X}(t)\right) = [B^*(t)](\delta\tilde{q}^*(t)). \tag{3.21c}$$

3.2.3 The Principle of Virtual Work for Multi-Body Systems

Let the virtual work $\delta W(t)$ due to the potential energy and the non-conservative forces be expressed using the *virtual essential generalized-displacement* $(\delta\tilde{q}^*(t))$. Then, the conjugate force defines the *essential generalized force* $(F^*(t))$ as:

$$\delta W(t) \equiv -\delta U(t) + \delta W_{nc}(t) = (\delta\tilde{q}^*(t))^T(F^*(t)). \tag{3.22a}$$

As a special case, if n bodies are free from joint constraints the virtual work is expressed as:

$$\delta W(t) = \sum_{\alpha=1}^{n}\left(\delta\tilde{X}^{(\alpha)}(t)\right)^T \begin{pmatrix} F_C^{(\alpha)\,I}(t) \\ M_C^{(\alpha)}(t) \end{pmatrix}, \tag{3.22b}$$

where $\mathbf{F}_C^{(\alpha)}(t) = \mathbf{e}^I F_C^{(\alpha)\,I}(t)$ is the resultant force acting on body-(α) and $\mathbf{M}_C^{(\alpha)}(t) = \mathbf{e}^{(\alpha)}(t)M_C^{(\alpha)}(t)$ is the external torque expressed with respect to $C^{(\alpha)}$.

Hamilton's principle, Eq. (3.6b), with Eqs. (3.9a, b) and (3.22a) gives

$$\int_{t_0}^{t_1} \left\{ \sum_{\alpha=1}^{n} \left(\delta \dot{X}^{(\alpha)}(t)\right)^T \left[\widehat{M}^{(\alpha)}\right] \left(\dot{X}^{(\alpha)}(t)\right) + (\delta \tilde{q}^*(t))^T (F^*(t)) \right\} dt = 0, \quad (3.23a)$$

where the variations vanish at $t = t_0$ and t_1:

$$\delta x_C^{(\alpha)}(t_0) = \delta x_C^{(\alpha)}(t_1) = \delta \pi^{(\alpha)}(t_0) = \delta \pi^{(\alpha)}(t_1) = 0_{3\times 1}. \quad (3.23b)$$

By substituting Eq. (19a) into Eq. (23a) and performing integration by parts using Eq. (3.23b), Eq. (3.23a) yields

$$\int_{t_0}^{t_1} \left[\sum_{\alpha=1}^{n} \left(\delta \tilde{X}^{(\alpha)}(t)\right)^T \left\{ \left[\widehat{M}^{(\alpha)}\right] \left(\ddot{X}^{(\alpha)}(t)\right) + \left[D^{(\alpha)}(t)\right] \left[\widehat{M}^{(\alpha)}\right] \left(\dot{X}^{(\alpha)}(t)\right) \right\} - (\delta \tilde{q}^*(t))^T (F^*(t)) \right] dt = 0.$$

The *principle of virtual work* is now obtained at each time from the integrand above as:

$$\sum_{\alpha=1}^{n} \left(\delta \tilde{X}^{(\alpha)}(t)\right)^T \left\{ \left[\widehat{M}^{(\alpha)}\right] \left(\ddot{X}^{(\alpha)}(t)\right) + \left[D^{(\alpha)}(t)\right] \left[\widehat{M}^{(\alpha)}\right] \left(\dot{X}^{(\alpha)}(t)\right) \right\} - \left(\delta \tilde{q}^*(t)\right)^T \left(F^*(t)\right) = 0. \quad (3.24a)$$

The principle is also expressed using system matrices defined in Eqs. (3.3), (3.8b), and (3.20a-c) as:

$$\left(\delta \tilde{X}(t)\right)^T \left\{ \left[\widehat{M}\right] \left(\ddot{X}(t)\right) + [D(t)] \left[\widehat{M}\right] \left(\dot{X}(t)\right) \right\} - \left(\delta \tilde{q}^*(t)\right)^T \left(F^*(t)\right) = 0. \quad (3.24b)$$

Compact equations of motion are now obtained for arbitrary $\left(\delta \tilde{q}^*(t)\right)$ by substituting Eqs. (3.22a), (3.21c) and (3.4c) into the virtual work equation, Eq. (3.24b), where Eqs. (3.4c) and (3.21c) fully satisfy kinematic constraints for jointed multi-body systems.

As the special case, if the virtual work is expressed by Eq. (3.22b) for free *n* bodies, Eq. (3.24a) yields the Newton and Euler equations for each body as it should:

$$\delta x_C^{(\alpha)}(t): \qquad \widehat{m}^{(\alpha)} I_3 \, \ddot{x}_C^{(\alpha)}(t) = F_C^{(\alpha)\,I}(t), \quad (3.25a)$$

$$\delta \pi^{(\alpha)}(t): \qquad \hat{J}_C^{(\alpha)} \, \dot{\omega}^{(\alpha)}(t) + \overleftrightarrow{\omega^{(\alpha)}(t)} \, \hat{J}_C^{(\alpha)} \omega^{(\alpha)}(t) = M_C^{(\alpha)}(t). \quad (3.25b)$$

Taking advantage of this recovery of Newton's and Euler's equations, the Newton-Euler-type equations with reaction forces and couples can be obtained by appending unsatisfied constraints in Eqs. (3.4a) and (3.21a) to the virtual work equation, Eq. (3.24a, b), using Lagrange multipliers [41, 42].

3.3 Equations of Motion for a Stewart Platform

Compact equations of motion for essential velocities ($\dot{q}^*(t)$) and accelerations ($\ddot{q}^*(t)$) are derived here for a base-moving Stewart platform utilizing the principle of virtual work, Eq. (3.24a) with Eq. (3.22a). Since the system has 14 bodies and is excited by prescribed generalized velocities of the base plate, $\left(\dot{X}^{(0)}(t)\right)$, the computations of Eqs. (3.22a) and (3.24a) become quite complicated. Therefore, it is helpful to perform computational tasks in step by step. These steps are:

(i) To write the principle of virtual work, Eq. (3.24a), specifically for the Stewart platform problem, *defining subsystem velocities and subsystem virtual displacements formed by* $\left(\dot{X}^{(\alpha)}\right)$ *and* $\left(\delta\tilde{X}^{(\alpha)}\right)$ *of adjacent constituent bodies*;

(ii) To express the grouped $\left(\dot{X}^{(\alpha)}\right)$ and $\left(\delta\tilde{X}^{(\alpha)}\right)$ of each subsystem using $(\dot{q}(t))$ and $(\delta\tilde{q}(t))$ *defining the coefficient [B]-submatrices*, as shown in Eq. (3.4a) and Eq. (3.21a);

(iii) To define the *virtual work of potential energy*, $-\delta U(t)$, in Eq. (3.22a) for the subsystems;

(iv) To define the *virtual work* $\delta W_{nc}(t)$ by non-conservative forces in Eq. (3.22a) including: (i) the virtual work by the leg actuators at ATJs and (ii) that by viscous frictions at UJ's and SJ's. The virtual work by the *linear actuator force* $f_L^{(k)}(t)$ of leg-(k) is expressed as $\delta d^{(k)}(t) f_L^{(k)}(t)$;

(v) To write the *loop closure constraints on velocities and virtual displacements* using $(\dot{q}(t))$ and $(\delta\tilde{q}(t))$ and identify *essential virtual displacements* $(\delta\tilde{q}^*(t))$ *as well as the corresponding essential velocities* $(\dot{q}^*(t))$. Further to express non-essential virtual displacements in $(\delta\tilde{q}(t))$ by $(\delta\tilde{q}^*(t))$. Similarly, to express the non-essential components of $(\dot{q}(t))$ by $(\dot{q}^*(t))$ by solving the constraint equations to *define* $[T(t)]$-*matrix* in Eqs. (3.4b) and (3.21b);

(vi) To incorporate the expression of $(\dot{q}(t))$ by $(\dot{q}^*(t))$ and that of $(\delta\tilde{q}(t))$ by $(\delta\tilde{q}^*(t))$, obtained in task (v), into the $[B]$-submatrix expressions in task (iii) to *form* $[B^*]$-*submatrices* defined in Eq. (3.4d);

(vii) To compute the *effective external force* $(F^*(t))$ in Eq. (3.22a) rewriting $-\delta U$ in task (iii) and δW_{nc} in task (iv) using the result of task (vi);

(viii) To substitute the $[B^*]$-expressions of subsystem velocities and virtual displacements of task (vi) into the virtual work equation in task (i) for the Stewart platform. Next, using $(F^*(t))$ derived in task (vii) to reduce the virtual work equation to the form: $(\delta\tilde{q}^*(t))^T$ {compact equations of motion}.

The above tasks (i)-(viii) are performed step-by-step in what follows.

3.3.1 Terms Associated with Variation of Kinetic Energy

In task (i), one first observes that the variation of body-(0) kinetic energy, $\delta K^{(0)}$, vanishes since the elements of $\left(\dot{X}^{(0)}\right)$ in Eq. (3.2a): $\dot{x}_C^{(0)}(t)$ and $\omega^{(0)}(t)$ are both prescribed at each time (using the measured values). This implies that the corresponding virtual displacements $\left(\delta\tilde{X}^{(0)}(t)\right)$ vanish. The remaining terms of total kinetic energy $\delta K(t)$ in Eq. (3.9a) are grouped into: (i) $\delta K^{(13)}$ of the top-plate and $\delta K^{(14)}$ of the attached manipulator and (ii) six pairs of $\delta K^{(2k-1)}$of body-(2k-1) and $\delta K^{(2k-1)}$ of body-(2k) of leg-(k) for $k = 1, 2, \cdots, 6$. The first pair consisting of body-(13) and body-(14) is referred to as *TP-subsystem*.

For TP-subsystem in Fig. 3.1, the following virtual displacement and velocity matrices are defined:

$$\left(\delta\tilde{X}_{TP}(t)\right)_{12\times 3} \equiv \begin{pmatrix} \delta x_C^{(13)}(t) \\ \delta\pi^{(13)}(t) \\ \delta x_C^{(14)}(t) \\ \delta\pi^{(14)}(t) \end{pmatrix}, \tag{3.26a}$$

$$\left(\dot{X}_{TP}(t)\right)_{12\times 3} \equiv \begin{pmatrix} \dot{x}_C^{(13)}(t) \\ \omega^{(13)}(t) \\ \dot{x}_C^{(14)}(t) \\ \omega^{(14)}(t) \end{pmatrix}. \tag{3.26b}$$

The associated mass and $[D]$ sub-matrices are defined, respectively, as:

$$\left[\widehat{M}_{TP}\right]_{12\times 12} \equiv \begin{bmatrix} \widehat{m}^{(13)}I_3 & 0_{3\times 3} & 0_{3\times 3} & 0_{3\times 3} \\ 0_{3\times 3} & \hat{J}_C^{(13)} & 0_{3\times 3} & 0_{3\times 3} \\ 0_{3\times 3} & 0_{3\times 3} & \widehat{m}^{(14)}I_3 & 0_{3\times 3} \\ 0_{3\times 3} & 0_{3\times 3} & 0_{3\times 3} & \hat{J}_C^{(14)} \end{bmatrix}, \tag{3.26c}$$

$$[D_{TP}(t)]_{12\times 12} \equiv \begin{bmatrix} 0_{3\times 3} & 0_{3\times 3} & 0_{3\times 3} & 0_{3\times 3} \\ 0_{3\times 3} & \overleftrightarrow{\omega^{(13)}(t)} & 0_{3\times 3} & 0_{3\times 3} \\ 0_{3\times 3} & 0_{3\times 3} & 0_{3\times 3} & 0_{3\times 3} \\ 0_{3\times 3} & 0_{3\times 3} & 0_{3\times 3} & \overleftrightarrow{\omega^{(14)}(t)} \end{bmatrix}. \tag{3.26d}$$

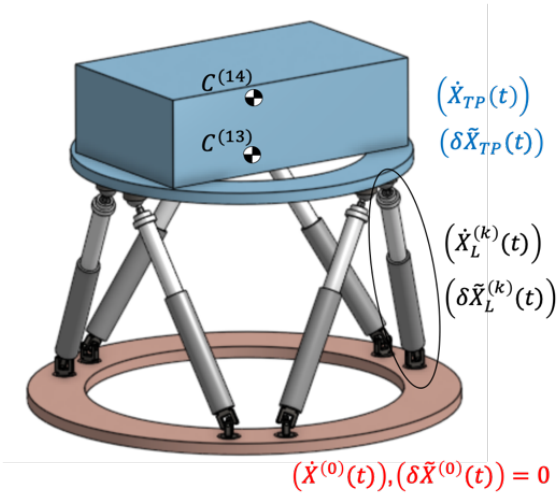

Figure 3.1: Subsystem velocities and virtual displacements

Similarly, for leg-(k) in Fig.3.1 the following virtual displacement, velocity, mass, and [D]-sub-matrices are defined:

$$\left(\delta\tilde{X}_L^{(k)}(t)\right)_{12\times3} \equiv \begin{pmatrix} \delta x_C^{(2k-1)}(t) \\ \delta\pi^{(2k-1)}(t) \\ \delta x_C^{(2k)}(t) \\ \delta\pi^{(2k)}(t) \end{pmatrix}, \tag{3.27a}$$

$$\left(\dot{X}_L^{(k)}(t)\right)_{12\times3} \equiv \begin{pmatrix} \dot{x}_C^{(2k-1)}(t) \\ \omega^{(2k-1)}(t) \\ \dot{x}_C^{(2k)}(t) \\ \omega^{(2k)}(t) \end{pmatrix}, \tag{3.27b}$$

$$\left[\widehat{M}_L^{(k)}\right]_{12\times12} \equiv \begin{bmatrix} \widehat{m}^{(2k-1)}I_3 & 0_{3\times3} & 0_{3\times3} & 0_{3\times3} \\ 0_{3\times3} & \hat{J}_C^{(2k-1)} & 0_{3\times3} & 0_{3\times3} \\ 0_{3\times3} & 0_{3\times3} & \widehat{m}^{(2k)}I_3 & 0_{3\times3} \\ 0_{3\times3} & 0_{3\times3} & 0_{3\times3} & \hat{J}_C^{(2k)} \end{bmatrix}, \tag{3.27c}$$

$$\left[D_L^{(k)}(t)\right]_{12\times12} \equiv \begin{bmatrix} 0_{3\times3} & 0_{3\times3} & 0_{3\times3} & 0_{3\times3} \\ 0_{3\times3} & \overleftrightarrow{\omega^{(2k-1)}(t)} & 0_{3\times3} & 0_{3\times3} \\ 0_{3\times3} & 0_{3\times3} & 0_{3\times3} & 0_{3\times3} \\ 0_{3\times3} & 0_{3\times3} & 0_{3\times3} & \overleftrightarrow{\omega^{(2k)}(t)} \end{bmatrix}. \tag{3.27d}$$

Using Eqs. (3.26a-d) and (3.27a-d), the principle of virtual work, Eq. (3.24a), is written for the Stewart platform as:

$$\begin{aligned} &\left(\delta\tilde{X}_{TP}(t)\right)^T\left\{\left[\widehat{M}_{TP}\right]\left(\ddot{X}_{TP}(t)\right) + \left[D_{TP}(t)\right]\left[\widehat{M}_{TP}\right]\left(\dot{X}_{TP}(t)\right)\right\} \\ &+\sum_{k=1}^{6}\left(\delta\tilde{X}_L^{(k)}(t)\right)^T\left\{\left[\widehat{M}_L^{(k)}\right]\left(\ddot{X}_L^{(k)}(t)\right) + \left[D_L^{(k)}(t)\right]\left[\widehat{M}_L^{(k)}\right]\left(\dot{X}_L^{(k)}(t)\right)\right\} - \left(\delta\tilde{q}^*(t)\right)^T\left(F^*(t)\right) = 0. \end{aligned} \tag{3.28}$$

3.3.2 Generalized Velocities and Virtual Displacements

In task (ii) the subsystem velocities, Eqs. (3.26b) and (3.27b), are expressed in the form of Eq. (3.4a) using appropriate generalized velocities. It is noted that the subsystem velocities are expressed not only by the generalized velocity ($\dot{q}(t)$) but also by $\left(\dot{X}^{(0)}(t)\right)$.

Starting from TP-subsystem, Eqs. (2.29) and (2.27) reveal that the generalized velocities of TP-subsystem are the velocity $\dot{s}_C^{(13/0)}(t)$ and angular velocity $\omega^{(13/0)}(t)$ of body-(13) relative to body-(0), as illustrated in Fig. 3.2. Therefore, the subsystem expression in the form of Eq. (3.4a) becomes

$$\left(\dot{X}_{TP}(t)\right) = \left[B_{TP/TP}(t)\right]\left(\dot{q}_{TP}(t)\right) + \left[B_{TP/BP}(t)\right]\left(\dot{X}^{(0)}(t)\right), \tag{3.29a}$$

where the *generalized velocities of TP-subsystem* are:

$$\left(\dot{q}_{TP}(t)\right) \equiv \begin{pmatrix} \dot{s}_C^{(13/0)}(t) \\ \omega^{(13/0)}(t) \end{pmatrix} \tag{3.29b}$$

and $[B]$ sub-matrices are

$$\left[B_{TP/TP}(t)\right]_{12\times 6} = \begin{bmatrix} R^{(0)}(t) & 0_{3\times 3} \\ 0_{3\times 3} & I_3 \\ R^{(0)}(t) & -R^{(13)}(t)\overleftrightarrow{e_3\hat{h}^{(14/13)}} \\ 0_{3\times 3} & I_3 \end{bmatrix}, \tag{3.29c}$$

$$\left[B_{TP/BP}(t)\right]_{12\times 6} = \begin{bmatrix} I_3 & -R^{(0)}(t)\overleftrightarrow{s_C^{(13/0)}(t)} \\ 0_{3\times 3} & \left(R^{(13/0)}(t)\right)^T \\ I_3 & -R^{(0)}(t)\overleftrightarrow{s_C^{(13/0)}(t) + R^{(13/0)}(t)e_3\hat{h}^{(14/13)}} \\ 0_{3\times 3} & \left(R^{(13/0)}(t)\right)^T \end{bmatrix}. \tag{3.29d}$$

Since $\left(\delta\tilde{X}^{(0)}(t)\right) = 0$, the corresponding relation for the virtual displacements in the form of Eq. (3.21a) becomes

$$\left(\delta\tilde{X}_{TP}(t)\right) = \left[B_{TP/TP}(t)\right](\delta\tilde{q}_{TP}(t)), \tag{3.30a}$$

where

$$\left(\delta\tilde{q}_{TP}(t)\right) \equiv \begin{pmatrix} \delta s_C^{(13/0)}(t) \\ \delta\pi^{(13/0)}(t) \end{pmatrix}, \tag{3.30b}$$

in which $\delta\pi^{(13/0)}(t)$ is the vector form of

$$\overleftrightarrow{\delta\pi^{(13/0)}(t)} = \left[\left(R^{(13/0)}(t,\varepsilon)\right)^T \frac{\partial}{\partial\varepsilon} R^{(13/0)}(t,\varepsilon)\right|_{\varepsilon=0}. \tag{3.30c}$$

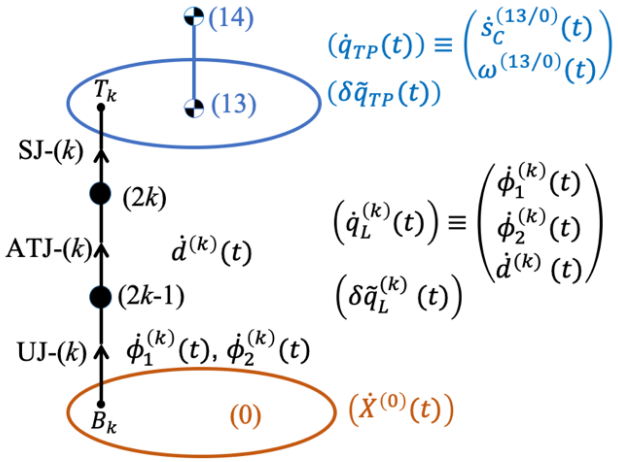

Figure 3.2: Velocities and virtual displacements of TB-subsystem and leg-(k)

For leg-(k) in Fig. 3.2, the subsystem velocities at the centers of body-(2k-1) and body-(2k) are written from Eqs. (2.41c), (2.40c), (2.42f), (2.42c), and (2.42b) in terms angular velocities $\dot{\phi}_1^{(k)}(t)$ and $\dot{\phi}_2^{(k)}(t)$ at the universal joint, UJ-(k), and the axial speed $\dot{d}^{(k)}(t)$ of the linear actuator, ATJ-(k):

$$\left(\dot{X}_L^{(k)}(t)\right) = \left[B_{L/L}^{(k)}(t)\right]\left(\dot{q}_L^{(k)}(t)\right) + \left[B_{L/BP}^{(k)}(t)\right]\left(\dot{X}^{(0)}(t)\right), \tag{3.31a}$$

where $\left(\dot{q}_L^{(k)}(t)\right)$ denotes the *generalized velocities of leg-(k)* defined as:

$$\left(\dot{q}_L^{(k)}(t)\right) \equiv \begin{pmatrix} \dot{\phi}_1^{(k)}(t) \\ \dot{\phi}_2^{(k)}(t) \\ d^{(k)}(t) \end{pmatrix}. \tag{3.31b}$$

In Eq. (3.31a) $[B]$ sub-matrices are

$$\left[B_{L/L}^{(k)}(t)\right]_{12\times 3} = \begin{bmatrix} -R^{(2k-1)}(t)\,\overleftrightarrow{\hat{s}_{C/B_k}^{(2k-1)}}\left(R_{2\,B_k\mathrm{UJ}}(\phi_2^{(k)}(t))\right)^T e_1 \\ \left(R_{2\,B_k\mathrm{UJ}}(\phi_2^{(k)}(t))\right)^T e_1 \\ -R^{(2k-1)}(t)\overleftrightarrow{e_3\left(\hat{l}_{\mathrm{UJ}}^{(2k-1)} + d^{(k)}(t)\right)}\left(R_{2\,B_k\mathrm{UJ}}(\phi_2^{(k)}(t))\right)^T e_1 \\ \left(R_{2\,B_k\mathrm{UJ}}(\phi_2^{(k)}(t))\right)^T e_1 \end{bmatrix}$$

$$\begin{bmatrix} -R^{(2k-1)}(t)\hat{s}_{C/B_k}^{(2k-1)} e_2 & 0_{3\times 1} \\ e_2 & 0_{3\times 1} \\ -R^{(2k-1)}(t)\overleftrightarrow{e_3\left(\hat{l}_{\mathrm{UJ}}^{(2k-1)} + d^{(k)}(t)\right)} e_2 & R^{(2k-1)}(t)e_3 \\ e_2 & 0_{3\times 1} \end{bmatrix}, \tag{3.31c}$$

$$\left[B_{L/BP}^{(k)}(t)\right]_{12\times 6}=\begin{bmatrix} I_3 & -R^{(0)}(t)\overleftarrow{R^{(2k-1/0)}(t)\hat{s}_{C/B_k}^{(2k-1)}+\hat{s}_{B_k}^{(0)}} \\ 0_{3\times 3} & \left(R^{(2k-1/0)}(t)\right)^T \\ I_3 & -R^{(0)}(t)\overleftarrow{R^{(2k-1/0)}(t)e_3\left(\hat{l}_{\mathrm{UJ}}^{(2k-1)}+d^{(k)}(t)\right)+\hat{s}_{B_k}^{(0)}} \\ 0_{3\times 3} & \left(R^{(2k-1/0)}(t)\right)^T \end{bmatrix}. \quad (3.31d)$$

in which from Eqs. (2.14c) and (2.41c)

$$R^{(2k-1/0)}(t)=R_{3\,B_k}(\hat{\theta}_k^{(0)})R_{1\,B_k\mathrm{UJ}}(\phi_1^{(k)}(t))R_{2\,B_k\mathrm{UJ}}(\phi_2^{(k)}(t)), \quad (3.31e)$$

$$R^{(2k-1)}(t)=R^{(0)}(t)R^{(2k-1/0)}(t). \quad (3.31f)$$

The corresponding relation for the virtual displacements of leg-(k) are

$$\left(\delta\tilde{X}_L^{(k)}(t)\right)=\left[B_{L/L}^{(k)}(t)\right]\left(\delta\tilde{q}_L^{(k)}(t)\right), \quad (3.32a)$$

where for the virtual displacements of leg-(k) are defined as:

$$\left(\delta\tilde{q}_L^{(k)}(t)\right)\equiv\begin{pmatrix}\delta\phi_1^{(k)}(t)\\ \delta\phi_2^{(k)}(t)\\ \delta d^{(k)}(t)\end{pmatrix}. \quad (3.32b)$$

In what follows, the relative axial rotation $\phi_3^{(2k/2k-1)}(t)$ between body-($2k$) and body-($2k$-1) defined in Eqs. (2.15a, b) is assumed negligible, $\phi_3^{(2k/2k-1)}(t)$=0. This approximation is based upon the hindsight of the paper [42], where the equation of motion for $\phi_3^{(2k/2k-1)}(t)$ was explicitly derived and found that $\phi_3^{(2k/2k-1)}(t)$ remains zero (since the axial moment of inertia $\hat{J}_{3C}^{(2k-1)}$ is extremely small compared to others). To justify the approximation: $\phi_3^{(2k/2k-1)}(t)$=0, the equation of motion for $\phi_3^{(2k/2k-1)}(t)$ is derived in the Appendix 3.A using a free-body-diagram. The adoption of the approximation at this stage makes the subsequent computations less complicated.

3.3.3 Virtual Work of Gravitational Potential Energy

For task (iii), the virtual work $-\delta U(t)$ of the gravitational potential energy is considered. The contribution comes from TP-subsystem and legs:

$$-\delta U(t)=\left(\delta\tilde{X}_{TP}(t)\right)^T\begin{pmatrix}-\hat{m}^{(13)}ge_3\\ 0_{3\times 1}\\ -\hat{m}^{(14)}ge_3\\ 0_{3\times 1}\end{pmatrix}+\sum_{k=1}^{6}\left(\delta\tilde{X}_L^{(k)}(t)\right)^T\begin{pmatrix}-\hat{m}^{(2k-1)}ge_3\\ 0_{3\times 1}\\ -\hat{m}^{(2k)}ge_3\\ 0_{3\times 1}\end{pmatrix}, \quad (3.33)$$

where g denotes the *gravitational acceleration* and $e_3\equiv(0\quad 0\quad 1)^T$.

3.3.4 Virtual Work by Linear Actuator Forces and Damping Couples

In task (iv) the virtual work $\delta W_{nc}(t)$ in Eq. (3.22a) is defined. It consists of: (i) the virtual work by the linear actuators at ATJs and (ii) that by viscous frictional couples at UJ's and SJ's. First, the virtual work of *linear actuator force* $f_L^{(k)}(t)$ is written as $\delta d^{(k)}(t) f_L^{(k)}(t)$ for $k = 1, \cdots, 6$. Second, the virtual work of the viscous frictional couples are at UJ-(k): $-\delta\phi_1^{(k)}(t)\mu_{\mathrm{UJ}}\dot{\phi}_1^{(k)}(t) - \delta\phi_2^{(k)}(t)\mu_{\mathrm{UJ}}\dot{\phi}_2^{(k)}(t)$ and at SJ-(k): $-\delta\pi_{T_k\mathrm{SJ}}^{(\mathrm{SJ}\ 13/\mathrm{SJ}\ 2k)}(t)\,\mu_{\mathrm{SJ}}\omega_{T_k\mathrm{SJ}}^{(\mathrm{SJ}\ 13/\mathrm{SJ}\ 2k)}(t)$, where μ_{UJ} and μ_{SJ} are the viscous damping coefficients at universal joints and spherical joints, respectively. Consequently, the non-conservative virtual work is expressed in matrix form as:

$$\delta W_{nc}(t) = \sum_{k=1}^{6} \left(\delta\tilde{q}_L^{(k)}(t)\right)^T e_3 f_L^{(k)}(t) + \sum_{k=1}^{6} \left\{ \left(\delta\tilde{q}_L^{(k)}(t)\right)^T \begin{pmatrix} -\mu_{\mathrm{UJ}}\dot{\phi}_1^{(k)}(t) \\ -\mu_{\mathrm{UJ}}\dot{\phi}_2^{(k)}(t) \\ 0 \end{pmatrix} - \left(\delta\pi_{T_k\mathrm{SJ}}^{(\mathrm{SJ}\ 13/\mathrm{SJ}\ 2k)}(t)\right)^T \mu_{\mathrm{SJ}}\omega_{T_k\mathrm{SJ}}^{(\mathrm{SJ}\ 13/\mathrm{SJ}\ 2k)}(t) \right\}, \tag{3.34a}$$

where $\delta\pi_{T_k\mathrm{SJ}}^{(\mathrm{SJ}\ 13/\mathrm{SJ}\ 2k)}(t)$ is the vector form of the skew-symmetric virtual relative angular-velocity matrix at SJ-(k):

$$\overleftrightarrow{\delta\pi_{T_k\mathrm{SJ}}^{(\mathrm{SJ}\ 13/\mathrm{SJ}\ 2k)}(t)} = \left[R_{T_k\mathrm{SJ}}^{(\mathrm{SJ}\ 13/\mathrm{SJ}\ 2k)}(t,\varepsilon)\frac{\partial}{\partial\varepsilon}R_{T_k\mathrm{SJ}}^{(\mathrm{SJ}\ 13/\mathrm{SJ}\ 2k)}(t,\varepsilon)\right|_{\varepsilon=0}. \tag{3.34b}$$

3.3.5 Loop Closure Constraints on Velocities and Virtual Displacements

In task (v) the first loop-closure constraint on velocities in Eqs. (2.46b) is rewritten using the subsystem generalized velocities as:

$$\left[I_3 \quad -R^{(13/0)}(t)\overleftrightarrow{\hat{s}_{T_k}^{(13)}}\right](\dot{q}_{TP}(t)) + R^{(2k-1/0)}(t)\left[A_L^{(k)}(t)\right]\left(\dot{q}_L^{(k)}(t)\right) + \left[0_{3\times3} \quad -\overleftrightarrow{\Delta s_{CL}^{(k)}(t)}\right](\dot{X}^{(0)}(t)) = 0_{3\times1}, \tag{3.35a}$$

where

$$\left[A_L^{(k)}(t)\right]_{3\times3} \equiv \left[\overleftrightarrow{e_3 l^{(k)}(t)}\left(R_{2B_kUJ}(\phi_2^{(k)}(t)\right)^T e_1 \quad \overleftrightarrow{e_2 l^{(k)}(t)} e_2 \quad -e_3\right] = \begin{bmatrix} 0 & -l^{(k)}(t) & 0 \\ l^{(k)}\cos\phi_2^{(k)}(t) & 0 & 0 \\ 0 & 0 & -1 \end{bmatrix}, \tag{3.35b}$$

in which $\Delta s_{CL}^{(k)}(t)$ was defined in Eq. (2.46c) as:

$$\Delta s_{CL}^{(k)}(t) \equiv \left(s_C^{(13/0)}(t) + R^{(13/0)}(t)\hat{s}_{T_k}^{(13)}\right) - \left(\hat{s}_{B_k}^{(0)} + R^{(2k-1/0)}(t)e_3 l^{(k)}(t)\right). \tag{3.35c}$$

The second closure equation (2.47) is written as:

$$\omega_{T_kSJ}^{(SJ13/SJ2k)}(t) = \left[0_{3\times3} \quad \left(R_{3T_k}(\hat{\theta}_k^{(13)})\right)^T\right](\dot{q}_{TP}(t)) - \left(R_{T_kSJ}^{(SJ13/SJ2k)}(t)\right)^T\left[\left(R_{2B_kUJ}(\phi_2^{(k)}(t)\right)^T e_1 \quad e_2 \quad 0_{3\times1}\right]\left(\dot{q}_L^{(k)}(t)\right) + \left[0_{3\times3} \quad \left(R^{(13/0)}(t)R_{3T} \ (\hat{\theta}_k^{(13)})\right)^T - \left(R^{(2k-1/0)}(t)R_{T_kSJ}^{(SJ13/SJ2k)}(t)\right)^T\right](\dot{X}^{(0)}(t)). \tag{3.36}$$

Corresponding to Eqs. (3.35a) and (3.36), the closure constraints on virtual displacements are

$$\left[I_3 \quad -R^{(13/0)}(t)\overleftrightarrow{\hat{s}_{T_k}^{(13)}}\right](\delta\tilde{q}_{TP}(t)) + R^{(2k-1/0)}(t)\left[A_L^{(k)}(t)\right]\left(\delta\tilde{q}_L^{(k)}(t)\right) = 0_{3\times1}, \tag{3.37}$$

$$\delta\pi_{T_k\mathrm{SJ}}^{(\mathrm{SJ}\ 13/\mathrm{SJ}\ 2k)}(t) = \left[0_{3\times3} \quad \left(R_{3T_k}(\hat{\theta}_k^{(13)})\right)^T\right](\delta\tilde{q}_{TP}(t)) - \left(R_{T_k\mathrm{SJ}}^{(\mathrm{SJ}\ 13/\mathrm{SJ}\ 2k)}(t)\right)^T\left[\left(R_{2B_k\mathrm{UJ}}(\phi_2^{(k)}(t)\right)^T e_1 \quad e_2 \quad 0_{3\times1}\right]\left(\delta\tilde{q}_L^{(k)}(t)\right). \tag{3.38}$$

Equations (3.36) and (3.38) show that $\omega_{T_kSJ}^{(SJ13/SJ2k)}(t)$ is not essential velocity since it depends on $(\dot{q}_{TP}(t))$, $(\dot{q}_{TP}(t))$ and $\left(\dot{X}^{(0)}(t)\right)$. The examination of Eqs. (3.37) and (3.35a) reveals that virtual essential displacements and essential velocities are $\left(\delta\tilde{q}_{TP}(t)\right)$ and $(\dot{q}_{TP}(t))$, respectively. They are written from now on as $(\delta\tilde{q}_{TP}^*(t))$ and $(\dot{q}_{TP}^*(t))$, respectively.

Using Eq. (3.37), $\left(\delta\tilde{q}_L^{(k)}(t)\right)$ is expressed by $(\delta\tilde{q}_{TP}^*(t))$ as:

$$\left(\delta\tilde{q}_L^{(k)}(t)\right) = \left[T_{L/TP}^{(k)}(t)\right](\delta\tilde{q}_{TP}^*(t)), \tag{3.39a}$$

where

$$\left[T_{L/TP}^{(k)}(t)\right]_{3\times6} \equiv -\left[A_L^{(k)}(t)\right]^{-1}\left(R^{(2k-1/0)}(t)\right)^T\left[I_3 \quad -R^{(13/0)}(t)\overleftrightarrow{\hat{s}_{T_k}^{(13)}}\right], \tag{3.39b}$$

and from Eq. (3.35b)

$$\left[A_L^{(k)}(t)\right]^{-1} = \begin{bmatrix} 0 & 1/l^{(k)}(t)\cos\phi_2^{(k)}(t) & 0 \\ -1/l^{(k)}(t) & 0 & 0 \\ 0 & 0 & -1 \end{bmatrix}. \tag{3.39c}$$

The substitution of Eq. (3.39a) into Eq. (3.38) yields

$$\delta\pi_{T_k\mathrm{SJ}}^{(\mathrm{SJ}\ 13/\mathrm{SJ}\ 2k)}(t) = \left[T_{T_k\mathrm{SJ}/TP}^{(k)}(t)\right](\delta\tilde{q}_{TP}^*(t)), \tag{3.40a}$$

where

$$\left[T_{T_k\mathrm{SJ}/TP}^{(k)}(t)\right]_{3\times6} \equiv \left[0_{3\times3} \quad \left(R_{3T_k}(\hat{\theta}_k^{(13)})\right)^T\right] - \left(R_{T_k\mathrm{SJ}}^{(\mathrm{SJ}\ 13/\mathrm{SJ}\ 2k)}(t)\right)^T\left[\left(R_{2B_k\mathrm{UJ}}(\phi_2^{(k)}(t)\right)^T e_1 \quad e_2 \quad 0_{3\times1}\right]\left[T_{L/TP}^{(k)}(t)\right]. \tag{3.40b}$$

Similarly, the non-essential velocity of leg-(k) is expressed using Eq. (3.35a) as

$$\left(\dot{q}_L^{(k)}(t)\right) = \left[T_{L/TP}^{(k)}(t)\right]\left(\dot{q}_{TP}^{*}(t)\right) + \left[T_{L/BP}^{(k)}(t)\right]\left(\dot{X}^{(0)}(t)\right), \tag{3.41a}$$

where

$$\left[T_{L/BP}^{(k)}(t)\right]_{3\times 6} = \left[0_{3\times 3} \quad \left[A_L^{(k)}(t)\right]^{-1}\left(R^{(2k-1/0)}(t)\right)^T\overleftarrow{\Delta s_{CL}^{(k)}(t)}\right]. \tag{3.41b}$$

Equation (3.36) gives

$$\omega_{T_k\mathrm{SJ}}^{(\mathrm{SJ}\ 13/\mathrm{SJ}\ 2k)}(t) = \left[T_{T_k\mathrm{SJ}/TP}^{(k)}(t)\right]\left(\dot{q}_{TP}^{*}(t)\right) + \left[T_{T_k\mathrm{SJ}/BP}^{(k)}(t)\right]\left(\dot{X}^{(0)}(t)\right), \tag{3.42a}$$

where

$$\left[T_{T_k\mathrm{SJ}/BP}^{(k)}(t)\right]_{3\times 6} = \left[0_{3\times 3} \quad \left(R^{(13/0)}(t)R_{3T_k}(\hat{\theta}_k^{(13)})\right)^T - \left(R^{(2k-1/0)}(t)R_{T_k\mathrm{SJ}}^{(\mathrm{SJ}\ 13/\mathrm{SJ}\ 2k)}(t)\right)^T\right]. \tag{3.42b}$$

3.3.6 [B^*]-Expressions Using Essential Velocities and Displacements

In task (vi) Eqs. (3.29a) and (3.30a) are expressed in terms of $(\dot{q}_{TP}^{*}(t))$ as in Eq. (3.4c) and $(\delta\tilde{q}_{TP}^{*}t))$ as in Eq. (3.21c), respectively:

$$\left(\dot{X}_{TP}(t)\right) = \left[B_{TP/TP}^{*}(t)\right]\left(\dot{q}_{TP}^{*}(t)\right) + \left[B_{TP/BP}^{*}(t)\right]\left(\dot{X}^{(0)}(t)\right), \tag{3.43a}$$

$$\left(\delta\tilde{X}_{TP}(t)\right) = \left[B_{TP/TP}^{*}(t)\right]\left(\delta\tilde{q}_{TP}^{*}t)\right), \tag{3.43b}$$

where

$$\left[B_{TP/TP}^{*}(t)\right] = \left[B_{TP/TP}(t)\right], \qquad \left[B_{TP/BP}^{*}(t)\right] = \left[B_{TP/BP}(t)\right]. \tag{3.43c,d}$$

For leg-(k) Equation (3.31a) is expressed using Eq. (3.41a) as:

$$\left(\dot{X}_L^{(k)}(t)\right) = \left[B_{L/TP}^{(k)*}(t)\right]\left(\dot{q}_{TP}^{*}(t)\right) + \left[B_{L/BP}^{(k)*}(t)\right]\left(\dot{X}^{(0)}(t)\right), \tag{3.44a}$$

whereas Eq. (3.32a) is written using Eq. (3.9a) as:

$$\left(\delta\tilde{X}_L^{(k)}(t)\right) = \left[B_{L/TP}^{(k)*}(t)\right]\left(\delta\tilde{q}_{TP}^{*}(t)\right), \tag{3.44b}$$

where $[B^*]$-submatrices are defined as follows:

$$\left[B_{L/TP}^{(k)*}(t)\right]_{3\times 6} \equiv \left[B_{L/L}^{(k)}(t)\right]\left[T_{L/TP}^{(k)}(k)\right], \tag{3.44c}$$

$$\left[B_{L/BP}^{(k)*}(t)\right]_{3\times 6} \equiv \left\{\left[B_{L/L}^{(k)}(t)\right]\left[T_{L/BP}^{(k)}(t)\right] + \left[B_{L/BP}^{(k)}(t)\right]\right\}. \tag{3.44d}$$

3.3.7 Virtual Work $\delta W(t)$ and Effective Force ($F^*(t)$)

In task (vii) both $-\delta U(t)$ defined in task (ii) and $\delta W_{nc}(t)$ defined in task (iv) are expressed using the essential velocities $(\dot{q}_{TP}^{*}(t))$ and the virtual essential displacements $(\delta\tilde{q}_{TP}^{*}(t))$. The virtual work of gravitational potential energy in Eq. (3.33) defines the *effective gravitational force* $\left(F_g^*(t)\right)$:

$$-\delta U = \left(\delta\tilde{q}_{TP}^{*}(t)\right)^T\left(F_g^*(t)\right). \tag{3.45a}$$

The effective gravitational force is explicitly computed using Eqs. (3.43b) and (3.44b):

$$\left(F_g^*(t)\right)_{6\times1} = \left[B_{TP/TP}^*(t)\right]^T \begin{pmatrix} -\widehat{m}^{(13)} g e_3 \\ 0_{3\times1} \\ -\widehat{m}^{(14)} g e_3 \\ 0_{3\times1} \end{pmatrix} + \sum_{k=1}^{6} \left[B_{L/TP}^{(k)*}(t)\right]^T \begin{pmatrix} -\widehat{m}^{(2k-1)} g e_3 \\ 0_{3\times1} \\ -\widehat{m}^{(2k)} g e_3 \\ 0_{3\times1} \end{pmatrix}. \tag{3.45b}$$

The virtual work $\delta W_{nc}(t)$ of non-conservative force in Eq. (3.34a) defines the effective force consisting of the *effective actuator force* $\left(F_{ATJ}^*(t)\right)$, the *effective damping couple* $\left(F_\mu^*(t)\right)$ at the joints. The virtual work at actuated translational joints (ATJs) is

$$\sum_{k=1}^{6} \delta d^{(k)}(t) f_L^{(k)}(t) = (\delta \tilde{q}_{TP}^*(t))^T \left(F_{ATJ}^*(t)\right). \tag{3.46a}$$

In *inverse dynamics* the amplitude $f_L^{(k)}(t)$ is sought from the equations of motion for prescribed $(\dot{q}_{TP}^*(t))$ and $(\ddot{q}_{TP}^*(t))$ as well as $\left(\dot{X}^{(0)}(t)\right)$ and $\left(\ddot{X}^{(0)}(t)\right)$. Therefore, for the application, it is convenient to express the effective actuator forces directly in terms of the six actuator forces $f_L^{(k)}(t)$ for $k = 1, \cdots, 6$ as:

$$\left(F_{ATJ}^*(t)\right) = \left[T_{ATJ}^*(t)\right]\left(f_{ATJ}^*(t)\right), \tag{3.46b}$$

where $\left(f_{ATJ}^*(t)\right)$ represents a 6×1 column matrix of the actuator forces:

$$\left(f_{ATJ}^*(t)\right)_{6\times1} \equiv \begin{pmatrix} f_L^{(1)}(t) \\ f_L^{(2)}(t) \\ \vdots \\ f_L^{(6)}(t) \end{pmatrix}. \tag{3.46c}$$

The computations, which follow, show that the 6×6 coefficient matrix $\left[T_{ATJ}^*(t)\right]$ is expressed as:

$$\left[T_{ATJ}^*(t)\right] = \begin{bmatrix} b^{(1)}(t) & \cdots & b^{(k)}(t) & \cdots & b^{(6)}(t) \\ \overleftrightarrow{\hat{s}_{T_1}^{(13)}} \left(R^{(13/0)}(t)\right)^T b^{(1)}(t) & \cdots & \overleftrightarrow{\hat{s}_{T_k}^{(13)}} \left(R^{(13/0)}(t)\right)^T b^{(k)}(t) & \cdots & \overleftrightarrow{\hat{s}_{T_6}^{(13)}} \left(R^{(13/0)}(t)\right)^T b^{(6)}(t) \end{bmatrix}, \tag{3.46d}$$

where

$$\left(b^{(k)}(t)\right) \equiv R^{(2k-1/0)}(t) e_3 = \begin{pmatrix} \cos\hat{\theta}_k^{(0)} \sin\phi_2^{(k)}(t) + \sin\hat{\theta}_k^{(0)} \sin\phi_1^{(k)}(t) \cos\phi_2^{(k)}(t) \\ \sin\hat{\theta}_k^{(0)} \sin\phi_2^{(k)}(t) - \cos\hat{\theta}_k^{(0)} \sin\phi_1^{(k)}(t) \cos\phi_2^{(k)}(t) \\ \cos\phi_1^{(k)}(t) \cos\phi_2^{(k)}(t) \end{pmatrix}. \tag{3.46e}$$

Proof: To derive Eqs. (3.46a, b) one modifies $\delta d^{(k)}(t) f_L^{(k)}(t)$ using Eq. (3.39a-c) as

$$\left(\delta \tilde{q}_L^{(k)}(t)\right)^T e_3 f_L^{(k)}(t) = (\delta \tilde{q}_{TP}^*(t))^T \left[I_3 \quad -R^{(13/0)}(t)\overleftrightarrow{\hat{s}_{T_k}^{(13)}}\right]^T \left(b^{(k)}(t)\right) f_L^{(k)}(t), \quad (3.47a)$$

where the following result obtained from Eq. (3.39c) is used:

$$\left[A_L^{(k)}(t)\right]^{-T} e_3 = -e_3. \quad (3.47b)$$

Then the k^{th} column of $\left[T_{ATJ}^*(t)\right]$ becomes $\left[I_3 \quad -R^{(13/0)}(t)\overleftrightarrow{\hat{s}_{T_k}^{(13)}}\right]^T \left(b^{(k)}(t)\right)$ as shown in Eq. (3.46d).

The virtual work of the viscous damping forces at the universal joints and the spherical joints in Eq. (3.34a) defines the *effective damping force* $\left(F_\mu^*(t)\right)$ as:

$$(\delta \tilde{q}_{TP}^*(t))^T \left(F_\mu^*(t)\right) = \sum_{k=1}^{6} \left(\delta \tilde{q}_L^{(k)}(t)\right)^T \begin{pmatrix} -\mu_{\text{UJ}} \dot{\phi}_1^{(k)}(t) \\ -\mu_{\text{UJ}} \dot{\phi}_2^{(k)}(t) \\ 0 \end{pmatrix} - \sum_{k=1}^{6} \left(\delta \pi_{T_k \text{SJ}}^{(\text{SJ } 13/\text{SJ } 2k)}(t)\right)^T \left(-\mu_{\text{SJ}} \omega_{T_k \text{SJ}}^{(\text{SJ } 13/\text{SJ } 2k)}(t)\right). \quad (3.48a)$$

Using Eqs. (3.39a) and (3.40a), the effective damping force becomes

$$\left(F_\mu^*(t)\right) = \sum_{k=1}^{6} \left[T_{L/TP}^{(k)}(t)\right]^T \begin{pmatrix} -\mu_{\text{UJ}} \dot{\phi}_1^{(k)}(t) \\ -\mu_{\text{UJ}} \dot{\phi}_2^{(k)}(t) \\ 0 \end{pmatrix} + \sum_{k=1}^{6} \left[T_{T_k \text{SJ}/TP}^{(k)}(t)\right]^T \left(-\mu_{\text{SJ}} \omega_{T_k \text{SJ}}^{(\text{SJ } 13/\text{SJ } 2k)}(t)\right). \quad (3.48b)$$

The effective generalized force $(F^*(t))$ of the virtual work $\delta W(t)$ in Eq. (3.22a) is the sum of the components obtained in Eqs. (3.45b), (3.46b), and (3.48b):

$$(F^*(t)) = \left(F_g^*(t)\right) + \left[T_{ATJ}^*(t)\right]\left(f_{ATJ}^*(t)\right) + \left(F_\mu^*(t)\right). \quad (3.49)$$

3.3.8 Compact Equations of Motion

Finally, in task (viii), by substituting Eqs. (3.43a, b), (3.44a, b), and (3.49) into the principle of virtual work, Eq. (3.28), the desired equations of motion are obtained for arbitrary variation of $(\tilde{q}_{TP}^*(t))^T$:

$$\left[M_{TP/TP}^*(t)\right](\ddot{q}_{TP}^*(t)) + \left[N_{TP/TP}^*(t)\right](\dot{q}_{TP}^*(t)) + \left[M_{TP/BP}^*(t)\right]\left(\ddot{X}^{(0)}(t)\right) + \left[N_{TP/BP}^*(t)\right]\left(\dot{X}^{(0)}(t)\right) = \left(F_g^*(t)\right) + \left[T_{ATJ}^*(t)\right]\left(f_{ATJ}^*(t)\right) + \left(F_\mu^*(t)\right), \quad (3.50a)$$

where $[M^*]$-mass submatrices and $[N^*]$-submatrices are

$$\left[M_{TP/TP}^*(t)\right] \equiv \left[B_{TP/TP}^*(t)\right]^T \left[\widehat{M}_{TP}\right] \left[B_{TP/TP}^*(t)\right] + \sum_{k=1}^{6} \left[B_{L/TP}^{(k)*}(t)\right]^T \left[\widehat{M}_L^{(k)}\right] \left[B_{L/TP}^{(k)*}(t)\right], \quad (3.50b)$$

$$\left[N^*_{TP/TP}(t)\right] \equiv \left[B^*_{TP/TP}(t)\right]^T\left\{\left[\widehat{M}_{TP}\right]\left[\dot{B}^*_{TP/TP}(t)\right] + \left[D_{TP}(t)\right]\left[\widehat{M}_{TP}\right]\left[B^*_{TP/TP}(t)\right]\right\}$$
$$+\sum_{k=1}^{6}\left[B^{(k)*}_{L/TP}(t)\right]^T\left\{\left[\widehat{M}^{(k)}_L\right]\left[\dot{B}^{(k)*}_{L/TP}(t)\right] + \left[D^{(k)}_L(t)\right]\left[\widehat{M}^{(k)}_L\right]\left[B^{(k)*}_{L/TP}(t)\right]\right\}, \quad (3.50c)$$

$$\left[M^*_{TP/BP}(t)\right] \equiv \left[B^*_{TP/TP}(t)\right]^T\left[\widehat{M}_{TP}\right]\left[B^*_{TP/BP}(t)\right] + \sum_{k=1}^{6}\left[B^{(k)*}_{L/TP}(t)\right]^T\left[\widehat{M}^{(k)}_L\right]\left[B^{(k)*}_{L/BP}(t)\right], \quad (3.50d)$$

$$\left[N^*_{TP/BP}(t)\right] \equiv \left[B^*_{TP/TP}(t)\right]^T\left\{\left[\widehat{M}_{TP}\right]\left[\dot{B}^*_{TP/BP}(t)\right] + \left[D_{TP}(t)\right]\left[\widehat{M}_{TP}\right]\left[B^*_{TP/BP}(t)\right]\right\}$$
$$+\sum_{k=1}^{6}\left[B^{(k)*}_{L/TP}(t)\right]^T\left\{\left[\widehat{M}^{(k)}_L\right]\left[\dot{B}^{(k)*}_{L/BP}(t)\right] + \left[D^{(k)}_L(t)\right]\left[\widehat{M}^{(k)}_L\right]\left[B^{(k)*}_{L/BP}(t)\right]\right\}. \quad (3.50e)$$

In Eqs. (3.50b-e), $\left[\dot{B}^*(t)\right]$ denotes the time derivative of $[B^*(t)]$ and are presented in the Appendix 3.B. In Eq. (3.50a), the term $\left[N^*_{TP/TP}(t)\right]\left(\dot{q}^*_{TP}(t)\right)$ includes centripetal- and Coriolis-accelerations.

If the inertia terms of legs are negligible, the simplified equations are easily obtained by setting $\left[\widehat{M}^{(k)}_L\right] = 0_{12\times12}$ in Eqs. (3.50b-e). Equation (3.50a) also yields the equations of motion for a Stewart platform with a fixed base plate by setting $\left(\dot{X}^{(0)}(t)\right) = \left(\ddot{X}^{(0)}(t)\right) = 0_{6\times1}$.

Readers who are interested in the Newton-Euler-type equations of motion for the top plate and the legs are referred to the authors' paper [43]. In the paper, the loop closure constraints are appended to Eq. (3.24a) using Lagrange multipliers, and the equations are further simplified to obtain compact equations of motion. (In the paper, instead of leg axial forces, leg displacements are treated as a control input.)

3.3.9 Static Equilibrium Equations

Dynamic equations of motion, Eq. (3.50a), reduce to *static equilibrium equations* by setting all the velocities and accelerations to zero:

$$\left(F^*_g(t)\right) + \left[T^*_{ATJ}(t)\right]\left(f^*_{ATJ}(t)\right) = 0_{6\times1}. \quad (3.51)$$

Equation (3.51) is useful for static strength design of legs, in which leg axial forces are sought for the prescribed position $s_C^{(13/0)}$ and rotation $R^{(13/0)}$ of the top plate relative to the base plate and its rotation, $R^{(0)}$. (The remaining displacements: $\phi_1^{(k)}$, $\phi_2^{(k)}$ and $l^{(k)}$, which appear in $\left[T^*_{ATJ}(t)\right]$ of Eq. (3.46d), are computed using the loop closure equations, Eq. (2.20e).) The static axial forces of legs for strength design are easily obtained by solving Eq. (3.51) for $\left(f^*_{ATJ}(t)\right)$.

3.4 Inverse Dynamics Control

The analytical equations of motion are utilized to control a base-moving Stewart platform employing the *inverse dynamics control* (IDC) or *computed torque control* [38, 40].

3.4.1 Control Objective

The control objective is to keep the position and attitude of the top plate, body-(13), in a desired configuration, expressed by body-(13**d**) frame:

$$\left(\mathbf{e}^{(13*d*)}(t) \quad \mathbf{r}_C^{(13*d*)}(t)\right) = \left(\mathbf{e}^I R^{(13*d*)}(t) \quad \mathbf{e}^I x_C^{(13*d*)}(t)\right), \tag{3.52a}$$

against the input motion of the base plate, body-(0):

$$\left(\mathbf{e}^{(0)}(t) \quad \mathbf{r}_C^{(0)}(t)\right) = \left(\mathbf{e}^I R^{(0)}(t) \quad \mathbf{e}^I x_C^{(0)}(t)\right). \tag{3.52b}$$

The base plate motion, expressed by body-(0) frame, $\left(\dot{\mathbf{e}}^{(0)}(t) \quad \dot{\mathbf{r}}_C^{(0)}(t)\right) = \left(\mathbf{e}^{(0)}(t)\overleftrightarrow{\omega^{(0)}(t)} \quad \mathbf{e}^I \dot{x}_C^{(0)}(t)\right)$, is measured at each time step and its velocities and accelerations are stored in the column matrices as:

$$\left(\dot{X}^{(0)}(t)\right) \equiv \begin{pmatrix} \dot{x}_C^{(0)}(t) \\ \omega^{(0)}(t) \end{pmatrix}, \quad \left(\ddot{X}^{(0)}(t)\right) = \begin{pmatrix} \ddot{x}_C^{(0)}(t) \\ \dot{\omega}^{(0)}(t) \end{pmatrix}. \tag{3.53a, b}$$

To utilize the measured body-(0) configuration and its velocities and accelerations, the current body-(13) frame and the desired body-(13**d**) frame are both expressed relative to body-(0) frame:

$$\left(\mathbf{e}^{(13)}(t) \quad \mathbf{r}_C^{(13)}(t)\right) = \left(\mathbf{e}^{(0)} R^{(13/0)}(t) \quad \mathbf{e}^{(0)} s_C^{(13/0)}(t)\right), \tag{3.54a}$$

$$\left(\mathbf{e}^{(13*d*)}(t) \quad \mathbf{r}_C^{(13*d*)}(t)\right) = \left(\mathbf{e}^{(0)} R^{(13*d*/0)}(t) \quad \mathbf{e}^{(0)} s_C^{(13*d*/0)}(t)\right). \tag{3.54b}$$

The current top-plate configuration relative to body-(0) frame is computed using the measured relative frame-velocities in Eq. (3.28b) and the accelerations, which are stores in the column matrices:

$$\left(\dot{q}_{TP}^*(t)\right) = \begin{pmatrix} \dot{s}_C^{(13/0)}(t) \\ \omega^{(13/0)}(t) \end{pmatrix}, \quad \left(\ddot{q}_{TP}^*(t)\right) = \begin{pmatrix} \ddot{s}_C^{(13/0)}(t) \\ \dot{\omega}^{(13/0)}(t) \end{pmatrix}. \tag{3.55a, b}$$

At each time, the desired relative velocities and accelerations are computed from Eq. (3.54b) and stored in the column matrices as:

$$\left(\dot{q}_{TP*d*}^*(t)\right) = \begin{pmatrix} \dot{s}_{C*d*}^{(13*d*/0)}(t) \\ \omega_{*d*}^{(13*d*/0)}(t) \end{pmatrix}, \quad \left(\ddot{q}_{TP*d*}^*\right) = \begin{pmatrix} \ddot{s}_{C*d*}^{(13*d*/0)}(t) \\ \dot{\omega}_{*d*}^{(13*d*/0)}(t) \end{pmatrix}. \tag{3.56a, b}$$

Using the measured base-plate and top-plate velocities in Eqs. (3.53-55), the velocities $\left(\dot{X}_{TP}(t)\right)$ and accelerations $\left(\ddot{X}_{TP}(t)\right)$ of the top-plate system, illustrated in Fig. 3.1, are computed from Eq. (3.43d).

From Eqs. (3.55, 56) the error velocities are defined in column matrices as:

$$(\dot{e}_{TP}(t)) \equiv \left(\dot{q}^*_{TP}(t)\right) - \left(\dot{q}^*_{TP*d*}(t)\right) = \begin{pmatrix} \dot{s}_C^{(13/0)}(t) - \dot{s}_{C*d*}^{(13*d*/0)}(t) \\ \omega^{(13/0)}(t) - \omega_{*d*}^{(13*d*/0)}(t) \end{pmatrix}. \quad (3.57)$$

The error in relative position of the top-plate between body-(13) frame in Eq. (3.54a) and body-(13*d*) frame in Eq. (3.54b) is $s_C^{(13/0)}(t) - s_{C*d*}^{(13*d*/0)}(t)$, while the error in rotation: $R^{(13/13*d*)}(t)$:

$$\mathbf{e}^{(13)}(t) = \mathbf{e}^{(13*d*)}(t)R^{(13/13*d*)}(t), \quad (3.58a)$$

necessary to rotate $\mathbf{e}^{(13*d*)}(t)$ to $\mathbf{e}^{(13)}(t)$, is computed from Eq. (3.54a, b) as:

$$R^{(13/13*d*)}(t) = \left(R^{(13*d*/0)}(t)\right)^T R^{(13/0)}(t). \quad (3.58b)$$

This error in the rotation is expressed by using three Tait-Bryan angles, which transform SO(3) to $\mathbb{R}^3$, as defined by Eqs. (2.A13, 2.A14) in chapter 2:

$$\psi^{TB}_{error}(t) = \text{Tait-Bryan angle transformation of } R^{(13/13*d*)}(t). \quad (3.59)$$

As a result, a 6×1 column matrix, $(e_{TP}(t))$, corresponding to $(\dot{e}_{TP}(t))$ in Eq. (3.57a) is defined as:

$$(e_{TP}(t)) = \begin{pmatrix} s_C^{(13/0)}(t) - s_{C*d*}^{(13*d*/0)}(t) \\ \psi^{TB}_{error}(t) \end{pmatrix}. \quad (3.60)$$

3.4.2 Implementation of Inverse Dynamics Control

In IDC [11, 38, 40], the equations of motion, Eq. (3.50a), is first solved for the actuator force $\left(f^*_{ATJ}(t)\right)$. Then the acceleration term $\left(\ddot{q}^*_{TP}(t)\right)$ is expressed by $\left(v(t)\right)$ in Eq. (3.61c), which consists of the desired top-plate acceleration $\left(\ddot{q}^*_{TP*d*}(t)\right)$ and PD- or PID-type error feedback-terms.

$$\left(f^*_{ATJ}(t)\right) = \left[\tilde{M}(t)\right]\left(v(t)\right) + \left(\tilde{N}(t)\right) + \left(\tilde{P}(t)\right) + \left(\tilde{F}(t)\right), \quad (3.61a)$$

where

$$\left[\tilde{M}(t)\right] = \left[T^*_{ATJ}(t)\right]^{-1}\left[M^*_{TP/TP}(t)\right], \quad (3.61b)$$

$$\left(v(t)\right) = \left(\ddot{q}^*_{TP*d*}(t)\right) - [K_d]\left(\dot{e}_{TP}(t)\right) - \left[K_p\right]\left(e_{TP}(t)\right) - [K_i]\int(e_{TP}(t))dt, \quad (3.61c)$$

$$\left(\tilde{N}(t)\right) = \left[T^*_{ATJ}(t)\right]^{-1}\left[N^*_{TP/TP}(t)\right](\dot{q}^*_{TP}(t)), \quad (3.61d)$$

$$\left(\tilde{P}(t)\right) = \left[T^*_{ATJ}(t)\right]^{-1}\left\{\left[M^*_{TP/BP}(t)\right]\left(\ddot{X}^{(0)}(t)\right) + \left[N^*_{TP/BP}(t)\right]\left(\dot{X}^{(0)}(t)\right)\right\}, \quad (3.61e)$$

$$\left(\tilde{F}(t)\right) = \left[T^*_{ATJ}(t)\right]^{-1}\left\{-\left(F^*_g(t)\right) - \left(F^*_\mu(t)\right)\right\}. \quad (3.61f)$$

In Eq. (3.61c) $[K_d]$, $\left[K_p\right]$, and $[K_i]$ show derivative, proportional, and integral gain matrices respectively. The substitution of Eq. (3.61a) into Eq. (3.50a) leads to the following differential equation for the error states

$$(\ddot{e}_{TP}(t)) + [K_d](\dot{e}_{TP}(t)) + [K_p](e_{TP}(t)) + [K_i]\int(e_{TP}(t))dt = 0 \qquad (3.62)$$

where $(\ddot{e}_{TP}(t)) = (\ddot{q}^*_{TP}(t)) - (\ddot{q}^*_{TP*d*}(t))$.

The flow chart of the IDC control flow is illustrated in Fig. 3.3.

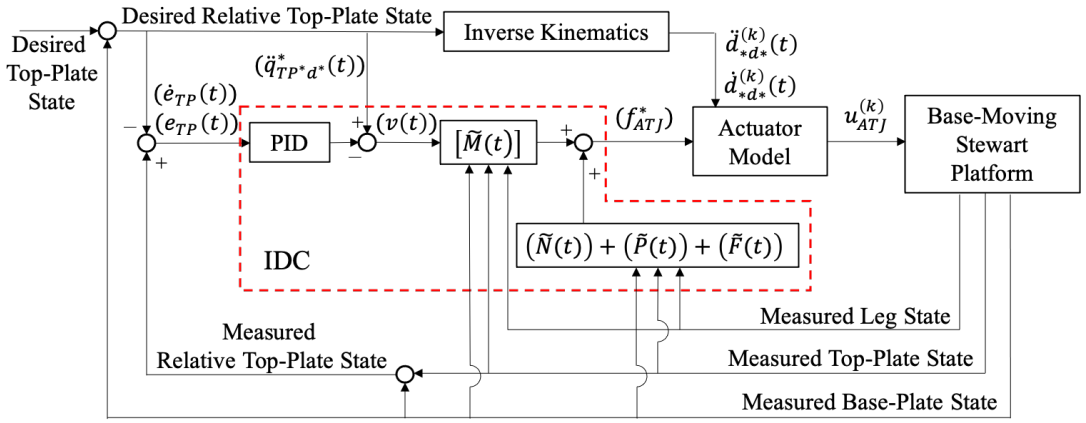

Figure 3.3: A control flowchart of the Stewart platform compensator

As illustrated in Fig. 3.3, the output of IDC, Eq. (3.61a) with components defined in Eq. (3.46c), includes the k^{th} actuator force $f_L^{(k)}(t)$ for $k = 1, \cdots, 6$. The actuator force $f_L^{(k)}(t)$ together with the desired ATJ acceleration $\ddot{d}^{(k)}_{*d*}(t)$, and velocities $\dot{d}^{(k)}_{*d*}(t)$ is used to compute the input signal for a linear electric-servo actuator model [10]. By considering that six actuators are identical, the equations of motion for the k^{th} electromechanical translational actuator (ATJ) are given as

$$M_a^*\ddot{d}^{(k)}_{*d*}(t) + C_a^*\dot{d}^{(k)}_{*d*}(t) = K_t^* i^{(k)}(t) - f_L^{(k)}(t), \qquad (3.63a)$$

$$L_i\frac{di^{(k)}(t)}{dt} + Ri^{(k)}(t) = -K_e^*\dot{d}^{(k)}_{*d*}(t) + u^{(k)}_{ATJ}(t), \qquad (3.63b)$$

where

$$M_a^* = M_s + \left(\frac{2\pi N}{l_p}\right)^2 \eta(J_m + J_l), \qquad C_a^* = C_s + \left(\frac{2\pi N}{l_p}\right)^2 \eta(B_m + B_l), \qquad (3.63c, d)$$

$$K_t^* = \frac{2\pi N\eta}{l_p}K_t, \qquad K_e^* = \frac{2\pi N}{l_p}K_e. \qquad (3.63e, f)$$

In Eq. (3.63a), the mechanical part of the actuator equations, the total mass M_a^* is expressed by the mass of the slider M_s, the mass moment of inertia of the motor J_m and lead screw J_l. C_a^* is the system viscous damping coefficient including the viscous damping coefficients of the slider C_s, motor B_m, and lead screw B_l. K_t^* denotes the torque coefficient. In Eq. (3.63b), the electric part of the equations, the resistance of the motor circuit is denoted by R and inductance of the armature is L_i. The current $i^{(k)}(t)$

is induced by the applied voltage or Pulse-Width Modulation signal $u_{ATJ}^{(k)}(t)$. K_e^* is the back electromotive force constant. The remaining parameters l_p, N, and η shown in Eq. (3.63c-f) represent the lead length, gear ratio, and lead screw efficiency, respectively. Given the two differential equations, Eq. (3.63a) and (3.63b), the state space equation of the actuator model is expressed by

$$\frac{d}{dt}\begin{pmatrix}\dot{d}_{*d*}^{(k)}(t)\\ i^{(k)}(t)\end{pmatrix}=\begin{bmatrix}-\frac{C_a^*}{M_a^*} & \frac{K_t^*}{M_a^*}\\ -\frac{K_e^*}{L_i} & -\frac{R}{L_i}\end{bmatrix}\begin{pmatrix}\dot{d}_{*d*}^{(k)}(t)\\ i^{(k)}(t)\end{pmatrix}+\begin{pmatrix}0\\ \frac{1}{L_i}\end{pmatrix}u_{ATJ}^{(k)}(t)+\begin{pmatrix}-\frac{1}{M_a^*}\\ 0\end{pmatrix}f_L^{(k)}(t) \tag{3.64}$$

Since the parameters of the actuator model are unknown in this study, they were experimentally estimated utilizing MATLAB from the measured output values $d^{(k)}(t)$, $\dot{d}^{(k)}(t)$, $i^{(k)}(t)$ for the inputs $u_{ATJ}^{(k)}(t)$ and $f_L^{(k)}(t)$.

3.5 Experimental Results

Experiments were performed on a scale model, shown in Fig. 3.4, to implement the IKC and IDC controller.

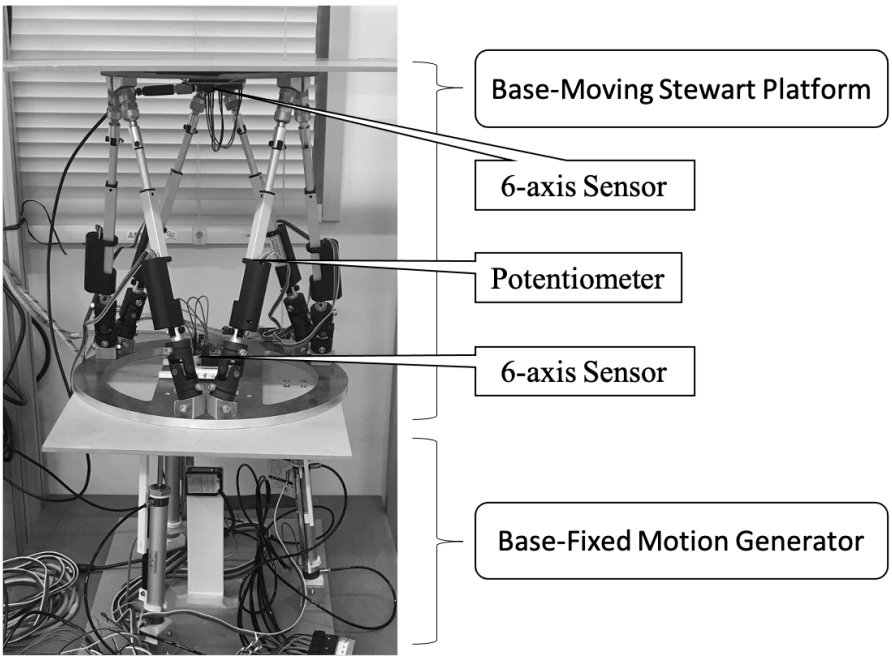

Figure 3.4: A scale model of a Stewart platform installed on a motion generator

3.5.1 Experimental Setup

Figure 3.4 illustrates an experimental setup utilizing a scale model of a Stewart platform, installed on the table of a base-fixed motion generator. The motion of the table is generated by the prescribed sinusoidal motion of three linear actuators. The geometry of the Stewart platform has been described in Table 2.1 in the Appendix 2.A of chapter 2. The mass and moment of inertia of the constituent bodies of the platform are presented in Table 3.1.

Table 3.1: Dynamic properties of a scale model Stewart platform

	Base plate (0)	Top plate (13)	Lower leg ($2k$-1) $k = 1, 2, \cdots, 6$	Upper leg ($2k$) $k = 1, 2, \cdots, 6$
Mass $\hat{m}^{(\alpha)}$	2.0 kg	0.8 kg	0.2 kg	0.1 kg
Moment of Inertia $\hat{J}_{1C}^{(\alpha)}$	0.023 $kg{\cdot}m^2$	0.004 $kg{\cdot}m^2$	0.00043 $kg{\cdot}m^2$	0.00017 $kg{\cdot}m^2$
Moment of Inertia $\hat{J}_{2C}^{(\alpha)}$	0.023 $kg{\cdot}m^2$	0.004 $kg{\cdot}m^2$	0.00043 $kg{\cdot}m^2$	0.00017 $kg{\cdot}m^2$
Moment of Inertia $\hat{J}_{3C}^{(\alpha)}$	0.047 $kg{\cdot}m^2$	0.008 $kg{\cdot}m^2$	0.000013 $kg{\cdot}m^2$	0.000003 $kg{\cdot}m^2$

For the Stewart platform, mounted on the motion generator, 6-axis sensors (3-axis accelerometer and 3-axis gyro sensor) are installed on both the base plate and the top plate to measure their accelerations and angular velocities. By using measured values of angular velocity components at each time, the rotation matrix of the base plate or top plate is updated [29, 39]. Then the Tait-Bryan angles are obtained from the updated rotation matrix. For linear servo actuators of ATJs, their velocities and extensions are measured by a potentiometer built in the actuators. The displacements of the top plate are calculated by correcting the second-order integral of the measured accelerations with the displacements obtained by forward kinematics computation using the measured actuator lengths of the base-moving Stewart platform. The displacements of the base plate can be calculated in the same way from the actuator lengths of the generator.

When this system is applied to the motion compensation of a ship, displacements and attitudes of the top plate and attitudes of the base plate can be measured by the same method as in this experiment. But this strategy cannot be applied to the measurement of displacements of the base plate since it is attached to a moving ship. It requires to calculate the displacements of the bottom plate by integrating the accurate gyro and accelerometer values. However, since the calculated displacement accumulates an error, the drift amount must be corrected to allow the Stewart platform to work within its range of motion.

In the case of application to a bed in an ambulance, an acceleration sensor is installed inside the vehicle, and the position and attitude of the top plate are controlled according to the time change of the measured acceleration. The displacements and attitude of the top plate can be measured in the same way as in the experiment.

In the experiments, the base plate was excited by the motion generator, which induces the base-plate motion by displacing three linear actuators with the amplitudes: $0.02\sin(2\pi f_1 t)$ m, $0.02\sin(2\pi f_2 t)$ m, and $0.02\sin(2\pi f_3 t)$ m, whose frequencies are f_1= 0.15 Hz, f_2= 0.1 Hz, and f_3= 0.05 Hz.

The control objective is to keep the top plate horizontal and stationary against the motion of the base plate. The desired top-plate configuration was selected to be the initial reference configuration of the top plate: $\left(\mathbf{e}^{(13*d*)}(t) \quad \mathbf{r}_C^{(13*d*)}(t)\right) =$

$\left(\mathbf{e}^I I_3 \quad \mathbf{e}^I x_C^{(13)}(0)\right)$, where $x_C^{(13)}(0) = e_3 \hat{h}^{(0)}$ in which $\hat{h}^{(0)}$ denotes the initial elevation of the top plate relative to the initial stationary base plate.

For the IKC controller, the gains are chosen by the trial-and-error method. For the IDC controller, the PID gains were tuned by a trial-and-error method so that the error states in Eq. (3.62) asymptotically approach zero. The time step of 0.01 seconds is utilized in the experiment.

To conduct the experiments described above, MATLAB software and Arduino microcontrollers were utilized for computations and signal transmission/reception, respectively.

3.5.2 Results and Discussion

Figures 3.5(a-f) illustrate the input base-plate configuration (in black curves) and the controlled top-plate configuration for IDC (in red curves) and IKC (in blue curves). Figures 3.5(a-c) show the translational displacements in the x_1-, x_2-, and x_3-directions, respectively. Figures 3.5(d-f) show the rotation matrices of the base plate, $R^{(0)}(t)$, and the top plate, $R^{(13)}(t)$, where each rotation matrix is expressed using Tait-Bryan angles, introduced in Eqs. (2.A13) and (2.A14), as:

$$R^{(0)}(t) = R_1(\psi_1^{TB(0)}(t))R_2(\psi_2^{TB(0)}(t))R_3(\psi_3^{TB(0)}(t)), \tag{3.65a}$$

$$R^{(13)}(t) = R_1(\psi_1^{TB(13)}(t))R_2(\psi_2^{TB(13)}(t))R_3(\psi_3^{TB(13)}(t)). \tag{3.65b}$$

In the experiments, the desired top-plate configuration is expressed by zero translational displacements and zero Tait-Bryan angles. This angular representation of a rotation matrix is explained in the Appendix 2.A to plot admissible workspace. For $R^{(13)}(t)$ the corresponding Tait-Bryan angles $\psi_i^{TB}(t), i = 1, 2, 3$ are computed by using Eq. (2.A14) applied to $R^{(13)}(t)$ instead of $R^{(13/0)}(t)$.

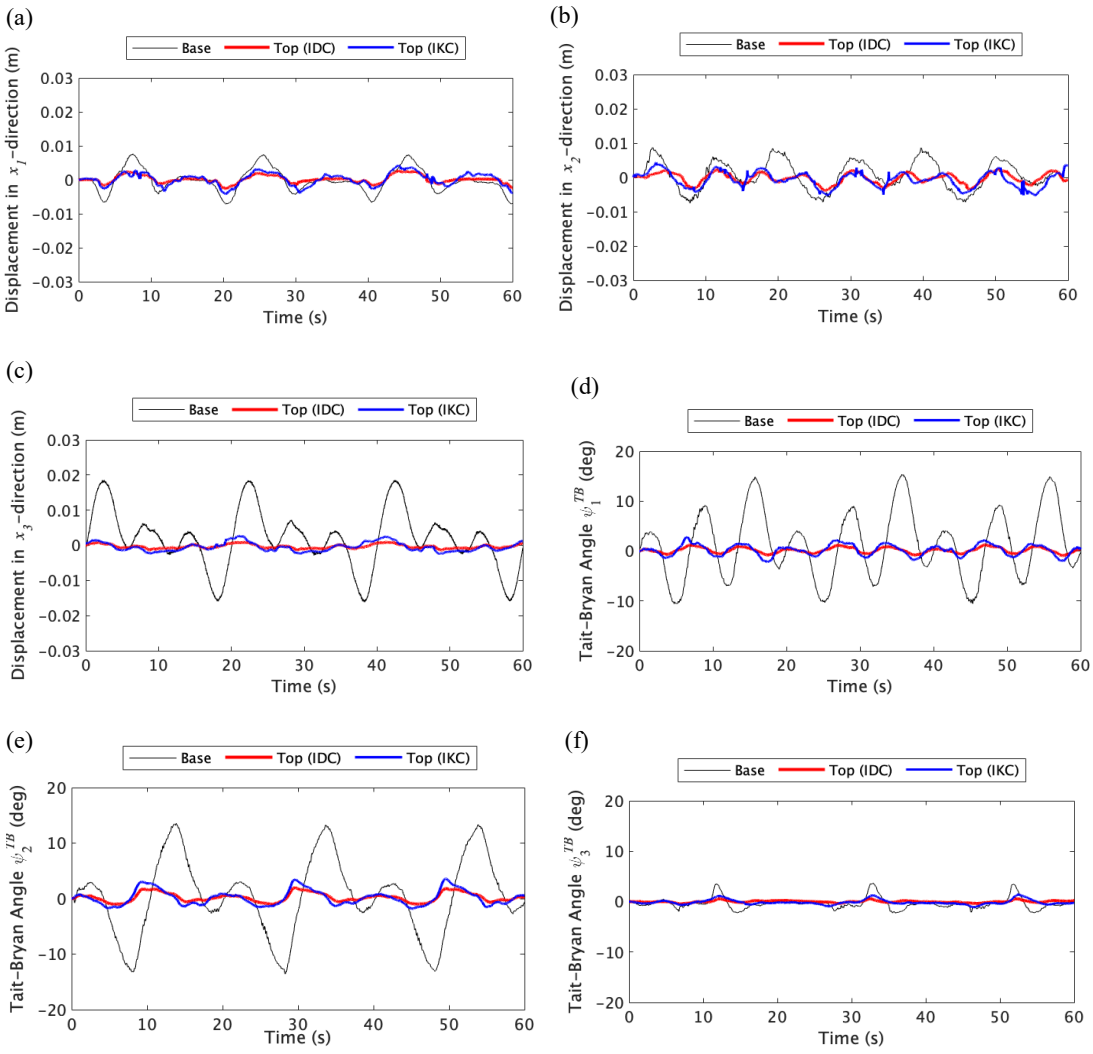

Figure 3.5: Plots of the input base-plate configuration and the controlled top-plate configuration: (a) displacement in the x_1-direction, (b) displacement in the x_2-direction, (c) displacement in the x_3-direction, (d) Tait-Bryan angle $\psi_1^{TB}(t)$, (e) Tait-Bryan angle $\psi_2^{TB}(t)$, and (f) Tait-Bryan angle $\psi_3^{TB}(t)$

To quantify the performance of IDC and IKC, root mean square errors (RMSE) and mean absolute errors (MAE) for the top plate configuration are calculated in Table 3.2. The rate of compensation indicates how much the top plate compensates the motion of the base plate. From the results of Figs. 3.5 and Table 3.2, it is observed that IDC achieves smaller errors, the higher rate of compensation, and better control performance compared to the purely kinematic IKC.

Table 3.2: Comparison of errors and compensation rates between IDC and IKC

	Controller	RMSE	MAE	Compensation Rate	
				RMSE	MAE
Displacement in x_1-direction	IDC	0.0011 m	0.0008 m	67.18 %	67.28 %
	IKC	0.0018 m	0.0015 m	51.25 %	52.12 %
Displacement in x_2-direction	IDC	0.0015 m	0.0012 m	64.51 %	65.60 %
	IKC	0.0020 m	0.0019 m	51.10 %	52.54 %
Displacement in x_3-direction	IDC	0.0011 m	0.0008 m	89.51 %	89.14 %
	IKC	0.0017 m	0.0015 m	81.82 %	80.50 %
Tait-Bryan Angle $\psi_1^{TB(13)}(t)$	IDC	0.5473°	0.4584°	88.87 %	88.66 %
	IKC	1.0768°	0.9048°	80.90 %	80.52 %
Tait-Bryan Angle $\psi_2^{TB(13)}(t)$	IDC	0.8059°	0.6482°	88.04 %	87.57 %
	IKC	1.4251°	1.1486°	78.85 %	77.97 %
Tait-Bryan Angle $\psi_3^{TB(13)}(t)$	IDC	0.1953°	0.1485°	83.48 %	83.04 %
	IKC	0.4115°	0.3411°	65.18 %	61.06 %

3.6 Control Simulations

In this section, control applications utilizing the derived equations by adopting two nonlinear robust controllers are described: (i) IDC with H_∞ control and (ii) integral sliding mode control (ISMC). The applications of each control law to a base-moving Stewart platform are presented. Then, a numerical simulation is carried out to evaluate effectiveness of each control method.

3.6.1 Nonlinear Robust Controller Design

3.6.1.1 IDC with H-infinity Controller

For the motion control of robot manipulators, inverse dynamics control or feedback linearization is a conventional nonlinear control method which strictly linearizes a nonlinear system by canceling nonlinear terms based on the results of inverse dynamic computation [44].

The implementation of the IDC requires accurate dynamic modeling of the Stewart platform using accurate parameter values. Inaccurate modeling or uncertainty of the parameters results in reduced accuracy of the controller performance. Therefore, to minimize the modeling errors and retain robustness, H_∞ control scheme is applied to the IDC as illustrated in Fig. 3.5.

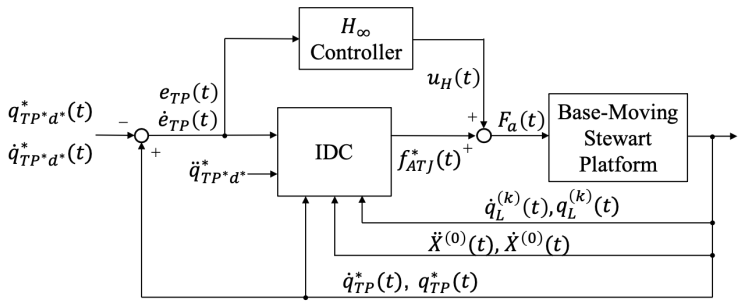

Figure 3.6: Block diagram of the IDC with H_∞ controller

The IDC with H_∞ law can be written as:

$$(F_a(t)) = \left[\widetilde{M}_n(t)\right]\left(v(t)\right) + \left(\widetilde{N}_n(t)\right) + \left(\widetilde{P}_n(t)\right) + \left(\widetilde{F}_n(t)\right) + u_H(t) \qquad (3.66)$$

where $\left[\widetilde{M}_n(t)\right]$, $\left(\widetilde{N}_n(t)\right)$, $\left(\widetilde{P}_n(t)\right)$, and $\left(\widetilde{F}_n(t)\right)$ are nominal matrices. $u_H(t)$ indicates an additional input derived from the H_∞ conotrol law to compensate the modeling errors. The error equation is obtained by substituting Eq. (3.66) into Eq. (3.50a)

$$(\ddot{e}_{TP}(t)) + [K_d](\dot{e}_{TP}(t)) + \left[K_p\right](e_{TP}(t)) + [K_i]\int(e_{TP}(t))dt = \left[\widetilde{M}_n(t)\right]^{-1} w(t) - \left[\widetilde{M}_n(t)\right]^{-1} u_H(t) \qquad (3.67a)$$

where

$$w(t) = \left(\left[\widetilde{M}(t)\right] - \left[\widetilde{M}_n(t)\right]\right)\left(\ddot{q}^*_{TP}(t)\right) + \left(\left(\widetilde{N}(t)\right) + \left(\tilde{P}(t)\right) + \left(\tilde{F}(t)\right)\right) - \left(\left(\widetilde{N}_n(t)\right) + \left(\tilde{P}_n(t)\right) + \left(\tilde{F}_n(t)\right)\right) \quad (3.67b)$$

Observing that the modeling error $w(t)$ represents disturbance of the Eq. (3.67a) caused by uncertainties, the generalized state space model of the error dynamics can be expressed as:

$$\begin{aligned} \dot{x}_e(t) &= Ax_e(t) + B_w w(t) + B_u u_H(t) \\ z(t) &= \begin{pmatrix} z_e(t) \\ z_u(t) \end{pmatrix} = C_z x_e(t) + D_{zw} w(t) + D_{zu} u_H(t) \\ y(t) &= C_y x_e(t) + D_{yw} w(t) + D_{yu} u_H(t) \end{aligned} \quad (3.68a)$$

where $x_e(t)$ is the state variables defined as:

$$x_e(t) = \begin{pmatrix} \int e_{TP}(t)dt \\ e_{TP}(t) \\ \dot{e}_{TP}(t) \end{pmatrix} \quad (3.68b)$$

and $z(t)$ represents the penalty outputs to be minimized and $y(t)$ is the measurement outputs. The coefficient matrices are defined as follows:

$$A = \begin{bmatrix} 0 & I_6 & 0 \\ 0 & 0 & I_6 \\ -K_i & -K_p & -K_d \end{bmatrix}, \quad B_w = \begin{bmatrix} 0_{6\times6} \\ 0 \\ \left[\widetilde{M}_n(t)\right]^{-1} \end{bmatrix} w_d, \quad B_u = \begin{bmatrix} 0_{6\times6} \\ 0 \\ -\left[\widetilde{M}_n(t)\right]^{-1} \end{bmatrix} \quad (3.68c, d, e)$$

$$C_z = \begin{bmatrix} w_e \\ 0_{6\times18} \end{bmatrix}, \quad D_{zw} = \begin{bmatrix} 0_{18\times6} \\ 0_{6\times6} \end{bmatrix}, \quad D_{zu} = \begin{bmatrix} 0_{18\times6} \\ w_u \end{bmatrix} \quad (3.68f, g, h)$$

$$C_y = I_{18}, \qquad D_{yw} = D_{yu} = 0_{18\times6} \quad (3.68i, j)$$

The inertia matrix in the coefficient matrices B_w and B_u is assumed to be constant for the subsequent calculations,

$$\left[\widetilde{M}_n(t)\right] \cong \left[\widehat{M}\right] \quad (3.69)$$

and the error in this assumption can be add to Eq. (3.67b) as disturbance. In Eqs. (3.68d), (3.68f), and (3.68h), w_d , w_e and w_u represent weight matrices associated with disturbance, error state variables, and control inputs. The H_∞ control scheme for the state space model of Eq. (3.68a) is shown in Fig. 3.6.

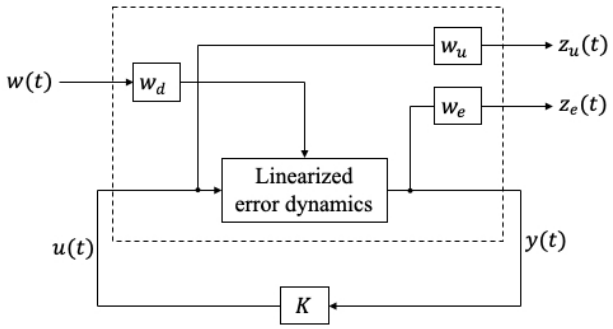

Figure 3.7: H_∞ control configuration

In order to find a state feedback controller

$$u_H(t) = Kx_e(t) \tag{3.70}$$

such that $A+B_uK$ becomes the Hurwitz matrix, and the H_∞ norm of the closed-loop transfer function $H(s)$ from $w(t)$ to $z(t)$ becomes $\|H\|_\infty < \gamma$, the following Linear Matrix Inequalities in terms of variables X and L are solved to calculate the smallest possible value of $\gamma > 0$

$$X > 0, \quad \begin{bmatrix} AX + XA^T + B_uL + L^TB_u{}^T & B_w & XC_z{}^T + L^TD_{zu}{}^T \\ B_w{}^T & -\gamma I_6 & D_{zw}{}^T \\ C_zX + D_{zu}L & D_{zw} & -\gamma I_{24} \end{bmatrix} < 0 \tag{3.71}$$

The feedback gain K for the additional input is obtained by

$$K = LX^{-1} \tag{3.72}$$

3.6.1.2 Integral Sliding Mode Controller

Sliding mode control is well known as a robust control method for linear and nonlinear systems with parametric and nonparametric uncertainties and disturbances. A process of SMC consists of two phases: (i) a reaching phase in which initial states are forced to reach a predesigned sliding surface in finite time, and (ii) a sliding phase in which the states move to the origin along the sliding surface. However, robustness of the system is not guaranteed during the reaching phase and the system response becomes sensitive.

Integral sliding mode control (ISMC) is a modified control method to overcome the drawback of the conventional SMC by removing the reaching phase. Since the initial system state is on the sliding surface, the robustness of the system can be ensured during an entire system response. Therefore, the ISMC is employed for the purpose of realizing enhanced robustness and quick response.

From Eq. (3.50a) and Eq. (3.61a), the matrices including the uncertainties are expressed by nominal and perturbed parts as:

$$[\widetilde{M}(t)] = [\widetilde{M}_n(t)] + [\Delta\widetilde{M}(t)] \tag{3.73a}$$

$$(\widetilde{N}(t)) = (\widetilde{N}_n(t)) + (\Delta\widetilde{N}(t)) \tag{3.73b}$$

$$(\tilde{P}(t)) = (\tilde{P}_n(t)) + (\Delta\tilde{P}(t)) \tag{3.73c}$$

$$(\tilde{F}(t)) = (\tilde{F}_n(t)) + (\Delta\tilde{F}(t)) \tag{3.73d}$$

It is assumed that the above parametric perturbations have the following bounds:

$$\|[\Delta\widetilde{M}(t)]\| \leq \bar{M} \tag{3.74a}$$

$$\|(\Delta\widetilde{N}(t))\| \leq \bar{N} \tag{3.74b}$$

$$\|(\Delta\widetilde{P}(t))\| \leq \bar{P} \tag{3.74c}$$

$$\|(\Delta\tilde{F}(t))\| \leq \bar{F} \tag{3.74d}$$

By defining the error state from Eq. (3.57) and Eq. (3.60),

$$q_e(t) = \begin{pmatrix} e_{TP}(t) \\ \dot{e}_{TP}(t) \end{pmatrix} \tag{3.75}$$

the nonlinear error dynamics can be expressed as

$$\dot{q}_e(t) = f(t) + g(t)u_s(t) + d(t) \tag{3.76a}$$

where

$$f(t) = \begin{pmatrix} \dot{e}(t) \\ (\ddot{q}^*_{TP*d*}(t)) - [\widetilde{M}_n(t)]^{-1}(-(\widetilde{N}_n(t)) - (\tilde{P}_n(t)) - (\tilde{F}_n(t))) \end{pmatrix} \tag{3.76b}$$

$$g(t) = \begin{pmatrix} 0 \\ -[\widetilde{M}_n(t)]^{-1} \end{pmatrix} \tag{3.76c}$$

$$d(t) = \begin{pmatrix} 0 \\ -[\widetilde{M}_n(t)]^{-1}(-[\Delta\widetilde{M}(t)](\ddot{q}^*_{TP}(t)) - (\Delta\widetilde{N}(t)) - (\Delta\tilde{P}(t)) - (\Delta\tilde{F}(t))) + h(t) \end{pmatrix} \tag{3.76d}$$

In the Eq. (3.76a), $d(t)$ represents purturbations including nonparametric uncertainties $h(t)$ which come from external disturbances and unmodeled dynamics. Here, it is assumed that $d(t)$ is bounded such that

$$\|d(t)\| \leq \bar{d} \tag{3.77}$$

The integral sliding-mode control-input $u_s(t)$ consists of nominal control input $u_0(t)$ and nonlinear control input $u_{nl}(t)$ as:

$$u_s(t) = u_0(t) + u_{nl}(t) \tag{3.78a}$$

where the nominal controller can be chosen as

$$u_0(t) = -(c^T g(t))^{-1}(c^T f(t) + c^T q_e(t)) \tag{3.78b}$$

and the discontinuous control input is

$$u_{nl}(t) = -\left(c^T g(t)\right)^{-1} K_s \text{sgn}(s(q_e(t))) \tag{3.78c}$$

where $s(q_e(t))$ is sliding surface function, and K_s is the gain of switching function. The gain K_s is chosen to satisfy the following stability condition for $\varepsilon > 0$,

$$K_s = \bar{d} + \varepsilon \tag{3.79}$$

Then, the sliding surface can be expressed as

$$s(q_e(t)) = c^T(q_e(t) - s_i(t)) \tag{3.80a}$$

where

$$c = \begin{pmatrix} \Lambda \\ I_6 \end{pmatrix} \tag{3.80b}$$

In Eq. (3.80b), Λ is a diagonal positive definite matrix, and $s_i(t)$ shows an integral term such that

$$\dot{s}_i(t) = f(q_T(t)) + g(q_T(t))u_0(t) \tag{3.81}$$

Then, the integral sliding surface in Eq. (3.80a) becomes

$$s(t) = c^T(q_e(t) - q_e(0) - \int (f(t) + g(t)u_0(t))dt) \tag{3.82}$$

To prove the stability of the controller, the Lyapunov candidate function is expressed as [45]:

$$V = \frac{1}{2} s^T(t)s(t) \tag{3.83}$$

The time derivative of the Lyapunov function yields

$$\begin{aligned} \dot{V} &= s^T(t)\dot{s}(t) \\ &= s^T(t)c^T(f(t) + g(t)u_s(t) + d(t) - f(t) - g(t)u_0(t)) \\ &= s^T(t)c^T(g(t)u_{nl}(t) + d(t)) \\ &= s^T(t)(c^T d(t) - K_s \text{sgn}(s(q_e(t)))) \\ &\leq \|d(t)\|\|s(t)\| - \left(\bar{d} + \varepsilon\right)\|s(t)\| \\ &\leq \left(\bar{d} - \bar{d} - \varepsilon\right)\|s(t)\| \\ &\leq -\varepsilon\|s(t)\| < 0 \end{aligned} \tag{3.84}$$

which implies that the resulting closed-loop system is asymptotically stable in the sense of Lyapunov.

Due to the use of the sign function, the sliding mode control input becomes discontinuous, which leads to the undesired chattering effect. In order to smoothly switch the controller and avoid the chattering, a hyperbolic tangent function is used instead of the sign function in Eq. (3.78c):

$$u_{nl}(t) = -\left(c^T g(t)\right)^{-1} K_s \tanh(\alpha s(q_e(t))) \tag{3.85}$$

where α is an experimentally determined parameter.

3.6.2 Simulation Results and Discussion

In this section, simulation results are described to access the effectiveness of the proposed nonlinear robust controllers. The same properties of a scale model of a Stewart platform in Table 2.1 and 2.2 are used for the simulation. All parameters shown in the Tables are included in the dynamic model, Eq. (3.50a).

The trajectories of the base plate used for this simulation, including heave, roll, and pitch motion are prescribed as:

$$\left(X^{(0)}(t)\right) = \begin{pmatrix} x_{1C}^{(0)}(t) \\ x_{2C}^{(0)}(t) \\ x_{3C}^{(0)}(t) \\ \psi_1^{TB(0)}(t) \\ \psi_2^{TB(0)}(t) \\ \psi_3^{TB(0)}(t) \end{pmatrix} = \begin{pmatrix} 0 \\ 0 \\ 0.01\sin(t) \\ 0.15\sin\left(\frac{2\pi}{5}t\right) \\ 0.15\sin\left(\frac{\pi}{5}t\right) \\ 0 \end{pmatrix} \tag{3.86}$$

where the maximum displacements of the base plate are in the range of workspace of the Stewart platform, and the desired top-plate accelerations, velocities, and trajectories are chosen as $\left(\ddot{q}_{TP*d*}^{*}(t)\right) = \left(\dot{q}_{TP*d*}^{*}(t)\right) = \left(q_{TP*d*}^{*}(t)\right) = 0$.

In the simulation, four types of control schemes are compared: simple PID, ISMC with linearized model, IDC with linear H_∞ control, and ISMC with nonlinear model. It is assumed that all states are known, but the parameters are not measured accurately and have errors within 20 percent. Additionally, the top plate of the Stewart platform is loaded by a cuboid whose parameters are uncertain. The load is placed so that its center of mass is located on the $s_3^{(13)}$ axis and assumed not to move. In order to impose nonparametric uncertainties and unmodeled dynamics, the mass and geometry of the cuboid are not included in the design of controllers. The controller parameters for the IDC-H_∞ control are chosen as follows: $K_p = 400$, $K_i = 200$, $K_d = 40$, $w_d = I_6$, $w_e = I_6$, $w_u = 0.2I_6$, and then H_∞ state feedback controller gain K is calculated from the LMI in Eq. (3.71). Here, PID gains are tuned by the trial-and-error method, and the weights are selected so that the control effort is reduced while keeping the control performance. For the ISMC, $K_s = 10$, $\Lambda = 5I_6$, and $\alpha = 10$ are assigned. The gain K_s is chosen to be larger than perturbations, and Λ is determined by the trial-and-error method.

Figure 3.7(a-c) show the results of the controlled top plate against the excitation of the base plate. It is observed that each controller compensates the base-plate excitation. In Fig. 3.7(a), the top plate slightly moves downward initially because of the uncertain load. From Figs. 3.7(b) and 3.7(c), the amplitudes of angles of the top plate are very small compared with those of the base plate. Also, it can be seen that the load has an insignificant effect on the rolling and pitching motions since the center of mass of the load is assumed to be located on the $s_3^{(13)}$ axis. While the IDC-H_∞ controller performs well around the neutral position, the control performance far from the neutral position is lower than that of the nonlinear ISMC. This is because the mass matrix used for the H_∞ control design is assumed to be a constant matrix (in Eq. (3.69)). The constant mass matrix is specified so that the extension of a translational joint becomes half length of the stroke. To quantify the performance of each controller, the RMS errors calculated from the results of the simulations are given in Table 3.2. From Table 3.2, the nonlinear ISMC achieves smallest maximum absolute errors and RMS errors. From the plots and the errors, it can be seen that the controllers based on the equations of motion: ISMC with linearized model, IDC with linear H_∞ control, ISMC with nonlinear model, show better results than simple PID controller. Also, the ISMC with nonlinear model converges more quickly and shows higher robustness compared to the performance of the other controllers.

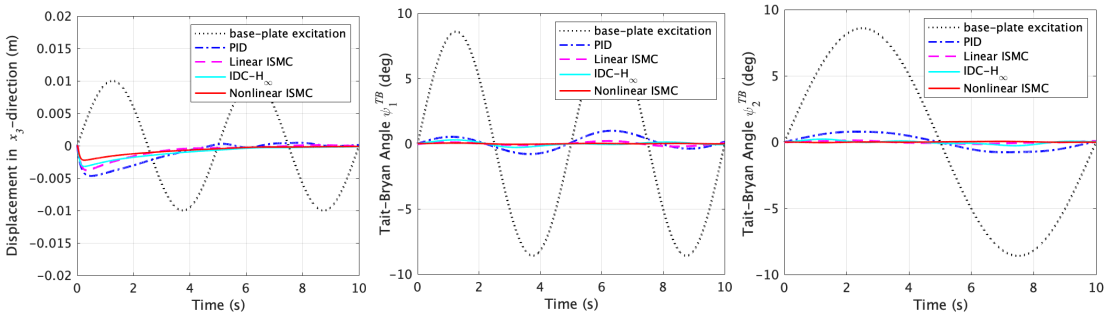

(a) (b) (c)

Figure 3.8: Simulation results of the input base-plate configuration and the controlled top-plate configuration: (a) displacement in the x_3-direction, (b) Tait-Bryan angle $\psi_1^{TB}(t)$, (c) Tait-Bryan angle $\psi_2^{TB}(t)$

Table 3.3: RMS errors

Control scheme	Displacement in x_3-direction	Tait-Bryan angle $\psi_1^{TB(13)}(t)$	Tait-Bryan angle $\psi_2^{TB(13)}(t)$
PID	0.005 m	0.0091°	0.011°
ISMC with linearized model	0.0017 m	0.0023°	0.0021°
IDC with linear H_∞ control	0.0011 m	0.0020°	0.0014°
ISMC with nonlinear model	0.00098 m	0.00056°	0.00067°

Figure 3.8 illustrates a comparison of the RMS errors for the linear ISMC and nonlinear ISMC when the frequency applied to the motion of the base plate is varied to 0.1 to 8 Hz. As the frequency of the base-plate motion becomes higher, RMS errors of the linear ISMC is larger than the nonlinear ISMC. The results show that nonlinear ISMC successfully compensate the influence of the nonlinearity of the system by elaborating the control input based on the nonlinear equations of motion.

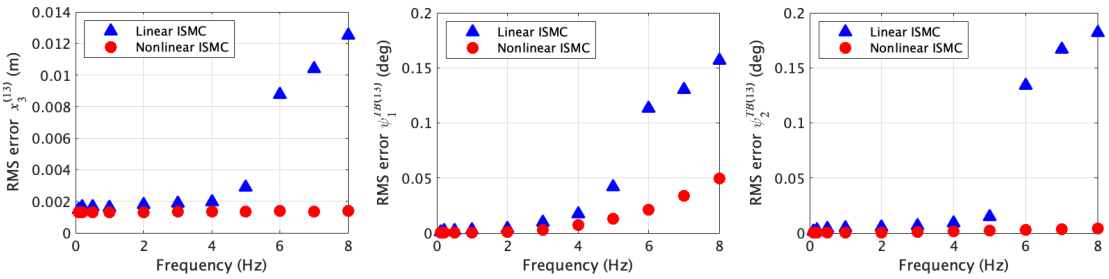

(a) (b) (c)

Figure 3.9: RMS errors of (a) displacement in the x_3-direction, (b) Tait-Bryan angle $\psi_1{}^{TB}(t)$, (c) Tait-Bryan angle $\psi_2{}^{TB}(t)$ versus frequency change (0.1-8 Hz)

3.7 Concluding Remarks

To derive analytical equations of motion, the principle of virtual work is variationally derived from Hamilton's principle for multi-body systems, whose configuration space is defined utilizing both vectors and rotation matrices of SO(3). The resulting virtual work equation yields the principle of virtual power [17], which is a weighted residual equation for the Newton and Euler equations.

Utilizing the velocities of constituent bodies, computed in chapter 2, a step-by-step derivation of the equations of motion incorporates the loop closure constraints analytically to yield compact analytical equations of motion in matrix form. In the equations for inverse dynamics control (IDC), the forces of the actuated translational joints (ATJs) are explicitly expressed.

Then, experimental results, performed on a scale model, are presented to assess the performance of the two control laws: IDC and IKC. The tracking performance was examined for both IDC and IKC. The experimental results demonstrate that the IDC controller utilizing the equations of motion is more effective to control a Stewart platform against input disturbance of its base plate than the IKC controller, described in chapter 2.

Finally, the IDC-H_∞ control and the ISMC were examined by numerical simulations. Utilizing the analytical equations of motion, each control law was elaborated. In the numerical simulations, the tracking performance and robustness were examined for each controller by intentionally introducing uncertainties to the system.

3.8 Appendix

3.8.1 Appendix 3.A: Equation of Motion for $\phi_3^{(2k/2k-1)}(t)$

The upper body of leg-(k), body-($2k$), is a circular cylinder with a spherical ball at one end, as illustrated in Fig. 2.7. One first observes that (i) the damping couple induced at a spherical joint is negligible since μ_{SJ} is small, and (ii) there is no external couple. The equations of motion for axial rotation $\phi_3^{(2k/2k-1)}(t)$ of body-($2k$) relative to body-($2k$-1) is written including viscous damping couple as:

$$\hat{J}_{3C}^{(2k)}\ddot{\phi}_3^{(2k/2k-1)}(t) + \mu\dot{\phi}_3^{(2k/2k-1)}(t) = 0, \tag{3.A1}$$

with the initial conditions:

$$\phi_3^{(2k/2k-1)}(0) = \dot{\phi}_3^{(2k/2k-1)}(0) = 0. \tag{3.A2}$$

However, the inertia term in Eq. (3.A1) is negligible since $\hat{J}_{3C}^{(2k)} \ll \hat{J}_{1C}^{(2k)} = \hat{J}_{2C}^{(2k)}$ and the axial rotational acceleration is of order (1). Neglecting the inertial term in Eq. (3.A1), the resulting equation with Eq. (3.A2) yields $\phi_3^{(2k/2k-1)}(t) = 0$.

3.8.2 Appendix 3.B: Time Derivatives of [B^*]-Submatrices

$\left[\dot{B}^*_{TP/TP}(t)\right]$ and $\left[\dot{B}^*_{TP/BP}(t)\right]$ are obtained, respectively, by taking the time derivatives of $\left[B^*_{TP/TP}(t)\right] = \left[B_{TP/TP}(t)\right]$ defined in Eq. (3.29c) and $\left[B^*_{TP/TP}(t)\right] = \left[B_{TP/TP}(t)\right]$ in Eq. (3.29d).

$$\left[\dot{B}^*_{TP/TP}(t)\right] = \begin{bmatrix} R^{(0)}(t)\overleftrightarrow{\omega^{(0)}(t)} & 0_{3\times3} \\ 0_{3\times3} & 0_{3\times3} \\ R^{(0)}(t)\overleftrightarrow{\omega^{(0)}(t)} & -R^{(13)}(t)\overleftrightarrow{\omega^{(13)}(t)}\,\overleftrightarrow{e_3\hat{h}^{(14/13)}} \\ 0_{3\times3} & 0_{3\times3} \end{bmatrix}, \tag{3.A3}$$

$$\left[\dot{B}^*_{TP/BP}(t)\right] = \begin{bmatrix} 0_{3\times3} & -R^{(0)}(t)\left(\overleftrightarrow{\omega^{(0)}(t)}\,\overleftrightarrow{s_C^{(13/0)}(t)} + \overleftrightarrow{\dot{s}_C^{(13/0)}(t)}\right) \\ 0_{3\times3} & -\overleftrightarrow{\omega^{(13/0)}(t)}\left(R^{(13/0)}(t)\right)^T \\ 0_{3\times3} & -R^{(0)}(t)\left\{\begin{array}{l}\overleftrightarrow{\omega^{(0)}(t)}\,\overleftrightarrow{s_C^{(13/0)}(t)} + R^{(13/0)}(t)e_3\hat{h}^{(14/13)} \\ +\overleftrightarrow{\dot{s}_C^{(13/0)}(t)} + R^{(13/0)}(t)\overleftrightarrow{\omega^{(13/0)}(t)}\,\overleftrightarrow{e_3\hat{h}^{(14/13)}}\end{array}\right\} \\ 0_{3\times3} & -\overleftrightarrow{\omega^{(13/0)}(t)}\left(R^{(13/0)}(t)\right)^T \end{bmatrix}. \tag{3.A4}$$

Taking the time derivatives of Eqs. (3.44c) and (3.44d), respectively, one finds

$$\left[\dot{B}^{(k)*}_{L/TP}(t)\right] = \left[\dot{B}^{(k)}_{L/L}(t)\right]\left[T^{(k)}_{L/TP}(t)\right] + \left[B^{(k)}_{L/L}(t)\right]\left[\dot{T}^{(k)}_{L/TP}(t)\right], \tag{3.A5}$$

$$\left[\dot{B}^{(k)*}_{L/BP}(t)\right] = \left[\dot{B}^{(k)}_{L/L}(t)\right]\left[T^{(k)}_{L/BP}(t)\right] + \left[B^{(k)}_{L/L}(t)\right]\left[\dot{T}^{(k)}_{L/BP}(t)\right] + \left[\dot{B}^{(k)}_{L/BP}(t)\right]. \tag{3.A6}$$

In Eqs. (3.A5) and (3.A6) $\left[\dot{B}^{(k)}_{L/L}(t)\right]$ and $\left[\dot{B}^{(k)}_{L/BP}(t)\right]$ are computed from Eqs. (3.31c, d) as:

$$\left[\dot{B}_{L/L}^{(k)}(t)\right]=\begin{bmatrix} \begin{matrix} -R^{(2k-1)}(t)\left\{\overleftarrow{\omega^{(2k-1)}(t)}\,\overleftarrow{\hat{s}_{C/B_k}^{(2k-1)}}\left(R_{2B_k\mathrm{UJ}}(\phi_2^{(k)}(t))\right)^T e_1+\overleftarrow{\hat{s}_{C/B_k}^{(2k-1)}}\,e_3\dot{\phi}_2^{(k)}(t)\right\} \\ e_3\dot{\phi}_2^{(k)}(t) \\ -R^{(2k-1)}(t)\begin{Bmatrix} \overleftarrow{\omega^{(2k-1)}(t)}\,\overleftarrow{e_3\left(\hat{l}_{\mathrm{UJ}}^{(2k-1)}+d^{(k)}(t)\right)}\left(R_{2B_k\mathrm{UJ}}\left(\phi_2^{(k)}(t)\right)\right)^T e_1 \\ +\overleftarrow{e_3\dot{d}^{(k)}(t)}\left(R_{2B_k\mathrm{UJ}}(\phi_2^{(k)}(t))\right)^T e_1+\overleftarrow{e_3\left(\hat{l}_{\mathrm{UJ}}^{(2k-1)}+d^{(k)}(t)\right)}\,e_3\dot{\phi}_2^{(k)}(t) \end{Bmatrix} \\ e_3\dot{\phi}_2^{(k)}(t) \end{matrix} & \begin{matrix} -R^{(2k-1)}(t)\overleftarrow{\omega^{(2k-1)}(t)}\hat{s}_{C/B_k}^{(2k-1)}e_2 & 0_{3\times1} \\ 0_{3\times1} & 0_{3\times1} \\ -R^{(2k-1)}(t)\left\{\overleftarrow{\omega^{(2k-1)}(t)}\,\overleftarrow{e_3\left(\hat{l}_{\mathrm{UJ}}^{(2k-1)}+d^{(k)}(t)\right)}\,e_2+\overleftarrow{e_3\dot{d}^{(k)}(t)}\,e_2\right\} & R^{(2k-1)}(t)\overleftarrow{\omega^{(2k-1)}(t)}\,e_3 \\ 0_{3\times1} & 0_{3\times1} \end{matrix} \end{bmatrix} \tag{3.A7}$$

$$\left[\dot{B}_{L/BP}^{(k)}(t)\right]=\begin{bmatrix} 0_{3\times1} & -R^{(0)}(t)\left\{\begin{matrix}\overleftarrow{\omega^{(0)}(t)}\,\overleftarrow{R^{(2k-1/0)}(t)\hat{s}_{C/B_k}^{(2k-1)}+\hat{s}_{B_k}^{(0)}} \\ +\overleftarrow{R^{(2k-1/0)}(t)\overleftarrow{\omega^{(2k-1/0)}(t)}\hat{s}_{C/B_k}^{(2k-1)}}\end{matrix}\right\} \\ 0_{3\times1} & -\overleftarrow{\omega^{(2k-1/0)}(t)}\left(R^{(2k-1/0)}(t)\right)^T \\ 0_{3\times1} & -R^{(0)}(t)\left\{\begin{matrix}\overleftarrow{\omega^{(0)}(t)}\,\overleftarrow{R^{(2k-1/0)}(t)e_3(\hat{l}_{\mathrm{UJ}}^{(2k-1)}+d^{(k)}(t))+\hat{s}_{B_k}^{(0)}} \\ +\overleftarrow{R^{(2k-1/0)}(t)\left(\overleftarrow{\omega^{(2k-1/0)}(t)}e_3\left(\hat{l}_{\mathrm{UJ}}^{(2k-1)}+d^{(k)}(t)\right)+e_3\dot{d}^{(k)}(t)\right)}\end{matrix}\right\} \\ 0_{3\times1} & -\overleftarrow{\omega^{(2k-1/0)}(t)}\left(R^{(2k-1/0)}(t)\right)^T \end{bmatrix}. \tag{3.A8}$$

In Eqs. (3.A5) and (3.A6) $\left[\dot{T}_{L/TP}^{(k)}(t)\right]$ is computed from Eq. (3.39b).

$$\begin{aligned}\left[\dot{T}_{L/TP}^{(k)}(t)\right]=&-\left(\frac{d}{dt}\left[A_L^{(k)}(t)\right]^{-1}\right)\left(R^{(2k-1/0)}(t)\right)^T\left[I_3 \quad -R^{(13/0)}(t)\overleftarrow{\hat{s}_{T_k}^{(13)}}\right] \\ &+\left[A_L^{(k)}(t)\right]^{-1}\left\{\overleftarrow{\omega^{(2k-1/0)}(t)}\left(R^{(2k-1/0)}(t)\right)^T\left[I_3 \quad -R^{(13/0)}(t)\overleftarrow{\hat{s}_{T_k}^{(13)}}\right]\right. \\ &\left.-\left(R^{(2k-1/0)}(t)\right)^T\left[0_{3\times3} \quad -R^{(13/0)}(t)\overleftarrow{\omega^{(13/0)}(t)}\,\overleftarrow{\hat{s}_{T_k}^{(13)}}\right]\right\},\end{aligned} \tag{3.A9}$$

where

$$\frac{d}{dt}\left[A_L^{(k)}(t)\right]^{-1}=\begin{bmatrix} 0 & \frac{-\dot{d}^{(k)}(t)\cos\phi_2^{(k)}(t)+l^{(k)}(t)\dot{\phi}_2^{(k)}(t)\sin\phi_2^{(k)}(t)}{\left(l^{(k)}(t)\cos\phi_2^{(k)}(t)\right)^2} & 0 \\ \frac{\dot{d}^{(k)}(t)}{(l^{(k)}(t))^2} & 0 & 0 \\ 0 & 0 & 0 \end{bmatrix}. \tag{3.A10}$$

In Eq. (A6) $\left[\dot{T}_{L/BP}^{(k)}(t)\right]$ is computed from Eq. (3.41b) as:

$$\begin{aligned}\left[\dot{T}_{L/BP}^{(k)}(t)\right]=&\left(\frac{d}{dt}\left[A_L^{(k)}(t)\right]^{-1}\right)\left(R^{(2k-1/0)}(t)\right)^T\overleftarrow{\Delta s_{CL}^{(k)}(t)}[0_{3\times3} \quad I_3] \\ &+\left[A_L^{(k)}(t)\right]^{-1}\left\{-\overleftarrow{\omega^{(2k-1/0)}(t)}\left(R^{(2k-1/0)}(t)\right)^T\overleftarrow{\Delta s_{CL}^{(k)}(t)}+\left(R^{(2k-1/0)}(t)\right)^T\overleftarrow{\dot{\Delta s}_{CL}^{(k)}(t)}\right\}[0_{3\times3} \quad I_3],\end{aligned} \tag{3.A11}$$

where from Eq. (3.35c)

$$\dot{\Delta s}_{CL}^{(k)}(t) = \dot{s}_C^{(13/0)}(t) + R^{(13/0)}(t)\overleftrightarrow{\omega^{(13/0)}}(t)\hat{s}_{T_k}^{(13)} - R^{(2k-1/0)}(t)\left(\omega^{(2k-1/0)}(t)e_3 l^{(k)}(t) + e_3\dot{d}^{(k)}(t)\right). \quad \text{(3.A12)}$$

CHAPTER 4: FORECASTING OF FUTURE BASE MOTION AND MODEL PREDICTIVE CONTROL

4.1 Introduction

For control of the base-moving Stewart platform, the following three features need to be considered.

The first one is constraints, which include kinematic constraints, joint constraints, and input/output constraints. Under these constraints, a controller is required to maximize the performance of the system and actuators for fast tracking.

The second one is the inertia and nonlinear terms acting on the system. Since one of the advantages of a Stewart platform is its capability of precise positioning of the loaded top table, inverse dynamic computation should be considered for feedforward element.

The third feature is that there exists a time delay due to the process of the signal measurement of the motion of the base plate, computation of the desired signal to each actuator, and tracking of desired top plate states. This is because the desired states of the top plate and each actuator are determined from the measured states of the base plate at each time step. To enhance control performance, the future motion of the base plate must be forecasted in some way. Here, for the time series data of the base-plate motion, LSTM is applied as a tool for forecasting its future value within a certain section.

In this chapter, first, forecasting using LSTM is described comparing with ARIMA model [46]. Then considering the above three features, as a control method combined with the forecasting of the base motion, MPC is adopted and designed. Finally, numerical simulations and scale model experiments show that the efficacy of the proposed method.

4.2 Time Series Forecasting of Future Base Motion

For control of the base-moving Stewart platform, in order to cancel out the time delay due to measurement and computation time, the future motions of the base plate caused by a ship or vehicle has to be forecasted in some way.

In recent years, a deep learning method using a recurrent neural network (RNN) has been applied as a time series forecasting approach to predict future values from past data [47-49]. The approach is especially effective for time series predictions involving

non-steady process data, as compared to prediction methods such as a conventional autoregressive (AR) model or an autoregressive integrated moving average (ARIMA) model. However, simple RNN architecture generally has a vanishing/exploding gradient problem in the error backpropagation algorithm when a long time series is used for training. Once the gradient disappears and an optimum solution cannot be found, the learning process stops. To deal with this problem, Long Short Term Memory (LSTM), a deep learning method that extends the RNN structure, has been developed [32]. LSTM is capable of learning long time series data and maintains long-term dependence to avoid gradient disappearance or explosion.

In this section, as an example of the use of LSTM, future vehicle accelerations are forecasted at sampling points in real time. The remainder of the section proceeds as follows: First, the RNN and LSTM architectures used here are briefly illustrated. Next, the training strategy for the time series forecasting of vehicle accelerations in each time step is discussed. The training of the LSTM using training data for the longitudinal and lateral directions is then described. Suitable hyperparameters—the number of hidden layers, hidden units, epochs, and the learning rate—are chosen by varying the parameter values. Real-time forecasting simulations are performed to evaluate the effectiveness of the LSTM trained from the measured acceleration data. Finally, the forecasting accuracy of the method is assessed by comparing forecast results with the results of a conventional ARIMA model.

4.2.1 Long Short Term Memory

4.2.1.1 Recurrent neural network

An LSTM model extends the unit of the RNN structure. Figure 4.1(a) shows a simple RNN divided into an input layer, hidden layers, and an output layer. Here, $x(t)$ is the observed value at discrete time t, $y(t)$ is the output, and $h(t)$ is the state of the hidden unit. A recurrent type of neural network can improve accuracy by using the output of the hidden state from the previous period, as shown in Fig. 4.1(b) [50]. Such a network is regarded as a suitable model for processing and predicting time series data. In neural network learning, an error backpropagation method is used in which the weights of each unit are updated so that the defined loss function based on the error between the output value and training data is minimized. To take into account the passage of time, backpropagation through time algorithm is commonly used as a way to expand the network of the RNN in the time direction via the hidden layer output [51].

This makes it possible to apply the error backpropagation method by considering the RNN as a neural network that includes the passage of time. Notably, however, when learning long time series data, an RNN has difficulty due to gradient disappearance, whereby information cannot be transmitted, or gradient explosion, whereby the number of calculations increases massively.

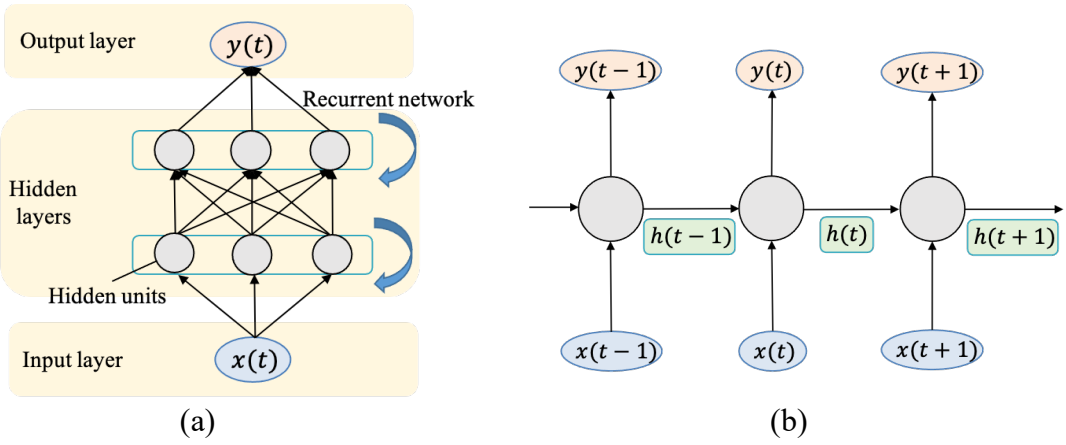

Figure 4.1: (a) RNN structure and (b) representation of RNN for a hidden unit over time

4.2.1.2 LSTM architecture

The LSTM model has been developed to overcome the limitations of RNN noted above. LSTM has a structure that introduces a memory cell controlled by three types of gates into the RNN structure. This makes it possible to learn long time series data and secure long-term dependence. The propagation equations of LSTM are as follows:

$$i(t) = \sigma_s(W_i x(t) + R_i h(t-1) + b_i) \tag{4.1a}$$

$$f(t) = \sigma_s\left(W_f x(t) + R_f h(t-1) + b_f\right) \tag{4.1b}$$

$$o(t) = \sigma_s(W_o x(t) + R_o h(t-1) + b_o) \tag{4.1c}$$

$$c_c(t) = \sigma_h(W_{cc} x(t) + R_{cc} h(t-1) + b_{cc}) \tag{4.1d}$$

$$c(t) = f(t) \odot c(t-1) + \; i(t) \odot c_c(t) \tag{4.1e}$$

$$h(t) = o(t) \odot \sigma_h\left(c(t)\right) \tag{4.1f}$$

$$y(t) = W_y h(t) \tag{4.1g}$$

where $i(t)$, $f(t)$, $o(t)$, $c_c(t)$, and $c(t)$ represent the input gate, the forget gate, the output gate, the memory cell candidate, and the memory cell state, respectively [52]; additionally, $\odot$ indicates the product of the designated terms. The memory cell $c(t)$ acts

in the role of long-term memory, while the hidden state $h(t)$ plays the role of short-term memory. W_i, W_f, W_o, and W_{cc} denote, respectively, the input weights for each gate and the cell candidate. In the same manner, R_i, R_f, R_o, and R_{cc} are the recurrent weights for each gate and cell candidate, and b_i, b_f, b_o, and b_{cc} are the bias weights. W_y shows the output weight, and σ represents the activation function. In this study, the sigmoid function σ_s is used for each gate, and the hyperbolic tangent function σ_h is used for the cell candidate and the hidden state which give the output state. This is because output accelerations have both plus and minus values (accelerations and decelerations). The LSTM block is illustrated in Fig. 4.2

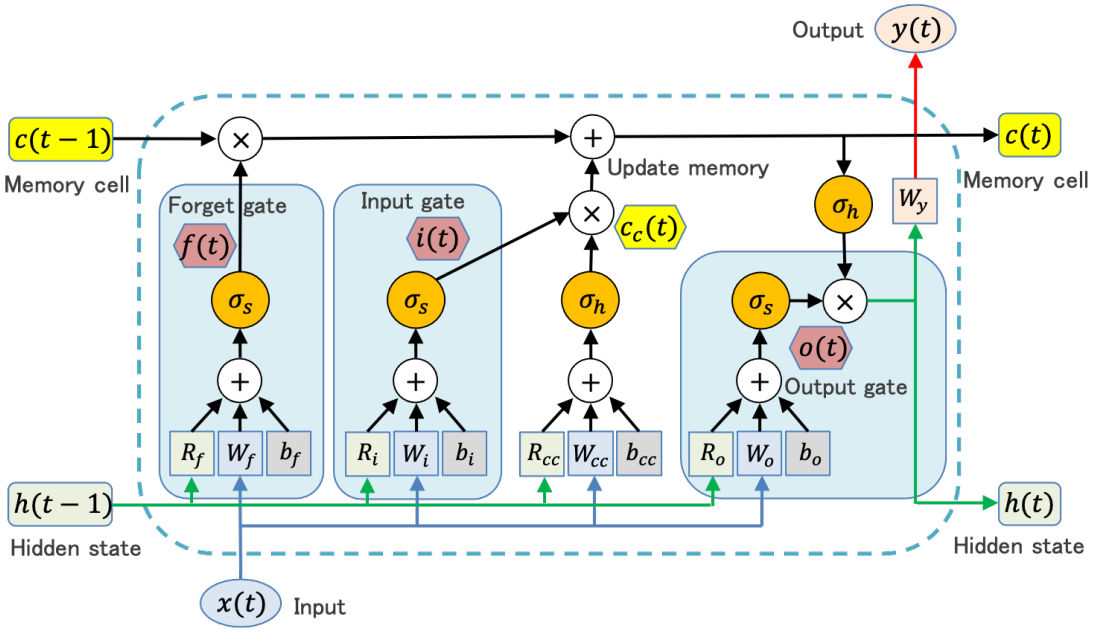

Figure 4.2: LSTM Block

4.2.1.3 Application of LSTM for real-time forecast

Figure 4.3 is a conceptual diagram showing how forecasts of the acceleration i steps ahead are produced from the measured acceleration data at each sampling point. In order to forecast future accelerations, the LSTM is trained with the output as the observed value in the next step, i.e., $x(t+1) = y(t)$. This makes it possible to sequentially forecast multiple steps ahead by using the forecasted data one step ahead as the input data for the next step. Then, to forecast the ith-step ahead data from the measured data at each sampling point, a series of LSTM blocks, from $x\ (t)$ to $x\ (t+i)$, are combined into the LSTM sequence, enabling us to forecast the ith-step ahead output state while updating the hidden state.

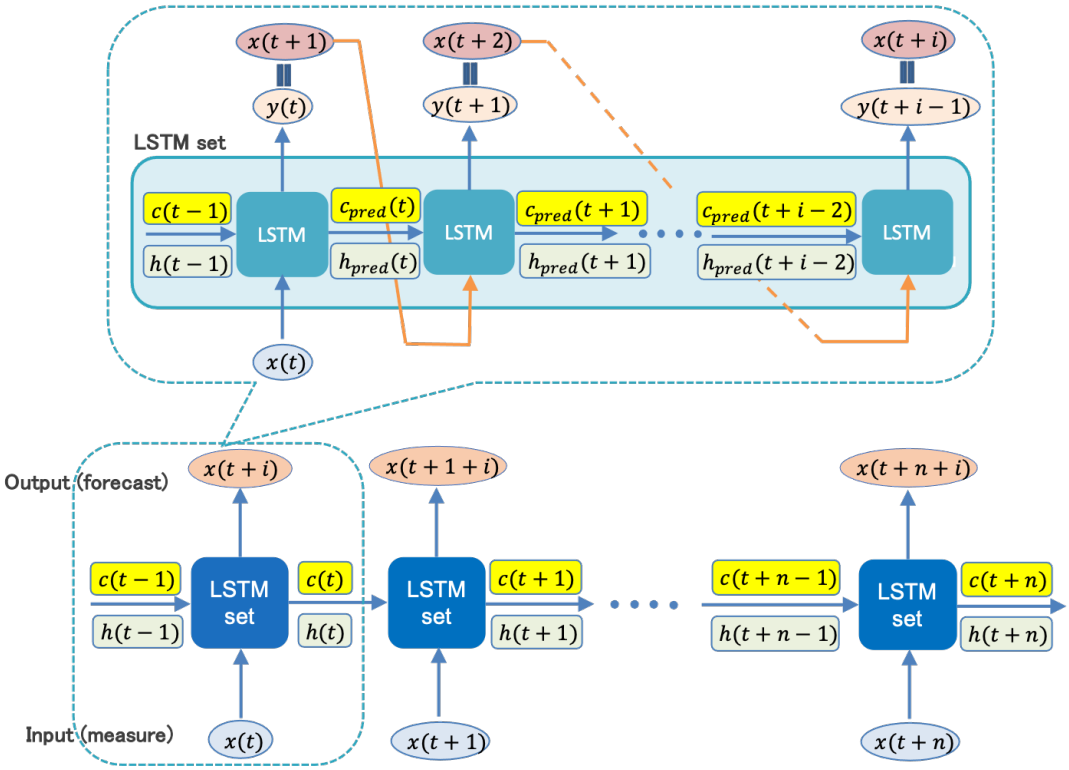

Figure 4.3: Forecasting of the *i*th-step ahead using LSTM

4.2.2 LSTM Training

Before performing real-time forecast, the LSTM block was first trained using the training data collected in advance. The accelerations were measured by an accelerometer attached to a representative vehicle. Different types of driving data were used for training. The actual measurement data were obtained by installing an acceleration sensor inside the vehicle; the data were smoothed by low-pass filtering to remove noise. Figure 4.4 shows the longitudinal and lateral accelerations for the training data and the validation data. The training data were used for the LSTM training; the validation data were used to check the LSTM during the training. Data group 1 and data group 3 of the training data include basic vehicle driving states: startup, straight driving, making a left turn, making a right turn, and stopping. In data group 2, in addition to the basic driving states, longitudinal accelerations when the vehicle stops suddenly are included. Data group 4 includes lateral acceleration when the vehicle quickly changes lanes. The maximum amplitudes of data group 2 and data group 4 are thus larger than those of data group 1 and data group 3.

For training, acceleration data were collected every 0.04 s, at which time the acceleration five steps ahead (i.e., 0.2 s ahead) was forecast. As the initial weighting parameters, the Glorot initializer [53] was used for the input weight and the recursive weight. The initial forget-gate bias b_f and the output weight W_y were each set to 1; the other initial bias weights, the memory cell and the hidden states, were set to 0. To assess forecast accuracy, the LSTM was trained using different numbers of hidden layers (1 and 2), hidden units per layer (100 and 200), and epochs (training set iterations) (200, 400, 600, and 800). MATLAB software was used for training and forecasting.

Figure 4.5 shows the training loss during the training process for various learning rates, with 1 layer, 100 units, and 600 epochs. The loss indicates the difference between the value predicted by the neural network and the correct value. In this study, the half-mean-squared-error of the predicted responses was used as the loss function. During training, the weighting parameters were tuned to minimize the loss so that the likelihood of the output of the network is maximized. The Adam (adaptive momentum estimation) algorithm [54], which combines the advantages of AdaGrad [55] and RMSProp [56], was used as the deep learning optimization algorithm. A learning rate of 10^{-3} was selected for subsequent applications in the current study, since, as shown in Fig. 4.5, the loss converges to 0 with stability. Figure 4.6 shows the training loss and validation loss when the learning rate is 10^{-3}. As shown in the figure, the losses for both the training and validation data decrease and converge as the number of epochs increases, indicating that the training was successful.

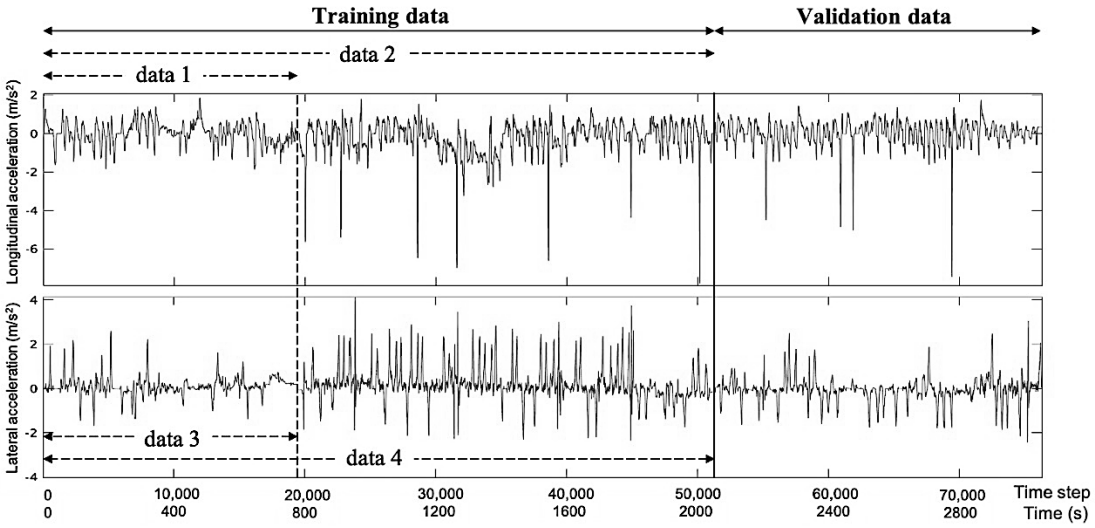

Figure 4.4: Training and validation data

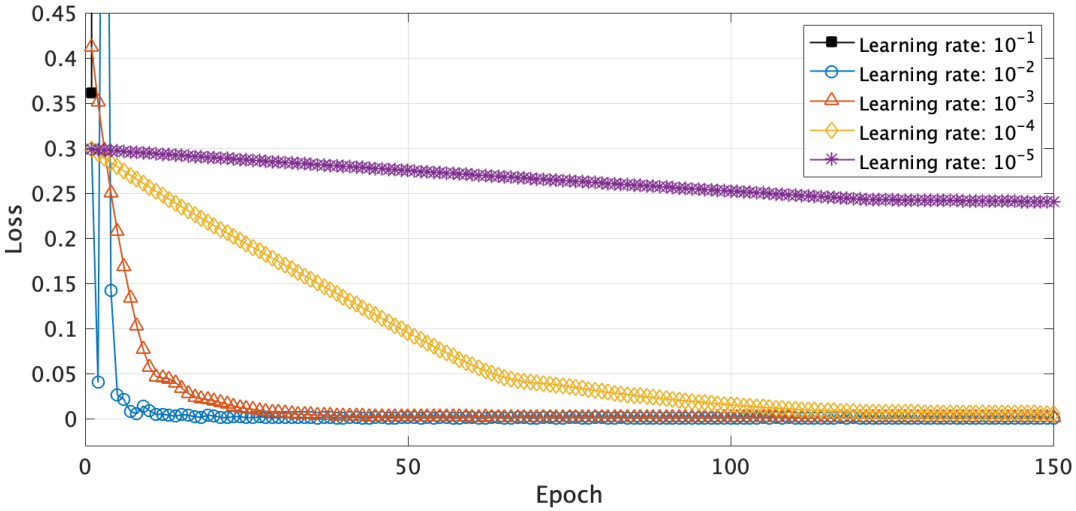

Figure 4.5: Comparison of training loss for different learning rates

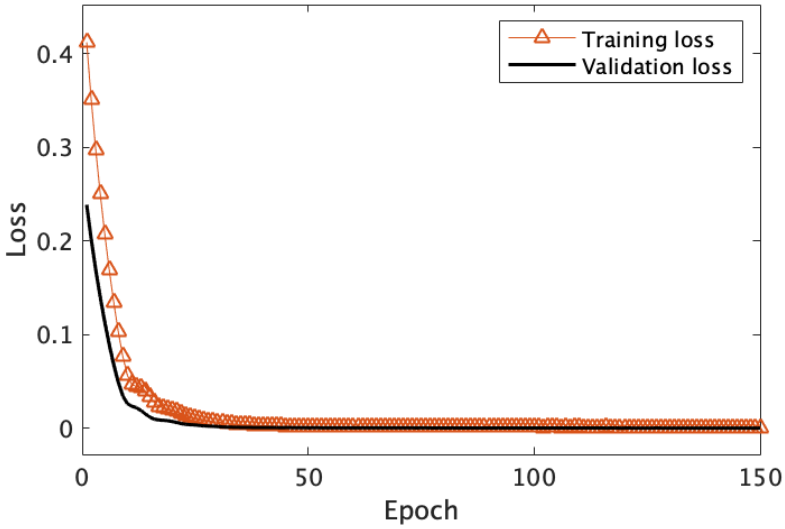

Figure 4.6: Training loss and validation loss

4.2.3 Real-Time Forecast

4.2.3.1 Forecasting results for different parameters

The trained LSTM was used to produce real-time forecasts of accelerations in both the longitudinal and lateral directions while updating the LSTM from the observed values at each time step. A time step of 0.04 s was selected in consideration of the computation time for the LSTM forecasting.

Figure 4.7(a) shows the root mean square error (RMSE) for the forecasted accelerations in the longitudinal direction for various combinations of hidden layers, units and epochs using training data 2. Fig. 4.7(b) shows the fitting rate. To find suitable hyperparameters, the number of epochs was set at 200, 400, 600, and 800. In addition, for each epoch pattern, four combinations of hidden layers and hidden units were considered (as shown in the figure legend). Given that the RMSE was 0.1813 for a delay of 0.2 s without forecasting, LSTM forecasting reduced the error in all cases. According to the results for Case 1, forecasting accuracy improved with an increase in the number of epochs, up to 600; however, increasing the number of epochs to 800 resulted in an increase in the RMSE and a decrease in the fitting rate, as the number of epochs became too large for the number of units, which caused overfitting. In Cases 2 and 3, the same type of pattern appears; however, the error begins to increase at a smaller number of epochs (i.e., after 400 epochs rather than after 600 epochs). This is likely because, in Case 2, the number of units becomes too large for the number of layers, while, in Case 3, the number of layers becomes too large for the number of units. Among the four cases shown in Fig. 4.7, Case 4 (with 800 epochs, two layers, and 200 units) showed the highest accuracy.

Figure 4.8 shows the RMSE and fitting rate when the forecasting horizon changes. It can be seen that forecasting accuracy decreases almost linearly as the forecasting horizon (i.e., the number of time steps ahead) increases.

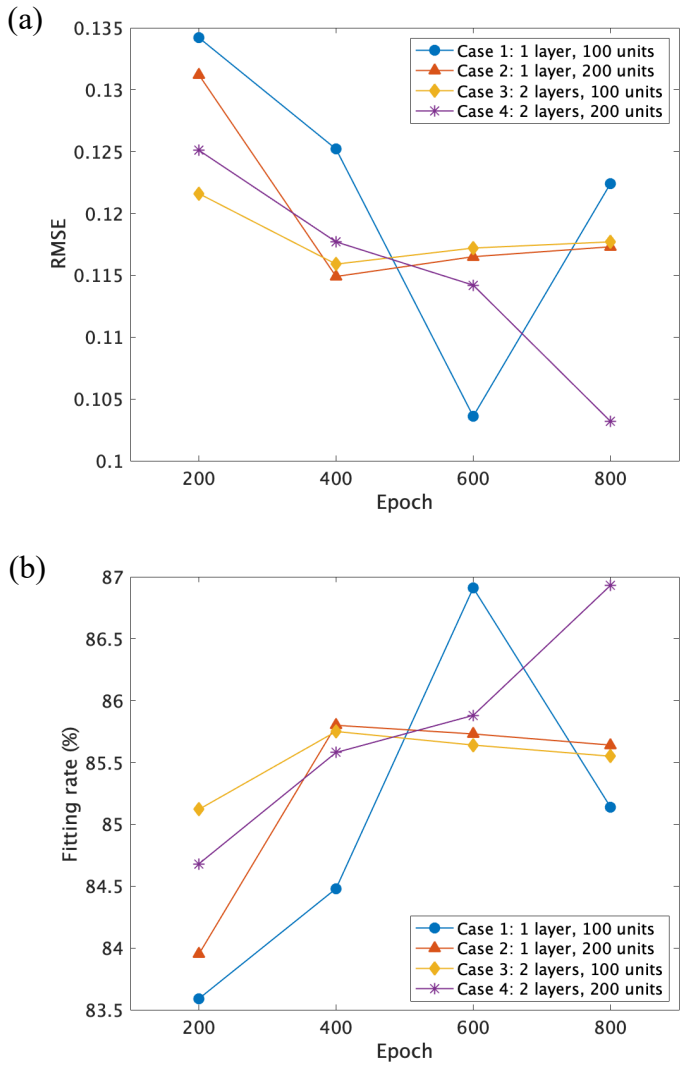

Figure 4.7: (a) RMSE and (b) fitting rate for different combinations of hidden layers, units, and epochs

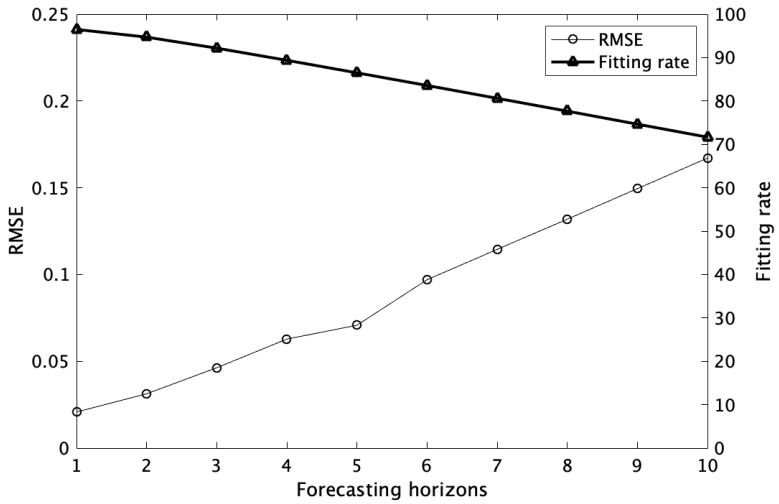

Figure 4.8: RMSE and fitting rate for different forecasting horizons

In this study, no experiment was conducted for the application of tilting a bed in an ambulance, but in order to improve the control performance during active control, the real-time forecasting of future vehicle acceleration was performed. Then, it was shown that the prediction can be made with an accuracy of 70% to 95% up to 10 steps ahead. The forecasting accuracy and horizon to be achieved are different depending on the equipment used. If higher forecasting accuracy is required, it is necessary to shorten the calculation time by using suitable algorithms and software. In addition, to adapt to all driving conditions, it is necessary to collect and learn as much driving data as possible on different road surfaces.

4.2.3.2 Forecasting comparison of the LSTM and ARIMA models

In time series analysis, the ARIMA model, a conventional time series forecasting model, serves as a tool for forecasting future values within a particular period of time. The ARIMA model consists of a p-order AR model, d-order deference, and a q-order MA model. If we let $x(t)$ be the acceleration signal at discrete time t, the ARIMA model is

$$x(t) - x(t-d) = \sum_{i=1}^{p} \alpha(i)x(t-i) + \sum_{j=1}^{q} \beta(j)W(t-j) + W(t) \tag{4.2}$$

where $\alpha(i)$ and $\beta(j)$ are the coefficients of autoregression and moving average, respectively. In the equation given here, p and q denote the order of each model, which can be selected by using Akaike's Information Criterion [57]. $W(t)$ represents Gaussian white noise. Once the model parameters are estimated, the ARIMA model is used repeatedly to produce forecasts for any future time.

Figures 4.9(a) and 4.9(b) show a portion of the actual measured values and the real-time forecast output from the LSTM model trained with the Case 4 settings (using 800 epochs) and from the ARIMA model. The parameters of the ARIMA model in Eq. (8) were set as p = 4, d = 1, q = 2, so that the prediction errors were minimized. The average computation time for the LSTM and ARIMA models was 0.0306 s and 0.0375 s, respectively. The results indicate that the future accelerations were successfully forecasted in each time step. Since the acceleration measurement data used here were for a vehicle in a moderate driving state, acceleration does not change rapidly in either the longitudinal or lateral direction, and the process is weakly non-stationary. From

Figs. 4.9(a) and 4.9(b), it can be seen that both the LSTM and ARIMA models forecasted the future acceleration values with some degree of accuracy; however, the prediction error of the ARIMA model was slightly larger when there was noise and at inflection points.

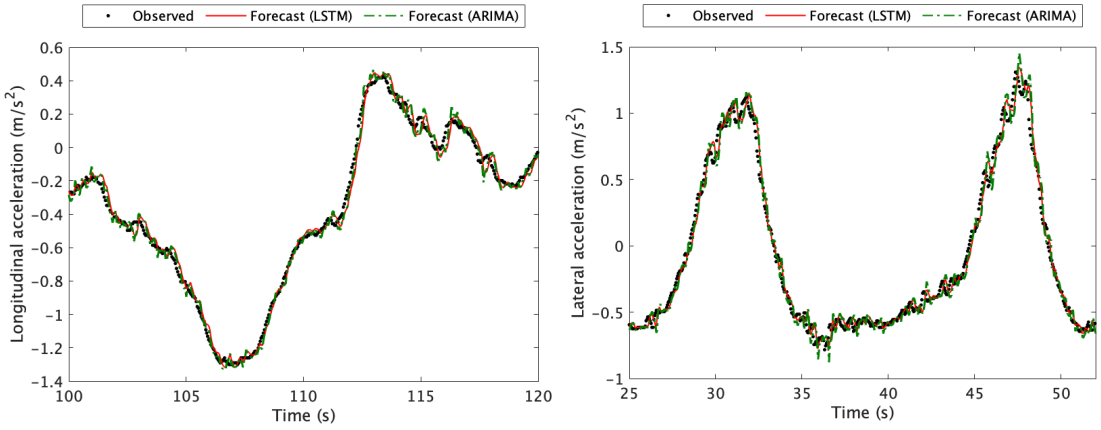

(a) (b)

Figure 4.9: Real-time forecasted accelerations in (a) the longitudinal direction and (b) the lateral direction

The forecasted longitudinal acceleration when the vehicle suddenly stops and the forecasted lateral acceleration when the vehicle rapidly changes lanes were also analyzed. Results for the Case 4 hyperparameter set with 800 epochs are described below.

Figure 4.10(a) shows the results for when the LSTM model trained with data 1, which does not include sudden stops, is used to forecast longitudinal accelerations. Figure 4.10(b) shows the results when data 2, which includes sudden stop data, is used as the training data. As can be observed here, by adding the sudden stop information, future accelerations are more accurately forecasted when the acceleration changes significantly. Figure 4.10(c) shows the results using the ARIMA statistical model. A comparison with the results of the LSTM model in Fig. 4.10(b) indicates that the ARIMA model produces a larger error due to large changes in acceleration and non-stationarity, whereas the LSTM model produces forecasts with a smaller error.

Figure 4.11(a) shows the results when the LSTM model trained with data 3, which does not include rapid lane change data, is used to forecast lateral accelerations. Figure 4.11(b) shows the results when the LSTM model is trained with data 4, which

includes lateral accelerations due to rapid lane change. It is apparent that prediction accuracy is improved by adding rapid lane change information. From Fig. 4.11(b) and 4.11(c), it can be seen that the LSTM model is able to produce more precise forecasts than the ARIMA model for large rates of change in acceleration.

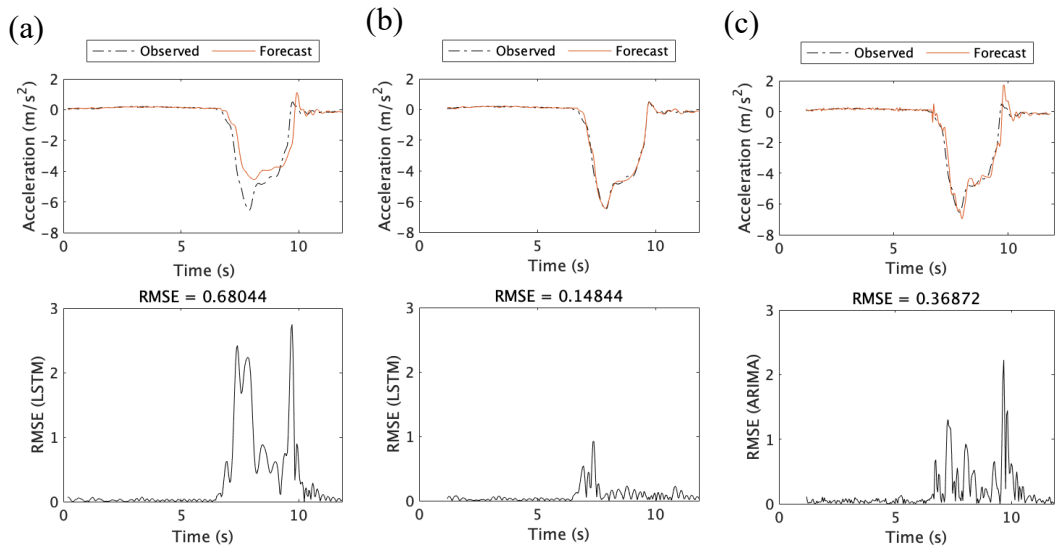

Figure 4.10: Comparison of 5 steps (0.2 s) ahead forecasted longitudinal response (sudden stop) by LSTM trained with (a) data 1 and (b) data 2, and (c) ARIMA model

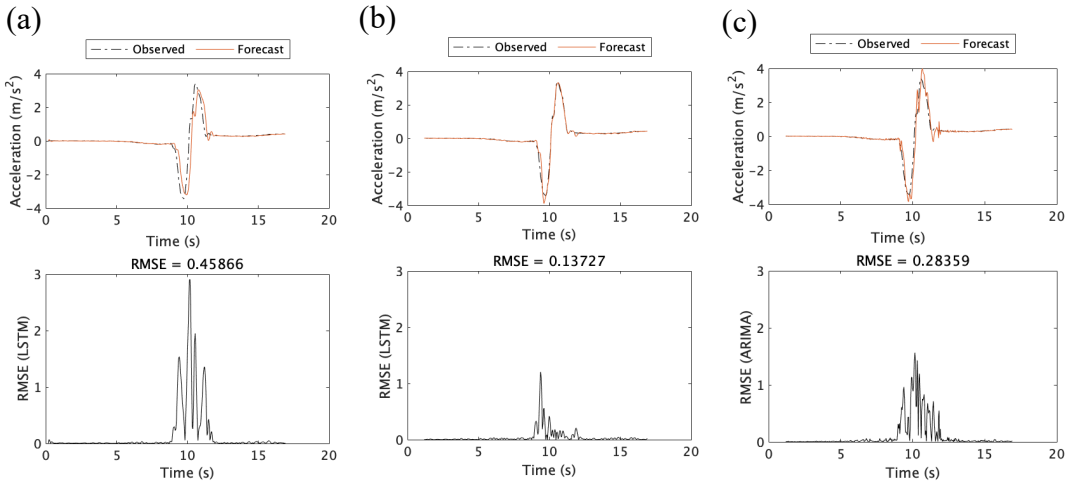

Figure 4.11: Comparison of 5 steps (0.2 s) ahead forecasted lateral response (rapid lane change) by LSTM trained with (a) data 3 and (b) data 4, and (c) ARIMA model

4.3 Model Predictive Controller Design

For the constrained system, model predictive control (MPC) is one of the effective control schemes. MPC is a control method that performs optimization and feedback control while predicting future responses at each time and calculating optimization problems online [58]. It is expected that higher performance control will be realized for complex systems, and it is receiving a great deal of attention in a wide range of industrial applications. MPC is also called real-time optimal control or receding Horizon control. One of the advantages of this method is the ease of design considering the constraint conditions for the behavior and control input. The use of the MPC allows us to handle this multi-input multi-output system while explicitly incorporating the constraints of each joint and actuator, which bound the workspace. Especially, an explicit incorporation of the constraints on the closed-loop mechanism of the Stewart platform is important for an accurate predictive model. It is noted that for a base-fixed Stewart platform model, some researchers applied linear MPC [24,25]. However, because of the nonlinearity and time-varying properties of the system, a challenge of the controller design is how to achieve accurate and fast speed tracking over the operating range. Therefore, in this study, the MPC scheme is adopted for nonlinear system.

The derived nonlinear system of the predictive model, Eq. (3.50a) can be expressed as the following nonlinear state equation:

$$\dot{q}(t) = f(q(t),\ u(t),\ p(t)) \tag{4.3}$$

where $q(t)$ denotes the state vector defined as $q(t) = (q_{TP}^{*}(t) \quad \dot{q}_{TP}^{*}(t))^{T}$ and $u(t)$ represents input actuation forces or signals, and $p(t)$ is the time-dependent parameters including the motion of the base plate and each leg. The control input $u(t)$ acting on the legs is determined by solving the following constrained optimization problem at each time *t* over the prediction horizon ($t \le \tau \le t + T$).

$$\min_{u(\tau|t)} J = \varphi\big(q(t+T|t)\big) + \int_{t}^{t+T} L\big(q(\tau|t), u(\tau|t)\big)d\tau \tag{4.4a}$$

subject to the constraints

$$\frac{\partial q}{\partial \tau} = f(q(\tau|t), u(\tau|t), p(\tau|t)) \tag{4.4b}$$

$$C_1\big(q(\tau|t)\big) \le 0 \tag{4.4c}$$

$$C_2\big(u(\tau|t)\big) \le 0 \tag{4.4d}$$

$$q(t|t) = q(t) \tag{4.4e}$$

where the function to be optimized is the control input $u(\tau|t)$. The predicted variable of the state starting from $q(t)$ at time t is represented by $q(\tau|t)$ along a fictitious time τ. Eqs. (4.4c) and (4.4d) are the constraints of joints and input, and Eq. (4.4e) expresses the initial condition of the optimal control problem. Let $q_e(t) = q_{ref}(t) - q(t)$ be errors of the state from the reference $q_{ref}(t)$, the cost function J consists of two terms defined by a quadratic form as:

$$\varphi\big(q(t+T|t)\big) \equiv W_1\|q_e(t+T|t)\|^2 \tag{4.4f}$$

$$L\big(q(\tau|t), u(\tau|t)\big) \equiv W_2\|q_e(\tau|t)\|^2 + W_3\|u(\tau|t)\|^2 \tag{4.4g}$$

where $\varphi\big(q(t+T|t)\big)$ and $L\big(q(\tau|t), u(\tau|t)\big)$ consist of the terminal cost and the energy of state errors and control input, respectively. Then, Eq. (4.4a) can be regarded as a problem that minimizes the energy of the system. W_1, W_2, and W_3 define weight matrices for each term. The response of the system is adjusted by changing the following control parameters: values of the weighting matrix of each term and the length of the prediction horizon. If relatively larger W_1 and W_2 are chosen, the evaluation of the tracking error becomes dominant, then a fast-tracking response can be realized. On the other hand, if relatively larger W_3 is chosen, the effect of suppressing changes in the actuation input will become stronger, and it is expected that tracking performance will become slower.

The above continuous time formulation of the optimization problem can be discretized as follows:

$$\min_{\{u(k+\varepsilon|k)\}_{\varepsilon=0}^{n}} J = W_1\|q_e(k+n|k)\|^2 + \sum_{\varepsilon=0}^{n-1}(W_2\|q_e(k+\varepsilon|k)\|^2 + W_3\|u(k+\varepsilon|k)\|^2)\Delta\tau \tag{4.5a}$$

subject to

$$q(k+\varepsilon+1|k) = q\,(k+\varepsilon|k) + f\big(q\,(k+\varepsilon|k), u\,(k+\varepsilon|k), p\,(k+\varepsilon|k)\big)\Delta\tau \tag{4.5b}$$

$$C_1\big(q(k+\varepsilon|k)\big) \le 0 \tag{4.5c}$$

$$C_2\big(u(k+\varepsilon|k)\big) \le 0 \tag{4.5d}$$

$$q(k|k) = q(k) \tag{4.5e}$$

where $(k+\varepsilon|k)$ denote the prediction obtained by iterating Eq. (4.5a) ε times from the current discrete time k. n indicates the prediction horizon (number of prediction step and future input variables to be optimized). $\Delta\tau = T/n$ defines the time step. At each discrete time k, the optimization problem associated with m steps ahead of control inputs is solved, and the first input of the obtained optimum input sequences is applied until the next time $k+1$.

To obtain necessary conditions for the above nonlinear optimization problem with inequality constraints, the Karush-Kuhn-Tucker (KKT) condition can be used [59]. Suppose u^* is a locally optimal solution and let q^* be the corresponding state, then there exists a vector of Lagrange multipliers λ, $\mu_1 \geq 0$, and $\mu_2 \geq 0$ such that

$$\nabla J(q^*, u^*) + \lambda^T \nabla f(q^*, u^*, p) + \mu_1^T \nabla C_1(q^*) + \mu_2^T \nabla C_2(u^*) = 0 \tag{4.6a}$$

$$\mu_1^T C_1(q^*) = \mu_2^T C_2(u^*) = 0 \tag{4.6b}$$

Since $\mu_1 \geq 0$, $\mu_2 \geq 0$ and $C_1(q^*) \leq 0$, $C_2(u^*) \leq 0$, Eq. (4.6b) is equivalent to that μ_1 and μ_2 may be nonzero only if the constraints are achieved. This can be observed as a complementary slackness condition: $C_1(q^*) < 0$ and $C_2(u^*) < 0$ imply $\mu_1 = \mu_2 = 0$, and $\mu_1 < 0$ and $\mu_2 < 0$ imply $C_1(q^*) = C_2(u^*) = 0$. Then there exists an adjoint variable such that

$$\frac{\partial H}{\partial u}(k+\varepsilon|k, q^*(k+\varepsilon|k), u^*(k+\varepsilon|k), \lambda(k+\varepsilon+1|k), p(k+\varepsilon|k)) = 0$$
$$\varepsilon = 0,1,\dots,n-1 \tag{4.7a}$$

where H denotes the Hamiltonian function,

$$H(k+\varepsilon|k, q, u, \lambda, p) = L(k+\varepsilon|k, q, u, p) + \lambda^T f(k+\varepsilon|k, q, u, p) \tag{4.7b}$$

By defining a vector of input and multipliers as

$$\begin{aligned} U(k+\varepsilon|k) \equiv [&u((k|k)), \mu_1((k|k)), \mu_2((k|k)), \dots \\ &, u(k+n-1|k), \mu_1(k+n-1|k), \mu_1(k+n-1|k)]^T \end{aligned} \tag{4.8}$$

then Eqs. (4.4b), (4.5a), and (4.6) can be regarded as one matrix as

$$F(U(k+\varepsilon|k), q(k+\varepsilon|k), k+\varepsilon|k) \equiv \begin{bmatrix} \frac{\partial H^T}{\partial u}\left(k|k, q(k|k), u(k|k), \lambda(k+1|k), p(k|k)\right) \\ C_1\left(q(k|k)\right) \\ C_2\left(u(k|k)\right) \\ \vdots \\ \frac{\partial H^T}{\partial u}\left(k+n-1|k, q(k+n-1|k), u(k+n-1|k),\right. \\ \left.\lambda(k+n|k), p(k+n-1|k)\right) \\ C_1\left(q(k+n-1|k)\right) \\ C_2\left(u(k+n-1|k)\right) \end{bmatrix} = 0 \tag{4.9}$$

To solve the above matrix equation, the C/GMRES method is adopted [33]. Applying the continuation method to this equation and tracking the time change of the control input, the condition can be written as

$$F(U(k|k), q(k|k), k|k) = 0 \tag{4.10a}$$

$$\dot{F}(U(k+\varepsilon|k), q(k+\varepsilon|k), k+\varepsilon|k) = -\zeta F(U(k+\varepsilon|k), q(k+\varepsilon|k), k+\varepsilon|k) \tag{4.10b}$$

where $\zeta > 0$. U is a vector containing the Lagrange multipliers for the discretized inputs and constraints on the evaluation interval. Eq. (4.10b) can be written in the form of simultaneous equations of $\dot{U}$ if $\partial F/\partial U$ is nonsingular,

$$\dot{U} = \left(\frac{\partial F}{\partial U}\right)^{-1}\left(-\zeta F - \frac{\partial F}{\partial q}\dot{q} - \frac{\partial F}{\partial k}\right). \tag{4.10c}$$

When $\partial F/\partial U$ does not become nonsingular, a barrier function can be adopted by adding constraint conditions to the evaluation function. Then the term inside sigma in Eq. (4.5c) can be defined as

$$L(k+\varepsilon|k, q, u, p) \equiv (W_2\|q_e(k+\varepsilon|k)\|^2 + W_3\|u(k+\varepsilon|k)\|^2)\Delta\tau - \sum_{i=1}^{m}\alpha\log(-C_i(q,u)) \tag{4.11}$$

for α >0. If U is calculated by numerically integrating $\dot{U}$, the iterative solution is not necessary. The simultaneous equations of $\dot{U}$ can be solved efficiently by the GMRES. This allows the optimum control input to be updated without iterative calculations.

Observing that any prediction includes some errors, which could deteriorate the control performance, we add robustness to the controller [60]. The forecasting errors of the motion of the base plate $q_{Bfe}(k)$ can be rewritten as:

$$q_{Bfe}(k) = q_{Bm}(k) - q_{Bf}(k|k-n) \tag{4.12}$$

where $q_{Bm}(k)$ and $q_{Bf}(k|k-n)$ represents actual measured motion at k and forecasted motion of the base plate at $k-n$, respectively. Here, each component of the forecasting errors of the base plate is bounded as $\left|q_{iBfe}(k)\right| \leq \hat{q}_{iBfe}$. The prediction errors of the state can be expressed by the function of $q_{Bfe}(k)$,

$$q(k+\varepsilon) - q(k+\varepsilon|k) = h(q_{Bfe}(k+\varepsilon-1)) \tag{4.13}$$

Then each component of the prediction errors of the states is bounded as

$$|q_i(k+\varepsilon) - q_i(k+\varepsilon|k)| \leq h_i(\hat{q}_{iBfe}) \tag{4.14}$$

By modifying the constraint in Eq. (4.5c), stricter constraint condition will be applied as:

$$C_1\left(q_i(k+\varepsilon|k) + h_i(\hat{q}_{iBfe})\right) \leq 0 \tag{4.15}$$

If there exists a solution of the optimization problem at each time, the original constraints of Eq. (4.5c) are satisfied.

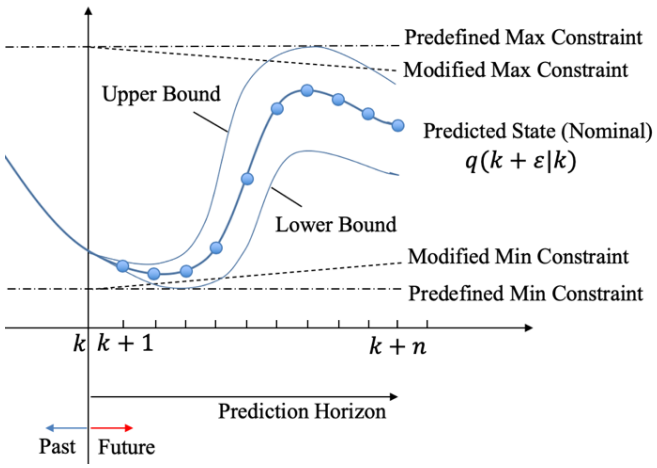

Figure 4.12: Prediction with modified constraint

Figure 4.12 illustrates refined constraints in the prediction horizon. By implicitly imposing a severe constraint plotted as the broken line on the set of predicted state, the control input which satisfies the constraint given by the one-dot chain line is determined.

4.4 Control Simulation and Experiment Using MPC with LSTM

In this section, numerical simulation and scale model experiment are described to show the effectiveness of the use of MPC with LSTM forecasting of future base motion. Here, an application of compensating the base motion of a Stewart platform mounted on a ship is considered. In both the simulation and experiment, the control performance of MPC with LSTM is compared to that of the IDC.

4.4.1 Settings for Control Simulation and Experiment

In the simulation and experiment, the same specifications of a scale model of Stewart platform in Table 2.1 and 2.2 were utilized. The parameters used for the MPC design are presented in Table 4.1. Here, the time step is set by considering sufficient computation time for LSTM forecasting and MPC. It is assumed that the time delay including sensor signal processing time and actuator response time is 0.2 seconds, and the prediction horizon steps are chosen as 5 steps. For weights, the larger weight matrices W_1 and W_2 are selected to realize high tracking performance and fast response.

Numerical simulations were performed by using MATLAB/Simulink and SimMechanics. It is assumed that all states are known, and the parameters are measured accurately and have errors within 1 percent. To simulate the motion of a ship, random waves with low frequency range $0.1 \sim 1$ Hz is applied, where the maximum amplitude of the waves are intentionally outside the range of the workspace of the platform.

In the scale model experiment, to simply examine the control performance, a low-frequency wave around 0.1 Hz is applied as base plate excitations. The maximum amplitude of the wave is in the range of the workspace of the platform.

Utilizing LSTM, the future motion of the base plate is forecasted at each time step in real time. Then the optimal control inputs for the future state are computed by the MPC. The framework of the MPC with LSTM forecasting is illustrated in Fig. 4.13.

Table 4.1: MPC parameters

Specification	Parameter
Time Step (s)	0.04
Prediction Horizon	n = 5
Weights	$W_1 = 100I_{12}, W_2 = 200I_{12}, W_3 = 0.2I_6$
Constraints	Range
Actuation Force (N)	$-20 \leq u \leq 20$
Leg Extension (m)	$0 \leq l \leq 0.1$
Universal Joint Angle (deg)	$-45 \leq \phi \leq 45$
Reference	Values
Displacements and orientations	$\left(q_{Tpref}(t)\right) = (0, 0, 0, 0, 0, 0)$
Velocities	$\left(\dot{q}_{Tpref}(t)\right) = (0, 0, 0, 0, 0, 0)$

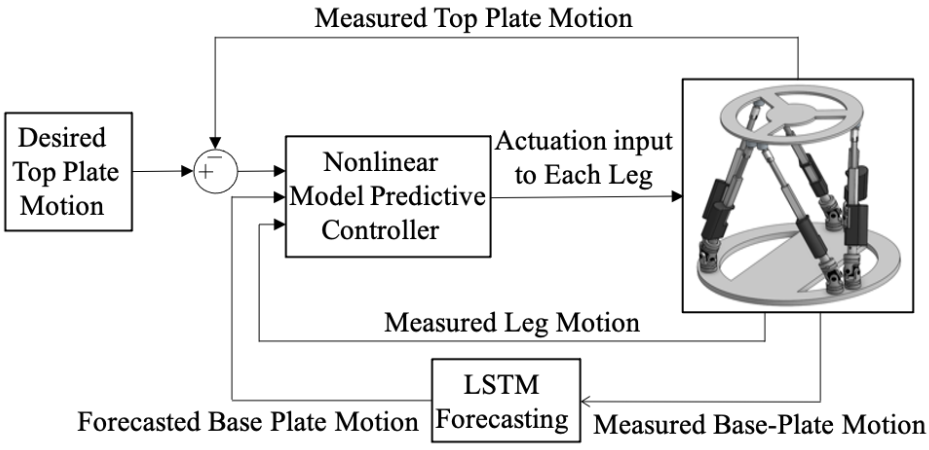

Figure 4.13: Framework of the Stewart platform compensator with LSTM forecasting

4.4.2 Simulation Results

Figures 4.14(a) and (b) show the extension of the actuator 1 when applying each of the IDC and MPC-LSTM. From the result of the MPC with LSTM, the time delay is compensated by forecasting the future base-plate motion. In the Figs., the motion of the base plate is outside the feasible range at t =13-14 s. At this time, the controlled actual extension stays inside the maximum boundary while the computed reference length of the actuator 1 goes outside the boundary. Also, input actuation force when using the MPC becomes zero as shown in Fig. 4.15. Therefore, the controller successfully keeps satisfying the defined constraints even if the reference state becomes outside the

workspace. Since the plotted data keeps staying inside the minimum and maximum boundaries, it can be observed that the controller works properly satisfying defined constraints.

(a)

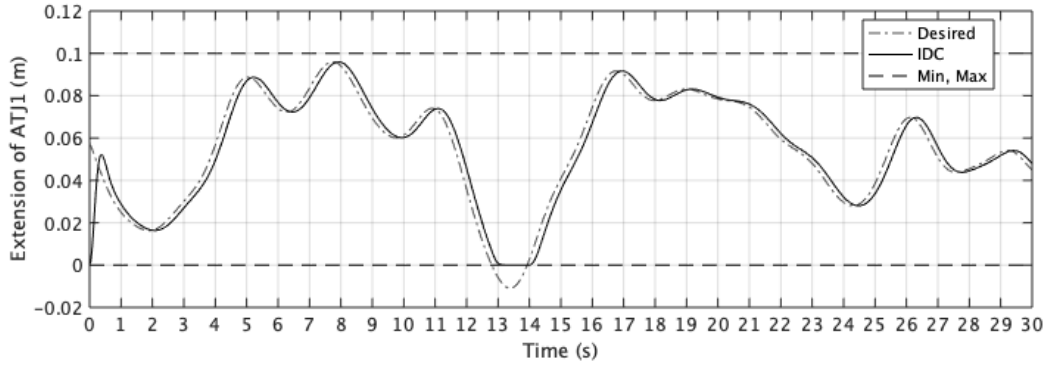

(b)

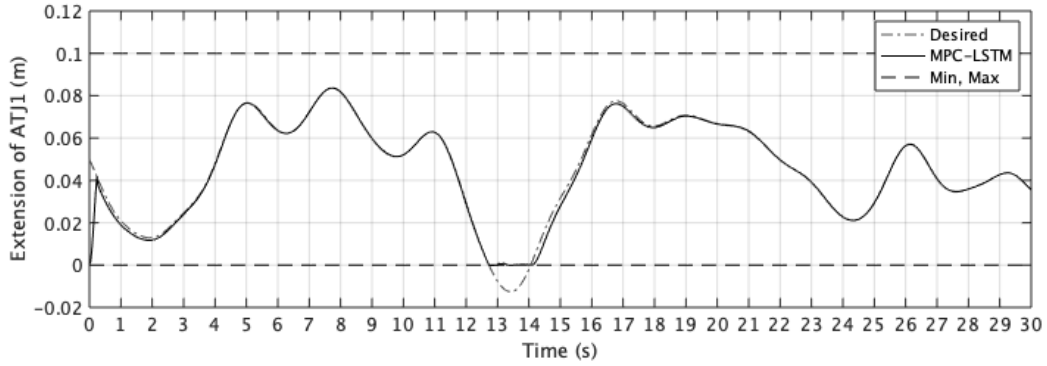

Figure 4.14: Extension of the actuator 1 when applying (a) IDC and (b) MPC with LSTM forecasting

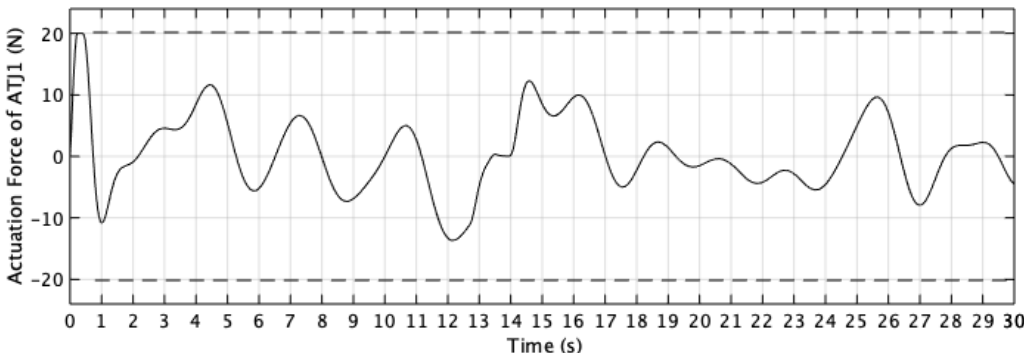

Figure 4.15: Input actuation force of the actuator 1 for when applying MPC with LSTM forecasting

Figures 4.16(a-c) show the results of the base-plate excitation and controlled top-plate configuration for IDC and MPC with LSTM forecasting. The top plate is controlled to remain horizontal and its center of mass stationary. Since near the time 13-14s the states are going outside the workspace, there exist the tracking errors for vertical displacement in x_3-direction and Tait-Bryan angle $\psi_2^{TB(13)}(t)$. Also, the other small tracking errors seen can be considered as local forecasting errors of the base plate.

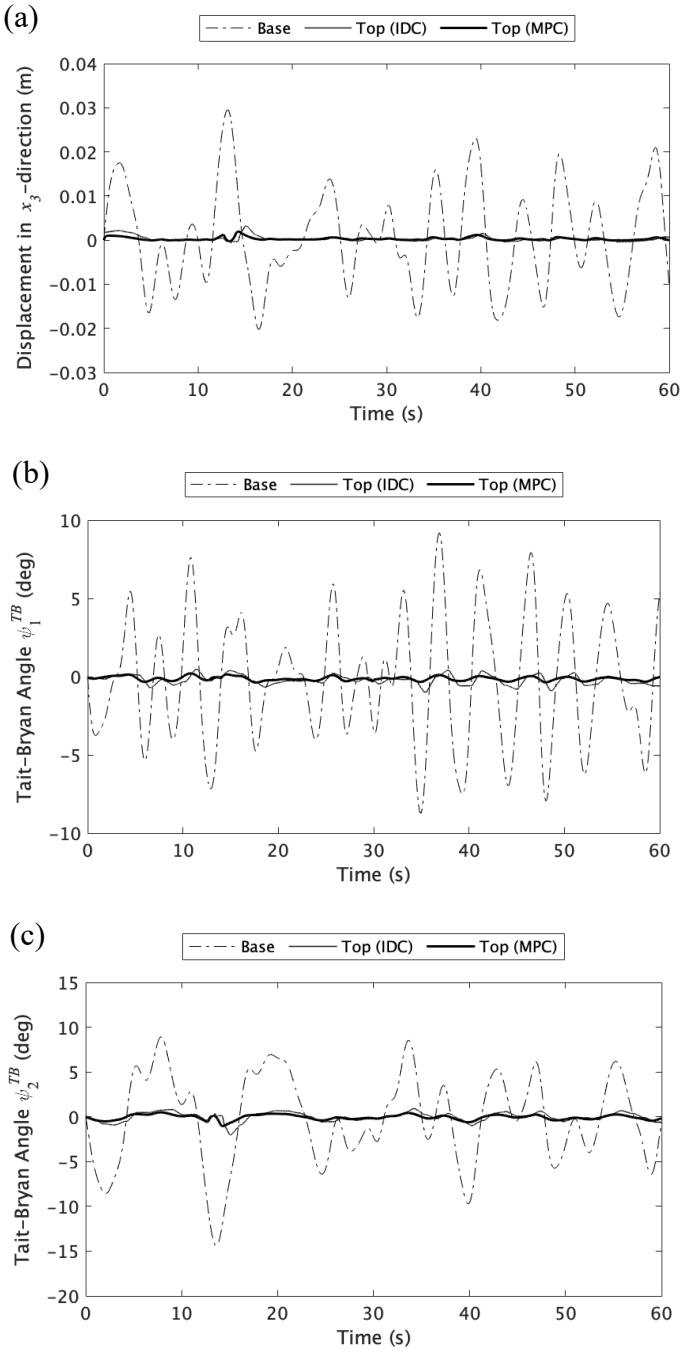

Figure 4.16: Comparison of simulation results by IDC and MPC with LSTM forecasting: (a) displacement in the x_3-direction, (b) Tait-Bryan angle $\psi_1{}^{TB}(t)$, (c) Tait-Bryan angle $\psi_2{}^{TB}(t)$

4.4.3 Experimental Results

Figure 4.17 shows that real time forecasted results of the rotation of the base plate. For the verification of the forecasting accuracy, the resulting data of forecasted response after 5 steps is plotted with the actually observed motion. Since the RMSE when purely delayed by 0.2 seconds without forecasting is 0.97, the LSTM achieves high forecasting accuracy, which indicates that the forecasting result is applicable for improvement of the tracking performance.

Figures 4.18(a-c) show the experimental results of the extension and actuator force of the actuator 1 by the IDC and MPC combined with LSTM forecasting. Similar to the results in the simulation, most of the time delays are successfully compensated through the use of the LSTM forecasting method.

The comparison of the control results of Tait-Bryan angle $\psi_1^{TB}(t)$ of the top plate by MPC-LSTM and IDC when the base plate rotates is illustrated in Fig. 4.19 and Table 4.2. From the results of plots, errors, and compensation rates, the MPC combined with LSTM forecasting achieves higher control performance than IDC without forecasting of base motion. It can be observed that the tracking error of MPC seen in Fig. 4.19 exists due to the local forecasting error of the base plate. In addition, although the time delay was assumed to be 0.2 s, the actual time delay is different at each time. Then, if the fitting rate described in Fig. 4.17 is improved and an accurate time delay is estimated at each time, the tracking performance can also be improved.

For application to a hospital ship, it has not been clarified to what accuracy the performance should be achieved since it has not been ergonomically verified. In this study, control methods are evaluated based on the rate of achievement for the goal of keeping the top plate as horizontal as possible. From the experimental results, about 88% was absorbed by using IDC mainly in the x_3-, ψ_1^{TB}-, and ψ_2^{TB}- directions, and about 93% was achieved in MPC with LSTM forecasting in the ψ_1^{TB}- direction. Although it has not reached the stage where it can be actually applied, in this study, it was confirmed that the compensation rate can be increased by applying dynamics, nonlinear control scheme and prediction compared to the simple PID in the previous research. In the future, to further improve the accuracy, it will be necessary to enhance the performance of sensors, actuators and the computational speed.

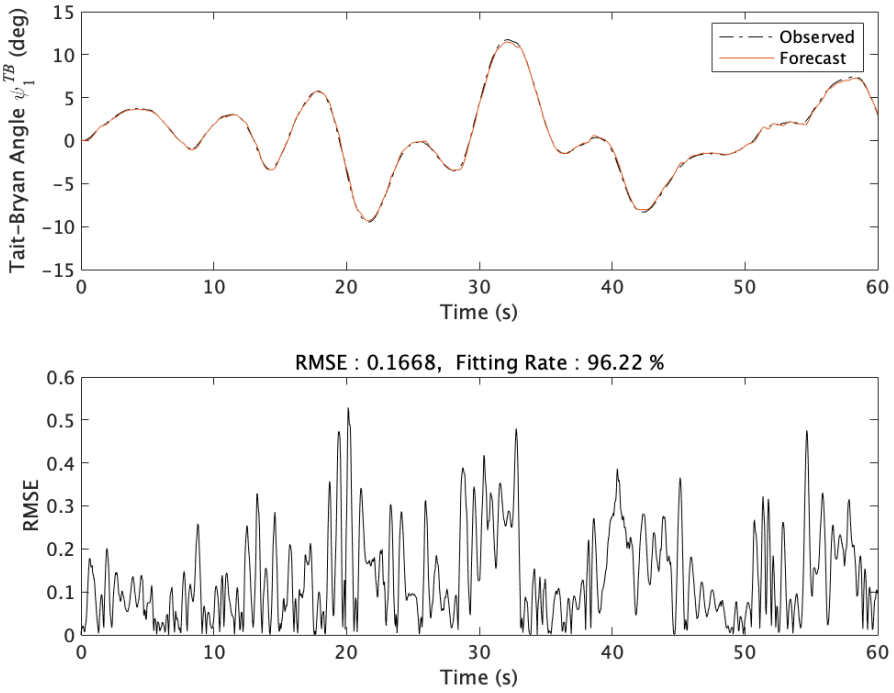

Figure 4.17: Real-time forecasted response of 5 steps (0.2 s) ahead Tait-Bryan angle $\psi_1{}^{TB}(t)$ by LSTM

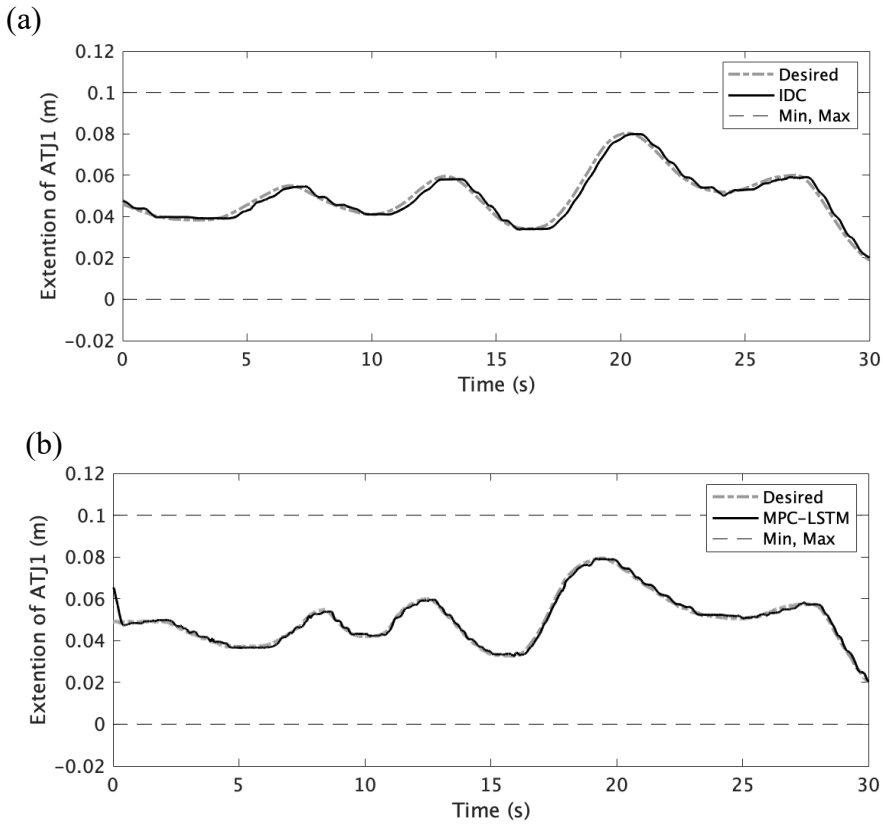

(c)

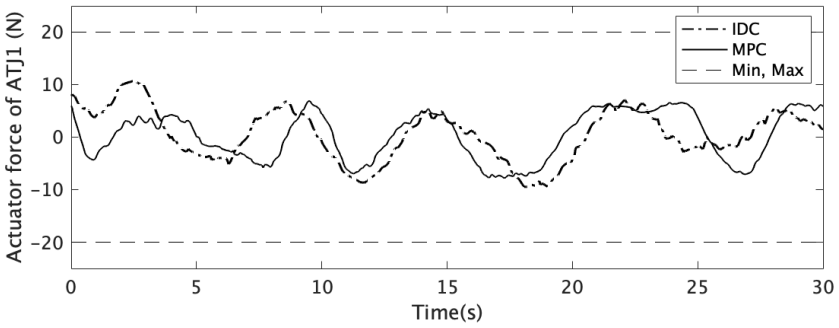

Figure 4.18: Experimental results of extension of the actuator 1 when applying (a) IDC and (b) MPC with LSTM forecasting, and (c) actuation force of the actuator 1 for each control method

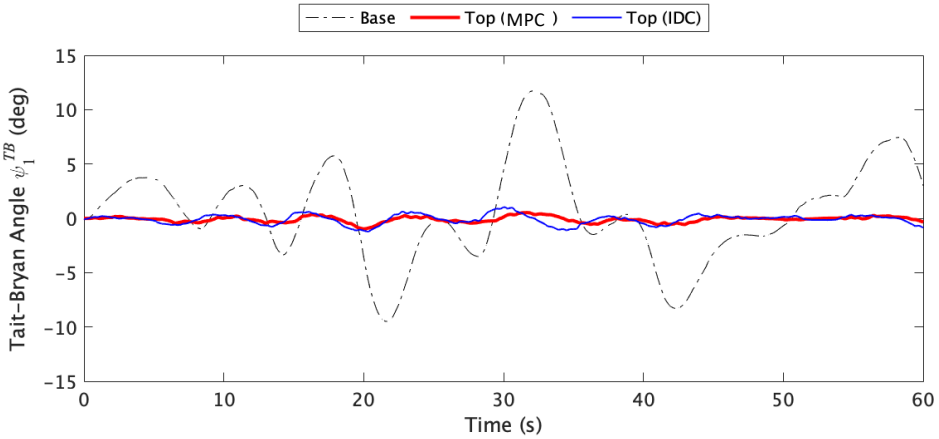

Figure 4.19: Results of Tait-Bryan angle $\psi_1{}^{TB}(t)$ of controlled top plate against the motion of the base plate for MPC with LSTM forecasting and IDC

Table 4.2: Comparison of errors and compensation rates between MPC with LSTM and IDC

	Controller	RMSE	MAE	Compensation Rate	
				RMSE	MAE
Tait-Bryan Angle $\psi_1^{TB(13)}(t)$	MPC	0.2912°	0.2216°	93.51 %	93.78 %
	IDC	0.5511°	0.3589°	88.65 %	89.11 %

4.5 Concluding Remarks

In this chapter, MPC with LSTM forecasting of mount motion was applied to the system. In order to forecast the future excitation of the base plate caused by the motion of the moving body, LSTM was adopted as a predictor of the time series data based on the past measured data.

To investigate the forecasting performance of the proposed approach, the LSTM model was trained with different parameters and different training data, as forecasting accuracy can be improved by tuning the hyperparameters and by training on driving data that includes multiple driving states. Through the use of LSTM, unsteady time series data that includes such elements as sudden or large acceleration changes can be forecasted with greater accuracy than can be achieved with the conventional ARIMA model, where forecasting accuracy deteriorates in such cases. Study results validate the capability of a pre-trained LSTM model to produce accurate real-time forecasts of future vehicle accelerations.

Then MPC was designed by developing a nonlinear dynamics model of the system by defining the constrained optimization problem for the computation of control input in each time step.

Finally, simulation and experiment results for the scale model of the base-moving Stewart platform were presented to assess the performance of the proposed controller and forecasting. The tracking performance of the top plate was examined and the results show that the proposed method is effective for stabilization of the top plate when there exists a time delay under low-frequency wave excitation of the base plate of the Stewart platform.

CHAPTER 5: CONCLUSION

This dissertation focused on kinematic and dynamic modeling and control of a Stewart platform as base motion compensators.

Chapter 2 presented kinematic computation and control results of scale model experiments. Utilizing body- and joint-attached, orthonormal coordinate frames, the configuration space is mathematically defined. Configurational loop closure constraints are presented for a representative closed loop and solved analytically for both inverse and forward kinematics. Also, velocities of each moving coordinate frame are computed.

Chapter 3 presented the derivation of equations of motion for a base-moving Stewart platform and inverse dynamics control experiment. To derive analytical equations of motion, the principle of virtual work is variationally derived from Hamilton's principle for multi-body systems. A step-by-step derivation of the equations of motion incorporates the loop closure constraints analytically to yield compact analytical equations of motion in matrix form. Furthermore, the numerical and experimental results demonstrated that the IDC controller utilizing the equations of motion is more effective to control a Stewart platform against input disturbance of its base plate than the IKC controller.

In Chapter 4, MPC with LSTM forecasting was applied to the system to compensate a time delay during control. In order to forecast the future excitation of the base plate caused by motion of moving body, LSTM was adopted as a predictor of the time series data based on the past measured data. The capability of real time forecasting of the future motion was validated showing the usefulness of the proposed method. Then MPC was designed by developing a nonlinear dynamics model of the system. Finally, the numerical and experimental results for the scale model of the base-moving Stewart platform were presented showing that the proposed method is effective for stabilization of the top plate when there exists a time delay under low-frequency wave excitation of the base plate of the Stewart platform.

From the above results, it was confirmed that the proposed methods, including the development of the kinematic and dynamic model and future forecasting, effectively contribute to the improvement of the motion compensation.

APPENDIX: PLANAR THREE DEGREES-OF-FREEDOM MANIPULATOR

This section presents dynamic modeling of a planar, three degrees-of-freedom manipulator consisting of two parallel plates, referred to as top and base plates, which are connected by three actuated legs. This system is an economical planar version of a six degrees-of-freedom base-moving Stewart platform.

In the derivation of analytical equations of motion, the moving frame method is utilized to describe the kinematics of the two-dimensional multibody system. For the manipulator system comprised of jointed bodies, a graph tree is utilized, which visually illustrates how the constituent bodies are connected to each other. For kinetics, the principle of virtual work is employed to derive the analytical equations of motion for the manipulator system.

The resulting equations of motion are used to numerically assess the performance of a SMC to stabilize the top plate from the motion of the translating and rotating base plate. In the numerical simulation, the SMC is compared with a simple PID controller to evaluate both the tracking performance and robustness.

A.1 Description of a Planar Three Degrees-Of-Freedom Manipulator

As shown in Fig. A.1, a planar, three degrees-of-freedom manipulator consists of a moving base plate and top plate, which are connected by three linear actuators. Each actuator consists of the lower body and upper body, which are connected to the base and top plate through a revolute joint (RJ). The axial distance between the centers of mass of the lower and upper bodies changes by actuating an actuated translational joint (ATJ) of each linear actuator. The motion of the top plate is manipulated with two translational degrees-of-freedom and one rotational degree-of-freedom. Since this manipulator rotates in only one degree-of-freedom, this system can be utilized for stabilization of either rolling or pitching angle. Therefore, if the moving object rotates in more than one dimension, a six degrees-of-freedom base-moving Stewart platform should be adopted. In this section, an economical version of the Stewart platform is considered. In order to facilitate the modeling of the planar manipulator, the body connection of the planer manipulator is effectively illustrated by utilizing a directed graph in Fig. A.2.

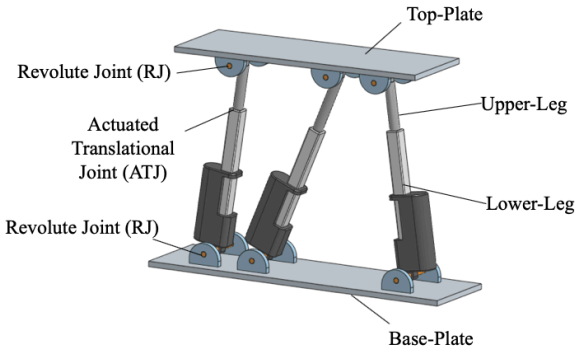

Figure A.1: A planar three degrees-of-freedom manipulator

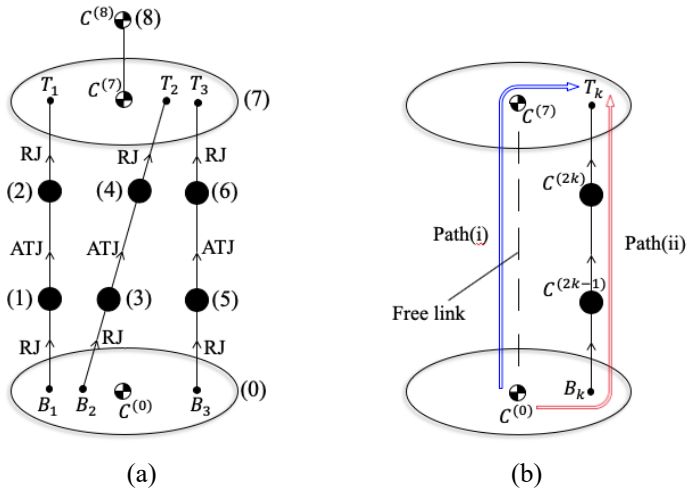

Figure A.2: (a) A modified directed graph and (b) representative closed loop

In Fig. A.2(a), vertices show rigid bodies identified by body numbers in parentheses, and lines indicate joint connections. Body-(0) and body-(7) represent the base plate and the top plate, respectively. The vertices B_1, B_2, B_3 and T_1, T_1, T_3 are the centers of revolute joints on the base plate, body-(0) and the top plate, body-(7). Body-(8) represents a manipulator or load. The k^{th} actuator, for k =1, 2, 3, consists of the lower body-(2k-1) and the upper body-(2k). The line between body-(0) and body-(2k-1), and that between body-(2k) and body-(7) show RJ. The line between the lower body-(2k-1) and the upper body-(2k) of the k^{th} actuator expresses an ATJ.

Figure A.2(b) shows a representative closed loop involving body-(0), body-(7) and the k^{th} actuator consisting of body (2k-1) and body-(2k). To effectively impose the loop closure constraints, a free link between body-(0) and body-(7), shown in a broken line, is introduced. Path (i) starts from the center of mass of body-(0), $C^{(0)}$, to that of body-(7), $C^{(7)}$, by the free link and to the center of the RJ, T_k, on body-(7). On the other

hand, path (ii) starts from $C^{(0)}$ to the point, B_k, of the k^{th} RJ on body-(0), then, moves along the axis of the k^{th} actuator passing the center of mass of body-(2k-1), $C^{(2k-1)}$, and the center of mass of body-(2k), $C^{(2k)}$, and finally, reaches the point, T_k. The loop closure constraints are imposed to assure that the translational and angular velocities of the coordinate frame at T_k on body-(7) remain the same for the path (i) and path (ii).

A.2 Kinematics of a 3-Dof Planar Platform

A.2.1 Body Frames and Connections

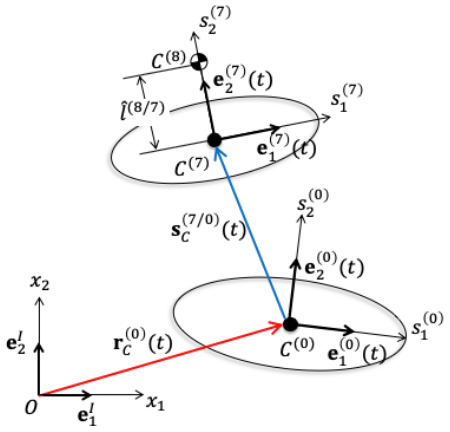

Figure A.3: Configuration of a 3-dof planar platform

Figure A.3 defines the configuration of a three degrees-of-Freedom planar platform. An orthonormal coordinate system $\{s_1^{(0)} \quad s_2^{(0)}\}$ is attached at its center of mass $C^{(0)}$ with the $s_2^{(0)}$-axis normal to the plane of the plate. The coordinate unit vectors are adopted as the vector basis $(\mathbf{e}_1^{(0)}(t) \quad \mathbf{e}_2^{(0)}(t))$ to describe vectors. An inertial coordinate system $\{x_1 \quad x_2\}$ is defined by using the body-attached coordinate system of body-(0) at time $t = 0$. The coordinate vector basis $(\mathbf{e}_1^I \quad \mathbf{e}_2^I)$ is used to express the components of position vectors of origins of the moving-coordinate systems. The inertial coordinate frame is now defined by the inertial vector basis $\mathbf{e}^I$ and the origin $\mathbf{0}$ as $(\mathbf{e}^I \quad \mathbf{0})$. The position vector $\mathbf{r}_C^{(0)}(t)$ of $C^{(0)}$ is expressed with respect to $\mathbf{e}^I$ with the components $x_C^{(0)}(t)$. For notational simplicity, the compact notation, adopted by Frankel is used for moving frames, where unit coordinate vectors are stored in 1 × 2 row matrices and components in 2 × 1 column matrices. The body-(0) coordinate vector basis $\mathbf{e}^{(0)}(t)$ is obtained by applying a 2 × 2 rotation matrix $R(\theta^{(0)}(t))$ starting from $\mathbf{e}^I$ as:

$$\mathbf{e}^{(0)}(t) = \mathbf{e}^I R(\theta^{(0)}(t)), \tag{A.1a}$$

where the body-(0) vector basis is compactly expressed as:

$$\mathbf{e}^{(0)}(t) \equiv \left(\mathbf{e}_1^{(0)}(t) \quad \mathbf{e}_2^{(0)}(t)\right). \tag{A.1b}$$

and the rotation matrix is

$$R(\theta^{(0)}(t)) = \begin{bmatrix} \cos(\theta^{(0)}(t)) & -\sin(\theta^{(0)}(t)) \\ \sin(\theta^{(0)}(t)) & \cos(\theta^{(0)}(t)) \end{bmatrix} \tag{A.1c}$$

and assume that $\theta^{(0)}(0) = 0$.

The inverse relation of Eq. (A.1a) is obtained as

$$\mathbf{e}^I = \mathbf{e}^{(0)}(t)\left(R(\theta^{(0)}(t))\right)^T. \tag{A.1d}$$

The position vector $\mathbf{r}_C^{(0)}(t)$ of $C^{(0)}$ is expressed with respect to $\mathbf{e}^I$ as:

$$\mathbf{r}_C^{(0)}(t) = \mathbf{e}^I x_C^{(0)}(t), \tag{A.2}$$

where $\mathbf{e}^I \equiv (\mathbf{e}_1^I \quad \mathbf{e}_2^I)$ and $x_C^{(0)}(t) = \left(x_{1C}^{(0)}(t) \quad x_{2C}^{(0)}(t)\right)^T$.

The connection of the body-(0) coordinate frame $\left(\mathbf{e}^{(0)}(t) \quad \mathbf{r}_C^{(0)}(t)\right)$ from the inertial frame $(\mathbf{e}^I \quad \mathbf{0})$ is compactly expressed by a 3×3 frame connection matrix as:

$$\left(\mathbf{e}^{(0)}(t) \quad \mathbf{r}_C^{(0)}(t)\right) = (\mathbf{e}^I \quad \mathbf{0}) \begin{bmatrix} R(\theta^{(0)}(t)) & x_C^{(0)}(t) \\ 0_{1\times 2}^T & 1 \end{bmatrix}. \tag{A.3}$$

The set of differentiable frame-connection matrices form the special Euclidean group, SE(2). In what follows, frame connection matrices are used to define coordinate frames. For path (i), the top-plate frame relative to the base-plate frame is expressed as:

$$\left(\mathbf{e}^{(7)}(t) \quad \mathbf{r}_C^{(7)}(t)\right) = \left(\mathbf{e}^{(0)}(t) \quad \mathbf{r}_C^{(0)}(t)\right) \begin{bmatrix} R(\phi^{(7/0)}(t)) & s_C^{(7/0)}(t) \\ 0_{1\times 2}^T & 1 \end{bmatrix} \tag{A.4a}$$

where

$$\begin{aligned} \mathbf{e}^{(7)}(t) &= \mathbf{e}^{(0)}(t)\, R(\phi^{(7/0)}(t)) \\ &= \mathbf{e}^I R(\theta^{(0)}(t)) R(\phi^{(7/0)}(t) \\ &= \mathbf{e}^I R(\theta^{(0)}(t) + \phi^{(7/0)}(t)) \\ &= \mathbf{e}^I R(\theta^{(7)}(t)) \end{aligned} \tag{A.4b}$$

$$\theta^{(7)}(t) = \theta^{(0)}(t) + \phi^{(7/0)}(t) \tag{A.4c}$$

$$\mathbf{r}_C^{(7)}(t) = \mathbf{r}_C^{(0)}(t) + \mathbf{e}^{(0)}(t)\, s_C^{(7/0)}(t) \tag{A.4d}$$

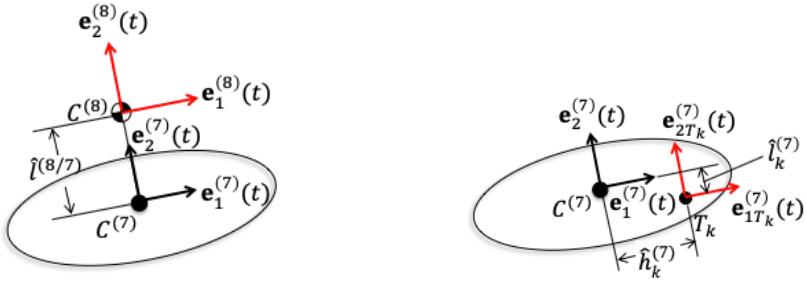

(a) (b)

Figure A.4: (a) A relative representation of the manipulator frame from the top-plate frame and (b) a relative representation of the T_k-frame from the top-plate frame

As shown in the Fig. A.4(a), the frame of the manipulator relative to the top plate is expressed as:

$$\left(\mathbf{e}^{(8)}(t) \quad \mathbf{r}_C^{(8)}(t)\right) = \left(\mathbf{e}^{(7)}(t) \quad \mathbf{r}_C^{(7)}(t)\right)\begin{bmatrix} I_2 & \begin{pmatrix}0\\ \hat{l}^{(8/7)}\end{pmatrix} \\ 0_{1\times 2}^T & 1 \end{bmatrix} \tag{A.5a}$$

where

$$\mathbf{e}^{(8)}(t) = \mathbf{e}^{(7)}(t) \tag{A.5b}$$

$$\mathbf{r}_C^{(8)}(t) = \mathbf{r}_C^{(7)}(t) + \mathbf{e}^{(7)}(t)\begin{pmatrix}0\\ \hat{l}^{(8/7)}\end{pmatrix} \tag{A.5c}$$

$$x_C^{(8)}(t) = x_C^{(7)}(t) + R(\theta^{(7)}(t))\begin{pmatrix}0\\ \hat{l}^{(8/7)}\end{pmatrix} \tag{A.5d}$$

Similarly, the T_k-frame of the top-plate(body-(7)) is expressed by

$$\left(\mathbf{e}_{T_k}^{(7)}(t) \quad \mathbf{r}_{T_k}(t)\right) = \left(\mathbf{e}^{(7)}(t) \quad \mathbf{r}_C^{(7)}(t)\right)\begin{bmatrix} I_2 & \begin{pmatrix}\hat{h}_k^{(7)}\\ -\hat{l}_k^{(7)}\end{pmatrix} \\ 0_{1\times 2}^T & 1 \end{bmatrix} \tag{A.6a}$$

where

$$\mathbf{e}_{T_k}^{(7)}(t) = \mathbf{e}^{(7)}(t) \tag{A.6b}$$

$$\mathbf{r}_{T_k}(t) = \mathbf{r}_C^{(7)}(t) + \mathbf{e}^{(7)}(t)\begin{pmatrix}\hat{h}_k^{(7)}\\ -\hat{l}_k^{(7)}\end{pmatrix} \tag{A.6c}$$

From the above, the flow of the frames on path (i) are $\left(\mathbf{e}^{(0)}(t) \quad \mathbf{r}_C^{(0)}(t)\right) \rightarrow \left(\mathbf{e}^{(7)}(t) \quad \mathbf{r}_C^{(7)}(t)\right) \rightarrow \left(\mathbf{e}_{T_k}^{(7)}(t) \quad \mathbf{r}_{T_k}(t)\right)$.

Next, frame connections along path (ii) are defined as illustrated in Fig. A.5 below.

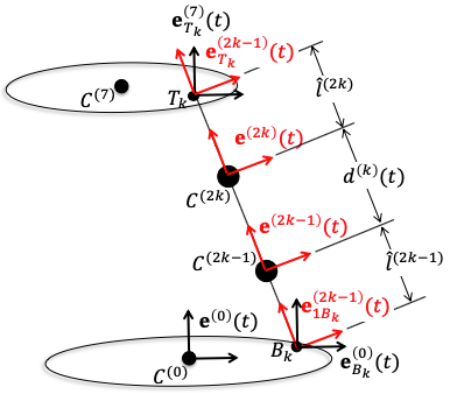

Figure A.5: Frame connections along path(ii)

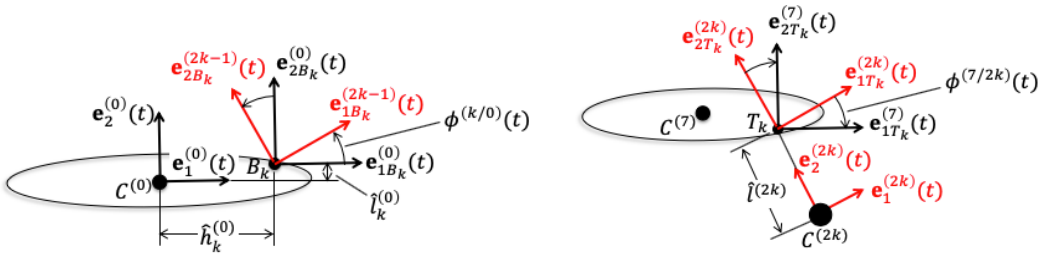

(a) (b)

Figure A.6: (a) Relative representations of the B_k-frame of body-(0) from the base-plate frame, and the B_k-frame of body-(2k-1) from the B_k-frame of body-(0), and (b) Relative representations of the T_k-frame of body-(2k) from the (2k)-frame, and T_k-frame of body-(7) from the T_k-frame of body-(2k)

Firstly, starting from the B_k-frame at point B_k on body-(0) as shown in Fig. A.6(a),

$$\left(\mathbf{e}_{B_k}^{(0)}(t) \quad \mathbf{r}_{B_k}(t)\right) = \left(\mathbf{e}^{(0)}(t) \quad \mathbf{r}_C^{(0)}(t)\right)\begin{bmatrix} I_2 & \begin{pmatrix}\hat{h}_k^{(0)} \\ \hat{l}_k^{(0)}\end{pmatrix} \\ 0_{1\times 2}^T & 1 \end{bmatrix} \tag{A.7}$$

Second, the B_k-frame of body-(2k-1) is expressed by rotating the B_k-frame of body-(0) as described in Fig. A.6(b):

$$\left(\mathbf{e}_{B_k}^{(2k-1)}(t) \quad \mathbf{r}_{B_k}(t)\right) = \left(\mathbf{e}_{B_k}^{(0)}(t) \quad \mathbf{r}_{B_k}(t)\right)\begin{bmatrix} R(\phi^{(k/0)}(t)) & 0_{2\times 1} \\ 0_{1\times 2}^T & 1 \end{bmatrix} \tag{A.8a}$$

where

$$\mathbf{e}_{B_k}^{(2k-1)}(t) = \mathbf{e}_{B_k}^{(0)}(t)R(\phi^{(k/0)}(t)) = \mathbf{e}^I\, R(\theta^{(0)}(t) + \phi^{(k/0)}(t)). \tag{A.8b}$$

Thirdly, the (2k-1)-frame at the center of mass of body-(2k-1) is expressed by parallel translating the B_k-frame of body-(2k-1) along the k^{th} actuator:

$$\left(\mathbf{e}^{(2k-1)}(t) \quad \mathbf{r}_C^{(2k-1)}(t)\right) = \left(\mathbf{e}_{B_k}^{(2k-1)}(t) \quad \mathbf{r}_{B_k}(t)\right)\begin{bmatrix} I_2 & \begin{pmatrix}0 \\ \hat{l}^{(2k-1)}\end{pmatrix} \\ 0_{1\times 2}^T & 1 \end{bmatrix} \tag{A.9}$$

Similarly, the (2k)-frame at the center of mass of body-(2k) is obtained by translating the (2k-1)-frame in $\mathbf{e}_2^{(2k-1)}(t)$ direction,

$$\left(\mathbf{e}^{(2k)}(t) \quad \mathbf{r}_C^{(2k)}(t)\right) = \left(\mathbf{e}^{(2k-1)}(t) \quad \mathbf{r}_C^{(2k-1)}(t)\right)\begin{bmatrix} I_2 & \begin{pmatrix}0\\ d^{(k)}(t)\end{pmatrix} \\ 0_{1\times 2}^T & 1 \end{bmatrix} \tag{A.10}$$

Then, the T_k-frame of body-(2k) is expressed by translating the (2k)-frame in $\mathbf{e}_2^{(2k)}(t)$ direction,

$$\left(\mathbf{e}_{T_k}^{(2k)}(t) \quad \mathbf{r}_{T_k}(t)\right) = \left(\mathbf{e}^{(2k)}(t) \quad \mathbf{r}_C^{(2k)}(t)\right)\begin{bmatrix} I_2 & \begin{pmatrix}0\\ \hat{l}^{(2k)}\end{pmatrix} \\ 0_{1\times 2}^T & 1 \end{bmatrix} \tag{A.11}$$

Finally, the connection to the T_k-frame of body-(7) is obtained by rotating the T_k-frame of body-(2k) as shown in Figure 8 above:

$$\left(\mathbf{e}_{T_k}^{(7)}(t) \quad \mathbf{r}_{T_k}(t)\right) = \left(\mathbf{e}_{T_k}^{(2k)}(t) \quad \mathbf{r}_{T_k}(t)\right)\begin{bmatrix} R(\phi^{(7/2k)}(t)) & 0_{2\times 1} \\ 0_{1\times 2}^T & 1 \end{bmatrix} \tag{A.12}$$

A.2.2 Velocities of the Frames

Translational velocities and angular velocities are easily obtained by taking time derivative of each frame. Firstly, he velocities of the frames along path (i) for bodies (0), (7), and (8) are computed. The velocities of the body-(0) frame become

$$\left(\dot{\mathbf{e}}^{(0)}(t) \quad \dot{\mathbf{r}}_C^{(0)}(t)\right) = \left(\mathbf{e}^{(0)}(t)\overleftrightarrow{\omega^{(0)}(t)} \quad \mathbf{e}^I \dot{x}_C^{(0)}(t)\right) \tag{A.13a}$$

where the skew-symmetric angular velocity matrix, which is the member of the Lie algebra of SO(2), se(2), is defined as:

$$\overleftrightarrow{\omega^{(0)}(t)} = \left(R(\theta^{(0)}(t))\right)^T \dot{R}(\theta^{(0)}(t)) = \begin{bmatrix}0 & -1\\ 1 & 0\end{bmatrix}\dot{\theta}^{(0)}(t) \tag{A.13b}$$

In the same manner, the velocities of the body-(7) can be expressed as:

$$\left(\dot{\mathbf{e}}^{(7)}(t) \quad \dot{\mathbf{r}}_C^{(7)}(t)\right) = \left(\mathbf{e}^{(7)}(t)\overleftrightarrow{\omega^{(7)}(t)} \quad \mathbf{e}^I \dot{x}_C^{(7)}(t)\right) \tag{A.14a}$$

For the computation of body-(7) frame velocities, the time derivative of Eq. (A.4b) yields

$$\begin{aligned}
\dot{\mathbf{e}}^{(7)}(t) &= \dot{\mathbf{e}}^{(0)}(t)\, R(\phi^{(7/0)}(t)) + \mathbf{e}^{(0)}(t)\, \dot{R}(\phi^{(7/0)}(t)) \\
&= \mathbf{e}^{(0)}(t)\begin{bmatrix}0 & -1\\ 1 & 0\end{bmatrix}\dot{\theta}^{(0)}(t)R(\phi^{(7/0)}(t)) + \mathbf{e}^{(7)}(t)\left(R(\phi^{(7/0)}(t))\right)^T \dot{R}(\phi^{(7/0)}(t)) \\
&= \mathbf{e}^{(7)}(t)\left\{\left(R(\phi^{(7/0)}(t))\right)^T \begin{bmatrix}0 & -1\\ 1 & 0\end{bmatrix}\dot{\theta}^{(0)}(t)R(\phi^{(7/0)}(t)) + \begin{bmatrix}0 & -1\\ 1 & 0\end{bmatrix}\dot{\phi}^{(7/0)}(t)\right\} \\
&= \mathbf{e}^{(7)}(t)\begin{bmatrix}0 & -1\\ 1 & 0\end{bmatrix}\left(\dot{\theta}^{(0)}(t) + \dot{\phi}^{(7/0)}(t)\right) \\
&= \mathbf{e}^{(7)}(t)\begin{bmatrix}0 & -1\\ 1 & 0\end{bmatrix}\dot{\theta}^{(7)}(t)
\end{aligned} \tag{A.14b}$$

where

$$\dot{\theta}^{(7)}(t) = \dot{\theta}^{(0)}(t) + \dot{\phi}^{(7/0)}(t) \tag{A.14c}$$

and

$$\theta^{(7)}(t) = \theta^{(0)}(t) + \phi^{(7/0)}(t) \tag{A.14d}$$

The time derivative of Eq. (A.4d) yields

$$\begin{aligned}\dot{\mathbf{r}}_C^{(7)}(t) &= \dot{\mathbf{r}}_C^{(0)}(t) + \dot{\mathbf{e}}^{(0)}(t)\, s_C^{(7/0)}(t) + \mathbf{e}^{(0)}(t)\, \dot{s}_C^{(7/0)}(t) \\ &= \mathbf{e}^I \dot{x}_C^{(0)}(t) + \mathbf{e}^{(0)}(t) \left\{ \begin{bmatrix} 0 & -1 \\ 1 & 0 \end{bmatrix} \dot{\theta}^{(0)}(t) s_C^{(7/0)}(t) + \dot{s}_C^{(7/0)}(t) \right\}\end{aligned} \tag{A.15a}$$

The translational velocities of body-(7) in Eq. (A.14a) with respect to inertial frame are obtained as:

$$\dot{x}_C^{(7)}(t) = \dot{x}_C^{(0)}(t) + R(\theta^{(0)}(t)) \left\{ \begin{pmatrix} -s_{2C}^{(7/0)}(t) \\ s_{1C}^{(7/0)}(t) \end{pmatrix} \dot{\theta}^{(0)}(t) + \dot{s}_C^{(7/0)}(t) \right\} \tag{A.15b}$$

The velocities of the body-(8) frame is obtained by taking the time derivatives of Eq. (A.5a):

$$\left(\dot{\mathbf{e}}^{(8)}(t) \quad \dot{\mathbf{r}}_C^{(8)}(t) \right) = \left(\mathbf{e}^{(8)}(t) \begin{bmatrix} 0 & -1 \\ 1 & 0 \end{bmatrix} \dot{\theta}^{(8)}(t) \quad \mathbf{e}^I \dot{x}_C^{(8)}(t) \right) \tag{A.16a}$$

where the angular velocities and the translational velocities are easily obtained as:

$$\dot{\theta}^{(8)}(t) = \dot{\theta}^{(7)}(t) \tag{A.16b}$$

$$\dot{x}_C^{(8)}(t) = \dot{x}_C^{(7)}(t) + R\left(\theta^{(0)}(t) + \phi^{(7/0)}(t)\right) \begin{pmatrix} -\hat{h}^{(8/7)} \\ 0 \end{pmatrix} \left(\dot{\theta}^{(0)}(t) + \dot{\phi}^{(7/0)}(t) \right) \tag{A.16c}$$

Substitution of Eq. (A.15b) into Eq. (A.16c) yields

$$\begin{aligned}\dot{x}_C^{(8)}(t) = \dot{x}_C^{(0)}(t) + R(\theta^{(0)}(t)) + R(\theta^{(0)}(t)) \left\{ \begin{pmatrix} -s_{2C}^{(7/0)}(t) \\ s_{1C}^{(7/0)}(t) \end{pmatrix} + R\left(\phi^{(7/0)}(t)\right) \begin{pmatrix} -\hat{h}^{(8/7)} \\ 0 \end{pmatrix} \right\} \dot{\theta}^{(0)}(t) \\ + R(\theta^{(0)}(t)) \left\{ \dot{s}_C^{(7/0)}(t) + R\left(\phi^{(7/0)}(t)\right) \begin{pmatrix} -\hat{h}^{(8/7)} \\ 0 \end{pmatrix} \dot{\phi}^{(7/0)}(t) \right\}\end{aligned} \tag{A.16d}$$

Finally, the time derivatives of Eq. (A.6a) become

$$\left(\dot{\mathbf{e}}_{T_k}^{(7)}(t) \quad \dot{\mathbf{r}}_{T_k}(t) \right) = \left(\mathbf{e}_{T_k}^{(7)}(t) \begin{bmatrix} 0 & -1 \\ 1 & 0 \end{bmatrix} \dot{\theta}_{T_k}^{(7)}(t) \quad \mathbf{e}^I \dot{x}_{T_k}(t) \right) \tag{A.17a}$$

where the angular velocities and the translational velocities for path (i) are

$$\dot{\theta}_{T_k}^{(7)}(t)_{path(i)} = \dot{\theta}^{(7)}(t) = \dot{\theta}^{(0)}(t) + \dot{\phi}^{(7/0)}(t) \tag{A.17b}$$

$$\dot{\mathbf{r}}_{T_k}(t)_{path(i)} = \mathbf{e}^I \left\{ \dot{x}_C^{(7)}(t) + R(\theta^{(7)}(t)) \begin{pmatrix} \hat{l}_k^{(7)} \\ \hat{h}_k^{(7)} \end{pmatrix} \dot{\theta}^{(7)}(t) \right\}. \tag{A.17c}$$

Then, the translational velocities of the T_k-frame of body-(7) with respect to inertial frame are

$$\begin{aligned}\dot{x}_{T_k}(t)_{path(i)} = \dot{x}_C^{(0)}(t) + R(\theta^{(0)}(t)) \left\{ \begin{pmatrix} -s_{2C}^{(7/0)}(t) \\ s_{1C}^{(7/0)}(t) \end{pmatrix} + R\left(\phi^{(7/0)}(t)\right) \begin{pmatrix} \hat{l}_k^{(7)} \\ \hat{h}_k^{(7)} \end{pmatrix} \right\} \dot{\theta}^{(0)}(t) \\ + R(\theta^{(0)}(t)) \left\{ \dot{s}_C^{(7/0)}(t) + R\left(\phi^{(7/0)}(t)\right) \begin{pmatrix} \hat{l}_k^{(7)} \\ \hat{h}_k^{(7)} \end{pmatrix} \dot{\phi}^{(7/0)}(t) \right\}.\end{aligned} \tag{A.17d}$$

Next, the velocities along path (ii) for bodies (0), (2k-1), (2k) and (7) are computed. First, the velocities of B_k-frame at point B_k on body-(0) are obtained from Eq. (A.7a)

$$\left(\dot{\mathbf{e}}_{B_k}^{(0)}(t) \quad \dot{\mathbf{r}}_{B_k}(t)\right) = \left(\mathbf{e}_B^{(0)}(t)\begin{bmatrix}0 & -1\\ 1 & 0\end{bmatrix}\dot{\theta}_{B_k}^{(0)}(t) \quad \mathbf{e}^I\dot{x}_{B_k}(t)\right) \tag{A.18a}$$

where

$$\dot{\theta}_{B_k}^{(0)}(t) = \dot{\theta}^{(0)}(t) \tag{A.18b}$$

$$\dot{x}_{B_k}(t) = \dot{x}_C^{(0)}(t) + R(\theta^{(0)}(t))\begin{pmatrix}-\hat{l}_k^{(0)}\\ \hat{h}_k^{(0)}\end{pmatrix}\dot{\theta}^{(0)}(t) \tag{A.18c}$$

Secondly, the velocities of B_k-frame at point B_k on body-(2k-1) are

$$\left(\dot{\mathbf{e}}_{B_k}^{(2k-1)}(t) \quad \dot{\mathbf{r}}_{B_k}(t)\right) = \left(\mathbf{e}_B^{(2k-1)}(t)\begin{bmatrix}0 & -1\\ 1 & 0\end{bmatrix}\dot{\theta}_{B_k}^{(2k-1)}(t) \quad \mathbf{e}^I\dot{x}_{B_k}(t)\right) \tag{A.19a}$$

where

$$\dot{\theta}_{B_k}^{(2k-1)}(t) = \dot{\theta}^{(0)}(t) + \dot{\phi}^{(k/0)}(t) \tag{A.19b}$$

Thirdly, the velocities of body-(2k-1) frame are

$$\left(\dot{\mathbf{e}}^{(2k-1)}(t) \quad \dot{\mathbf{r}}_C^{(2k-1)}(t)\right) = \left(\mathbf{e}^{(2k-1)}(t)\begin{bmatrix}0 & -1\\ 1 & 0\end{bmatrix}\dot{\theta}^{(2k-1)}(t) \quad \mathbf{e}^I\dot{x}_C^{(2k-1)}(t)\right) \tag{A.20a}$$

where

$$\dot{\theta}^{(2k-1)}(t) = \dot{\theta}_{B_k}^{(2k-1)}(t) \tag{A.20b}$$

and also

$$\theta^{(2k-1)}(t) = \theta^{(0)}(t) + \phi^{(k/0)}(t) \tag{A.20c}$$

$$\dot{x}_C^{(2k-1)}(t) = \dot{x}_C^{(0)}(t) + R(\theta^{(0)}(t))\left\{\begin{pmatrix}-\hat{l}_k^{(0)}\\ \hat{h}_k^{(0)}\end{pmatrix} + R\left(\phi^{(k/0)}(t)\right)\begin{pmatrix}-\hat{h}^{(2k-1)}\\ 0\end{pmatrix}\right\}\dot{\theta}^{(0)}(t) + R\left(\theta^{(0)}(t) + \phi^{(k/0)}(t)\right)\begin{pmatrix}-\hat{h}^{(2k-1)}\\ 0\end{pmatrix}\dot{\phi}^{(k/0)}(t) \tag{A.20d}$$

Similarly, the velocities of body-(2k) frame become

$$\left(\dot{\mathbf{e}}^{(2k)}(t) \quad \dot{\mathbf{r}}_C^{(2k)}(t)\right) = \left(\mathbf{e}^{(2k)}(t)\begin{bmatrix}0 & -1\\ 1 & 0\end{bmatrix}\dot{\theta}^{(2k)}(t) \quad \mathbf{e}^I\dot{x}_C^{(2k)}(t)\right) \tag{A.21a}$$

where

$$\dot{\theta}^{(2k)}(t) = \dot{\theta}^{(2k-1)}(t) \tag{A.21b}$$

$$\dot{x}_C^{(2k)}(t) = \dot{x}_C^{(0)}(t) + R(\theta^{(0)}(t))\left\{\begin{pmatrix}-\hat{l}_k^{(0)}\\ \hat{h}_k^{(0)}\end{pmatrix} + R\left(\phi^{(k/0)}(t)\right)\begin{pmatrix}-\left(\hat{h}^{(2k-1)} + d^{(k)}(t)\right)\\ 0\end{pmatrix}\right\}\dot{\theta}^{(0)}(t) + R\left(\theta^{(0)}(t) + \phi^{(k/0)}(t)\right)\begin{pmatrix}-\left(\hat{h}^{(2k-1)} + d^{(k)}(t)\right)\\ 0\end{pmatrix}\dot{\phi}^{(k/0)}(t) + R\left(\theta^{(0)}(t) + \phi^{(k/0)}(t)\right)\begin{pmatrix}0\\ \dot{d}^{(k)}(t)\end{pmatrix} \tag{A.21c}$$

Then, the velocities of T_k-frame at point T_k on body-(2k) are

$$\left(\dot{\mathbf{e}}_{T_k}^{(2k)}(t) \quad \dot{\mathbf{r}}_{T_k}(t)\right) = \left(\mathbf{e}_{T_k}^{(2k)}(t)\begin{bmatrix}0 & -1\\ 1 & 0\end{bmatrix}\dot{\theta}_{T_k}^{(2k)}(t) \quad \mathbf{e}^I\dot{x}_{T_k}(t)\right) \tag{A.22a}$$

where

$$\dot{\theta}_{T_k}^{(2k)}(t) = \dot{\theta}^{(2k)}(t) \tag{A.22b}$$

$$\dot{x}_{T_k}(t) = \dot{x}_C^{(0)}(t) + R(\theta^{(0)}(t)) \left\{ \begin{pmatrix} -\hat{l}_k^{(0)} \\ \hat{h}_k^{(0)} \end{pmatrix} + R\big(\phi^{(k/0)}(t)\big) \begin{pmatrix} -l^{(k)}(t) \\ 0 \end{pmatrix} \right\} \dot{\theta}^{(0)}(t)$$

$$+ R\big(\theta^{(0)}(t) + \phi^{(k/0)}(t)\big) \begin{pmatrix} -l^{(k)}(t) \\ 0 \end{pmatrix} \dot{\phi}^{(k/0)}(t) + R\big(\theta^{(0)}(t) + \phi^{(k/0)}(t)\big) \begin{pmatrix} 0 \\ \dot{d}^{(k)}(t) \end{pmatrix} \tag{A.22c}$$

where $l^{(k)}(t)$ is the length of the k^{th} leg:

$$l^{(k)}(t) = \hat{l}^{(2k-1)} + d^{(k)}(t) + \hat{l}^{(2k)} \tag{A.22d}$$

Finally, the velocities of T_k-frame on body (7) along path(ii) are obtained as:

$$\big(\dot{\mathbf{e}}_{T_k}^{(7)}(t) \quad \dot{\mathbf{r}}_{T_k}(t)\big) = \Big(\mathbf{e}_{T_k}^{(7)}(t) \begin{bmatrix} 0 & -1 \\ 1 & 0 \end{bmatrix} \dot{\theta}_{T_k}^{(7)}(t) \quad \mathbf{e}^I \dot{x}_{T_k}(t)\Big) \tag{A.23a}$$

where

$$\dot{\theta}_{T_k}^{(7)}(t)_{path(ii)} = \dot{\theta}_{T_k}^{(2k)}(t) + \dot{\phi}^{(7/2k)}(t) = \dot{\theta}^{(0)}(t) + \dot{\phi}^{(k/0)}(t) + \dot{\phi}^{(7/2k)}(t) \tag{A.23b}$$

and also,

$$\theta_{T_k}^{(7)}(t) = \theta^{(0)}(t) + \phi^{(k/0)}(t) + \phi^{(7/2k)}(t). \tag{A.23c}$$

A.2.3 Loop Closure Constraints on Velocities and Virtual Displacements

Assuming that the loop is closed at $t = 0$, we equate the velocities of the T_k-frame of body-(7) computed along path (i) and path (ii) to ensure that the loop remains closed at each time. Before adopting the loop closure constrains, the essential velocities for the top plate, base plate, and k^{th} leg are defined as

$$\big(\dot{q}_{Tp}(t)\big)_{3\times1} \equiv \begin{pmatrix} \dot{s}_C^{(7/0)}(t) \\ \dot{\phi}^{(7/0)}(t) \end{pmatrix}, \qquad \big(\dot{q}_{Bp}(t)\big)_{3\times1} \equiv \begin{pmatrix} \dot{x}_C^{(0)}(t) \\ \dot{\theta}^{(0)}(t) \end{pmatrix}, \qquad \big(\dot{q}_L^{(k)}(t)\big)_{2\times1} \equiv \begin{pmatrix} \dot{\phi}^{(k/0)}(t) \\ \dot{d}^{(k)}(t) \end{pmatrix} \tag{A.24a, b, c}$$

and the virtual displacements of the top-plate and k^{th} leg are defined as:

$$\big(\delta q_{Tp}(t)\big) \equiv \begin{pmatrix} \delta s_C^{(7/0)}(t) \\ \delta\phi^{(7/0)}(t) \end{pmatrix}, \qquad \big(\delta q_L^{(k)}(t)\big) \equiv \begin{pmatrix} \delta\phi^{(k/0)}(t) \\ \delta d^{(k)}(t) \end{pmatrix} \tag{A.25a, b}$$

Since the translational and angular displacements of the base plate, $x_C^{(0)}(t)$ and $\theta^{(0)}(t)$, are prescribed at each time, the variations of the base plate can be defined as $\big(\delta q_{Bp}(t)\big) \equiv \mathbf{0}$. The first loop closure constraint can be defined as:

$$\dot{\theta}_{T_k}^{(7)}(t)_{path(i)} = \dot{\theta}_{T_k}^{(7)}(t)_{path(ii)} \tag{A.26a}$$

From Eqs. (A.17b) and (A.23b), the above constraint gives

$$\dot{\phi}^{(7/2k)}(t) = \dot{\phi}^{(7/0)}(t) - \dot{\phi}^{(k/0)}(t) \tag{A.26b}$$

and the corresponding variational constraint is expressed as:

$$\delta\phi^{(7/2k)}(t) = \delta\phi^{(7/0)}(t) - \delta\phi^{(k/0)}(t) \tag{A.26c}$$

Next, the second loop closure constraint is defined as:

$$\dot{x}_{T_k}(t)_{path(i)} = \dot{x}_{T_k}(t)_{path(ii)} \tag{A.27a}$$

and from Eqs. (A.17d) and (A.22c), the above condition leads to the following loop closure constraint expressed by the essential velocities.

$$\begin{aligned}\left(\dot{q}_L^{(k)}(t)\right) = &\begin{bmatrix} \frac{-1}{l^{(k)}(t)} & 0 \\ 0 & 1 \end{bmatrix}\Bigg[\left(R\left(\phi^{(k/0)}(t)\right)\right)^T\left\{\dot{s}_C^{(7/0)}(t) + R\left(\phi^{(7/0)}(t)\right)\begin{pmatrix}\hat{l}_k^{(7)} \\ \hat{h}_k^{(7)}\end{pmatrix}\dot{\phi}^{(7/0)}(t)\right\} \\ &+\left[\left(R\left(\phi^{(k/0)}(t)\right)\right)^T\left\{\begin{pmatrix}-s_{2C}^{(7/0)}(t) + \hat{l}_k^{(0)} \\ s_{1C}^{(7/0)}(t) - \hat{h}_k^{(0)}\end{pmatrix} + R\left(\phi^{(7/0)}(t)\right)\begin{pmatrix}\hat{l}_k^{(7)} \\ \hat{h}_k^{(7)}\end{pmatrix}\right\} - \begin{pmatrix}-l^{(k)}(t) \\ 0\end{pmatrix}\right]\dot{\theta}^{(0)}(t)\Bigg] \\ = &\left[Q_{qL/Tp}^{(k)}(t)\right]\left(\dot{q}_{Tp}(t)\right) + \left[Q_{qL/Bp}^{(k)}(t)\right]\left(\dot{q}_{Bp}(t)\right)\end{aligned} \tag{A.27b}$$

where Q-matrices for the top-plate and base-plate velocities are defined as:

$$\left[Q_{qL/Tp}^{(k)}(t)\right] = \begin{bmatrix} \frac{-1}{l^{(k)}(t)} & 0 \\ 0 & 1 \end{bmatrix}\left(R\left(\phi^{(k/0)}(t)\right)\right)^T\begin{pmatrix} I_2 & R\left(\phi^{(7/0)}(t)\right)\begin{pmatrix}\hat{l}_k^{(7)} \\ \hat{h}_k^{(7)}\end{pmatrix}\end{pmatrix} \tag{A.27c}$$

and

$$\begin{aligned}\left[Q_{qL/Bp}^{(k)}(t)\right] = &\begin{bmatrix} \frac{-1}{l^{(k)}(t)} & 0 \\ 0 & 1 \end{bmatrix}(0_{2\times1} \quad 0_{2\times1} \\ &\left(R\left(\phi^{(k/0)}(t)\right)\right)^T\left\{\begin{pmatrix}-s_{2C}^{(7/0)}(t) + \hat{l}_k^{(0)} \\ s_{1C}^{(7/0)}(t) - \hat{h}_k^{(0)}\end{pmatrix} + R\left(\phi^{(7/0)}(t)\right)\begin{pmatrix}\hat{l}_k^{(7)} \\ \hat{h}_k^{(7)}\end{pmatrix}\right\} - \begin{pmatrix}-l^{(k)}(t) \\ 0\end{pmatrix}\Bigg)\end{aligned} \tag{A.27d}$$

Then, the corresponding variational constraint is expressed by the virtual displacements of the k^{th} leg and top plate.

$$\left(\delta q_L^{(k)}(t)\right) = \left[Q_{qL/Tp}^{(k)}(t)\right]\left(\delta q_{Tp}(t)\right) \tag{A.27e}$$

Here, we let $\delta d^{(k)}(t)$ vary to allow the actuating force to be used for the feedback control.

A.3 Kinetics of a 3-Dof Planar Platform

In this section, the equations of motion are derived by utilizing the principle of virtual work obtained from Hamilton's principle. Firstly, the kinetic energy and potential energy as well as those variations are defined.

A.3.1 Kinetic Energy

The system kinetic energy is obtained as the sum of the kinetic energy of the top-plate with body-(8) and that for three legs:

$$K = K_{Tp}(t) + \sum_{k=1}^{3} K_L^{(k)}(t). \tag{A.28}$$

In Eq. (A.28), the kinetic energy of the top-plate with body-(8) is expressed as:

$$K_{Tp}(t) = \frac{1}{2}\left(\dot{X}_{Tp}(t)\right)^T \left[\widehat{M}_{Tp}\right]\left(\dot{X}_{Tp}(t)\right) \tag{A.29a}$$

where the generalized velocities for the top-plate with body-(8) are

$$\left(\dot{X}_{Tp}(t)\right) \equiv \begin{pmatrix} \dot{x}_C^{(7)}(t) \\ \dot{\theta}^{(7)}(t) \\ \dot{x}_C^{(8)}(t) \\ \dot{\theta}^{(8)}(t) \end{pmatrix} \tag{A.29b}$$

and the mass matrix is expressed by mass: m and mass moment of inertia: J_C,

$$\left[\widehat{M}_{Tp}\right]_{6\times 6} = \begin{bmatrix} m^{(7)}I_2 & 0_{2\times 1} & 0_{3\times 3} & \\ 0_{1\times 2}^T & J_{3c}^{(7)} & & \\ & & m^{(8)}I_2 & 0_{2\times 1} \\ 0_{3\times 3} & & 0_{1\times 2}^T & J_{3c}^{(8)} \end{bmatrix} \tag{A.29c}$$

In the Eq. (A.28), the kinetic energy of the k^{th} leg is expressed as:

$$K_L^{(k)}(t) = \frac{1}{2}\left(\dot{X}_L^{(k)}(t)\right)^T \left[\widehat{M}_L^{(k)}\right]\left(\dot{X}_L^{(k)}(t)\right) \tag{A.30a}$$

where the generalized velocities for the upper and lower legs are defined as

$$\left(\dot{X}_L^{(k)}(t)\right) \equiv \begin{pmatrix} \dot{x}_C^{(2k-1)}(t) \\ \dot{\theta}^{(2k-1)}(t) \\ \dot{x}_C^{(2k)}(t) \\ \dot{\theta}^{(2k)}(t) \end{pmatrix} \tag{A.30b}$$

and the mass matrix is

$$\left[\widehat{M}_L^{(k)}\right]_{6\times 6} = \begin{bmatrix} m^{(2k-1)}I_2 & 0_{2\times 1} & 0_{3\times 3} & \\ 0_{1\times 2}^T & J_{3c}^{(2k-1)} & & \\ & & m^{(2k)}I_2 & 0_{2\times 1} \\ 0_{3\times 3} & & 0_{1\times 2}^T & J_{3c}^{(2k)} \end{bmatrix} \tag{A.30c}$$

The generalized velocities in Eq. (A.29a) are expressed by the essential velocities of the top-plate, Eq. (A.24a) and the base-plate excitation velocities, Eq. (A.24b) as

$$\left(\dot{X}_{Tp}(t)\right) = \left[B_{Tp}(t)\right]\left(\dot{q}_{Tp}(t)\right) + \left[B_{Tp/Bp}(t)\right]\left(\dot{q}_{Bp}(t)\right) \tag{A.31a}$$

where B-matrices for the top-plate and base-plate velocities are

$$\left[B_{Tp}(t)\right] = \begin{bmatrix} R(\theta^{(0)}(t)) & 0_{2\times 1} \\ 0_{1\times 2} & 1 \\ R(\theta^{(0)}(t)) & R\left(\theta^{(0)}(t) + \phi^{(7/0)}(t)\right)\begin{pmatrix} -\hat{l}^{(8/7)} \\ 0 \end{pmatrix} \\ 0_{1\times 2} & 1 \end{bmatrix} \tag{A.31b}$$

and

$$\left[B_{Tp/Bp}(t)\right]=\begin{bmatrix} I_2 & R(\theta^{(0)}(t))\begin{pmatrix}-s_{2C}^{(7/0)}(t)\\ s_{1C}^{(7/0)}(t)\end{pmatrix} \\ 0_{1\times 2} & 1 \\ I_2 & R(\theta^{(0)}(t))\left\{\begin{pmatrix}-s_{2C}^{(7/0)}(t)\\ s_{1C}^{(7/0)}(t)\end{pmatrix}+R(\phi^{(7/0)}(t))\begin{pmatrix}-\hat{l}^{(8/7)}\\ 0\end{pmatrix}\right\} \\ 0_{1\times 2} & 1 \end{bmatrix} \quad \text{(A.31c)}$$

The generalized velocities of the k^{th} leg are also expressed by its essential velocities and the excitation velocities as:

$$\left(\dot{X}_L^{(k)}(t)\right)=\left[B_L^{(k)}(t)\right]\left(\dot{q}_L^{(k)}(t)\right)+\left[B_{L/Bp}^{(k)}(t)\right]\left(\dot{q}_{Bp}(t)\right) \quad \text{(A.32a)}$$

where B-matrices for the k^{th} leg and base-plate velocities are

$$\left[B_L^{(k)}(t)\right]=\begin{bmatrix} R\left(\theta^{(0)}(t)+\phi^{(k/0)}(t)\right)\begin{pmatrix}-\hat{l}^{(2k-1)}\\ 0\end{pmatrix} & 0_{2\times 1} \\ 1 & 0 \\ R\left(\theta^{(0)}(t)+\phi^{(k/0)}(t)\right)\begin{pmatrix}-\left(\hat{l}^{(2k-1)}+d^{(k)}(t)\right)\\ 0\end{pmatrix} & R\left(\theta^{(0)}(t)+\phi^{(k/0)}(t)\right)\begin{pmatrix}0\\ 1\end{pmatrix} \\ 1 & 0 \end{bmatrix} \quad \text{(A.32b)}$$

and

$$\left[B_{L/Bp}^{(k)}(t)\right]=\begin{bmatrix} I_2 & R(\theta^{(0)}(t))\left\{\begin{pmatrix}0\\ \hat{h}_k^{(0)}\end{pmatrix}+R(\phi^{(k/0)}(t))\begin{pmatrix}-\hat{l}^{(2k-1)}\\ 0\end{pmatrix}\right\} \\ 0_{1\times 2} & 1 \\ I_2 & R(\theta^{(0)}(t))\left\{\begin{pmatrix}0\\ \hat{h}_k^{(0)}\end{pmatrix}+R(\phi^{(k/0)}(t))\begin{pmatrix}-\left(\hat{l}^{(2k-1)}+d^{(k)}(t)\right)\\ 0\end{pmatrix}\right\} \\ 0_{1\times 2} & 1 \end{bmatrix} \quad \text{(A.32c)}$$

A.3.2 Potential Energy

The virtual potential energy due to the gravitational force is expressed as:

$$\delta U_g=\left(\delta U_g\right)_{Tp}+\sum_{k=1}^{3}\left(\delta U_g\right)_L^{(k)} \quad \text{(A.33a)}$$

where $\left(\delta U_g\right)_{Tp}$ represents the virtual potential energy due to the gravitational force, of the top-plate with body-(7):

$$\left(\delta U_g\right)_{Tp}=-\left(\delta X_{Tp}(t)\right)^T\left(\hat{F}_{gTp}\right)=-\left(\delta q_{Tp}(t)\right)^T\left(F_{gTp}(t)\right) \quad \text{(A.33b)}$$

$$\left(\hat{F}_{gTp}\right)=\begin{pmatrix}0\\ -m^{(7)}g\\ 0\\ 0\\ -m^{(8)}g\\ 0\end{pmatrix},\quad \left(F_{gTp}(t)\right)=\left[B_{Tp}(t)\right]^T\left(\hat{F}_{gTp}\right) \quad \text{(A.33c, d)}$$

and where the virtual potential energy $\left(\delta U_g\right)_L^{(k)}$ of the k^{th} leg due to the gravitational force is

$$\left(\delta U_g\right)_L^{(k)}=-\left(\delta X_L^{(k)}(t)\right)^T\left(\hat{F}_{gL}^{(k)}\right)=-\left(\delta q_L^{(k)}(t)\right)^T\left(F_{gL}^{(k)}(t)\right) \quad \text{(A.33e)}$$

$$\left(\hat{F}_{gL}^{(k)}\right) = \begin{pmatrix} 0 \\ -m^{(2k-1)}g \\ 0 \\ 0 \\ -m^{(2k)}g \\ 0 \end{pmatrix}, \quad \left(F_{gL}^{(k)}(t)\right) = \left[B_L^{(k)}(t)\right]^T \left(\hat{F}_{gL}^{(k)}\right) \tag{A.33f,g}$$

A.3.3 Derivation of Equations of Motion

Hamilton's principle expressed by velocities are defined as

$$\int_{t_0}^{t_1} \left(\delta K - \delta U_g + \delta W_A\right) dt = 0 \tag{A.34a}$$

where the virtual work by non-conservative force δW_A is obtained from the k^{th} leg actuation force

$$\delta W_A = \sum_{k=1}^{3} \delta d^{(k)}(t) F_A^{(k)}(t) \tag{A.34b}$$

The variational velocities which correspond to Eqs. (A.29b) and (A.30b) are

$$\left(\delta X_{Tp}(t)\right) \equiv \begin{pmatrix} \delta x_C^{(7)}(t) \\ \delta\theta^{(7)}(t) \\ \delta x_C^{(8)}(t) \\ \delta\theta^{(8)}(t) \end{pmatrix} = \left[B_{Tp}(t)\right]\left(\delta q_{Tp}(t)\right) \tag{A.35a}$$

and

$$\left(\delta X_L^{(k)}(t)\right) \equiv \begin{pmatrix} \delta x_C^{(2k-1)}(t) \\ \delta\theta^{(2k-1)}(t) \\ \delta x_C^{(2k)}(t) \\ \delta\theta^{(2k)}(t) \end{pmatrix} = \left[B_L^{(k)}(t)\right]\left(\delta q_L^{(k)}(t)\right) \tag{A.35b}$$

In order to obtain the equations of motion for the top plate, the loop closure constrains on variations, Eq. (A.27e) and velocities, Eq. (A.27b) are applied. Then, Eq. (A.33a) can be expressed by $\left(\delta q_{Tp}(t)\right)$ as:

$$\delta U_g = -\left(\delta q_{Tp}(t)\right)^T \left(F_g(t)\right) \tag{A.36a}$$

where

$$\left(F_g(t)\right) = \left(\left(F_{gTp}(t)\right) + \sum_{k=1}^{3} \left[Q_{qL/Tp}^{(k)}(t)\right]^T \left(F_{gL}^{(k)}(t)\right)\right) \tag{A.36b}$$

and Eq.(A.34b) is also expressed by $\left(\delta q_{Tp}(t)\right)$:

$$\delta W_A = \left(\delta q_{Tp}(t)\right)^T [Q_A(t)]^T (F_A(t)) \tag{A.37a}$$

where

$$[Q_A(t)]_{3\times 3} = \begin{bmatrix} \left[Q_{qL/Tp}^{(1)}(t)\right]_2 \\ \left[Q_{qL/Tp}^{(2)}(t)\right]_2 \\ \left[Q_{qL/Tp}^{(3)}(t)\right]_2 \end{bmatrix}, \qquad (F_A(t)) = \begin{pmatrix} F_A^{(1)}(t) \\ F_A^{(2)}(t) \\ F_A^{(3)}(t) \end{pmatrix} \tag{A.37b, c}$$

and $\left[Q_{qL/Tp}^{(k)}(t)\right]_2$ for k=1,2,3, represents the second row of the k^{th} Q-matrix. Substitution of Eqs. (A.35a, b), (A.36a), and (A.37a) into Eq.(A.34a) yields

$$\int_{t_0}^{t_1}\Big(\big(\delta\dot{X}_{Tp}(t)\big)^T\big[\widehat{M}_{Tp}\big]\big(\dot{X}_{Tp}(t)\big)+\sum_{k=1}^{3}\Big(\delta\dot{X}_L^{(k)}(t)\Big)^T\Big[\widehat{M}_L^{(k)}\Big]\Big(\dot{X}_L^{(k)}(t)\Big) +\big(\delta q_{Tp}(t)\big)^T\Big(\big(F_g(t)\big)+[Q_A(t)]^T(F_A(t))\Big)\Big)dt=0 \tag{A.38}$$

Then, from the Eqs. (A.31a), (A.32a), (A.35a, b), and (A.38), the equations of motion for the top plate in configuration space are obtained as:

$$\big[M_{Tp}(t)\big]\big(\ddot{q}_{Tp}(t)\big)+\big[N_{Tp}(t)\big]\big(\dot{q}_{Tp}(t)\big)-\big(F_g(t)\big)=-(F_B(t))+[Q_A(t)]^T(F_A(t)) \tag{A.39a}$$

where the mass matrix is

$$\big[M_{Tp}(t)\big]=\big[B_{Tp}(t)\big]^T\big[\widehat{M}_{Tp}\big]\big[B_{Tp}(t)\big]+\sum_{k=1}^{3}\Big[Q_{qL/Tp}^{(k)}(t)\Big]^T\big[B_L^{(k)}(t)\big]^T\big[\widehat{M}_L^{(k)}\big]\big[B_L^{(k)}(t)\big]\Big[Q_{qL/Tp}^{(k)}(t)\Big] \tag{A.39b}$$

and the nonlinear matrix due to centripetal and Coriolis accelerations is

$$\big[N_{Tp}(t)\big]=\big[B_{Tp}(t)\big]^T\big[\widehat{M}_{Tp}\big]\big[\dot{B}_{Tp}(t)\big] +\sum_{k=1}^{3}\Big[Q_{qL/Tp}^{(k)}(t)\Big]^T\big[B_L^{(k)}(t)\big]^T\big[\widehat{M}_L^{(k)}\big]\Big(\big[\dot{B}_L^{(k)}(t)\big]\Big[Q_{qL/Tp}^{(k)}(t)\Big]+\big[B_L^{(k)}(t)\big]\Big[\dot{Q}_{qL/Tp}^{(k)}(t)\Big]\Big) \tag{A.39c}$$

and $(F_B(t))$ comes from the motion of the base plate as

$$(F_B(t))=\big[M_{Tp/Bp}(t)\big]\big(\ddot{q}_{Bp}(t)\big)+\big[M_{Tp/Bp}(t)\big]\big(\dot{q}_{Bp}(t)\big) \tag{A.39d}$$

where the mass matrix and the nonlinear matrix of the excitation accelerations and velocities of the base plate are

$$\big[M_{Tp/Bp}(t)\big]=\big[B_{Tp}(t)\big]^T\big[\widehat{M}_{Tp}\big]\big[B_{Tp/Bp}(t)\big] +\Sigma_{k=1}^{3}\Big[Q_{qL/Tp}^{(k)}(t)\Big]^T\big[B_L^{(k)}(t)\big]^T\big[\widehat{M}_L^{(k)}\big]\Big(\Big[B_{L/Bp}^{(k)}(t)\Big]+\big[B_L^{(k)}(t)\big]\Big[Q_{qL/Bp}^{(k)}(t)\Big]\Big) \tag{A.39e}$$

$$\big[N_{Tp/Bp}(t)\big]=\big[B_{Tp}(t)\big]^T\big[\widehat{M}_{Tp}\big]\big[\dot{B}_{Tp/Bp}(t)\big] +\Sigma_{k=1}^{3}\Big[Q_{qL/Tp}^{(k)}(t)\Big]^T\big[B_L^{(k)}(t)\big]^T\big[\widehat{M}_L^{(k)}\big]\Big(\Big[\dot{B}_{L/Bp}^{(k)}(t)\Big]+\big[\dot{B}_L^{(k)}(t)\big]\Big[Q_{qL/Bp}^{(k)}(t)\Big]+\big[B_L^{(k)}(t)\big]\Big[\dot{Q}_{qL/Bp}^{(k)}(t)\Big]\Big) \tag{A.39f}$$

ACKNOWLEDGEMENTS

I first would like to thank my advisor, Professor Junya Yamakawa for the continuous support of my doctoral study and research. Since the first day I walked into his office as an undergraduate student, he has taken me under his wing.

I would also wish to express my gratitude to Research Associate Ryosuke Eto for all the support and encouragement he gave me. Without his knowledge and experience, none of the experiments of this study would have been possible.

I would like to express my sincere gratitude to Professor Emeritus Hidenori Murakami, University of California, San Diego, U.S.A., for the continuous support from my M.S. study and research. His guidance and immerse knowledge helped me throughout research and writing papers. Thank you for all the great years of research.

I would also like to thank my committee members, Professor Masanori Harada, Professor Hiroyuki Fujiwara, and Professor Taichi Shiiba of Meiji University, for their invaluable suggestions and advice on the projects.

I would further like to thank the other members of the lab, Mr. Ryuya Kato, Mr. Katsuyoshi Aota, and Mr. Yasuhiro Ichikado. The help they provided throughout my years in graduate school was essential for me to focus on this study.

Lastly, I would like to thank my family, especially my wife and parents for their support throughout my education.

REFERENCES

[1] Suzuki, N., Kitsuta, Y. and Sugiyama, M., 2002, "Rebleeding attack of the cerebral aneurysm at emergency scenes," *Journal of Japanese Society for Emergency Medicine*, Vol.5, No.3, pp.269–274 (in Japanese).

[2] Sagawa, K., Inooka, H. and Inooka, E., 1997, "Development of an Actively Controlled Stretcher for an Ambulance," *Transactions of the Japan Society of Mechanical Engineers*, Series C, Vol.63, No.609, pp.1533–1539 (in Japanese).

[3] Sagawa, K., Inooka, H. and Inooka, E., 1999, "The Effect of an Actively Controlled Stretcher for an Ambulance on the Reduction of Blood Pressure Variation," *Japanese Journal of Medical Electronics and Biological Engineering*, Vol.37, No.3, pp.260–268 (in Japanese).

[4] Ono, T. and Inooka, H., 2005, "2 Degree-of-freedom Actively-controlled Bed for Ambulances," *Transactions of the Japan Society of Mechanical Engineers*, Series C, Vol.71, No.711, pp.46–52 (in Japanese).

[5] Ono, T. and Inooka, H., 2009, "Actively-controlled beds for ambulances, International Journal of Automation and Computing," *Transactions of the Japan Society of Mechanical Engineers*, Series C, Vol.6, No.1, pp.1–6.

[6] Stewart, D., 1965, "A platform with six degrees of freedom," *Proceedings of the IMechE*, Vol. 180, Pt. 1, No. 15, pp.371-385, 1965-66.

[7] Fichter, E.F. 1986, "A Stewart platform based manipulator: General theory and practical construction," *International Journal of Robotics Research* 5(2):157-181.

[8] Lebret, G., Liu, K., and Lewis, F. L., 1993, "Dynamic Analysis and Control of a Stewart Platform Manipulator," *Journal of Field Robotics* Vol.10 No.5: pp. 629-655

[9] Dasgupta, B. and Mruthyunjaya, T., 1998, "A Newton-Euler Formulation for the Inverse Dynamics of the Stewart Platform Manipulator," *Mechanism and Machine Theory* Vol.33 No.8: pp. 1135-1152.

[10] Becerra-Vergus, M. and Belo, E., 2015, "Dynamic Modeling of a Six Degree-of-Freedom Flight Simulator Motion Base," *Journal of Computational and Nonlinear Dynamics* Vol. 10 No.5: p. 051020.

[11] Lee, S. H., Song, J. B., Choi, W. C., Hong, D., 2003, "Position control of a Stewart platform using inverse dynamics control with approximate dynamics." *Mechatronics*.

[12] Do, W. Q. D. and Yang, D. C. H., 1988, "Inverse Dynamic Analysis and Simulation of a Platform Type of Robot," *Journal of Field Robotics* Vol.5 No.3: pp. 209-227.

[13] Liu, K., Fitzgerald, M., Dawson, D. and Lewis, F. L., 1991, "Modelling and Control of a Stewart Platform Manipulator," *ASME DSC* Vol. 33, Control of Systems with Inexact Dynamic Models, pp. 83-89.

[14] Geng, Z., Haynes, L. S., Lee, J. D. and Carroll, R. L., 1992, "On the dynamic model and kinematic analysis of a class of Stewart platforms," *Journal of Robotics and Autonomous Systems* Vol. 9 No. 4: pp. 237-254.

[15] Gallardo, J., Rico, J.M., Frisoli, A., Checcacci, D., and Bergamasco, M., 2003, "Dynamics of parallel manipulators by means of screw theory" *Mechanism and Machine Theory* Vol.38 No.11: pp. 1113-1131.

[16] Liu, M. J., Li, C. X., and Li, C. N., 2000, "Dynamics Analysis of the Gough-Stewart Platform Manipulator," *IEEE Transactions on Robotics and Automation* Vol.16 No.1: pp. 94–98.

[17] Wittenburg, J., 2008, *Dynamics of Multibody Systems, Second Edition,* Springer-Verlag, Berlin, ISBN 978-3-540-73913-5.

[18] Becerra-Vargas, M., Morgado Belo, E., 2012, "Application of H∞ theory to a 6 DOF flight simulator motion base." *Journal of the Brazilian Society of Mechanical Sciences and Engineering*.

[19] Huangl, C.-I., Chang', C.-F., Yu, M.-Y., & Fu, L.-C., 2004, "Sliding-Mode Tracking Control of the Stewart Platform.", *Proceedings of* 2004 5th Asian Control Conference.

[20] Dongsu, W., and Hongbin, G., 2007, "Adaptive sliding control of six-DOF flight simulator motion platform." *Chinese Journal of Aeronautics*.

[21] Iqbal, S., & Bhatti, A. I., 2007, "Robust sliding-mode controller design for a Stewart platform." *Proceedings of International Bhurban Conference on Applied Sciences and Technology, IBCAST*.

[22] Kumar P., R., Chalanga, A., and Bandyopadhyay, B., 2015, "Smooth integral sliding mode controller for the position control of Stewart platform." *ISA Transactions*, *58*, 543–551.

[23] Shiferaw D, Jain A., 2011, "Comparison of joint space and task space integral sliding mode controller implementations of a 6-DOF parallel robot." *Proceedings of the 11th WSEAS international conference on robotics, control and manufacturing technology*.

[24] E. Nadimi, T. Bak, and R. Izadi-Zamanabadi, 2006, "Model predictive controller combined with LQG controller and velocity feedback to control the Stewart platform," *9th IEEE International Workshop on Advanced Motion Control*, pp. 44–49.

[25] F. Lara-Molina, J. Rosário and D. Dumur, 2011, "Robust generalized predictive control of stewart-gough platform", *Robotics Symposium 2011 IEEE IX Latin American*

and IEEE Colombian Conference on Automatic Control and Industry Applications (LARC), pp. 1-6.

[26] Campos, A., Quintero, J., Saltarén, R., Ferre, M., & Aracil, R., 2008, "An active helideck testbed for floating structures based on a stewart-gough platform," 2008 *IEEE/RSJ International Conference on Intelligent Robots and Systems*, *IROS*.

[27] Niwa, S., Tanaka, Y., Goto, H., and Nomiyama, N., 2017, "Active Vibration Compensation for Catwalk by Hydraulic Parallel Mechanism," *Proceedings of The 10th JFPS International Symposium on Fluid Power 2017 FUKUOKA*, 2D22.

[28] Kayano, J., Hanawa, N., Ohtsu, K., Ito, M., 2000, "On An Artificial Horizontal Stabilizing Platform Using AR Model-I." *Journal of Japan Institute of Navigation*, vol. 102, pp. 127-134.

[29] Murakami, H., 2013, "A Moving Frame Method for Multi- Body Dynamics," *Proceedings of the ASME 2013 International Mechanical Engineering Congress & Exposition*, IMECE2013-62833: pp. V04AT04A079; 12 pages. San Diego, CA, November 15–21.

[30] Murakami, H., 2015, "A Moving Frame Method for Multi-Body Dynamics Using SE(3)," *Proceedings of the ASME 2015 International Mechanical Engineering Congress & Exposition*, IMECE2015-51192: pp. V04BT04A003; 19 pages. Houston, Texas, November 13–19.

[31] Frankel, T., 2012, *The Geometry of Physics: An Introduction, 3rd ed*., Cambridge University Press, New York.

[32] Hochreiter, S., and Schmidhuber, 1997, J., Long short-term memory, *Neural computation*. Vol. 9, Number 8, pp.1735‑1780.

[33] Ohtsuka, T., 2004, "A Continuation/GMRES method for fast computation of nonlinear receding horizon control," *Automatica*, vol. 40, pp. 563–574.

[34] Arnold, V. I., 1989, *Mathematical Methods of Classical Mechanics, 2nd ed*., Springer-Verlag, New York.

[35] Holm, D. D., 2008, *Geometric Mechanics: PartII: Rotating, Translating, Rolling*, Imperial College Press, London, UK.

[36] Ball, R. S., 1900, *A Treatise on the Theory of Screws*, Cambridge University Press.

[37] Brockett, R. W., 1984, "Robot Manipulators and the Product of Exponentials Formula," in P. A. Fuhrman, editor, *Mathematical Theory of Networks and Systems*, pp. 120-129, Springer-Verlag.

[38] Murray, R. M., Li, Z., and Sastry, S. S., 1994, *A Mathematical Introduction to Robotic Manipulation*, CRC Press, Boca Raton, FL.

[39] Murakami, H., Rios, O., and Impelluso T. J., 2016, "A Theoretical and Numerical Study of the Dzhanibekov and Tennis Racket Phenomena," *ASME Journal of Applied Mechanics* Vol. 83 No. 11: 111006 (10 pages). DOI: 10.1115/1.4034318.

[40] Asada, H. and Slotine, J.-J. E., 1986, *Robot Analysis and Control*, John Wiley and Sons, New York.

[41] Smith, D., 1974, *Variational Methods in Optimization*, Prentice-Hall, Englewood Cliffs, New Jersey.

[42] Byron, F. W., JR., Fuller, R. W., 1974, *Mathematics of Classical and Quantum Physics*, Dover Publications, Inc., New York.

[43] Ono, T., Eto, R., Yamakawa, J., and Murakami, H., 2018, "Development of Equations of Motion for a Stewart Platform Under Prescribed Mount Motion," *Proceedings of the ASME IMECE 2018*, Paper IMECE2018-87253.

[44] Jazar, R. N., 2010, *Theory of Applied Robotics, Kinematics, Dynamics, and Control,* second edition, Springer New York Dordrecht Heidelberg London.

[45] Khalil, H. K., 2002, *Nonlinear Systems, Third Edition*, Prentice Hall, Upper Saddle River, New Jersey.

[46] Box, G. E. P., Jenkins, G. M., and Reinsel, G. C., 1994, *Time Series Analysis, Forecasting and Control,* 2nd ed. New York: Prentice-Hall.

[47] Kumar, D. N., Raju, K. S., and Sathish, T., 2004, "River Flow Forecasting using Recurrent Neural Networks," *Water Resources Management* 18**,** 143–161.

[48] Mandal, S., Prabaharan, N., 2006, "Ocean wave forecasting using recurrent neural networks," *Ocean Engineering*, Volume 33, Issue 10, pp. 1401-1410.

[49] Cao, Q., Ewing, B. T., Thompson, M. A., 2012, "Forecasting wind speed with recurrent neural networks," *European Journal of Operational Research*, Volume 221, Issue 1, pp. 148-154.

[50] Williams, R. J. and Zipser, D., 1989, "A Learning Algorithm for Continually Running Fully Recurrent Neural Networks," *Neural Computation*, Vol. 1, No. 2, pp. 270–280.

[51] Werbos, P. J., 1990, "Backpropagation Through Time: What It Does and How to Do It," *Proceedings of the IEEE*, Vol. 78, No. 10, pp. 1550–1560.

[52] Gers, F. A., Schmidhuber, J., and Cummins, F., 2000, "Learning to Forget: Continual Prediction with LSTM," *Neural Computation*, Vol. 12, Issue 10, pp. 2451-2471.

[53] Glorot, X., Bengio, Y., 2010, “Understanding the difficulty of training deep feedforward neural networks,” *Proceedings of the thirteenth international conference on artificial intelligence and statistics*, (2010), pp. 249-256.

[54] Kingma, D. P. and Ba, J. L., Adam, 2014, “A method for stochastic optimization”, arXiv:1412.6980.

[55] Duchi, J., Hazan, E., and Singer, Y., 2011, “Adaptive subgradient methods for online learning and stochastic optimization”, *The Journal of Machine Learning Research*, 12:2121–2159.

[56] Tieleman, T. and Hinton, G., 2012, *Lecture 6.5 - RMSProp, COURSERA: Neural Networks for Machine Learning*, Technical report.

[57] Ohtsu, K., Iseki, T., 1995, “Study on the Onboard Predictive Ship Motion Analyser-I.” *Journal of Japan Institute of Navigation*, vol. 92, pp. 177-186.

[58] D.E. Seborg, T.F. Edgar and D.A. Mellichamp, 2011, *Process dynamics and control*, John Wiley & Sons, Inc..

[59] D. G. Luenberger, Y. Ye, 2008, *Linear and Nonlinear Programing, third edition*, Springer, New York.

[60] Bemporad, A., Morari, M., 1999, *Robust model predictive control：A survey；Robustness In Identification and Control*（Eds. by A .Garulli, A. Tesi and A. Vicino） Springer Verlag.

PUBLICATIONS

Journal Papers

1. Ono, T., Eto, R., Yamakawa, J., and Murakami, H., 2021, "Analysis and Control of a Stewart Platform as Base Motion Compensators - Part I: Kinematics Using Moving Frames," *Nonlinear Dynamics*. (accepted for publication)

2. Ono, T., Eto, R., Yamakawa, J., and Murakami, H., 2021, "Analysis and Control of a Stewart Platform as Base Motion Compensators - Part II: Dynamics," *Nonlinear Dynamics*. (accepted for publication)

3. Ono, T., Eto, R., and Yamakawa, J., 2021, "Forecasting Vehicle Accelerations Using LSTM," *Mechanical Engineering Journal*, Vol.8, No.4, pp.21-00045.

International Conference Papers (Peer-Reviewed Full Papers)

4. Rios, O., Ono, T., Murakami, H., Impelluso T.J., 2016, "An Analytical and Geometrical Study of the Dzhanibekov and Tennis Racket Phenomena." *Proceedings of the ASME 2016 International Mechanical Engineering Congress & Exposition*, Paper: IMECE2016-65570, 10 pages, ASME, New York.

5. Rios, O., Ono, T., Murakami, H., 2016, "Development of Active Mechanical Models for Flexible Robots to Duplicate the Motion of Inch Worms and Snakes." *Proceedings of the ASME 2016 International Mechanical Engineering Congress & Exposition*, Paper: IMECE2016-65550, 13 pages, ASME, New York.

6. Murakami, H., Rios, O., Ono, T., 2017. "Development of a Nonlinear, C1-Beam Finite- Element Code for Actuator Design of Slender Flexible Robots." *Proceedings of the ASME 2017 International Mechanical Engineering Congress & Exposition*, Paper IMECE2017-70106, 17 pages, ASME, New York.

7. Ono, T., Eto, R., Yamakawa, J., and Murakami, H., 2018, "Development of Equations of Motion for a Stewart Platform Under Prescribed Mount Motion," *Proceedings of the ASME 2018 International Mechanical Engineering Congress & Exposition*, Paper IMECE2018-87253, 21 pages, ASME, New York.

8. Murakami, H., Ono, T., 2018, "A Variational Derivation of Equations of motion with Contact Constrains using SE(3)," *Proceedings of the ASME 2018 International Mechanical Engineering Congress & Exposition*, Paper: IMECE2018-87126, 12 pages, ASME, New York.

9. Ono, T., Eto, R., Yamakawa, J., and Murakami, H., 2019, "A Control Simulations for a Stewart Platform Compensator Mounted on Moving Base," *Proceedings of the ASME 2019 International Mechanical Engineering Congress & Exposition*, Paper: IMECE2019-10780, 8 pages, ASME, New York.

10. Ono, T., Eto, R., Yamakawa, J., and Murakami, H., 2019, "Dynamic Modeling and Analysis of a Planar Three Degrees-of-Freedom Manipulator Under Prescribed Mount Motion," *Proceedings of the ASME 2019 International Mechanical*

Engineering Congress & Exposition, Paper: IMECE2019-10781, 12 pages, ASME, New York.

11. Murakami, H., Ono, T., 2019, "Analysis and Design of Twin Gyroscopes for Ocean Wave Energy Converters and Ship Roll Stabilizers," *Proceedings of the ASME 2019 International Mechanical Engineering Congress & Exposition*, Paper: IMECE2019-11435, 15 pages, ASME, New York.

12. Ono, T., Eto, R., Yamakawa, J., and Murakami, H., 2020, "Nonlinear Model Predictive Control of a Stewart Platform Motion Stabilizer" *Proceedings of the ASME 2020 International Mechanical Engineering Congress & Exposition*, Paper: IMECE2019-10781, 7 pages, ASME, New York.

Domestic Conference Papers

13. 大野建幸, 江藤亮輔, 山川淳也, "移動体上にあるスチュワートプラットフォームのモデル化と制御", Dynamics and Design Conference 2019 講演論文集, 509, 2019.

14. 大野建幸, 江藤亮輔, 山川淳也, "スチュワートプラットフォームを用いた動揺安定化システムの作業空間解析とモデル予測制御", Dynamics and Design Conference 2020 講演論文集, 552, 2020.

15. 大野建幸, 江藤亮輔, 山川淳也, "LSTM を用いた車両に作用する加速度の予測", 日本機械学会 2020 年度年次大会講演論文集, J16103, 2020.